PHYSICS BEYOND THE STANDARD MODEL: QUARK AND LEPTON FLAVOR MODELS

by

Shu Tian Eu

A dissertation submitted in partial fulfillment of
the requirements for the degree of

Doctor of Philosophy

(Physics)

at the

UNIVERSITY OF WISCONSIN–MADISON

2025

Date of final oral examination: August 12 2024

The dissertation is approved by the following members of the Final Oral Committee:
Lisa L Everett, Professor, Physics
Vernon Barger, Vilas Research Professor and Van Vleck Professor, Physics
Yang Bai, Professor, Physics
Elena D' Onghia, Associate Professor, Astronomy

This thesis is dedicated to my parents, Kwee Guan and Soo Kian, and my siblings, Xi Hao and Cai Le, who have lovingly and unconditionally supported me throughout this long journey.

ACKNOWLEDGMENTS

I am deeply grateful to my advisor, Lisa Everett, for her unwavering support and guidance throughout my academic journey. I could not have been more fortunate to have such an exceptional mentor. Without her, this PhD would not have been possible. She has inspired me not only with her profound knowledge of physics but also with her humility, kindness, passion for educating the next generation of physicists, and wisdom in life. I am extremely grateful for her patience and encouragement—whether it was her understanding and support when I faced unforeseen challenges that forced me to step away from research at times, or her kindness when reviewing my paper drafts, despite the inevitable grammar mistakes.

I also want to express my heartfelt gratitude to my collaborator and mentor, George Wojcik. Working with him has been an extraordinary experience. George, one of the most brilliant and diligent young physicists I have ever met, has selflessly taught me so much about BSM model building and has guided me on an entirely new journey of applying machine learning techniques in this field. I would like to extend my thanks to my collaborators and academic siblings, Ariel Rock and Ricardo Ximenes, for all the insightful discussions and conversations we have shared over the years—both about physics and beyond. I also want to thank the other members of my defense committee, Vernon Barger, Yang Bai, and Elena D'Onghia, for their valuable input and thought-provoking questions on my thesis.

A special thanks to my roommate, Yunlei Liang, for striking up a conversation with me at the airport on the very first day I arrived in this country and for years of friendship thereafter—especially for keeping me sane during the tough pandemic years. I am also deeply grateful to Yuling Dai, Vicky Wen, Yuhan Ji, and Nidhi Sudhir for all the unforgettable moments we shared in Madison. Additionally, I extend my heartfelt thanks to my fellow Malaysians in the U.S., Han Kheng Teoh and Suo Jun Tan, for a friendship that has spanned years and continents and for all the wonderful trips we experienced together. Many thanks to my colleagues, office mates, and friends—both here in the U.S. and back in Malaysia and Singapore—for their unwavering support and friendship throughout this journey.

Most of all, I would like to thank my beloved family for their years of unconditional love, support, and care. Even though I am the only one in the family who studies science and none of them fully understand what I am working on, they have always been incredibly

supportive and proud of me. I am deeply indebted to my parents, who have given me the freedom to pursue my passions beyond societal norms, and to my siblings, who have spent countless hours texting and video calling me, despite the three of us living in completely different time zones.

CONTENTS

LIST OF TABLES

LIST OF FIGURES

ABSTRACT

The origin of the masses and mixing angles of quarks and leptons remains one of the most intriguing problems to explore in particle physics. In the quark sector, we studied a minimal flavored gauge-mediated supersymmetry breaking model in which the Higgs and messenger doublets are embedded in multiplets of the $\mathcal{S}_3$ symmetry. This discrete non-Abelian symmetry correlates the flavor structure of the quark and lepton Yukawa couplings with the structure of the messenger Yukawa couplings that contribute to the soft supersymmetry breaking mass parameters. In the lepton sector, we focused our studies in a class of leptonic portal matter models with an additional $U(1)_D$ symmetry, as motivated by sub-GeV dark matter models. We presented a minimal construction of such leptonic model that address the muon $g-2$ anomaly, and we provided a more complete theory based on a $SU(2) \times SU(2)$ dark gauge group. We also employed new machine learning techniques, namely reinforcement learning, to develop a machine learning model builder to explore this framework. We successfully trained a reinforcement learning agent to explore this model space and found new possible portal matter models that are consistent with experimental constraints including the anomalous muon magnetic moment.

Chapter 1

Introduction

The Standard Model of particle physics (SM) [6–8] has proven to be strikingly successful in describing nature at and below the Tera-electron-volt (TeV) energy scale, having satisfied numerous stringent tests at collider and intensity frontier experiments. The SM is a $SU(3)_c \times SU(2)_L \times U(1)_Y$ gauge theory which describes all the fundamental interactions except gravitational interaction. These fundamental forces are mediated by gauge bosons associated with each gauge symmetry. The strong interaction (also denoted as quantum chromodynamics, QCD) that confines quarks into hadrons, is mediated by 8 massless gluons g of $SU(3)_c$. The electroweak interaction, which is a unified description of electromagnetism and the weak interactions, is mediated by the W and B bosons corresponding to the $SU(2)_L \times U(1)_Y$ group, respectively. The electroweak gauge boson masses are not permitted by gauge invariance. Instead, the charged W and neutral $Z = \cos\theta_W W_3 - \sin\theta_W B$, where θ_W is the weak mixing angle, gain their masses via the Higgs mechanism, in which the vacuum expectation value (vev) of the Higgs boson (a scalar doublet of $SU(2) \times U(1)$) breaks $SU(2)_L \times U(1)_Y$ down to $U(1)_{EM}$, which describes the electromagnetic interactions. The W and Z masses of $m_W = 80.3692 \pm 0.0133$ GeV and $m_Z = 91.1880 \pm 0.0020$ GeV [1] are near the scale of the Higgs vev (~ 100 GeV), and there is one massless gauge boson remaining ($A = \cos\theta_W B + \sin\theta_W W_3$, which is the photon, associated with the unbroken $U(1)_{EM}$.

The SM is a chiral theory, as only the left-handed matter particles carry non-trivial $SU(2)_L$ charges. There are two main categories of fermions: quarks, which are charged under $SU(3)_c$, and leptons, which are $SU(3)_c$ singlets. Labeling the gauge group representations as $(SU(3)_c, SU(2)_L)_{U(1)_Y}$, the matter content of the SM can then be described as follows: the left-handed quark doublets $Q_i = (u_{Li}, d_{Li})$ contains a left-handed up-type quark and down-type quark in the $(\mathbf{3}, \mathbf{2})_{1/6}$ representation. The right-handed up-type quark

singlet u_{Ri} and down-type quark singlet d_{Ri} are in the $(\mathbf{3},\mathbf{1})_{2/3}$ and $(\mathbf{3},\mathbf{1})_{-1/3}$ representations. Here the label $i = \{1,2,3\}$ denotes the generation, since each up (down)-type quark comes in three families: up (down), charm (strange), top (bottom). The left-handed lepton doublets $L_i = (e_{Li}, \nu_{Li})$ contains a left-handed charged lepton and a left-handed neutrino in the $(\mathbf{1},\mathbf{2})_{-1/2}$ representation. The right-handed leptons e_{Ri} have the representation $(\mathbf{1},\mathbf{1})_{-1}$. As before, i denotes the generation index, as there are also three families of charged leptons: electron (e), muon (μ) and tau (τ) and three families of left-handed neutrinos (ν_e, ν_μ, ν_τ). The particle content of the SM is summarized in Table 1.1.

Despite the successes of the Standard Model, the theory has several shortcomings which motivate the model building of physics beyond the SM. In particular, there are several fundamental questions that the SM cannot answer directly, and which require the presence of new physics at some scale to answer. There is a particular subset of questions that we will focus on attempting to address while working on modelling extensions for the SM. The first question is the origin of fermion masses and mixing angles that is unanswered in the SM. This problem, sometimes denoted as the "SM flavor puzzle," includes the questions of why there exist exactly three generations of fermions, and why there exists a hierarchy of scales when it come to the masses and mixing angles of these fermions.

Though the first part of SM flavor puzzle, which is the absence of an underlying reason of why there exist three copies of each particle species (i.e. up-type quarks with electric

Particle Content of The Standard Model			
Field			Representation
Fermions	Quarks	$Q_i = (u_{Li}, d_{Li}) = (u_L, d_L), (c_L, s_L), (t_L, b_L)$	$(\mathbf{3},\mathbf{2})_{1/6}$
		$u_{Ri} = u_R, c_R, t_R$	$(\mathbf{3},\mathbf{1})_{2/3}$
		$d_{Ri} = (d_R, s_R, b_R)$	$(\mathbf{3},\mathbf{1})_{-1/3}$
	Leptons	$L_i = (e_{Li}, \nu_{Li}) = (e_L, \nu_e), (\mu_L, \nu_\mu), (\tau_L, \nu_\tau)$	$(\mathbf{1},\mathbf{2})_{-1/2}$
		$e_{Ri} = e_R, \mu_R, \tau_R$	$(\mathbf{1},\mathbf{1})_{-1}$
Bosons	Gauge Bosons	W	$(\mathbf{1},\mathbf{3})_0$
		B	$(\mathbf{1},\mathbf{1})_0$
		G	$(\mathbf{8},\mathbf{1})_0$
	Scalars	$H = (\phi^+, \phi^0)$	$(\mathbf{1},\mathbf{2})_{1/2}$

Table 1.1: The particle content of the SM and the gauge representations of each field under $(SU(3)_c, SU(2)_L)_{U(1)_Y}$.

Standard Model Particle Masses			
Fermions			
Generation	1	2	3
u-type quarks	u	c	t
Masses	2.16 ± 0.07 MeV	1.2730 ± 0.0046 GeV	172.57 ± 0.29 GeV
d-type quarks	d	s	b
Masses	4.70 ± 0.07 MeV	93.5 ± 0.8 MeV	4.183 ± 0.007 GeV
charged leptons	e	μ	τ
Masses	$0.511 \pm 1.5 \times 10^{-10}$ MeV	$105.658 \pm 2.3 \times 10^{-6}$ MeV	1776.93 ± 0.09 MeV
Bosons			
Gauge Bosons	Photon and Gluon	W	Z
Masses	0	80.3692 ± 0.0133 GeV	91.1880 ± 0.0020 GeV
Scalars	H		
Masses	125.20 ± 0.11 GeV		

Table 1.2: The Standard Model particle masses, where the u, d, s quark masses are the $\overline{MS}$ masses at the scale $\mu = 2$ GeV, the c, b quarks masses are the $\overline{MS}$ masses renormalized at at the $\overline{MS}$ mass, and the t quark mass is the directly measured value [1].

charge $2/3$), may seem like just an aesthetic concern, it is a profound question from the point of view of finding a fundamental description of nature in that it appears to require theoretical input beyond simply constructing an effective quantum field theory (QFT) extending the SM where the particle content is just an input. The second aspect of the flavor puzzle, which is understanding the origin of the fermion masses and mixing angles in both the quark and lepton sectors, is a problem which can in principle be addressed within the general framework effective quantum field theory, though it too might require further ultraviolet (UV) information for a complete description. It is this second problem that will be the focus of the work in this thesis.

To get a better understanding of this aspect of the SM flavor problem, here we discuss quark mixing and lepton mixing in greater detail. Since all three generations of any given particle species have the same SM quantum numbers, we can construct a Lagrangian consisting of their mass terms in term of the flavor eigenstates. In the quark sector, for example, this then gives rise to a 3×3 complex mass matrix for the up-type quarks, and also a 3×3 complex mass matrix for the down-type quarks. These matrices are not diagonal in general and thus they need to be diagonalized using a biunitary transformation to obtain the mass eigenstates. The three generations of quarks and leptons then refer to the lightest,

Observable	**Central Value** $\pm 1\sigma$
A	$0.8215^{+0.0047}_{-0.00882}$
λ	$0.22498^{+0.00023}_{-0.00043}$
$\bar{\rho}$	$0.1562^{+0.0112}_{-0.0040}$
$\bar{\eta}$	$0.3551^{+0.0051}_{-0.0057}$

Table 1.3: The latest results for Wolfenstein parameters from CKM global fit [2].

next lightest and heaviest flavors of the given particle species, in ascending order. As seen in Table 1.2, the range of quark and charged lepton masses span many orders of magnitude, ranging from $\mathcal{O}(0.1)$ MeV to $\mathcal{O}(100)$ GeV.

In the quark sector, this diagonalization process that transforms flavor eigenstates to mass eigenstates also gives rise to flavor-changing processes mediated by W bosons, which couple to both the up-type and down-type quarks. The mixing matrix that mixes generations and encompasses flavor-changing interactions in the quark sector is known as the Cabibbo-Kobayashi-Maskawa (CKM) matrix V_{CKM} [9, 10]. Using the Wolfenstein parametrization [11], V_{CKM} can be expressed in the following form:

$$V_{\text{CKM}} = \begin{pmatrix} 1-\lambda^2/2 & \lambda & A\lambda^3(\rho - i\eta) \\ -\lambda & 1-\lambda^2/2 & A\lambda^2 \\ A\lambda^3(1-\rho-i\eta) & -A\lambda^2 & 1 \end{pmatrix} + \mathcal{O}(\lambda^4) \tag{1}$$

where A, ρ, η are all real and of $\mathcal{O}(1)$, and λ serves like a perturbation parameter with $\lambda = 0.225$. We can see that V_{CKM} is almost diagonal with small non-vanishing off-diagonal entries. The latest results for all these Wolfenstein parameters from CKM global fit are summarized in Table 1.3 [2].

In the lepton sector, with the SM strictly defined as above to include the above-mentioned matter content and only renormalizable operators, the neutrinos are massless. For massless neutrinos, the transformation of the charged leptons into the mass eigenstates via the diagonalization of the charged lepton mass matrix does lead to analogous flavor-changing effects from W boson couplings. However, it is known from neutrino oscillation experiments [12] that neutrinos have masses, and thus flavor-changing effects do arise in suitable extensions of the SM that accommodate neutrino masses. The lepton sector flavor mixing matrix is known as the Pontecorvo-Maki-Nakagawa-Sakata (PMNS) matrix V_{PMNS} [13, 14]. The elements in this matrix are far less precisely known compared to those of

V_{CKM}. However, unlike V_{CKM} that features a nearly diagonal structure, it is know that V_{PMNS} has large off-diagonal entries, most notably a large 23-element that is indicative of maximal or near-maximal mixing. Since the SM lacks the explanation for the hierarchies in masses and mixing angles for both the quark and lepton sectors, it strongly suggests that there might be a more complete theory with an underlying structure for flavor physics at a higher scale, which will be then broken down to the SM after symmetry breaking by some new set of Higgs fields charged under the new family symmetry.

We note that the question of the origin of neutrino masses and the observed lepton mixing angles of the PMNS matrix, is an area of intense study (see for example the PDG review in [15]). However, in the work presented in this thesis, we do not address the origin of neutrino masses and instead focus on the physics of the charged fermions (the quark and charged lepton sectors).

Another problem of the SM that will be considered in our work on physics beyond the SM is the naturalness problem, which is also known as the Higgs hierarchy problem. Unlike fermion masses that are protected from large radiative corrections by the chiral symmetry, the masses of scalar particles like the Higgs boson generally suffer from large radiative corrections. More precisely, the Higgs potential takes the following form:

$$V(H) = \mu^2|H|^2 + \lambda|H|^4, \tag{2}$$

in which μ^2 has dimension of mass-squared and λ is dimensionless. One example of large radiative corrections arising in the SM is the one loop correction from the top Yukawa coupling:

$$\delta\mu^2 = -\frac{3|y_t|^2}{8\pi^2}\Lambda_{\text{UV}}^2 + ..., \tag{3}$$

in which y_t is the top quark Yukawa coupling and Λ_{UV} can be interpreted as the scale of new physics. This form of radiative correction shows that the Higgs mass and vev are unprotected against new physics appearing at the higher scale Λ_{UV}. For example, the Higgs boson mass $m_H \sim 125$ GeV is so much lighter than the Planck scale $M_{\text{PL}} \sim 10^{19}$ GeV in which gravitational physics exists. If $\Lambda_{\text{UV}} \sim M_{\text{PL}}$, this would requires an extreme fine-tuning for the tree-level μ_0 in the bare Lagrangian so that exact cancellation occurs for the Higgs mass to remain small. A more natural treatment to protect the Higgs mass from these large radiative corrections is therefore important to be considered in model building of new physics beyond the SM.

Another question that is not addressed by the SM is the existence of dark matter.

It is evidenced that this not-yet-observed hypothetical form of matter outnumbers the baryonic matter in our universe, and thus far its presence is only observed through the existence of gravitational effects which cannot be explained by general relativity unless more matter is present than what is observed in the universe. These gravitational effects include gravitational lensing, formation and evolution of galaxies, cosmic microwave background anisotropies, the motion of galaxies within galaxy clusters and others [16–20]. Since we have not yet observed dark matter from any direct detection, it suggests that dark matter should have very weak electromagnetic interaction and strong interactions. The SM does not have feasible candidates for dark matter with calculable interactions, and hence any extension of the SM should take this into account. The various models we have studied considered different dark matter candidates that possess minimal couplings to the SM within the corresponding new physics framework of the SM extension in question.

In addition to these three questions arising from the SM, in this thesis, our model-building process also focuses on explaining the long-standing potential muon $g-2$ anomaly. This possible anomaly arises from long-running experiments (first at Brookhaven, and now the current Muon $g-2$ experiment at Fermilab) that measures the anomalous magnetic dipole moment of the muon, which is a sensitivity test of the Standard Model. The first results of the FNAL measurement [5] combined with the BNL measurement [21] now place the discrepancy between the measured value of a_μ and the theoretical expectation of the Standard Model [22–42] at

$$\Delta a_\mu = a_\mu^{\text{exp}} - a_\mu^{\text{SM}} = (251 \pm 59) \times 10^{-11}, \tag{4}$$

indicating a significance of 4.2σ. However, recently there is a disagreement in Δa_μ between the data driven Muon $g-2$ Theory Initiative calculation of its SM value [22] and the lattice calculation of the hadronic vacuum polarization contribution [43–47]. If this discrepancy is indeed due to new physics instead of the hadronic vacuum polarization contribution, any extensions of the SM should then be able to explain this anomaly. For all the model-building projects presented in this thesis, we follow the assumption that the current value quoted by the Theory Initiative is representative of the SM theoretical prediction, and explore new physics scenarios that can address the corresponding anomaly. It should be noted though that if the SM theory prediction is adjusted along the lines of some current lattice computations, reducing the significance of any potential anomaly in the muon $g-2$ observable, this would simply change the viable parameter space region for the new physics theories considered here.

Of the many possible beyond-the-Standard-Model (BSM) extensions that attempt to address these questions, in this thesis, we have considered two general classes of models: the minimal supersymmetric standard model (MSSM) with gauge-mediated supersymmety breaking (GMSB), and the (non-supersymmetric) portal matter models which feature vector-like particles charged under a dark $U(1)$ group. We focused on the quark sector in the former and the lepton sector in the latter. In addition to the traditional approaches employed in exploring the large parameter space of various couplings, we also employed machine learning techniques, namely reinforcement learning (RL) to explore BSM parameter spaces. By expressing any BSM model with pre-specified gauge group as graphs, the RL agent can explore spaces of models without user-specified fixed particle content. As a proof of concept, we applied this technique to the class of simple leptonic portal matter model studied. The minimal models found include both known and previously unstudied examples that can accommodate the muon anomalous magnetic moment and satisfy precision electroweak and flavor constraints. This method represents a step forward in enabling an automated model-building process for physics beyond the Standard Model.

In Chapter 2, we present work done in collaboration with Lisa L. Everett, Neil Leonard and Todd Garon [48], which proposes a minimal flavored gauge-mediated supersymmetry breaking model (FGM) within the MSSM framework in which the Higgs and messenger doublets are embedded in multiplets of the $\mathcal{S}_3$ symmetry. This discrete non-Abelian symmetry correlates the flavor structure of the quark and lepton Yukawa couplings with the structure of the messenger Yukawa couplings that contribute to the soft supersymmetry breaking mass parameters. This class of theories is of interest, since it explores the regions of parameter space in which the MSSM with gauge-mediated supersymmetry can remain viable given the Higgs mass constraint and the search for TeV-scale new physics at the Large Hadron Collider (LHC).

To provide a brief background for this project, supersymmetry is a symmetry that maps every SM particle to a superpartner of opposite spin statistics (e.g. each boson has a fermionic superpartner and vice versa). The general paradigm that supersymmetry might be present in nature, and softly broken at TeV scales, as for example in MSSM as defined to be the minimal supersymmetric extension of the SM, with two electroweak Higgs doublets and conserved R-parity, has been of profound interest over many decades in the search for BSM physics [49–53] This paradigm has numerous phenomenological motivations, including improving gauge coupling unification, providing a resolution to the Higgs hierarchy problem, providing a good dark matter candidate, and potentially

explaining the possible discrepancy in a_μ as described above, among others.

Since every particle has its own superpartner within supersymmetric theories, the scalar superpartner will generate a one loop correction in addition to the fermionic contribution given in Eq. 3. This scalar loop correction has the same magnitude but opposite sign to its fermionic counterpart, thus the cancellation is exact to all orders as long as the relationship between dimensionless coupling constants for fermion and scalar loops hold in unbroken supersymmetry. Supersymmetry must be broken spontaneously, which cannot occur at tree level due to the Supertrace theorem. For a discussion of this issue, see e.g. [49]. The standard approach is to work within the hidden sector paradigm, in which there exists a fully renormalizable theory where supersymmetry is broken in some hidden sector at a higher scale and then communicated to the observable sector via some mediation mechanism. There are several promising mediation mechanisms, and the one we focus on here is gauge mediation. In gauge-mediated models, supersymmetry is broken in the hidden sector by the F component of a Standard Model singlet field X, that couples to messenger fields, which are vectorlike pairs of SM-charged fermions. The messenger fields couple to SM matter fields through SM gauge interactions, thus communicating supersymmetry breaking from the hidden sector at the loop level. This mechanism thus communicates supersymmetry breaking effects to our observable sector through these new messenger fields.

In the minimal implementation of gauge mediation (mGMSB), the messenger fields have Yukawa couplings only to the hidden sector field X, and not directly to any of the SM matter or Higgs particles. However, there are some problems with mGMSB. Most notably, to get a Higgs mass around 125 GeV as constrained by experimental data, we need to have very heavy stops (the superpartners of top quarks) or maximal stop mixing. The stop quarks predicted within this theory are generically extremely heavy, making them beyond the reach of the LHC, and rendering the minimal scenario difficult to test experimentally. This suggests that possible variations of this minimal model should be considered. One such interesting possible extension is FGM which allows mixing between Higgs and the messengers. A discrete non-Abelian symmetry $\mathcal{S}_3$ controls the messenger Yukawa couplings and contributes to the generation of hierarchical Yukawa couplings for the quarks and charged leptons of the Standard Model. The choice of a discrete non-Abelian symmetry for this purpose not only provides more predictive power than the often-used case of $U(1)$ symmetries in the literature, it also has further motivation from the fact that such symmetries are often used in generating the fermion masses and mixing angles in

both the quark and lepton sectors.

The famous μ/B_μ problem associated with the MSSM Higgs sector that commonly exists in gauge-mediated theories [54], is a significant constraint due to the predicted messenger-Higgs mixing as governed by the $\mathcal{S}_3$ symmetry. However, this problem can be alleviated through an extended Higgs-messenger sector that involves both $\mathcal{S}_3$ singlet and doublet fields, which allows for independent tuning of both μ and B_μ to phenomenologically acceptable ranges. This extended set of Higgs-messenger fields has significant implications not only for the low energy phenomenology, but also for the paths for addressing the SM flavor puzzle within this framework. To be more precise, we have studied the relationship between different coupling constants in the superpotential that gives rise to the right low energy phenomena - the observed quark mass hierarchy. There are two different limits: when we assume the coupling constant for the $\mathcal{S}_3$ singlet term dominates, and when we assume the coupling constant for the $\mathcal{S}_3$ doublet dominates. In the case of singlet-dominated limit, we also consider a specific scenario based on the flavor democratic limit in which all coupling constants are set to unity, and perturbations are introduced to break the $\mathcal{S}_3$ flavor symmetry. The perturbation parameters are estimated using known fermion masses, and we examined their effects on the superpartner mass spectra and the estimation of V_{CKM}. The theory does predict heavy superpartners, though not as heavy as in mGMSB, and can be tested at near-future and longer-term runs of the LHC.

In Chapter 3, which presents research done in collaboration with George N. Wojcik, Lisa L. Everett and Ricardo Ximenes [55], we shifted our focus to another class of models known as the vector portal matter model of dark matter. In this setup, the SM is augmented to include a dark Abelian gauge symmetry, $U(1)_D$. The dark matter candidate then consists of some particle that is uncharged under the SM gauge group and charged under $U(1)_D$ and a dark photon which serves as the force carrier of the $U(1)_D$. The minimal interaction between the dark matter and ordinary matter can then be explained by the small kinetic mixing between the dark $U(1)_D$ and the SM $U(1)_Y$. This small kinetic mixing is induced at loop level by heavy vector-like particles - the portal matter that are charged under both $U(1)_D$ and $U(1)_Y$, with kinetic mixing strength characterized by a parameter $\epsilon \sim 10^{-(3-5)}$. The dark matter and dark photon in this model would be of sub-GeV range. It was previously found that a minimal model of portal matter would have tension with the observed $g-2$ anomaly [56]. In this work, we demonstrated that with the addition of several portal matter particle species (say a singlet and a doublet under $SU(2)_L$), and hence more mass scales in the system, the chiral enhancement term stemming from the SM Higgs coupling between

the two portal matter species can have a sufficient contribution to the anomalous muon magnetic moment.

In Chapter 4, which presents work done in collaboration with George N. Wojcik, Lisa L. Everett and Ricardo Ximenes [4], we extended the minimal construction of leptonic portal matter model discussed in Chapter 3 with a $SU(2)_A \times SU(2)_B$ dark gauge group and associate it with a flavor symmetry in the second and third lepton generations. In this extended dark gauge sector, SM and portal matter fields exist as members of the same dark gauge multiplets, which provides a natural UV extension of simple portal matter models. In addition to having kinetic mixing and anomaly-free features similar to the minimal model, the multiplet structure we choose in this extended model relates some of the Higgs Yukawa couplings between isospin singlet and doublet portal matter directly with observed SM lepton masses. Constraints on flavor-changing neutral currents are significantly mitigated with the addition of a Z_2 global discrete symmetry to the theory. We discover two qualitatively different scenarios in which muon $g-2$ anomaly can be addressed. We also find that a multi-TeV muon collider has excellent prospects for constraining or measuring the crucial parameters of this model.

In Chapter 5, which describes work done in collaboration with George N. Wojcik and Lisa L. Everett [57, 58], we took a first step toward automating the model-building process for BSM physics using a machine learning technique called reinforcement learning (RL). RL is a machine learning technique that trains an agent to make decisions towards achieving a goal, by interacting with a designed environment. Unlike supervised learning and unsupervised learning where an agent learns from a set of data, the RL agent learns by trial-and-error similar to how humans learn. An RL agent makes observations and takes actions within an environment, and receives feedback in the form of rewards or punishments. Over time, the agent learns to maximize cumulative rewards by developing a policy that maps states of the environment to the optimal actions. This learning process is typically modeled using Markov Decision Processes (MDP). As a proof of concept, we used the graph grammar method developed by our collaborator George N. Wojcik, which is a novel method that translates any BSM models into mathematical graphs that can be processed by graph neural network, to represent our simple leptonic portal matter theories. We then use this graph grammar to create a RL environment tasked with creating models with these vector-like leptons that are consistent with a list of a variety of precision observables. The agent succeeds in developing models that can address the observed muon anomalous magnetic moment discrepancy while remaining consistent with flavor violation

and electroweak precision observables, including both constructions that have previously been studied (similar to the one in Chapter 3) as well as new models which have not, to our knowledge, previously been identified. The method demonstrates a new possible direction and technique in BSM model building, with a more efficient automated exploration of the enormous space of possible BSM extensions.

Chapter 2

Flavored Gauge-Mediated Supersymmetry Breaking Model with Discrete Non-Abelian Symmetry

2.1 Introduction

In the LHC era, the search for physics beyond the Standard Model (SM) has proven elusive, and standard frameworks for TeV-scale new physics are highly constrained. For the well-studied case of extensions of the Standard Model to include softly broken $\mathcal{N} = 1$ supersymmetry, such as the minimal supersymmetric standard model (MSSM), the LHC bounds indicate that if softly broken supersymmetry does indeed play a role in any new physics at the next rung of the energy ladder, its implementation is necessarily more complicated and ostensibly fine-tuned than originally anticipated. In this context, given the vast nature of the parameter space associated with the soft supersymmetry breaking sector, frameworks such as the MSSM can remain viable. However, patterns of possibly viable MSSM parameter regions would then be indicated, perhaps pointing to a specific organizing principle at higher energies.

One such example is within the context of gauge-mediated supersymmetry breaking (GMSB). In its minimal implementation, its distinctive phenomenology is characterized by a superpartner mass spectrum with a sizable splitting between the $SU(3)_c$-charged superpartners (squarks and gluinos) and the superpartners charged only under the electroweak symmetry (sleptons and electroweakinos), with the splitting governed by the messenger mass scale and the number of messenger pairs (taken to be $\mathbf{5}$, $\overline{\mathbf{5}}$ with respect to $SU(5)$). However, the minimal implementation does not easily allow for a 125 GeV Higgs mass, requiring very high messenger scales and subsequent squark and gluino masses that are far out of reach of the LHC [59, 59–74]. As such, nonminimal implementations of gauge

mediation, such as general gauge mediation [75], or scenarios in which the MSSM fields and the messenger fields interact directly via renormalizable superpotential couplings, have now long been explored [68, 69, 73, 74, 76–92].

Of the many intriguing options for direct couplings between the messenger and matter sectors, the *flavored gauge mediation* framework, which exploits the fact that the electroweak Higgs fields can mix with the doublet components of the messenger pairs, has been of particular interest in the literature [77, 84–90, 93–97]. In flavored gauge mediation (FGM) models, Higgs-messenger mixing leads to the generation of messenger Yukawa couplings, which affect the prediction of the soft supersymmetry breaking mass parameters at the input (messenger mass) scale. The messenger Yukawa contributions not only affect the superpartner mass spectrum, but also can generically can lead to the nontrivial possibility of flavor mixing in the soft terms. In viable FGM scenarios, therefore, the messenger Yukawa couplings are controlled by additional symmetries, and their forms are also intimately connected to the generation of the MSSM Yukawa couplings of the quarks and leptons. The case of $U(1)$ symmetries, as explored extensively for example in [74], allows for great flexibility in constructing viable models with one or more vectorlike pairs of messengers. In addition, it was shown in [93] that flavor-mixing contributions to the soft terms in such scenarios are much smaller than naive expectations might suggest, and can be consistent with stringent bounds from flavor-changing processes, depending on the model in question.

Instead of using Abelian symmetries to control the messenger Yukawa couplings, an alternative is to build models based on discrete non-Abelian symmetries. Such symmetries have been extensively used as governing principles for the generation of viable SM fermion masses and mixing parameters [98–100]. In flavored gauge mediation, this possibility was first explored in detail in [85], where the authors constructed a two-family scenario based on the discrete non-Abelian symmetry $\mathcal{S}_3$, with the Higgs and messenger fields connected within $\mathcal{S}_3$ doublets. This idea was then extended to incorporate three families [95, 96, 101]. Most notably, it was realized in [95] that to avoid a severe μ/B_μ problem, the Higgs-messenger sector should be extended to include $\mathcal{S}_3$ singlet representations as well as doublet representations. This leads to scenarios with a minimal number $N = 2$ of messenger pairs (in contrast to the $U(1)$ cases, which allow for one messenger pair), which enhances the splitting of the squark and gluino masses compared to the slepton and electroweakino masses. Further embedding of the MSSM fields in $\mathcal{S}_3$ representations allows for the possibility that $\mathcal{S}_3$ can play a role as part of the family symmetry that governs the SM fermion masses and mixings. A specific implementation of this idea was explored

in [96], as well as in [101], in which the Higgs-messenger singlets play a dominant role in generating the third family SM fermion masses.

To get a better understanding of the μ/B_μ problem and why an extended messenger-Higgs sector helps in alleviating this problem, here we give a brief overview of this issue. The μ/B_μ problem is a variant of the supersymmetric μ-problem that arises in GMSB. μ is the supersymmetric Higgs mass parameter that appears in the higgsino mass terms in MSSM Lagrangian as well as in the Higgs squared-mass terms in the scalar potential $V \sim |\mu|^2(|H_u|^2 + |H_d|^2)$. For electroweak symmetry breaking to occur and the Higgs vev to remain at $\mathcal{O}(100)$ GeV, μ needs to be around $\mathcal{O}(10^2 - 10^3)$ GeV to allow for the needed cancellation with the negative soft squared-mass term. This mass scale of μ and the exact cancellation is unnatural, since there is no reason why $|\mu|^2$ should be around the same order as m^2_{soft} and also so much smaller than M^2_{PL}. This is called "the μ problem" in supersymmetry. In GMSB, there is a further complication, as GMSB generically predicts that the $b = B_\mu\mu$ term arising in the soft terms of Higgs potential $V_{\text{soft}} = m^2_{H_u}|H_u|^2 + m^2_{H_d}|H_d|^2 + (bH_uH_d + \text{h.c.})$ arises at the same loop order as the μ term. Therefore, it is generally related to μ by $b = 16\pi^2\mu^2 \gg \mu^2$. Therefore, if μ is at the weak scale, B_μ will be parametrically larger and will violate the naturalness criterion [102], but if instead B_μ is set the weak scale, then μ would be too small.

As mentioned above, in the scenarios analyzed here, this problem is alleviated through an extended Higgs-messenger sector that involves both $\mathcal{S}_3$ singlet and doublet fields, which allows for independent tuning of both μ and B_μ to phenomenologically acceptable ranges. In short, if we have only the $\mathcal{S}_3$ doublet fields in the Higgs-messenger sector, then the B_μ term is predicted to be too large (at the messenger scale), which would not allow for viable electroweak symmetry [95]. The addition of the $\mathcal{S}_3$ singlet Higgs-messenger field introduces an additional degree of freedom that allows for the decoupling of the generation of the μ and B_μ terms, which enables them to be tuned separately to acceptable values. While this does not provide a dynamical solution to the μ problem of supersymmetry since tuning is required, what has been achieved is the possible of a phenomenologically viable Higgs sector within this class of FGM models [95].

This class of $\mathcal{S}_3$ Higgs-messenger mixing FGM models has been explored previously for the case of only one generation of quark fields [95, 96], and the question of the origin of first and second quark generation mixing within this scenario was presented in [101]. In this chapter, in work published in [48], we provide a comprehensive analysis of the FGM $\mathcal{S}_3$ scenario, summarizing and extending this previous work. The aim is to explore

other viable corners of parameter space of these theories and the subsequent effects of including nonleading corrections to the fermion masses. We identify several viable parameter regions, describe their phenomenological consequences, and compare them to the $U(1)$ FGM benchmark scenarios in the literature. We will see that quite generally, it is not easy to generate viable fermion masses while maintaining flavor-diagonal soft terms, and we will characterize the extent to which such flavor nondiagonal terms are constrained in these theories. The examples studied here all feature very heavy squarks and gluinos, very heavy Higgs fields, and lighter sleptons, charginos, and neutralinos. As such, they provide working examples of currently allowed MSSM parameter space that will continue to be constrained at the LHC and future colliders.

This chapter is structured as follows. We begin with a brief overview of the flavored gauge mediation framework studied here, and describe various options for obtaining hierarchical quark and charged lepton masses. Next, we describe several concrete models, and analyze their mass spectra in detail. Finally, we present our summary and conclusions.

2.2 Theoretical Background

As described in [95], the FGM $\mathcal{S}_3$ scenario studied here assumes a specific set of Higgs-messenger fields and supersymmetry-breaking fields. The quantum numbers of these fields with respect to $\mathcal{S}_3$ are given in Table 2.1. Here the $\mathcal{H}^{(2)}_{u,d}$ are Higgs-messenger $\mathcal{S}_3$ doublets, the

	$\mathcal{H}^{(2)}_u$	$\mathcal{H}^{(1)}_u$	$\mathcal{H}^{(2)}_d$	$\mathcal{H}^{(1)}_d$	$T_{\bar{d}k}$	T_{dk}	X_H	X_T
$\mathcal{S}_3$	$\mathbf{2}$	$\mathbf{1}$	$\mathbf{2}$	$\mathbf{1}$	$\mathbf{1}$	$\mathbf{1}$	$\mathbf{2}$	$\mathbf{1}$

Table 2.1: The field content and $\mathcal{S}_3$ charges for the messenger and supersymmetry breaking sectors.

$\mathcal{H}^{(1)}_{u,d}$ are Higgs-messenger $\mathcal{S}_3$ singlets, and X_H is a supersymmetry breaking field that also breaks the $\mathcal{S}_3$ symmetry. The $T_{\bar{d}k,dk}$ denote the $SU(3)_c$ triplets which have the appropriate quantum numbers to complete approximate $\mathbf{5}$, $\overline{\mathbf{5}}$ multiplets with the messengers and X_T is the supersymmetry breaking field that couples to these triplets [1]. Focusing on the

[1]The triplet messengers and the X_T field are chosen for simplicity to be singlets with respect to the $\mathcal{S}_3$ Higgs-messenger symmetry. Note that this choice is not consistent with a full embedding of this scenario into a grand unified theory. This would require more extended model-building that would also need to address the well-known doublet-triplet splitting issue in grand unified models).

Higgs-messenger fields, we can write $\mathcal{H}_{u,d}^{(2)}$ and $\mathcal{H}_{u,d}^{(1)}$ as

$$\begin{aligned}
\mathcal{H}_u &\equiv \begin{pmatrix} (\mathcal{H}_u^{(2)})_1 \\ (\mathcal{H}_u^{(2)})_2 \\ \mathcal{H}_u^{(1)} \end{pmatrix} \equiv \begin{pmatrix} \mathcal{H}_{u1}^{(2)} \\ \mathcal{H}_{u2}^{(2)} \\ \mathcal{H}_u^{(1)} \end{pmatrix} = \mathcal{R}_u \begin{pmatrix} H_u \\ M_{u1} \\ M_{u2} \end{pmatrix} \\
\mathcal{H}_d &\equiv \begin{pmatrix} (\mathcal{H}_d^{(2)})_1 \\ (\mathcal{H}_d^{(2)})_2 \\ \mathcal{H}_d^{(1)} \end{pmatrix} \equiv \begin{pmatrix} \mathcal{H}_{d1}^{(2)} \\ \mathcal{H}_{d2}^{(2)} \\ \mathcal{H}_d^{(1)} \end{pmatrix} = \mathcal{R}_d \begin{pmatrix} H_d \\ M_{d1} \\ M_{d2} \end{pmatrix},
\end{aligned} \tag{5}$$

in which $H_{u,d}$ are the electroweak Higgs fields of the MSSM, $M_{u1,d1}$ and $M_{u2,d2}$ are gauge mediation messenger doublets, and $\mathcal{R}_{u,d}$ are unitary matrices whose form is governed by the couplings of the Higgs-messenger fields to X_H, which obtains both a scalar and F-component vacuum expectation value (VEV). As shown in [95], consistency requirements and obtaining the needed mass hierarchy between the MSSM Higgs fields $H_{u,d}$ and the heavy messengers $M_{ui,di}$ require that $\mathcal{R}_{u,d}$ are given by

$$\mathcal{R}_{u,d} = \begin{pmatrix} \frac{1}{\sqrt{3}} & \mp\frac{1}{2}\left(1+\frac{1}{\sqrt{3}}\right) & \frac{1}{2}\left(1-\frac{1}{\sqrt{3}}\right) \\ \frac{1}{\sqrt{3}} & \pm\frac{1}{2}\left(1-\frac{1}{\sqrt{3}}\right) & -\frac{1}{2}\left(1+\frac{1}{\sqrt{3}}\right) \\ \frac{1}{\sqrt{3}} & \pm\frac{1}{\sqrt{3}} & \frac{1}{\sqrt{3}} \end{pmatrix}. \tag{6}$$

We turn now to the MSSM fields and their interactions with the Higgs-messenger fields. Although various possibilities exist, as discussed in [95], we make the key assumption that the three generations of SM quarks and leptons are embedded into doublet and singlet representations of $\mathcal{S}_3$, as summarized in Table 2.2. With these $\mathcal{S}_3$ charge assignments, the

	$\mathcal{H}_u^{(2)}$	$\mathcal{H}_u^{(1)}$	$\mathcal{H}_d^{(2)}$	$\mathcal{H}_d^{(1)}$	$Q_{\mathbf{2}}$	$Q_{\mathbf{1}}$	$\bar{u}_{\mathbf{2}}$	$\bar{u}_{\mathbf{1}}$	$\bar{d}_{\mathbf{2}}$	$\bar{d}_{\mathbf{1}}$	$L_{\mathbf{2}}$	$L_{\mathbf{1}}$	$\bar{e}_{\mathbf{2}}$	$\bar{e}_{\mathbf{1}}$	X_H
$\mathcal{S}_3$	$\mathbf{2}$	$\mathbf{1}$	$\mathbf{2}$	$\mathbf{1}$	$\mathbf{2}$	$\mathbf{1}$	$\mathbf{2}$	$\mathbf{1}$	$\mathbf{2}$	$\mathbf{1}$	$\mathbf{2}$	$\mathbf{1}$	$\mathbf{2}$	$\mathbf{1}$	$\mathbf{2}$

Table 2.2: Charges for an $\mathcal{S}_3$ model of the Higgs-messenger fields and the MSSM matter fields. Here the $SU(3)$ triplet messengers and the associated X_T field are not displayed for simplicity.

superpotential couplings of the MSSM matter fields and the Higgs-messenger fields, for example for the up quarks, are given by

$$W^{(u)} = \tilde{y}_u\Big[Q_{\mathbf{2}}\bar{u}_{\mathbf{2}}\mathcal{H}_u^{(2)} + \beta_{1u}Q_{\mathbf{2}}\bar{u}_{\mathbf{2}}\mathcal{H}_u^{(1)} + \beta_{2u}Q_{\mathbf{2}}\bar{u}_{\mathbf{1}}\mathcal{H}_u^{(2)} + \beta_{3u}Q_{\mathbf{1}}\bar{u}_{\mathbf{2}}\mathcal{H}_u^{(2)} + \beta_{4u}Q_{\mathbf{1}}\bar{u}_{\mathbf{1}}\mathcal{H}_u^{(1)}\Big]. \tag{7}$$

In Eq. (7), $\tilde{y}_u$ is a dimensionless overall factor, and the quantities β_{1u}, β_{2u}, β_{3u}, and β_{4u} are dimensionless quantities that characterize the different couplings as allowed by $\mathcal{S}_3$. (Analogous forms hold for the down quarks and the charged leptons; we will ignore the effects of neutrino masses.) In the basis given by

$$Q = (Q_{\mathbf{2}}, Q_{\mathbf{1}})^T = ((Q_{\mathbf{2}})_1, (Q_{\mathbf{2}})_2, Q_{\mathbf{1}})^T, \qquad \overline{u} = (\overline{u}_{\mathbf{2}}, \overline{u}_{\mathbf{1}})^T = ((\overline{u}_{\mathbf{2}})_1, (\overline{u}_{\mathbf{2}})_2, \overline{u}_{\mathbf{1}})^T, \tag{8}$$

the superpotential couplings of Eq. (7) can be expressed in matrix form as

$$W^{(u)} = \tilde{y}_u Q^T \begin{pmatrix} \mathcal{H}^{(2)}_{u1} & \beta_{1u}\mathcal{H}^{(1)}_{u} & \beta_{2u}\mathcal{H}^{(2)}_{u2} \\ \beta_{1u}\mathcal{H}^{(1)}_{u} & \mathcal{H}^{(2)}_{u2} & \beta_{2u}\mathcal{H}^{(2)}_{u1} \\ \beta_{3u}\mathcal{H}^{(2)}_{u2} & \beta_{3u}\mathcal{H}^{(2)}_{u1} & \beta_{4u}\mathcal{H}^{(1)}_{u} \end{pmatrix} \bar{u}. \tag{9}$$

From here, we can easily identify the MSSM Yukawa coupling Y_u and the messenger Yukawa couplings Y'_{u1}, Y'_{u2}, as

$$Y_u = \frac{\tilde{y}_u}{\sqrt{3}} \begin{pmatrix} 1 & \beta_{1u} & \beta_{2u} \\ \beta_{1u} & 1 & \beta_{2u} \\ \beta_{3u} & \beta_{3u} & \beta_{4u} \end{pmatrix}, \tag{10}$$

and

$$Y'_{u1} = \tilde{y}_u \begin{pmatrix} -\frac{1}{2} - \frac{1}{2\sqrt{3}} & \frac{\beta_{1u}}{\sqrt{3}} & \frac{\beta_{2u}}{2} - \frac{\beta_{2u}}{2\sqrt{3}} \\ \frac{\beta_{1u}}{\sqrt{3}} & \frac{1}{2} - \frac{1}{2\sqrt{3}} & -\frac{\beta_{2u}}{2} - \frac{\beta_{2u}}{2\sqrt{3}} \\ \frac{\beta_{3u}}{2} - \frac{\beta_{3u}}{2\sqrt{3}} & -\frac{\beta_{3u}}{2} - \frac{\beta_{3u}}{2\sqrt{3}} & \frac{\beta_{4u}}{\sqrt{3}} \end{pmatrix} \tag{11}$$

$$Y'_{u2} = \tilde{y}_u \begin{pmatrix} \frac{1}{2} - \frac{1}{2\sqrt{3}} & \frac{\beta_{1u}}{\sqrt{3}} & -\frac{\beta_{2u}}{2} - \frac{\beta_{2u}}{2\sqrt{3}} \\ \frac{\beta_{1u}}{\sqrt{3}} & -\frac{1}{2} - \frac{1}{2\sqrt{3}} & \frac{\beta_{2u}}{2} - \frac{\beta_{2u}}{2\sqrt{3}} \\ -\frac{\beta_{3u}}{2} - \frac{\beta_{3u}}{2\sqrt{3}} & \frac{\beta_{3u}}{2} - \frac{\beta_{3u}}{2\sqrt{3}} & \frac{\beta_{4u}}{\sqrt{3}} \end{pmatrix}. \tag{12}$$

These results are for the up sector; again, analogous relations hold for the down quarks and charged leptons, with the replacements $u \to d, e$ in all parameters, respectively.

For arbitrary values of the coefficients, Eq. (10) does not result in hierarchical fermion masses. It is only at special values of the couplings, corresponding to various enhanced symmetry points, that we can obtain a realistic quark mass hierarchy at leading order. To see this, we note that we can diagonalize this system explicitly and examine parameter sets where viable eigenvalue hierarchies can be obtained. For example, in the up quark sector, we can follow standard procedures and consider the Hermitian combinations $Y_u Y_u^\dagger$

and $Y_u^\dagger Y_u$. It is straightforward to calculate following exact results for their eigenvalues (denoted by $\lambda_{1u,2u,3u}$):

$$\lambda_{1u} = \frac{\tilde{y}_u^2}{3}(1-\beta_{1u})^2, \qquad \lambda_{2u,3u} = \frac{\tilde{y}_u^2}{6}\left((1+\beta_{1u})^2 + 2(\beta_{2u}^2+\beta_{3u}^2) + \beta_{4u}^2 \mp \sqrt{\Lambda_u}\right), \tag{13}$$

in which Λ_u is given by

$$\begin{aligned}\Lambda_u &= (1+\beta_{1u})^4 + 4(\beta_{2u}^4+\beta_{3u}^4) + \beta_{4u}^4 + 4((1+\beta_{1u})^2+\beta_{4u}^2)(\beta_{2u}^2+\beta_{3u}^2) - 2(1+\beta_{1u})^2\beta_{4u}^2 \\ &- 8\beta_{2u}^2\beta_{3u}^2 + 16(1+\beta_{1u})\beta_{2u}\beta_{3u}\beta_{4u}.\end{aligned} \tag{14}$$

Clearly, for arbitrary values of the parameters, the eigenvalues are not hierarchical. However, in looking for leading-order results in which only one eigenvalue is sizable, we can easily identify two general scenarios of interest, depending on the ordering of the mass eigenvalues. One option is that λ_{1u} is one of the small eigenvalues, which would have $\beta_{1u} \to 1$, and λ_{2u} is the other, and hence λ_{3u} generically has an $O(1)$ value. Another option is that λ_{1u} is the large eigenvalue, such that $\beta_{1u} \neq 1$, and both $\lambda_{2u,3u}$ are small. We now discuss each possibility in turn.

In what follows, we will focus on the up quarks, but our default assumption will be that the down quarks and the charged leptons will take similar forms. Mixing possible options for eigenvalue hierarchies in the different charged fermion sectors will not be considered here for simplicity.

Case 1: $\lambda_{1u,2u} \ll \lambda_{3u}$ (encompassing the "singlet-dominated" and "democratic" limits)

We begin with the situation that $\beta_{1u} \to 1$, such that λ_{1u} is a small eigenvalue, and explore parameter regimes in which λ_{2u} is also small. For simplicity, we first consider the case in which both vanish, such that to this order of approximation we have one massive third-generation, and two massless generations. It is easily verified that in this regime, both eigenvalues vanish for

$$\beta_{1u} = 1, \qquad \beta_{2u}\beta_{3u} = \beta_{4u}. \tag{15}$$

This case includes what we call the *democratic* limit, in which all the $\beta_{iu} = 1$, and thus the MSSM Yukawas take on the well-known democratic form [99]. The democratic limit

was originally studied at leading order in [95], and will be studied in more detail below, including subleading corrections. This case also includes what we will call the *singlet-dominated* limit, which is the case in which $\beta_{4u} \gg \beta_{1u,2u,3u}$, as β_{4u} is the parameter related to the strength of the superpotential coupling involving only $\mathcal{S}_3$ singlet fields. In the singlet-dominated limit, the MSSM and messenger Yukawa couplings at leading order, in the diagonal quark mass basis, only have nonvanishing $3-3$ entries, allowing for sizable stop mixing and consequently lighter superpartner masses than the other examples we will consider (as we will see). This limiting case was studied in some detail in [96] and [101], and will be considered below as a benchmark scenario for purposes of comparison.

For Case 1, incorporating Eq. (15) and up to possible rephasings to ensure that the fermion masses are real and positive, the diagonalization matrices U_{uL} and U_{uR} take the form

$$U_{uL} = \begin{pmatrix} \frac{1}{\sqrt{2}} & -\frac{\beta_{3u}}{\sqrt{2}\sqrt{2+\beta_{3u}^2}} & \frac{1}{\sqrt{2+\beta_{3u}^2}} \\ -\frac{1}{\sqrt{2}} & -\frac{\beta_{3u}}{\sqrt{2}\sqrt{2+\beta_{3u}^2}} & \frac{1}{\sqrt{2+\beta_{3u}^2}} \\ 0 & \frac{\sqrt{2}}{\sqrt{2+\beta_{3u}^2}} & \frac{\beta_{3u}}{\sqrt{2+\beta_{3u}^2}} \end{pmatrix}, \qquad U_{uR} = \begin{pmatrix} \frac{1}{\sqrt{2}} & -\frac{\beta_{2u}}{\sqrt{2}\sqrt{2+\beta_{2u}^2}} & \frac{1}{\sqrt{2+\beta_{2u}^2}} \\ -\frac{1}{\sqrt{2}} & -\frac{\beta_{2u}}{\sqrt{2}\sqrt{2+\beta_{2u}^2}} & \frac{1}{\sqrt{2+\beta_{2u}^2}} \\ 0 & \frac{\sqrt{2}}{\sqrt{2+\beta_{2u}^2}} & \frac{\beta_{2u}}{\sqrt{2+\beta_{2u}^2}} \end{pmatrix}. \tag{16}$$

Assuming these forms with no further rephasings, the messenger Yukawa couplings in the diagonal quark mass basis then take the form

$$Y'_{u1} = \tilde{y}_u \begin{pmatrix} -\frac{\sqrt{3}}{2} & \frac{3\beta_{2u}}{2\sqrt{2+\beta_{2u}^2}} & \frac{\beta_{2u}^2-1}{\sqrt{2}\sqrt{2+\beta_{2u}^2}} \\ \frac{3\beta_{3u}}{2\sqrt{2+\beta_{3u}^2}} & \frac{3\sqrt{3}\beta_{2u}\beta_{3u}}{2\sqrt{2+\beta_{2u}^2}\sqrt{2+\beta_{3u}^2}} & \frac{\sqrt{3}(\beta_{2u}^2-1)\beta_{3u}}{\sqrt{2}\sqrt{2+\beta_{2u}^2}\sqrt{2+\beta_{3u}^2}} \\ \frac{\beta_{3u}^2-1}{\sqrt{2}\sqrt{2+\beta_{3u}^2}} & \frac{\sqrt{3}(\beta_{3u}^2-1)\beta_{2u}}{\sqrt{2}\sqrt{2+\beta_{2u}^2}\sqrt{2+\beta_{3u}^2}} & \frac{(\beta_{2u}^2-1)(\beta_{3u}^2-1)}{\sqrt{3}\sqrt{2+\beta_{2u}^2}\sqrt{2+\beta_{3u}^2}} \end{pmatrix} \tag{17}$$

$$Y'_{u2} = \tilde{y}_u \begin{pmatrix} -\frac{\sqrt{3}}{2} & -\frac{3\beta_{2u}}{2\sqrt{2+\beta_{2u}^2}} & \frac{\beta_{2u}^2-1}{\sqrt{2}\sqrt{2+\beta_{2u}^2}} \\ -\frac{3\beta_{3u}}{2\sqrt{2+\beta_{3u}^2}} & \frac{3\sqrt{3}\beta_{2u}\beta_{3u}}{2\sqrt{2+\beta_{2u}^2}\sqrt{2+\beta_{3u}^2}} & \frac{\sqrt{3}(\beta_{2u}^2-1)\beta_{3u}}{\sqrt{2}\sqrt{2+\beta_{2u}^2}\sqrt{2+\beta_{3u}^2}} \\ -\frac{\beta_{3u}^2-1}{\sqrt{2}\sqrt{2+\beta_{3u}^2}} & \frac{\sqrt{3}(\beta_{3u}^2-1)\beta_{2u}}{\sqrt{2}\sqrt{2+\beta_{2u}^2}\sqrt{2+\beta_{3u}^2}} & \frac{(\beta_{2u}^2-1)(\beta_{3u}^2-1)}{\sqrt{3}\sqrt{2+\beta_{2u}^2}\sqrt{2+\beta_{3u}^2}} \end{pmatrix}. \tag{18}$$

From these forms, we see that in the democratic limit, the messenger Yukawas only have nonvanishing entries in the upper 2×2 block, as follows:

$$Y'_{u1} = \tilde{y}_u \begin{pmatrix} -\frac{\sqrt{3}}{2} & \frac{\sqrt{3}}{2} & 0 \\ \frac{\sqrt{3}}{2} & \frac{\sqrt{3}}{2} & 0 \\ 0 & 0 & 0 \end{pmatrix}, \qquad Y'_{u2} = \tilde{y}_u \begin{pmatrix} -\frac{\sqrt{3}}{2} & -\frac{\sqrt{3}}{2} & 0 \\ -\frac{\sqrt{3}}{2} & \frac{\sqrt{3}}{2} & 0 \\ 0 & 0 & 0 \end{pmatrix}. \tag{19}$$

In the singlet-dominated limit, the $3-3$ entries dominate, with $Y'_{u1,u2} = \text{Diag}\left(0, 0, \frac{\tilde{y}_u \beta_{2u} \beta_{3u}}{\sqrt{3}}\right)$.

Case 2: $\lambda_{2u,3u} \ll \lambda_{1u}$ (the "doublet-dominated" limit)

For this case, it is necessary that $\beta_{1u} \neq 1$ such that $\lambda_{1u} \gg \lambda_{2u,3u}$. For concreteness, we take $\beta_{1u} \to -1$, and thus require $\beta_{2u,3u,4u} \ll 1$, as well as $\Lambda_u \to 0$. Indeed, $\lambda_{2u,3u} = 0$ is achieved for $\beta_{1u} = -1, \beta_{2u} = \beta_{3u} = \beta_{4u} = 0$. To see this, we note that for $\beta_1 = -1$ only, the condition for $\Lambda_u = 0$ is as follows:

$$-8\beta_{2u}^2\beta_{3u}^2 + 4(\beta_{2u}^4 + \beta_{3u}^4) + 4(\beta_{2u}^2 + \beta_{3u}^2)\beta_{4u}^2 + \beta_{4u}^2 = 0, \tag{20}$$

which is zero only for $\beta_{4u} = 0$ and $\beta_{2u} = \beta_{3u}$. We will take $\beta_{1u} = -1$ and $\beta_{4u} = 0$, but leave β_{2u} and β_{3u} unconstrained at present, recalling that we will need to restrict ourselves to the case that $\beta_{2u,3u} \ll |\beta_{1u}| = 1$. This limit is the *doublet-dominated* limit, since now $|\beta_{1u}| \gg \beta_{2u,3u} \gg \beta_{4u} = 0$, and β_{1u} controls the superpotential coupling involving only $\mathcal{S}_3$ doublet fields. In this limit, the mass eigenvalues take the form (assuming for concreteness that $\beta_{3u} > \beta_{2u}$):

$$\lambda_{1u} = \frac{2\tilde{y}_u^2}{3}, \qquad \lambda_{2u} = \frac{2\tilde{y}_u^2\beta_{2u}^2}{3}, \qquad \lambda_{3u} = \frac{2\tilde{y}_u^2\beta_{3u}^2}{3}, \tag{21}$$

such that $\lambda_{2u} < \lambda_{3u} < \lambda_{1u}$. (For $\beta_{3u} < \beta_{2u}$, the placement of β_{2u} and β_{3u} in λ_{2u} and λ_{3u} is reversed.) We now take $\sqrt{3}\tilde{y}_u/2 = y_t$ to identify y_t as the top quark Yukawa coupling to leading order. The diagonalization matrices U_{uL} and U_{uR} now take the following particularly simple forms:

$$U_{uL} = \begin{pmatrix} \frac{1}{\sqrt{2}} & 0 & \frac{1}{\sqrt{2}} \\ \frac{1}{\sqrt{2}} & 0 & -\frac{1}{\sqrt{2}} \\ 0 & 1 & 0 \end{pmatrix}, \qquad U_{uR} = \begin{pmatrix} 0 & \frac{1}{\sqrt{2}} & \frac{1}{\sqrt{2}} \\ 0 & \frac{1}{\sqrt{2}} & -\frac{1}{\sqrt{2}} \\ 1 & 0 & 0 \end{pmatrix}. \tag{22}$$

The messenger Yukawas in the diagonal quark basis are then given by

$$Y'_{u1} = y_t \begin{pmatrix} -\frac{\beta_{2u}}{2\sqrt{2}} & -\frac{3}{4} & -\frac{\sqrt{3}}{4} \\ 0 & -\frac{\beta_{3u}}{2\sqrt{2}} & \frac{\sqrt{3}\beta_{3u}}{2\sqrt{2}} \\ \frac{\sqrt{3}\beta_{2u}}{2\sqrt{2}} & -\frac{\sqrt{3}}{4} & \frac{1}{4} \end{pmatrix}, \qquad Y'_{u2} = y_t \begin{pmatrix} -\frac{\beta_{2u}}{2\sqrt{2}} & -\frac{3}{4} & \frac{\sqrt{3}}{4} \\ 0 & -\frac{\beta_{3u}}{2\sqrt{2}} & -\frac{\sqrt{3}\beta_{3u}}{2\sqrt{2}} \\ -\frac{\sqrt{3}\beta_{2u}}{2\sqrt{2}} & \frac{\sqrt{3}}{4} & \frac{1}{4} \end{pmatrix}. \tag{23}$$

2.3 Models

As described in the previous subsection, we have identified two cases with hierarchical quark and charged lepton masses. The first (Case 1) satisfies Eq. (15), and includes two possible scenarios at leading order: the singlet-dominated limit, in which it is the $\mathcal{S}_3$ singlet couplings of the MSSM fields and the Higgs-messenger fields that dominate the superpotential, and the democratic limit, in which all the couplings of $\mathcal{S}_3$ representations in the superpotential are precisely equal at leading order, resulting in an enhanced $\mathcal{S}_{3L} \times \mathcal{S}_{3R}$ symmetry. The singlet-dominated limit was explored in [96] and [101], and the democratic limit at leading order in [95]. The second (Case 2) is what we call the doublet-dominated limit, as in this case the dominant couplings are those involving only $\mathcal{S}_3$ doublets. In what follows, we will discuss these scenarios in greater detail.

Case 1 models

We begin the discussion of Case 1 models with the singlet-dominated limit, which was studied in detail in [96, 101]. In this scenario, sizable stop mixing can occur due to the FGM contributions to the third-generation soft trilinear scalar coupling. This in turn allows for the squarks and gluinos to be in the $O(5-6$ TeV) range, which is relatively light compared to generic parameter choices for this class of FGM models. A variety of subleading corrections to this limit can be considered, including the possibility of generating nontrivial masses for the second-generation fields and the possibility of viable quark mixing at the first subleading order. For the case described in [101], the corrections to the soft terms that result from these terms have only minimal effects on the superpartner masses. Furthermore, in this case flavor-violating contributions to the soft terms also do not result at the first subleading order in the quantities that control the lighter generation quark and lepton masses, though this is not necessarily generic. Here we will not revisit this case in detail other than as a point of comparison for the new scenarios considered in this work.

Let us now turn to the democratic limit, for which the Yukawa coupling parameters $\beta_{1i} = \beta_{2i} = \beta_{3i} = \beta_{4i} = 1$, where $i = u, d, e$. In this case, the MSSM Yukawa matrices take the form

$$Y_i = \frac{\tilde{y}_i}{\sqrt{3}} \begin{pmatrix} 1 & 1 & 1 \\ 1 & 1 & 1 \\ 1 & 1 & 1 \end{pmatrix}. \tag{24}$$

This is the well-known flavor democratic mass matrix form, which exhibits an $\mathcal{S}_{3L} \times \mathcal{S}_{3R}$

symmetry. At leading order, this mass matrix has two vanishing eigenvalues, and one $O(1)$ eigenvalue, to be identified with the third-generation. As shown in [95], the messenger Yukawa matrices have nonzero entries only in the upper 2×2 block in the diagonal quark mass basis.

We now address the generation of the first- and second-generation fermion masses and the effects on the sfermion masses through the messenger Yukawa corrections. Here we choose to break the $\mathcal{S}_{3L} \times \mathcal{S}_{3R}$ symmetry to $\mathcal{S}_{2L} \times \mathcal{S}_{2R}$ and then to $\mathcal{S}_{1L} \times \mathcal{S}_{1R}$, which generates a nonzero mass for the first- and second-generation fermions (see e.g. [100]). This can be achieved via the following terms:

$$Y_i^{(\text{corr})} = \frac{\tilde{y}_i \epsilon_i}{\sqrt{3}} \begin{pmatrix} 0 & 0 & 1 \\ 0 & 0 & 1 \\ 1 & 1 & 1 \end{pmatrix} + \frac{\tilde{y}_i \sigma_i}{\sqrt{3}} \begin{pmatrix} 1 & 0 & -1 \\ 0 & -1 & 1 \\ -1 & 1 & 0 \end{pmatrix}, \tag{25}$$

in which ϵ_i and σ_i are real dimensionless perturbative parameters associated with symmetry breaking from $\mathcal{S}_3$ to $\mathcal{S}_2$ and $\mathcal{S}_2$ to $\mathcal{S}_1$ respectively. In our scenario, the ϵ perturbations of the up quarks (the down quarks and charged leptons have analogous structures) can be generated in superpotential at the renormalizable level by

$$\epsilon_u y_u [\beta_{2u} Q_{\mathbf{2}} \bar{u}_{\mathbf{1}} \mathcal{H}_u^{(2)} + \beta_{3u} Q_{\mathbf{1}} \bar{u}_{\mathbf{2}} \mathcal{H}_u^{(2)} + \beta_{4u} Q_{\mathbf{1}} \bar{u}_{\mathbf{1}} \mathcal{H}_u^{(1)}], \tag{26}$$

while the σ perturbations can be generated via non-renormalizable operators. These superpotential terms add corrections of the form of Eq. (25) to the Yukawa matrix for the up-type quarks, and corrections of the following form to the up-type messenger Yukawa matrices:

$$\begin{aligned} Y_{u1}'^{(\text{corr})} &= \tilde{y}_u \epsilon_u \begin{pmatrix} 0 & 0 & \frac{1}{2} - \frac{1}{2\sqrt{3}} \\ 0 & 0 & -\frac{1}{2} - \frac{1}{2\sqrt{3}} \\ \frac{1}{2} - \frac{1}{2\sqrt{3}} & -\frac{1}{2} - \frac{1}{2\sqrt{3}} & \frac{1}{\sqrt{3}} \end{pmatrix} + \tilde{y}_u \sigma_u \begin{pmatrix} \frac{1}{2} - \frac{1}{2\sqrt{3}} & 0 & \frac{1}{2} + \frac{1}{2\sqrt{3}} \\ 0 & \frac{1}{2} + \frac{1}{2\sqrt{3}} & \frac{1}{2} - \frac{1}{2\sqrt{3}} \\ \frac{1}{2} + \frac{1}{2\sqrt{3}} & \frac{1}{2} - \frac{1}{2\sqrt{3}} & 0 \end{pmatrix} \\ Y_{u2}'^{(\text{corr})} &= \tilde{y}_u \epsilon_u \begin{pmatrix} 0 & 0 & -\frac{1}{2} - \frac{1}{2\sqrt{3}} \\ 0 & 0 & \frac{1}{2} - \frac{1}{2\sqrt{3}} \\ -\frac{1}{2} - \frac{1}{2\sqrt{3}} & \frac{1}{2} - \frac{1}{2\sqrt{3}} & \frac{1}{\sqrt{3}} \end{pmatrix} + \tilde{y}_u \sigma_u \begin{pmatrix} -\frac{1}{2} - \frac{1}{2\sqrt{3}} & 0 & -\frac{1}{2} + \frac{1}{2\sqrt{3}} \\ 0 & -\frac{1}{2} + \frac{1}{2\sqrt{3}} & -\frac{1}{2} - \frac{1}{2\sqrt{3}} \\ -\frac{1}{2} + \frac{1}{2\sqrt{3}} & -\frac{1}{2} - \frac{1}{2\sqrt{3}} & 0 \end{pmatrix}. \end{aligned} \tag{27}$$

Including these correction terms along with the leading order results, the eigenvalues

$\lambda_{1u,2u,3u}$, are then found to be

$$\lambda_{1u} = 0, \qquad \lambda_{2u} = \frac{4y_t^2\epsilon_u^2}{81} + O(\epsilon^3), \qquad \lambda_{3u} = y_t^2 + O(\epsilon_u^3). \tag{28}$$

In these relations, we have identified the top quark Yukawa coupling y_t through $\tilde{y}_u = (y_t/\sqrt{3})(1 - 5\epsilon_u/9 + O(\epsilon_u)^2$, which follows from setting $\lambda_{3u} = y_t^2$ through second order in ϵ_u. As expected, ϵ_u controls the charm quark mass [2].

In the diagonal quark mass basis, the messenger Yukawa matrices for the up-type quark sector are given to order in σ_u/ϵ_u by

$$\begin{aligned} Y'^{(\mathrm{diag})}_{u1} &= y_t \begin{pmatrix} -\frac{1}{2} + \frac{5\epsilon_u}{18} - \frac{3\sqrt{3}\sigma_u}{2\epsilon_u} & -\frac{1}{2} - \frac{\epsilon_u}{18} + \frac{3\sqrt{3}\sigma_u}{2\epsilon_u} & -\frac{5\epsilon_u}{9\sqrt{2}} \\ -\frac{1}{2} - \frac{\epsilon_u}{18} + \frac{3\sqrt{3}\sigma_u}{2\epsilon_u} & \frac{1}{2} + \frac{\epsilon_u}{6} + \frac{3\sqrt{3}\sigma_u}{2\epsilon_u} & \frac{\epsilon_u}{3\sqrt{2}} \\ -\frac{5\epsilon_u}{9\sqrt{2}} & \frac{\epsilon_u}{3\sqrt{2}} & -\frac{\epsilon_u}{9} \end{pmatrix} \\ Y'^{(\mathrm{diag})}_{u2} &= y_t \begin{pmatrix} -\frac{1}{2} + \frac{5\epsilon_u}{18} + \frac{3\sqrt{3}\sigma_u}{2\epsilon_u} & \frac{1}{2} + \frac{\epsilon_u}{18} + \frac{3\sqrt{3}\sigma_u}{2\epsilon_u} & \frac{5\epsilon_u}{9\sqrt{2}} \\ \frac{1}{2} + \frac{\epsilon_u}{18} + \frac{3\sqrt{3}\sigma_u}{2\epsilon_u} & \frac{1}{2} + \frac{\epsilon_u}{6} - \frac{3\sqrt{3}\sigma_u}{2\epsilon_u} & \frac{\epsilon_u}{3\sqrt{2}} \\ \frac{5\epsilon_u}{9\sqrt{2}} & \frac{\epsilon_u}{3\sqrt{2}} & -\frac{\epsilon_u}{9} \end{pmatrix}. \end{aligned} \tag{29}$$

Analogous forms are easily obtained for the MSSM and messenger Yukawa matrices for down-type quarks and leptons in the diagonal quark mass basis with the replacements $\epsilon_u \to \epsilon_{d,e}$ and $y_t \to y_{b,\tau}$. The relative strengths of the parameters $\epsilon_{u,d,e}$ and $\sigma_{u,d,e}$ can be estimated from the fact that these parameters govern the fermion masses of the lighter generations. More precisely, up to $O(1)$ prefactors, $\epsilon_{u,d,e}$ is related to $m_{c,s,\mu}/m_{t,b,\tau}$, while $\sigma_{u,d,e}$ is constrained by $m^2_{u,d,e}/m^2_{t,b,\tau} \sim \sigma^2_{u,d,e}/\epsilon_{u,d,e}$. From these relations, it is straightforward to obtain that $\epsilon_u \approx 3 \times 10^{-2}$ and $\sigma_u \approx 1 \times 10^{-3}$. Similarly, $\epsilon_d \approx 0.1$, $\sigma_d \approx 9 \times 10^{-3}$, $\epsilon_e \approx 0.3$, and $\sigma_e \approx 8 \times 10^{-3}$. These parameter values also yield hierarchical quark mixing angles of the Cabibbo-Kobayashi-Maskawa (CKM) matrix, in which the largest angle is the Cabibbo angle, $\sin\theta_c \sim 0.17$. While the quark mixing angles are not fully realistic (the Cabibbo angle is clearly too small compared to its experimentally determined value), for the purposes of this study it is a reasonable starting point for the analysis.

We now find the nonvanishing corrections to the soft supersymmetry breaking terms, assuming for simplicity that the ratio of the F terms to the scalar VEVs for the X_H and

[2] Note that if we neglect the subleading σ perturbations, this scheme is equivalent to replacing $\beta_{2u,3u,4u} = 1 + \epsilon_u$ in the general form for the superpotential couplings. As such, the mixing matrices are easily obtained using the results of Eq. (16) with the appropriate substitutions.

X_T terms are identical (both will be denoted as Λ). We provide the expressions for these correction terms in the Appendix. As expected, in the limit that the perturbation parameters are set to zero, the result is what was found in [95]. When the perturbations are added, the diagonal entries of the soft mass-squared terms are corrected at second order in the ϵ parameters. This generates nonzero (but small) diagonal $3-3$ entries. In addition, with nonzero perturbations, flavor off-diagonal contributions to the corrections to the soft terms are generated. More precisely, the $\epsilon_{u,d,e}$ parameters introduce nonvanishing $\delta m^2_{f_{23}}$ terms at first order in ϵ, while the $\sigma_{u,d,e}$ introduce nonvanishing $\delta m^2_{f_{12}}$ and $\delta m^2_{f_{21}}$ terms. Therefore, the dominant effects are expected to be seen in the $2-3$ sfermion mixings. Further details will be discussed in the next section.

Case 2 models

This case corresponds to the doublet-dominated limit. Here we need $\lambda_1 \gg \lambda_{2,3}$. In the limit that $\lambda_{2,3} \to 0$, we see from Eqs. (13)-(14) this can be achieved for $\beta_1 \to -1$ and $\beta_{i=2,3,4} \ll 1$, and we need $\tilde{\Lambda} \to 0$. For $\beta_1 = -1$, the condition for $\tilde{\Lambda} = 0$ is as follows:

$$-8\beta_2^2\beta_3^2 + 4(\beta_2^4 + \beta_3^4) + 4(\beta_2^2 + \beta_3^2)\beta_4^2 + \beta_4^2 = 0, \tag{30}$$

which is zero only for $\beta_4 = 0$, $\beta_2 = \beta_3$. In the up quark sector, we will now set $\lambda_1 = y_t^2$, such that $\tilde{y}_u^2 = (3/4)y_t^2$ (analogous relations hold for the down quark and charged lepton sectors). The $\lambda_{2i,3i}$ are directly related to $\beta_{2i,3i}$, with the specific identification dependent on the values of the $\beta_{2i,3i}$.

• *Ordering* $\beta_{3i} > \beta_{2i}$. Let us first consider the case in which $\beta_{3i} > \beta_{2i}$, for which we have

$$U_{iL}^\dagger Y_i U_{iR} = Y_i^{(\text{diag})} = y_{t,b,\tau}\text{Diag}\left(\frac{\beta_{2i}}{\sqrt{2}}, \frac{\beta_{3i}}{\sqrt{2}}, 1\right), \tag{31}$$

in which $U_{iL,iR}$ take the simple forms

$$U_{iL} = \begin{pmatrix} \frac{1}{\sqrt{2}} & 0 & \frac{1}{\sqrt{2}} \\ \frac{1}{\sqrt{2}} & 0 & -\frac{1}{\sqrt{2}} \\ 0 & 1 & 0 \end{pmatrix}, \qquad U_{iR} = \begin{pmatrix} 0 & \frac{1}{\sqrt{2}} & \frac{1}{\sqrt{2}} \\ 0 & \frac{1}{\sqrt{2}} & -\frac{1}{\sqrt{2}} \\ 1 & 0 & 0 \end{pmatrix}. \tag{32}$$

We see that for this ordering, the β_{3i} control the second-generation masses and the β_{2i} control the first-generation masses. The messenger Yukawas in the diagonal fermion mass

basis (the SCKM basis) are given by

$$Y'_{i1} = y_{t,b,\tau} \begin{pmatrix} -\frac{\beta_{2i}}{2\sqrt{2}} & -\frac{3}{4} & -\frac{\sqrt{3}}{4} \\ 0 & -\frac{\beta_{3i}}{2\sqrt{2}} & \frac{\beta_{3i}}{2}\sqrt{\frac{3}{2}} \\ \frac{\beta_{2i}}{2}\sqrt{\frac{3}{2}} & -\frac{\sqrt{3}}{4} & \frac{1}{4} \end{pmatrix}, \qquad Y'_{i2} = y_{t,b,\tau} \begin{pmatrix} -\frac{\beta_{2i}}{2\sqrt{2}} & -\frac{3}{4} & +\frac{\sqrt{3}}{4} \\ 0 & -\frac{\beta_{3i}}{2\sqrt{2}} & -\frac{\beta_{3i}}{2}\sqrt{\frac{3}{2}} \\ -\frac{\beta_{2i}}{2}\sqrt{\frac{3}{2}} & \frac{\sqrt{3}}{4} & \frac{1}{4} \end{pmatrix}. \quad (33)$$

Given that we can identify $\beta_{2i,3i}$ with the first and second-generation masses, respectively, we can write for example for the up-type quarks (with $y_{u,d,e} = \beta_{2u,d,}y_t/\sqrt{2}$ and $y_c = \beta_{3u}y_t/\sqrt{2}$):

$$Y'_{u1} = \begin{pmatrix} -\frac{y_u}{2} & -\frac{3y_t}{4} & -\frac{\sqrt{3}y_t}{4} \\ 0 & -\frac{y_c}{2} & -\frac{\sqrt{3}y_c}{2} \\ -\frac{\sqrt{3}y_u}{2} & \frac{\sqrt{3}y_t}{4} & \frac{y_t}{4} \end{pmatrix}, \qquad Y'_{u2} = \begin{pmatrix} -\frac{y_u}{2} & -\frac{3y_t}{4} & -\frac{\sqrt{3}y_t}{4} \\ 0 & -\frac{y_c}{2} & \frac{\sqrt{3}y_c}{2} \\ \frac{\sqrt{3}y_u}{2} & -\frac{\sqrt{3}y_t}{4} & \frac{y_t}{4} \end{pmatrix}. \quad (34)$$

From the quark and charged lepton masses, we can roughly estimate (neglecting running effects) that $\beta_{2u}/\beta_{3u} \sim 2 \times 10^{-3}$, $\beta_{2d}/\beta_{3d} \sim 0.05$, $\beta_{2l}/\beta_{3l} \sim 0.005$, while $\beta_{3d}/\beta_{3l} \sim 0.4$. Hence, to leading order we can neglect the effects proportional to the first-generation masses (here the β_{2i}), and treat the effects due to the second-generation masses (the β_{3i}) perturbatively. We thus calculate the corrections to the soft supersymmetry terms in this limit. As before, we assume for simplicity that the ratio of the F terms to the scalar vevs for the X_H and X_T terms are identical. The detailed forms of these soft supersymmetry breaking terms are presented in the Appendix.

We note that in this case, there are flavor off-diagonal contributions in the $\delta m^2_{Q,L_{12}}$ that are proportional to the β_{3i}, and thus scale with the second-generation quark and lepton masses. This is reminiscent of the Case 1 democratic limit with perturbations, though the dominant off-diagonal contributions occurred there in the $2-3$ sector, and here they arise in the more dangerous $1-2$ sector. We will discuss their effects in the next section.

• *Ordering* $\beta_{2i} > \beta_{3i}$. We now consider the case in which $\beta_{2i} > \beta_{3i}$, for which the roles of β_{2i} and β_{3i} are switched in Eq. (31). We now have

$$U_{iL} = \begin{pmatrix} 0 & \frac{1}{\sqrt{2}} & -\frac{1}{\sqrt{2}} \\ 0 & \frac{1}{\sqrt{2}} & \frac{1}{\sqrt{2}} \\ 1 & 0 & 0 \end{pmatrix}, \qquad U_{iR} = \begin{pmatrix} \frac{1}{\sqrt{2}} & 0 & -\frac{1}{\sqrt{2}} \\ \frac{1}{\sqrt{2}} & 0 & \frac{1}{\sqrt{2}} \\ 0 & 1 & 0 \end{pmatrix}. \quad (35)$$

The messenger Yukawa matrices in the diagonal quark mass basis are of the form

$$Y'_{i1} = y_{t,b,\tau} \begin{pmatrix} -\frac{\beta_{3i}}{2\sqrt{2}} & 0 & -\frac{\sqrt{3}\beta_{3i}}{2\sqrt{2}} \\ -\frac{3}{4} & -\frac{\beta_{2i}}{2\sqrt{2}} & \frac{\sqrt{3}}{4} \\ \frac{\sqrt{3}}{4} & -\frac{\beta_{2i}}{2}\sqrt{\frac{3}{2}} & \frac{1}{4} \end{pmatrix}, \qquad Y'_{i2} = y_{t,b,\tau} \begin{pmatrix} -\frac{\beta_{2i}}{2\sqrt{2}} & 0 & \frac{\sqrt{3}\beta_{3i}}{2\sqrt{2}} \\ -\frac{3}{4} & -\frac{\beta_{2i}}{2\sqrt{2}} & -\frac{\sqrt{3}}{4} \\ -\frac{\sqrt{3}}{4} & \frac{\beta_{2i}}{2}\sqrt{\frac{3}{2}} & \frac{1}{4} \end{pmatrix}. \quad (36)$$

As in the previous section, we can ignore effects that scale with the first-generation fermion masses and keep leading contributions involving the second-generation fermion masses. Thus, we now neglect the terms proportional to β_{3i} and keep leading-order terms proportional to the β_{2i}. We can again calculate the soft supersymmetry breaking terms, subject to the same assumptions as given for the alternate ordering. The detailed forms are included in the Appendix.

One interesting feature of this mass ordering ($\beta_{2i} > \beta_{3i}$) is the corrections to the soft supersymmetry breaking mass terms are flavor-diagonal if we neglect effects proportional to the first-generation fermion masses. As in the alternate ordering, here we obtain contributions to $\delta m^2_{Q,L_{12}}$ that are proportional to the β_{3i}, but now these quantities must be much smaller since they govern the masses of the first-generation. Given the high degree of suppression of the flavor off-diagonal elements, in this case the model is clearly safe from flavor-changing neutral current constraints.

2.4 Results and Discussion

In this section, we analyze the mass spectra of these scenarios and their phenomenological implications. We start with Case 1, focusing solely on the democratic limit with symmetry breaking effects, and then study Case 2, the doublet-dominated limit, with both orderings of the β_{2i} and β_{3i}. The model parameters are M_{mess}, Λ, $\tan\beta = \langle H_u\rangle/\langle H_d\rangle$, the sign of μ (sgn(μ), taken here to be $+1$), and the relevant perturbation parameters, which depend on the scenario in question. Here we have followed standard procedures and replaced $|\mu|$ and B_μ with $\tan\beta$ and the Z boson mass. The renormalization group equations are run using SoftSUSY 4.1.4 [103].

Case 1 models

We start with the flavor democratic limit, which was explored in [95] for the case of third-generation masses only, i.e. in the absence of the small perturbations that break the $\mathcal{S}_{3L}\times\mathcal{S}_{3R}$

symmetry. It was shown in [95] that this scenario leads to heavy superpartner masses, which can be traced to the absence of large stop mixing in this limit. In the presence of nonvanishing perturbations, this picture generically continues except for specific small regions of parameter space where the Higgs mass constraint can be satisfied without being bolstered by very heavy squarks.

In Figure 2.1, we show a representative mass spectrum for an intermediate messenger mass scale of $M_{mess} = 10^{12}$ GeV and $\tan\beta = 10$, where Λ is chosen to satisfy the Higgs mass constraint [104]. As seen, the heavy Higgs particles are nearly 8 TeV, the gluino is approximately 10 TeV, and the squarks fall into three groupings: a lightest set that is close in mass to the heavy Higgs particles, a set in between, and a heavier set that is similar to the gluino mass. The sleptons are close in mass to the lightest neutralino, and the next-to-lightest superpartner (NLSP) is the lightest slepton. The effects of nonzero $\sigma_{u,d,e}$ lead to small ($O(1\ GeV)$) splittings in the masses of $\tilde{d}_1$ and $\tilde{d}_2$, and $\tilde{u}_4$ and $\tilde{u}_5$, which are each originally identical up to order 10^{-2} GeV. The effect of $\epsilon_{u,d,e}$ is larger, which is expected as these have larger numerical values. For nonzero ϵ_u, there is a splitting of order ~ 70 GeV in the masses of $\tilde{u}_1$ and $\tilde{u}_2$, which are also identical up to order of 10^{-2} GeV in the $\mathcal{S}_{3L} \times \mathcal{S}_{3R}$ limit. Similar features are seen for $\tilde{u}_4$ and $\tilde{u}_5$. The ϵ_u corrections also introduce a small (~ 25 GeV) mass splitting for $\tilde{d}_1$ and $\tilde{d}_2$, which is a sign of the symmetry breaking from $\mathcal{S}_{3L} \times \mathcal{S}_{3R}$ to $\mathcal{S}_{2L} \times \mathcal{S}_{2R}$.

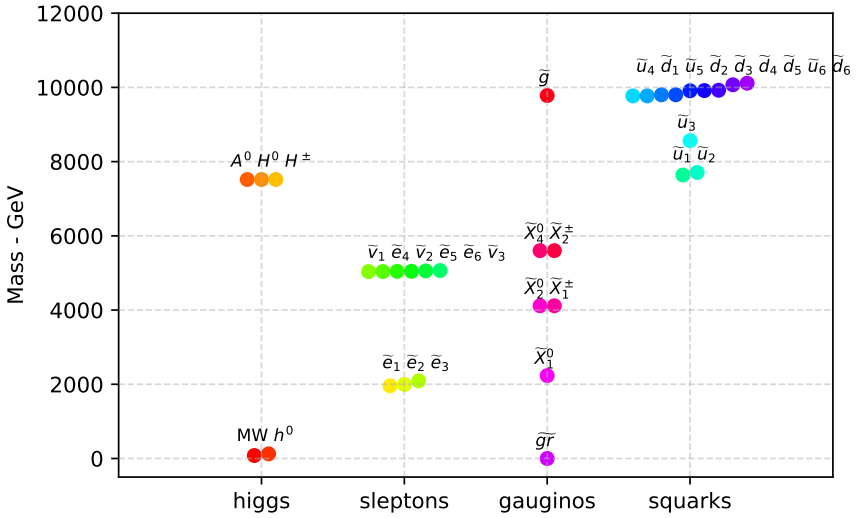

Figure 2.1: The sfermion mass spectrum in the Case 1 democratic limit, with $M_{\text{mess}} = 10^{12}$ GeV, $\Lambda = 8.1 \times 10^5$ GeV, $\tan\beta = 10$, $\epsilon_u = 0.033$, $\epsilon_d = 0.108$, $\epsilon_e = 0.281$, $\sigma_u = 0.001$, $\sigma_d = 0.009$, and $\sigma_e = 0.008$.

As noted previously, this scenario has flavor off-diagonal contributions to the corrections to the soft supersymmetry breaking terms, with the dominant contributions in the $2-3$ sector. To get an estimate of the potential sizes of these effects, we employ the standard mass insertion approximation (MIA) method, in which the quantities of interest for the quarks are $(\delta_f^{IJ})_{XY} = (\Delta_f^{IJ})_{XY}/((m_{fI})_{XX}(m_{fJ})_{YY})$, where f denotes the relevant matter superfield, I, J are flavor indices, X, Y are chirality labels, and $(\Delta_f^{IJ})_{XY}$ is an off-diagonal contribution to the sfermion soft terms [3]. We expect rather mild constraints due to the heavy sfermion and gluino masses and the suppression factors in the off-diagonal contributions to the soft terms. For the set of model parameters in Fig. 2.1, we obtain $2-3$ squark and slepton mass insertion parameters of the order $|(\delta_u^{23})_{LL}| \sim 5 \times 10^{-3}$, $|(\delta_u^{23})_{RR}| \sim 10^{-2}$, $|(\delta_d^{23})_{LL}| \sim 5 \times 10^{-3}$, $|(\delta_d^{23})_{RR}| \sim 7 \times 10^{-4}$, $|(\delta_l^{23})_{LL}| \sim 2 \times 10^{-3}$, and $|(\delta_l^{23})_{RR}| \sim 3 \times 10^{-2}$, as well as small contributions to LR mixings in the $2-3$ sector (ranging from 10^{-4} to 10^{-7}. The $1-3$ and $1-2$ mass insertions are parametrically smaller, with limits that range from 10^{-4} to 10^{-12}, except for $|(\delta_l^{12})_{RR}| \sim 3 \times 10^{-3}$. The resulting effects are small and within the allowed ranges (see e.g. [106]).

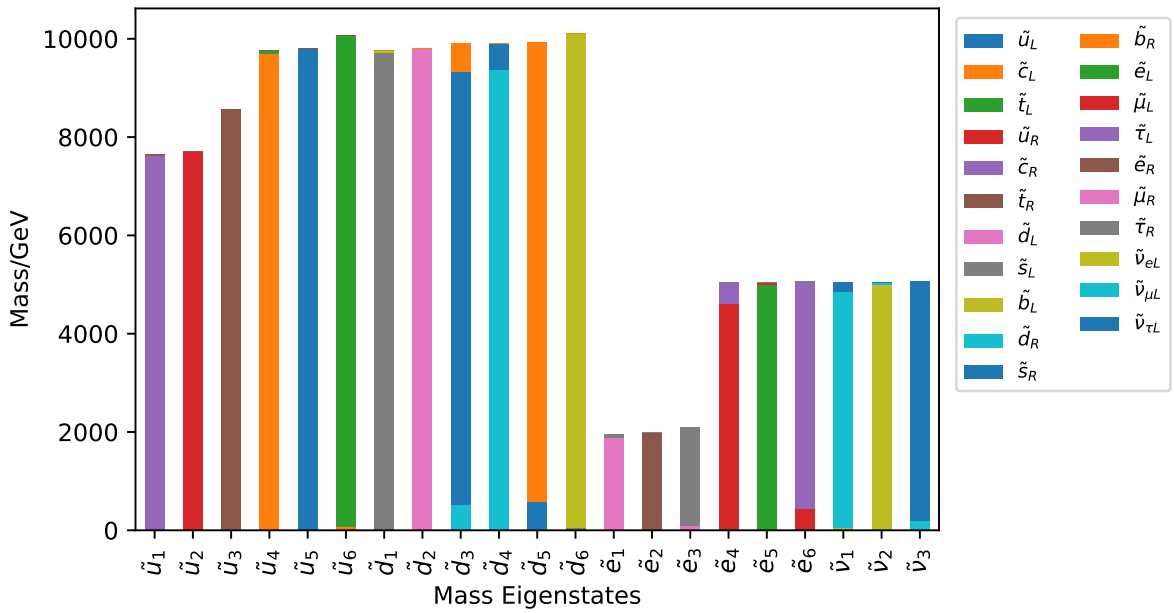

Figure 2.2: The sfermion mass eigenstates in the democratic limit with $\epsilon_u = 0.033$, $\epsilon_d = 0.108$, $\epsilon_e = 0.281$, $\sigma_u = 0.001$, $\sigma_d = 0.009$, and $\sigma_e = 0.008$, with $M_{\text{mess}} = 10^{12}$ GeV, $\Lambda = 8.1 \times 10^5$ GeV, and $\tan\beta = 10$.

[3] Note that MIA is a good approximation in this scenario although we have non-degenerate squark masses, since the squark masses are not strongly hierarchical [105].

The composition of the mass eigenstates of the sfermions is shown in Fig. 2.2. Without perturbations, there is almost no mixing between different flavor eigenstates. The lightest $SU(3)_c$ charged particles are the first and second-generation right-handed squarks and the lightest sleptons are the first and second-generation right-handed sleptons. In Fig. 2.2, the results are shown for $\epsilon_u = 0.033$, $\epsilon_d = 0.108$, $\epsilon_e = 0.281$, $\sigma_u = 0.001$, $\sigma_d = 0.009$, and $\sigma_e = 0.008$. The lighter squarks $\tilde{u_1}$ and $\tilde{u}_2$ are again the right-handed scharm and sup. Mixing between the second and third-generations for the left handed sparticles is observed in $\tilde{u}_4$ and $\tilde{u}_6$. There is also small but nonvanishing 2-3 generational mixing among right-handed up-type squarks. For the down sector, apart from the 1-2 and 2-3 generational mixing which are larger compared to the up sector, there is also a small but nonvanishing left-right mixing between $\tilde{b}_L$ and $\tilde{b}_R$ observed in $\tilde{d}_1$. For the sleptons, we again observe small mixing between the second and third-generation sleptons with the same handedness.

It is illustrative to compare this scenario with the singlet-dominated limit [96, 101]. In this case, the dominant contributions to the soft terms arise in the diagonal third-generation (33) entries, rendering this case similar to flavored gauge mediation models in which the Higgs-messenger mixing is controlled by Abelian symmetries. Generally this case has a light spectrum, with masses below 6 TeV. Unlike the democratic case, the heavy Higgs particles are heavier than or comparable to the $SU(3)$-charged superpartners, with masses at the $5 - 6$ TeV range. The large stop mixing due to the nonvanishing A term for the third-generation fields at the messenger mass scale allows for a viable Higgs mass at smaller values of Λ compared to the democratic limit, in which the A terms vanish in the absence of the small symmetry breaking perturbations. Adding nonrenormalizable corrections as in [101] to generate the light quark and charged lepton masses does not alter this feature and generically leads to very small $(O(10^{-1}\ \mathrm{G}eV))$

Case 2 models

We now turn to the Case 2 models, for which the superpotential couplings only involving the $\mathcal{S}_3$-doublets dominate. As described in the previous section, in this case there are two sub-categories, depending on whether the β_{3i} or the β_{2i} parameters control the second-generation quark and charged lepton masses. Here we will label the mass ordering $\beta_{3i} > \beta_{2i}$ by Case 2a, and the alternate mass ordering $\beta_{2i} > \beta_{3i}$ as Case 2b. The soft supersymmetry breaking terms for Case 2a are given in Eq. (39), and the analogous quantities for Case 2b are given in Eq. (39).

In Case 2 models, there is a nonvanishing trilinear scalar parameter A_t that is present in

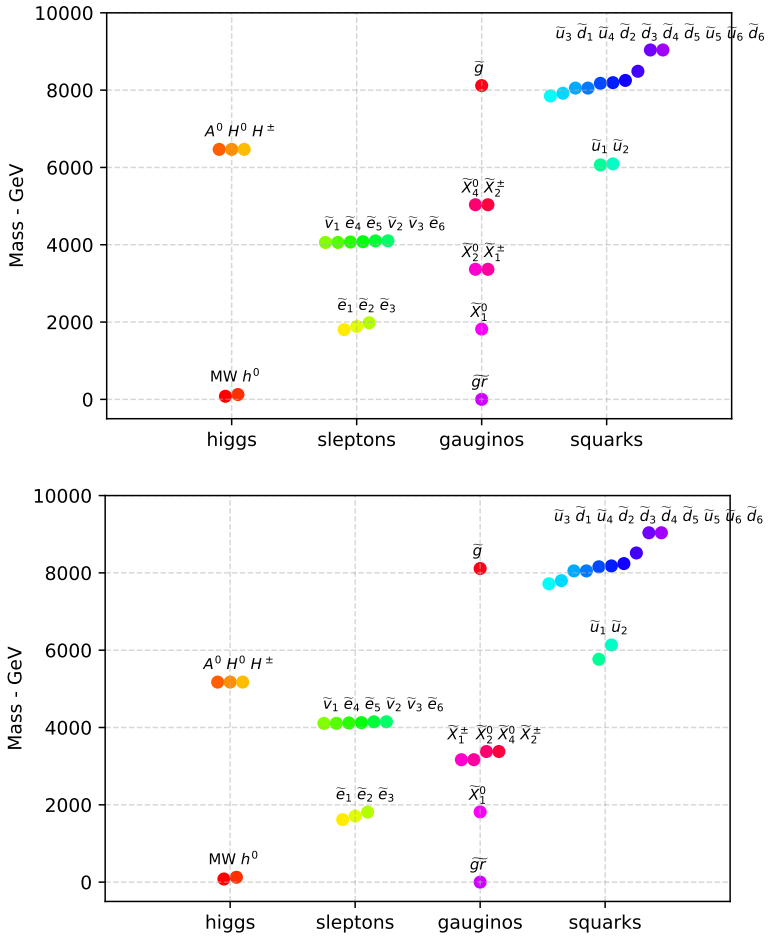

Figure 2.3: The sfermion mass spectra in the doublet-dominated (Case 2) limit, with $M_{\text{mess}} = 10^{12}$ GeV, $\Lambda = 6.6 \times 10^5$ GeV, for (a) Case 2a $\beta_{3d} = 0.03$, $\beta_{3u} = 0.01$, $\beta_{3l} = 0.08$, $\beta_{2u} = \beta_{2d} = \beta_{2l} = 0$ (left), and (b) Case 2b with $\beta_{2d} = 0.03$, $\beta_{2u} = 0.01$, $\beta_{2l} = 0.08$, $\beta_{3u} = \beta_{3d} = \beta_{3l} = 0$ (right).

the absence of the first and second-generation quark and charged lepton masses, in contrast to the Case 1 democratic limit. Hence, the Higgs and superpartner masses are lighter than their Case 1 democratic counterparts, though not as light as in the Case 1 singlet-dominated limit. In Fig. 2.3, we show characteristic mass spectra for $M_{mess} = 10^{12}\ GeV$ and $\Lambda = 6.6 \times 10^5$ GeV. Here we have included nonvanishing values for the parameters that fix the second-generation quark and charged lepton masses (β_{3i} for Case 2a, β_{2i} for Case 2b), and neglected the effects of the first-generation masses. The values of the perturbation parameters are chosen to yield appropriate values for the SM fermion mass values. We note here that if these quantities are taken to zero, the mass spectra are almost unchanged,

with small changes that are at most $O(10^{-1}\ GeV)$, primarily in the slepton sector due to the relatively large value of the corresponding $\beta_{3l,2l}$ parameter.

We see that in both Case 2a and Case 2b, the gluino and squark masses are similar, with the gluino at about 8 TeV and the squarks ranging from approximately $8 - 10$ TeV. Unlike the Case 1 singlet-dominated limit as in Fig. 2.1 in which the squark masses are generally comparable to heavy Higgses, in this case the squarks are always much heavier than the heavy Higgs bosons. The slepton masses fall into two different ranges, with the NLSP as the lightest selectron $\tilde{e}_1$. The three lightest slectrons have their masses below 2 TeV, while the other sleptons have their masses between 3−4 TeV. The lightest charginos and neutralinos are gaugino-dominated, with a binolike lightest neutralino, while the heavier set is higgsino-dominated.

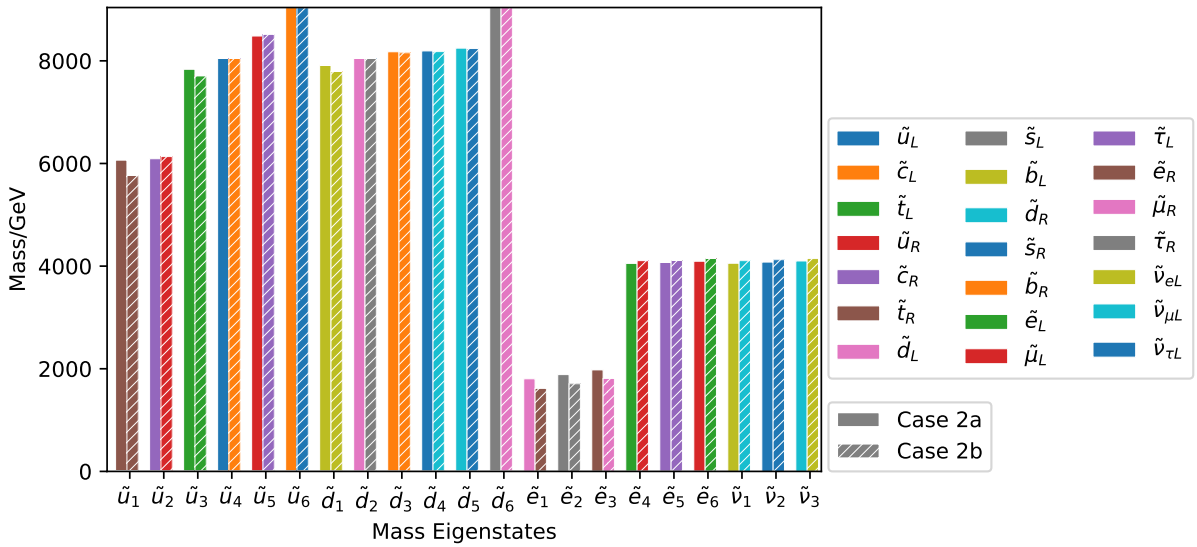

Figure 2.4: The sfermion mass spectrum in the doublet-dominated scenarios, with ordering $\beta_{3i} > \beta_{2i}$ (Case 2a) and $\beta_{2i} > \beta_{3i}$ (Case 2b), respectively, with $M_{\text{mess}} = 10^{12}$ GeV and $\tan\beta = 10$. For Case 2a, $\beta_{3d} = 0.03$, $\beta_{3u} = 0.01$, $\beta_{3l} = 0.08$. For Case 2b, $\beta_{2d} = 0.03$, $\beta_{2u} = 0.01$, $\beta_{2l} = 0.08$.

An intriguing difference between Case 2a and Case 2b is that in Case 2b, the heavy Higgs states and the heavy charginos and neutralinos are lighter than they are in Case 2a. For the model parameters as given in Fig. 2.3, we see that in Case 2b the heavy Higgs masses are in the 5-6 TeV range, while they are over 6 TeV in Case 2a, and the heavy charginos/neutralinos are also reduced by approximately 1 TeV in Case 2b compared to Case 2a. This indicates that in Case 2b, smaller values of the μ and B_μ parameters are needed for successful electroweak symmetry breaking.

Another significant difference between Case 2a and Case 2b is that Case 2a has nonvanishing off-diagonal contributions to squark mixing, as discussed in the previous subsection. The most significant off-diagonal sfermion mixing in Case 2a is given by $|(\delta_u^{12})_{LL}| \sim 1 \times 10^{-4}$. These effects are small because the flavor off-diagonal contributions are proportional to the small quantities that govern the second-generation SM quark and charged lepton masses. In both cases, as shown in Fig. 2.4, sfermion mixing is not significant due to the small size of the perturbation parameters. For larger values of the messenger mass scale, nontrivial left-right mixing is observed for the third-generation down-type squarks (left-right mixing in the other sfermion sectors is negligible for all values of the messenger mass scale).

Discussion

In comparing the mass spectra of these scenarios (Case 1: democratic, and Cases 2a and 2b: doublet-dominated, as well as the Case 1: singlet-dominated limit as studied in [95]), there are several features of interest. For fixed M_{mess}, the mass spectra are more compressed for larger values of $\tan\beta$ ($\tan\beta > 10$) because the contributions from the bottom and tau Yukawa couplings are more significant than in the low $\tan\beta$ regime. For smaller $\tan\beta$ values, the sparticle masses are heavier as the tree-level contribution to the light Higgs mass has decreased, requiring larger radiative corrections to boost its mass to its experimentally allowed range. The superpartner masses in this limit are thus highly split, with heavy squarks and gluinos, and lighter sleptons. For fixed $\tan\beta$ (here taken to be $\tan\beta = 10$), lower values of the messenger mass scale generally lead to heavier spectra, as larger values of Λ are needed to satisfy the light Higgs mass constraint. For higher messenger scales, due to increased renormalization group running effects, the μ and b/μ terms needed to satisfy the electroweak symmetry breaking constraints are smaller, and thus the heavy charginos and neutralinos become lighter.

To further investigate the dependence of the mass spectra on M_{mess} and $\tan\beta$, we show the Higgs mass curve for fixed Λ, with the color representing the mass of the lightest squark. We show these results in Fig. 2.5 for the Case 1 democratic scenario, which show several excluded regions. When $\epsilon_u = \epsilon_d = \epsilon_e = 0$, the central big “hole" appears because the mass-squared of the lightest slepton is negative. When the ϵ parameters are nonzero, the size of the holes increases, and there are also small holes that appear above the central void because A^0 becomes tachyonic in those regions. Quite generally, we see that the parameters that satisfy the Higgs mass constraint could be very different in these two cases. The lightest value for the mass of the $\tilde{u}_3$ squark is in the region with high $\tan\beta$ and high messenger

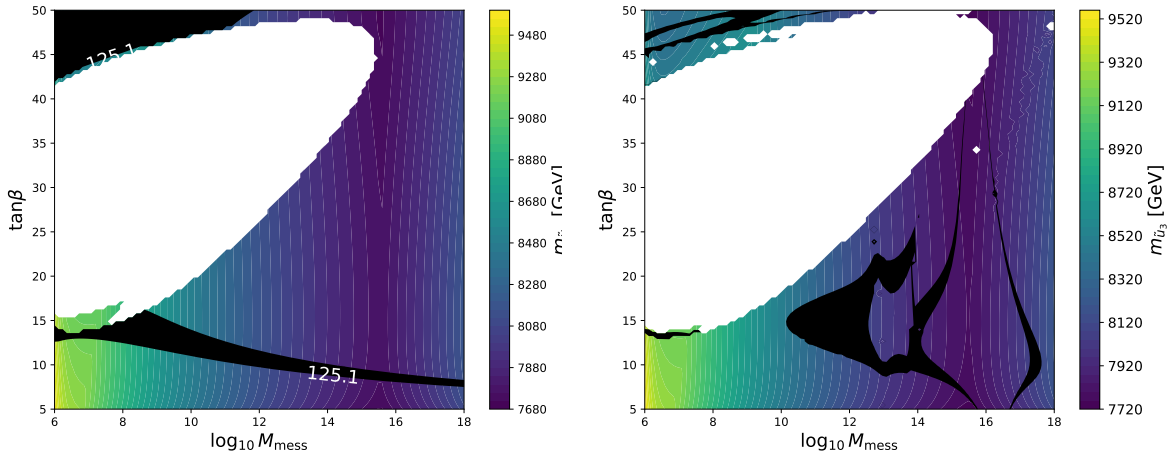

Figure 2.5: (a) The Higgs mass (black band) and $\tilde{u}_3$ squark mass (color shading) for Case 1 in the democratic limit without perturbations, with $\Lambda = 7.7 \times 10^5$ GeV (left). (b) The same as (a), but with $\epsilon_u = 0.033$, $\epsilon_d = 0.108$, $\epsilon_e = 0.281$, $\sigma_u = 0.001$, $\sigma_d = 0.009$, $\sigma_e = 0.008$ (right).

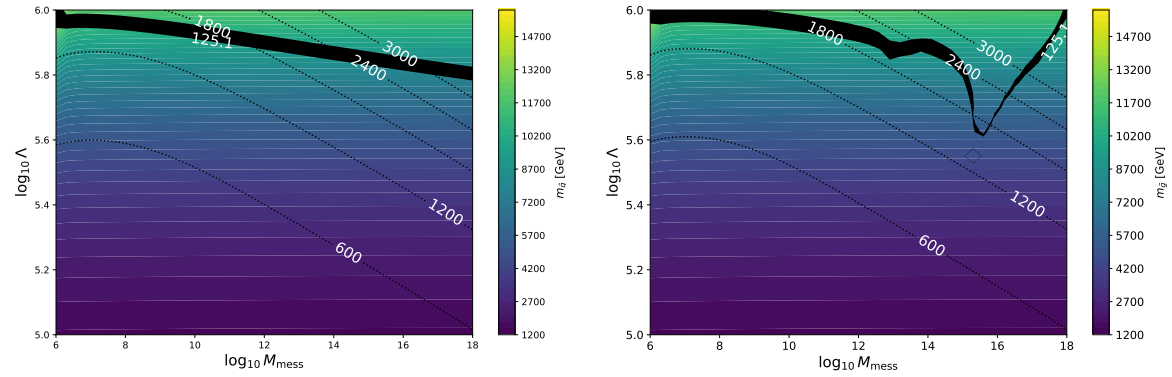

Figure 2.6: (a) The Higgs mass (black band), gluino mass (color shading) and $\tilde{e}_1$ mass (dotted curves) as a function of Λ and M_{mess}, for Case 1 in the democratic limit with $\tan\beta = 10$, for (a) no perturbations (left), and (b) nonzero perturbations, with $\epsilon_u = 0.033$, $\epsilon_d = 0.108$, $\epsilon_e = 0.281$, $\sigma_u = 0.001$, $\sigma_d = 0.009$, $\sigma_e = 0.008$.

scales. In Fig. 2.6, we show the gluino and lightest slepton (NLSP) masses, both without perturbations (left panel) and with perturbations (right panel). The introduction of the perturbations pushes the slepton mass down to smaller values. The change in the shape of the viable Higgs mass region is even more apparent here. For low values of M_{mess}, a higher value of Λ is needed to satisfy the light Higgs mass constraint. For higher messenger

scales $M_{\text{mess}} \sim 10^{14} - 10^{16}$ GeV, there is a sharp drop in the Higgs mass region that is observed. In that region, there is generally larger left-right mixing in the sbottom sector as well larger scharm-stop mixing, which result in nontrivial contributions to the Higgs mass. However, there are potential numerical instabilities related to the challenges of the Higgs mass calculation in this parameter region. A detailed resolution of these issues is beyond the scope of this chapter, and is deferred to future study.

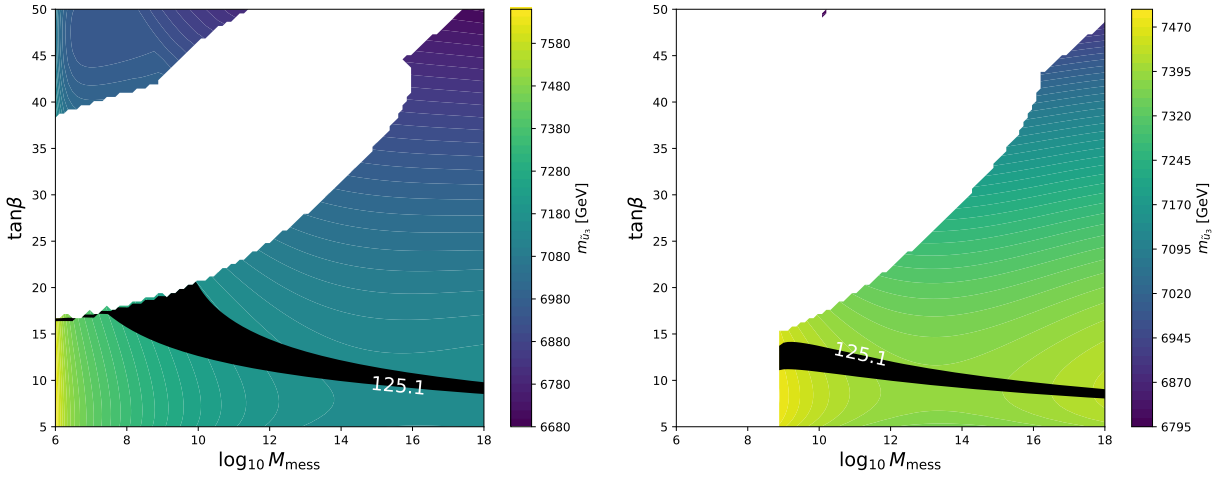

Figure 2.7: The mass of the Higgs (black band) and the mass of the lightest squark $\tilde{u}_3$ (color shading) for (a) Case 2a with fixed $\Lambda = 6 \times 10^5$ GeV, $\beta_{3d} = 0.03$, $\beta_{3u} = 0.01$, $\beta_{3l} = 0.08$, $\beta_{2u} = \beta_{2d} = \beta_{2l} = 0$ (left), and (b) Case 2b with fixed $\Lambda = 6.3 \times 10^5$ GeV, $\beta_{2d} = 0.03$, $\beta_{2u} = 0.01$, $\beta_{2l} = 0.08$, $\beta_{3u} = \beta_{3d} = \beta_{3l} = 0$ (right).

For the Case 2 models, we also see excluded regions in the parameter scan in Fig. 2.7. Here, for both Case 2a and 2b, Λ is chosen to maximize viable parameter regions, and the perturbations have a minimal effect on the size of the void. In Case 2a, the void appears due to tachyonic slepton masses, and the phenomenologically viable parameter region generally lies between $\tan\beta \approx 5 - 15$, $M_{\text{mess}} = 10^6 - 10^{18}$ GeV, with a fixed choice of $\Lambda = 6 \times 10^5$ GeV. For Case 2b, apart from the central hole where the lightest slepton becomes tachyonic, the region on the left of the spectrum, which is from $M_{\text{mess}} \sim 10^6 - 10^9$ GeV and $\tan\beta \sim 5 - 50$, is ruled out because the desired electroweak minimum is not present. We also see that in both cases, the viable Higgs region does not generally intersect with the region where $\tilde{e}_1$ is lighter. In Fig 2.8, we fix $\tan\beta = 10$ and show both Case 2a and Case 2b with nonzero perturbations. Note that the effects of the perturbations only slightly shift the mass curve of the NLSP upward, and have almost no effect on the viable Higgs mass region and the

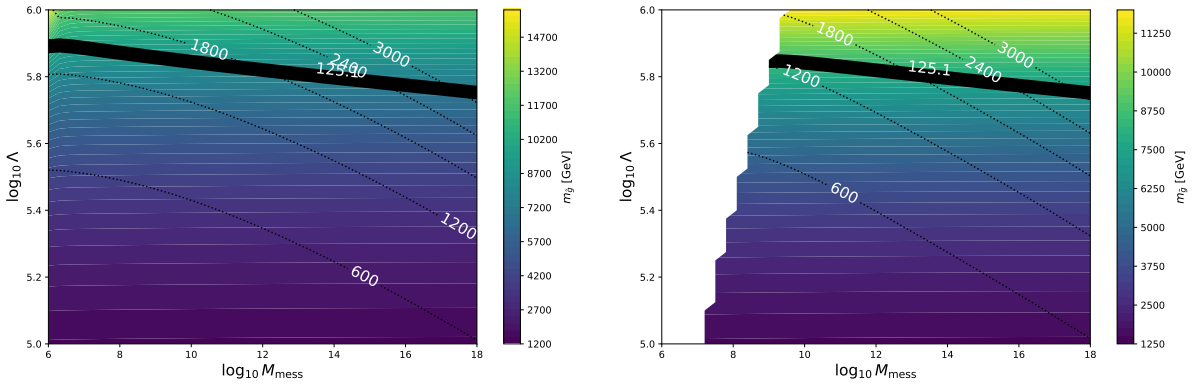

Figure 2.8: The light Higgs mass (black band), gluino mass (color shading), and $\tilde{e}_1$ mass (dotted curves) with $\Lambda = 6 \times 10^5$ GeV, for (a) Case 2a $\beta_{3d} = 0.03$, $\beta_{3u} = 0.01$, $\beta_{3l} = 0.08$, $\beta_{2u} = \beta_{2d} = \beta_{2l} = 0$ (left), and (b) Case 2b with $\beta_{2d} = 0.03$, $\beta_{2u} = 0.01$, $\beta_{2l} = 0.08$, $\beta_{3u} = \beta_{3d} = \beta_{3l} = 0$ (right).

gluino masses, in contrast to what we have seen in the democratic limit.

We close this section by commenting on further phenomenological aspects of this set of models. For all cases described here (both democratic and doublet-dominated models), the superpartner masses are generally heavy and split, in a way that is reminiscent of minimal gauge mediation with $N = 2$. As previously discussed, the constraints of the non-Abelian Higgs-messenger symmetry have led us to include at least two messenger pairs to avoid a catastrophic μ/B_μ problem. Ultimately, this means that the scenarios studied in this chapter have heavier and more split spectra than what can be obtained in Abelian flavored gauge mediation models (where a judicious choice of $U(1)$ charges can be made to avoid the μ/B_μ issue seen here, without increasing the number of messenger pairs), such as in [93], or in general gauge mediation scenarios [75]. We recall that in our scenario in the singlet-dominated limit as studied in [96, 101], it is also possible to minimize the splitting of the mass spectra, though not to the extent that is possible in the Abelian flavored gauge mediation models.

As a result, the discovery potential for the scenarios studied here either via direct LHC searches or indirect constraints is not as promising as it can be in Abelian flavored gauge mediation models, or even in the singlet-dominated non-Abelian scenario. For example, it is straightforward to see that the supersymmetric contribution to muon anomalous magnetic moment (MDM) in the democratic and doublet-dominated non-Abelian flavored gauge mediation scenarios studied here is generically about two orders smaller than the current

experimental value [107]. This is both due to the heavy superpartner masses as described above, and that we are generally precluded from having large values of $\tan\beta$ in these scenarios, which usually provide the largest enhancement to the MDM. Therefore, if new physics is required to resolve any future confirmed discrepancy between the SM prediction and the measured value of the muon anomalous magnetic moment, this set of flavored gauge mediation models would need to be extended to accommodate the experimental result.

One notable difference in the non-Abelian flavored gauge mediation scenarios studied here compared to minimal gauge mediation with $N = 2$ as well as the non-Abelian singlet-dominated flavored gauge mediation scenario is in regards to the NLSP composition. Here, for messenger mass scales of 10^{12} GeV as displayed in Fig. 2.1 and Fig. 2.3, the NLSP is the lightest slepton, which is a right-handed smuon. This is different from the minimal GMSB scenario and the singlet-dominated non-Abelian FGM scenario in which either staus or binolike neutralinos are the NLSP. In the scenarios studied in this chapter, for this intermediate to high messenger scale, the smuon NLSP has a lifetime of $\mathcal{O}(0.001\,\mathrm{s})$, and the NLSP mass is generically close to about 2 TeV. This currently lies above the limits from direct production searches at $\sqrt{s} = 13$ TeV [108]. For lower values of the messenger scale ($\sim 10^6$ GeV), the lightest slepton is still the NLSP, which has a very rapid decay to the gravitino due to the lower supersymmetry breaking scale, while for very high messenger scales ($\sim 10^{14}$ GeV), the NLSP is now a long-lived binolike neutralino. We also note that in the non-Abelian flavored gauge mediation scenarios studied here, there is no significant co-NLSP behavior, both in the low messenger scale and the intermediate to high messenger scale cases. This is in contrast to minimal $N = 2$ GMSB for low messenger scales ($\sim 10^6$ GeV), for which there is appreciable co-NLSP behavior among the lighter sleptons for the binolike neutralino NLSP.

We also note that in both minimal $N = 2$ GMSB and our non-Abelian flavored gauge-mediation scenarios, for messenger scales of $M_{\text{mess}} = 10^{12}$ GeV, the gravitino has a mass of $\mathcal{O}(0.1\,\text{GeV})$, and the NLSP is not long-lived enough to decay during or after Big Bang nucleosynthesis (BBN). Therefore, the successful predictions of BBN will not be spoiled (see e.g. [109–111]). For gravitinos of this mass range, there are well-known mechanisms to ensure the desired reheating temperatures and late entropy production to avoid having the gravitinos overclose the universe, so that gravitinos can then be a plausible dark matter candidate. For lower values of the messenger scale, the situation is further improved, as the gravitinos are lighter (with masses of the order of tenths of keV for $M_{\text{mess}} = 10^6$ GeV)

and the NLSP decays to gravitinos much more rapidly than in the higher messenger scale case, thus avoiding the need for gravitino dilution.

2.5 Conclusions

In this chapter, we have explored MSSM flavored gauge mediation models in which the Higgs-messenger mixing is controlled by a discrete non-Abelian symmetry, here taken for simplicity to be $\mathcal{S}_3$. Building on previous analyses [95] which showed that viable models can be constructed for an extended Higgs-messenger sector that includes both $\mathcal{S}_3$ doublet and singlet fields that mix to yield one light MSSM Higgs pair and two messenger pairs, we studied various possibilities for generating plausible SM quark and charged lepton masses in the case in which the MSSM matter fields also carry $\mathcal{S}_3$ quantum numbers. While additional relations beyond $\mathcal{S}_3$ are generically needed to obtain the desired hierarchical SM fermion masses, we have identified two general categories of solutions that we broadly categorized as Case 1 and Case 2 models. The Case 1 models obey Eq. (15), and encompass two regimes of interest: (i) the singlet-dominated limit, in which the Yukawa couplings involving only the $\mathcal{S}_3$ singlets dominate, and (ii) the democratic limit, in which the Yukawa superpotential for the MSSM fields has an enhanced $\mathcal{S}_{3L} \times \mathcal{S}_{3R}$ symmetry. The Case 2 models, in contrast, include the doublet-dominated limit, in which the Yukawa couplings involving only the $\mathcal{S}_3$ doublet fields dominate. The singlet-dominated limit was previously investigated in [96, 101] and served here as a point of comparison for a general analysis of the Case 1 democratic limit and the Case 2 doublet-dominated models. We include corrections to obtain nonvanishing masses for one or both of the lighter families, as well as for the third family. In certain cases such corrections lead to off-diagonal corrections to the soft supersymmetry breaking mass terms, but these corrections are relatively mild (a feature that is known in the literature for flavored gauge mediation models of this general type) and as a result, do not immediately lead to insurmountable problems with flavor-changing neutral current constraints.

Within Case 1 models, our analysis shows that while the singlet-dominated limit allows for examples with optimized parameter sets that yield gluino and squark masses in the 4-5 TeV range, the Case 1 democratic limit generically has significantly heavier squark and gluino masses. The Case 2 models generally also yield heavier superpartner masses, with the heavier squarks and gluino in the 7 TeV mass range. Ultimately, the fact that the squark and gluino masses cannot be made lighter than 4-5 TeV even in the singlet-dominated limit

is related to the fact that this non-Abelian Higgs-messenger mixing scenario requires at the minimum two vectorlike messenger pairs that contribute to the loop diagrams that generate the corrections to the soft terms, to tune the μ and B_μ terms independently. This should be contrasted with Abelian models, which can have just one messenger pair, and as a result can lead to benchmark scenarios in flavored gauge mediation with lighter $SU(3)$-charged superpartners that are more accessible for searches for supersymmetry at present and future colliders.

While the spectra in all our examples remain quite heavy, and while we have not constructed fully realistic models of the SM fermion masses and mixing angles (including CP violating effects, not included here for simplicity), we nonetheless find it encouraging that this class of non-Abelian flavored gauge mediation models can include examples that survive this next level of model-building scrutiny. More work is of course needed to see if such scenarios (or plausible extensions of such scenarios) can be embedded into a more complete high-energy model. In the meantime, however, analyses such as this one can serve as a reminder of the rich framework of TeV-scale $\mathcal{N} = 1$ supersymmetry, and the many ways in which it might still be hiding at or just above TeV energies. As the Terascale continues to be explored in this data-rich era for high energy physics, hopefully we will know relatively soon if TeV-scale supersymmetry is indeed part of our physical world.

Appendix A: FGM corrections to soft SUSY breaking terms

Case 1 models

We present the corrections to the soft supersymmetry breaking terms in the Case 1 democratic limit. All relevant terms with magnitudes larger than the smallest perturbation parameter σ_u are included. In this case all terms with coefficients of order $O(10^{-3})$GeV are taken into account. For notational simplicity, we define the following quantities:

$$\begin{aligned}
&\tilde{g}_u^2 = \frac{16}{3}g_3^2 + 3g_2^2 + \frac{13}{15}g_1^2, \quad \tilde{g}_d^2 = \frac{16}{3}g_3^2 + 3g_2^2 + \frac{7}{15}g_1^2, \quad \tilde{g}_e^2 = 3g_2^2 + \frac{9}{5}g_1^2, \\
&\delta_Q = 6y_t^4 + 6y_b^4 + 2y_b^2y_t^2 + y_b^2y_\tau^2 - \tilde{g_u}^2y_t^2 - \tilde{g_d}^2y_b^2, \\
&\delta_{\epsilon_u} = 8y_t^4 + y_b^2y_t^2 - \tilde{g_u}^2y_t^2, \quad \delta_{\epsilon_d} = 8y_b^4 + y_b^2y_t^2 + y_b^2y_\tau^2 - \tilde{g_d}^2y_b^2, \\
&\delta_{\epsilon_e} = \frac{4}{81}\epsilon_e^2y_b^2y_\tau^2 - \frac{8}{729}\epsilon_e^3y_b^2y_\tau^2 - \frac{244}{6561}\epsilon_e^4y_b^2y_\tau^2, \quad \delta_L = 4y_\tau^4 + 3y_b^2y_\tau^2 - \tilde{g_e}^2y_\tau^2.
\end{aligned} \tag{37}$$

In what follows, all soft scalar mass-squared parameters are assumed to include a factor of $\Lambda^2/(4\pi)^4$ and all trilinear scalar couplings are assumed to include a factor of $\Lambda/(4\pi)^2$, where $\Lambda = F/M_{\mathrm{m}ess}$. The nonvanishing corrections to the soft supersymmetry breaking terms are as follows:

$$\begin{aligned}
\delta m_{Q_{11}}^2 &= \delta_Q - \frac{4}{9}\epsilon_u\delta_{\epsilon_u} - \frac{4}{9}\epsilon_d\delta_{\epsilon_d} + \frac{4}{27}\epsilon_d\epsilon_e y_b^2y_\tau^2 - \frac{82}{729}\epsilon_d\epsilon_e^2y_b^2y_\tau^2 \\
&\quad + \epsilon_d^2\left(-\frac{26}{81}y_b^2\tilde{g}_d^2 + \frac{5}{27}y_b^2y_t^2 + \frac{26}{81}y_b^2y_\tau^2 + \frac{367}{81}y_b^4\right) + \delta_{\epsilon_e}, \\
\delta m_{Q_{22}}^2 &= (\delta_Q + \frac{4}{9}\epsilon_u\delta_{\epsilon_u} + \frac{4}{9}\epsilon_d\delta_{\epsilon_d} + \frac{4}{81}\epsilon_d\epsilon_e y_b^2y_\tau^2 - \frac{2}{243}\epsilon_d\epsilon_e^2y_b^2y_\tau^2 \\
&\quad + \epsilon_d^2\left(\frac{2}{3}y_b^2\tilde{g}_d^2 - \frac{88}{81}y_b^2y_t^2 - \frac{2}{3}y_b^2y_\tau^2 - \frac{289}{81}y_b^4\right) + \delta_{\epsilon_e}, \\
\delta m_{Q_{23}}^2 &= \delta m_{Q_{32}}^2 = \frac{4\sqrt{2}}{9}\epsilon_u(\delta_{\epsilon_u} - 2y_t^4) + \frac{4\sqrt{2}}{9}\epsilon_d\left(\delta_{\epsilon_d} - 2y_b^4\right) - \frac{4\sqrt{2}}{81}\epsilon_d\epsilon_e y_b^2y_\tau^2 + \frac{38\sqrt{2}}{729}\epsilon_d\epsilon_e^2y_b^2y_\tau^2 \\
&\quad + \sqrt{2}\epsilon_d^2\left(\frac{14}{81}y_b^2\tilde{g}_d^2 - \frac{25}{162}y_b^2y_t^2 - \frac{14}{81}y_b^2y_\tau^2 - \frac{59}{81}y_b^4\right), \\
\delta m_{Q_{12}}^2 &= \delta m_{Q_{21}}^2 = \frac{4\sqrt{3}}{3}\sigma_d\left(8y_b^4 - \tilde{g}_d^2y_b^2 + 2y_t^2y_b^2 + y_b^2y_\tau^2\right) + \frac{4\sqrt{3}}{3}\sigma_u\left(8y_t^4 - \tilde{g}_u^2y_b^2 + 2y_t^2y_b^2\right), \\
\delta m_{Q_{33}}^2 &= \frac{8}{81}\epsilon_d\epsilon_e y_b^2y_\tau^2 - \frac{44}{729}\epsilon_d\epsilon_e^2y_b^2y_\tau^2 + \epsilon_d^2\left(-\frac{4}{9}y_b^2\tilde{g}_d^2 + \frac{17}{81}y_b^2y_t^2 + \frac{4}{9}y_b^2y_\tau^2 + 2y_b^4\right),
\end{aligned}$$

$$\delta m^2_{\tilde{Q}_{13}} = \delta m^2_{\tilde{Q}_{31}} = \sqrt{\frac{2}{3}}\sigma_d\left(12y_b^4 - 2\tilde{g}_d^2 y_b^2 + 2y_t^2 y_b^2 + 2y_b^2 y_\tau^2\right) + 4\sqrt{\frac{2}{3}}\sigma_u\left(y_t^4 + y_t^2 y_b^2 - \tilde{g}_u^2 y_t^2\right),$$

$$\delta m^2_{\tilde{u}_{11}} = (2\delta_{\epsilon_u} - 4y_t^4) - \frac{8}{9}\epsilon_u\delta_{\epsilon_u} - \frac{8}{27}\epsilon_d^2 y_b^2 y_t^2,$$

$$\delta m^2_{\tilde{u}_{12}} = \delta m^2_{\tilde{u}_{21}} = \frac{8}{\sqrt{3}}\sigma_u\delta_{\epsilon_u}, \qquad \delta m^2_{\tilde{u}_{13}} = \delta m^2_{\tilde{u}_{31}} = 8\sqrt{\frac{2}{3}}\sigma_u(\delta_{\epsilon_u} - 2y_t^4),$$

$$\delta m^2_{\tilde{u}_{22}} = (2\delta_{\epsilon_u} - 4y_t^4) + \frac{8}{9}\epsilon_u\delta_{\epsilon_u} - \frac{8}{27}\epsilon_d^2 y_b^2 y_t^2,$$

$$\delta m^2_{\tilde{u}_{23}} = \delta m^2_{\tilde{u}_{32}} = \frac{8\sqrt{2}\epsilon_u}{9}\left(\delta_{\epsilon_u} - 2y_t^4\right),$$

$$\delta m^2_{\tilde{u}_{33}} = -\frac{8}{9}\epsilon_d^2 y_t^2 y_b^2,$$

$$\begin{aligned}\delta m^2_{\tilde{d}_{11}} &= (2\delta_{\epsilon_d} - 4y_b^4) - \frac{8\epsilon_d}{9}\delta_{\epsilon_d} + \frac{8}{27}\epsilon_d\epsilon_e y_b^2 y_\tau^2 - \frac{164}{729}\epsilon_d\epsilon_e^2 y_b^2 y_\tau^2 \\ &\quad + \epsilon_d^2\left(-\frac{52}{81}y_b^2\tilde{g}_d^2 + \frac{52}{81}y_b^2 y_t^2 + \frac{52}{81}y_b^2 y_\tau^2 + \frac{680}{81}y_b^4\right) + 2\delta_{\epsilon_e},\end{aligned}$$

$$\begin{aligned}\delta m^2_{\tilde{d}_{22}} &= (2\delta_{\epsilon_d} - 4y_b^4) + \frac{8\epsilon_d}{9}\delta_{\epsilon_d} + \frac{8}{81}\epsilon_d\epsilon_e y_b^2 y_\tau^2 - \frac{4}{243}\epsilon_d\epsilon_e^2 y_b^2 y_\tau^2 \\ &\quad + \epsilon_d^2\left(\frac{3}{4}y_b^2\tilde{g}_d^2 - \frac{116}{81}y_b^2 y_t^2 - \frac{4}{3}y_b^2 y_\tau^2 - \frac{592}{81}y_b^4\right) + 2\delta_{\epsilon_e},\end{aligned}$$

$$\begin{aligned}\delta m^2_{\tilde{d}_{23}} = \delta m^2_{\tilde{d}_{32}} &= \frac{8\sqrt{2}}{9}\epsilon_d\delta_{\epsilon_d} - \frac{8\sqrt{2}}{81}\epsilon_d\epsilon_e y_b^2 y_\tau^2 + \frac{76\sqrt{2}}{729}\epsilon_d\epsilon_e^2 y_b^2 y_\tau^2 \\ &\quad + \epsilon_d^2\left(\frac{28\sqrt{2}}{81}y_b^2\tilde{g}_d^2 - \frac{28\sqrt{2}}{81}y_b^2 y_t^2 - \frac{28\sqrt{2}}{81}y_b^2 y_\tau^2 - \frac{128\sqrt{2}}{81}y_b^4\right),\end{aligned}$$

$$\delta m^2_{\tilde{d}_{33}} = \frac{16}{81}\epsilon_d\epsilon_e y_b^2 y_\tau^2 - \frac{88}{729}\epsilon_d\epsilon_e^2 y_b^2 y_\tau^2 + \epsilon_d^2\left(-\frac{9}{8}y_b^2\tilde{g}_d^2 + \frac{8}{9}y_b^2 y_t^2 + \frac{8}{9}y_b^2 y_\tau^2 + \frac{392}{81}y_b^4\right),$$

$$\delta m^2_{\tilde{d}_{12}} = \delta m^2_{\tilde{d}_{12}} = \sigma_d\left(-\frac{3}{8\sqrt{3}}y_b^2\tilde{g}_d^2 + \frac{8y_b^2 y_t^2}{\sqrt{3}} + \frac{8y_b^2 y_\tau^2}{\sqrt{3}} + \frac{64y_b^4}{\sqrt{3}}\right),$$

$$\delta m^2_{\tilde{d}_{13}} = \delta m^2_{\tilde{d}_{31}} = \sigma_d\left(-\frac{1}{4}\sqrt{\frac{3}{2}}y_b^2\tilde{g}_d^2 + 4\sqrt{\frac{2}{3}}y_b^2 y_t^2 + 4\sqrt{\frac{2}{3}}y_b^2 y_\tau^2 + 8\sqrt{6}y_b^4\right),$$

$$\begin{aligned}\delta m^2_{L_{11}} &= \delta_L - \frac{4\epsilon_e}{9}\left(\delta_L + 2y_\tau^4\right) + \frac{4}{9}\epsilon_d\epsilon_e y_b^2 y_\tau^2 - \frac{22}{81}\epsilon_d\epsilon_e^2 y_b^2 y_\tau^2 + \frac{4}{27}\epsilon_d^2 y_b^2 y_\tau^2 \\ &\quad + \epsilon_e^2\left(\frac{26}{27}y_b^2 y_\tau^2 - \frac{81}{26}\tilde{g}_e^2 y_\tau^2 + \frac{283}{81}y_\tau^4\right) + \epsilon_e^3\left(-\frac{64}{243}y_b^2 y_\tau^2 + \frac{729}{64}\tilde{g}_e^2 y_\tau^2 - \frac{1778}{729}y_\tau^4\right) \\ &\quad + \epsilon_e^4\left(-\frac{238}{729}y_b^2 y_\tau^2 + \frac{2187}{238}\tilde{g}_e^2 y_\tau^2 + \frac{862}{2187}y_\tau^4\right),\end{aligned}$$

$$\begin{aligned}\delta m^2_{L_{22}} &= \delta_L + \frac{4\epsilon_e}{9}\left(\delta_L + 2y_\tau^4\right) + \frac{4}{27}\epsilon_d\epsilon_e y_b^2 y_\tau^2 + \frac{10}{243}\epsilon_d\epsilon_e^2 y_b^2 y_\tau^2 + \frac{4}{27}\epsilon_d^2 y_b^2 y_\tau^2 \\ &\quad + \epsilon_e^2\left(-2y_b^2 y_\tau^2 + \frac{3}{2}\tilde{g}_e^2 y_\tau^2 - \frac{197}{81}y_\tau^4\right) + \epsilon_e^3\left(\frac{424}{243}y_b^2 y_\tau^2 - \frac{729}{424}\tilde{g}_e^2 y_\tau^2 + \frac{370}{243}y_\tau^4\right) \\ &\quad + \epsilon_e^4\left(-\frac{1642}{2187}y_b^2 y_\tau^2 + \frac{6561}{1642}\tilde{g}_e^2 y_\tau^2 - \frac{1832}{6561}y_\tau^4\right),\end{aligned}$$

$$
\begin{aligned}
\delta m^2_{L_{23}} &= \delta m^2_{L_{32}} = \frac{4\sqrt{2}}{9}\epsilon_e\delta_L - \frac{4}{27}\sqrt{2}\epsilon_d\epsilon_e y_b^2 y_\tau^2 + \frac{14}{243}\sqrt{2}\epsilon_d\epsilon_e^2 y_b^2 y_\tau^2 \\
&\quad + \epsilon_e^2\left(-\frac{14}{27}\sqrt{2}y_b^2y_\tau^2 + \frac{81}{7\sqrt{2}}\tilde{g}_e^2y_\tau^2 - \frac{23}{81}\sqrt{2}y_\tau^4\right) + \epsilon_e^3\left(-\frac{4}{9}\sqrt{2}y_b^2y_\tau^2 + \frac{27}{2\sqrt{2}}\tilde{g}_e^2y_\tau^2 - \frac{530}{729}\sqrt{2}y_\tau^4\right) \\
&\quad + \epsilon_e^4\left(\frac{2402\sqrt{2}}{2187}y_b^2y_\tau^2 - \frac{6561}{1201\sqrt{2}}\tilde{g}_e^2y_\tau^2 + \frac{7660\sqrt{2}}{6561}y_\tau^4\right), \\
\delta m^2_{L_{33}} &= \frac{8}{27}\epsilon_d\epsilon_e y_b^2y_\tau^2 - \frac{76}{243}\epsilon_d\epsilon_e^2y_b^2y_\tau^2 \\
&\quad + \epsilon_e^2\left(\frac{4}{3}y_b^2y_\tau^2 - \frac{9}{4}\tilde{g}_e^2y_\tau^2 + \frac{74}{81}y_\tau^4\right) + \epsilon_e^3\left(-\frac{376}{243}y_b^2y_\tau^2 + \frac{729}{376}\tilde{g}_e^2y_\tau^2 - \frac{244}{243}y_\tau^4\right) \\
&\quad + \epsilon_e^4\left(\frac{1868}{2187}y_b^2y_\tau^2 - \frac{6561}{1868}\tilde{g}_e^2y_\tau^2 + \frac{436}{729}y_\tau^4\right), \\
\delta m^2_{L_{12}} &= \delta m^2_{L_{21}} = \sigma_e\left(4\sqrt{3}y_b^2y_\tau^2 - \frac{3}{4}\sqrt{3}\tilde{g}_e^2y_\tau^2 + 8\sqrt{3}y_\tau^4\right), \\
\delta m^2_{L_{13}} &= \delta m^2_{L_{31}} = \sigma_e\left(2\sqrt{6}y_b^2y_\tau^2 - 3\sqrt{\frac{3}{2}}\tilde{g}_e^2y_\tau^2 + 8\sqrt{\frac{2}{3}}y_\tau^4\right), \\
\delta m^2_{\bar{e}_{11}} &= 2\delta_L - \frac{8\epsilon_e}{9}\left(\delta_L + 2y_\tau^4\right) + \frac{8}{9}\epsilon_d\epsilon_e y_b^2y_\tau^2 - \frac{44}{81}\epsilon_d\epsilon_e^2y_b^2y_\tau^2 + \frac{8}{27}y_b^2\epsilon_d^2y_\tau^2 \\
&\quad + \epsilon_e^2\left(\frac{52}{27}y_b^2y_\tau^2 - \frac{81}{52}\tilde{g}_e^2y_\tau^2 + \frac{512}{81}y_\tau^4\right) + \epsilon_e^3\left(-\frac{128}{243}y_b^2y_\tau^2 + \frac{729}{128}\tilde{g}_e^2y_\tau^2 - \frac{3016}{729}y_\tau^4\right) \\
&\quad + \epsilon_e^4\left(-\frac{476}{729}y_b^2y_\tau^2 + \frac{2187}{476}\tilde{g}_e^2y_\tau^2 + \frac{914}{2187}y_\tau^4\right), \\
\delta m^2_{\bar{e}_{22}} &= 2\delta_L + \frac{8\epsilon_e}{9}\left(\delta_L + 2y_\tau^4\right) + \frac{8}{27}\epsilon_d\epsilon_e y_b^2y_\tau^2 + \frac{20}{243}\epsilon_d\epsilon_e^2y_b^2y_\tau^2 + \frac{8}{27}\epsilon_d^2y_b^2y_\tau^2 \\
&\quad + \epsilon_e^2\left(-4y_b^2y_\tau^2 + \frac{3}{4}\tilde{g}_e^2y_\tau^2 - \frac{136}{27}y_\tau^4\right) + \epsilon_e^3\left(\frac{848}{243}y_b^2y_\tau^2 - \frac{729}{848}\tilde{g}_e^2y_\tau^2 + \frac{776}{243}y_\tau^4\right) \\
&\quad + \epsilon_e^4\left(-\frac{3284}{2187}y_b^2y_\tau^2 + \frac{6561}{3284}\tilde{g}_e^2y_\tau^2 - \frac{1138}{2187}y_\tau^4\right), \\
\delta m^2_{\bar{e}_{23}} &= \delta m^2_{\bar{e}_{32}} = \frac{8\sqrt{2}}{9}\epsilon_e\delta_L - \frac{8}{27}\epsilon_d\epsilon_e\sqrt{2}y_b^2y_\tau^2 + \frac{28}{243}\sqrt{2}\epsilon_d\epsilon_e^2y_b^2y_\tau^2 \\
&\quad + \epsilon_e^2\left(-\frac{28}{27}\sqrt{2}y_b^2y_\tau^2 + \frac{81}{14\sqrt{2}}\tilde{g}_e^2y_\tau^2 - \frac{56}{81}\sqrt{2}y_\tau^4\right) + \epsilon_e^3\left(-\frac{8}{9}\sqrt{2}y_b^2y_\tau^2 + \frac{27}{4\sqrt{2}}\tilde{g}_e^2y_\tau^2 - \frac{1096}{729}\sqrt{2}y_\tau^4\right) \\
&\quad + \epsilon_e^4\left(\frac{4804\sqrt{2}}{2187}y_b^2y_\tau^2 - \frac{6561}{2402\sqrt{2}}\tilde{g}_e^2y_\tau^2 + \frac{16918\sqrt{2}}{6561}y_\tau^4\right), \\
\delta m^2_{\bar{e}_{33}} &= \frac{16}{27}\epsilon_d\epsilon_e y_b^2y_\tau^2 - \frac{152}{243}\epsilon_d\epsilon_e^2y_b^2y_\tau^2 + \epsilon_e^2\left(\frac{8}{3}y_b^2y_\tau^2 - \frac{9}{8}\tilde{g}_e^2y_\tau^2 + \frac{8}{3}y_\tau^4\right) \\
&\quad + \epsilon_e^3\left(-\frac{752}{243}y_b^2y_\tau^2 + \frac{81}{28}\tilde{g}_e^2y_\tau^2 - \frac{704}{243}y_\tau^4\right) + \epsilon_e^4\left(\frac{3736}{2187}y_b^2y_\tau^2 - \frac{6561}{3736}\tilde{g}_e^2y_\tau^2 + \frac{10028}{6561}y_\tau^4\right), \\
\delta m^2_{\bar{e}_{12}} &= \delta m^2_{\bar{e}_{21}} = \sigma_e\left(8\sqrt{3}y_b^2y_\tau^2 - \frac{3}{8}\sqrt{3}\tilde{g}_e^2y_\tau^2 + 16\sqrt{3}y_\tau^4\right),
\end{aligned}
$$

$$
\begin{aligned}
\delta m^2_{\tilde{e}_{13}} &= \delta m^2_{\tilde{e}_{31}} = \sigma_e \left(4\sqrt{6} y_b^2 y_\tau^2 - \frac{3}{2}\sqrt{\frac{3}{2}} \tilde{g}_e^2 y_\tau^2 + 16\sqrt{\frac{2}{3}} y_\tau^4 \right), \\
\delta m^2_{H_u} &= -\frac{4}{3}\epsilon_d^2 y_b^2 y_t^2, \\
\delta m^2_{H_d} &= \epsilon_d^2 \left(-\frac{4}{27} y_b^2 y_t^2 - \frac{40}{9} y_b^4 \right) - \frac{40}{27}\epsilon_e^2 y_\tau^4 + \frac{368}{243}\epsilon_e^3 y_\tau^4 - \frac{1376}{2187}\epsilon_e^4 y_\tau^4,
\end{aligned}
$$

$$
\begin{aligned}
(\tilde{A}_u)_{13} &= 2\sqrt{\frac{2}{3}}\sigma_d y_t y_b^2 + 4\sqrt{\frac{2}{3}}\sigma_u y_t^3, & (\tilde{A}_u)_{31} &= 8\sqrt{\frac{2}{3}}\sigma_u y_t^3, \\
(\tilde{A}_u)_{22} &= -\frac{2\epsilon_u}{9}(3y_t^3 + y_t y_b^2), & (\tilde{A}_u)_{33} &= \frac{4}{9}\epsilon_d^2 y_t y_b^2, \\
(\tilde{A}_u)_{23} &= \frac{4\sqrt{2}}{9}\epsilon_u y_t^3 + \frac{4\sqrt{2}}{9}\epsilon_d y_t y_b^2 - \frac{14\sqrt{2}}{81}\epsilon_d^2 y_t y_b^2, & (\tilde{A}_u)_{32} &= \frac{8\sqrt{2}\epsilon_u}{9} y_t^3, \\
(\tilde{A}_d)_{13} &= 2\sqrt{\frac{2}{3}}\sigma_d y_b^3 + 4\sqrt{\frac{2}{3}}\sigma_u y_b y_t^2, & (\tilde{A}_d)_{31} &= 4\sqrt{\frac{2}{3}}\sigma_d y_b^3, \\
(\tilde{A}_d)_{22} &= -\frac{2\epsilon_d}{9}(3y_b^3 + y_t^2 y_b) - \frac{2\epsilon_d^2}{81}(9y_b^3 - y_t^2 y_b), & (\tilde{A}_d)_{23} &= \frac{4\sqrt{2}\epsilon_d}{9} y_b^3 + \frac{4\sqrt{2}\epsilon_u}{9} y_t^2 y_b - \frac{10\sqrt{2}}{27}\epsilon_d^2 y_b^3, \\
(\tilde{A}_d)_{32} &= \frac{8\sqrt{2}\epsilon_d}{9} y_b^3 - \frac{4\sqrt{2}}{9}\epsilon_d^2 y_b^3, & (\tilde{A}_d)_{33} &= \frac{4}{3}\epsilon_d^2 y_b^3, \\
(\tilde{A}_e)_{13} &= 2\sqrt{\frac{2}{3}}\sigma_e y_\tau^3, & (\tilde{A}_e)_{31} &= 4\sqrt{\frac{2}{3}}\sigma_e y_\tau^3, \\
(\tilde{A}_e)_{22} &= -\frac{2}{3}\epsilon_e y_\tau^3 - \frac{2}{9}\epsilon_e^2 y_\tau^3 + \frac{178}{243}\epsilon_e^3 y_\tau^3 - \frac{382}{729}\epsilon_e^4 y_\tau^3, \\
(\tilde{A}_e)_{23} &= \frac{4\sqrt{2}}{9}\epsilon_e y_\tau^3 - \frac{10}{27}\sqrt{2}\epsilon_e^2 y_\tau^3 - \frac{4}{81}\sqrt{2}\epsilon_e^3 y_\tau^3 + \frac{3274\sqrt{2}}{6561}\epsilon_e^4 y_\tau^3, \\
(\tilde{A}_e)_{32} &= \frac{8\sqrt{2}}{9}\epsilon_e y_\tau^3 - \frac{4}{9}\sqrt{2}\epsilon_e^2 y_\tau^3 - \frac{20}{81}\sqrt{2}\epsilon_e^3 y_\tau^3 + \frac{5240\sqrt{2}}{6561}\epsilon_e^4 y_\tau^3, \\
(\tilde{A}_e)_{33} &= \frac{4}{3}\epsilon_e^2 y_\tau^3 - \frac{376}{243}\epsilon_e^3 y_\tau^3 + \frac{1868}{2187}\epsilon_e^4 y_\tau^3.
\end{aligned}
\tag{38}
$$

Case 2 models

• *Ordering* $\beta_{3i} > \beta_{2i}$. As before, all soft scalar mass-squared parameters are assumed to include a factor of $\Lambda^2/(4\pi)^4$, all trilinear scalar couplings are assumed to include a factor of $\Lambda/(4\pi)^2$, and we define $g_{\tilde{u}}^2 = \tilde{g}_u^2/2$, $g_{\tilde{d}}^2 = \tilde{g}_d^2/2$, and $g_{\tilde{l}}^2 = \tilde{g}_e^2/2$ (see Eq. (37)). Including all the relevant terms up to second order in β_{3u}, the nonvanishing corrections to the soft

supersymmetry breaking terms take the form:

$$
\begin{aligned}
(\delta m^2_{\tilde{Q}})_{11} &= \frac{195}{16}(y_t^4+y_b^4)+\frac{15}{4}y_t^2y_b^2+\frac{27}{16}y_b^2y_\tau^2-3y_t^2g_{\tilde{u}}^2-3y_b^2g_{\tilde{d}}^2+\frac{9}{16}\beta_{3d}^2y_b^2(6y_b^2+y_t^2)+\frac{9}{16}\beta_{3l}^2y_\tau^2y_b^2\\
&\quad+\frac{9}{16}\beta_{3u}^2y_t^2(6y_t^2+y_b^2),\\
(\delta m^2_{\tilde{Q}})_{22} &= \beta_{3d}^2\left(-2g_{\tilde{d}}^2y_b^2+\frac{21}{8}y_b^4+\frac{9}{16}y_b^2y_t^2+\frac{5}{8}y_b^2y_\tau^2\right)+\beta_{3u}^2\left(-2g_{\tilde{u}}^2y_t^2+\frac{21}{8}y_t^4+\frac{9}{16}y_b^2y_t^2\right)+\frac{3}{8}\beta_{3u}\beta_{3d}y_b^2y_t^2,\\
(\delta m^2_{\tilde{Q}})_{33} &= \frac{39}{16}(y_t^4+y_b^4)+\frac{5}{4}y_t^2y_b^2+\frac{11}{16}y_b^2y_\tau^2-y_t^2g_{\tilde{u}}^2-y_b^2g_{\tilde{d}}^2-\frac{3}{4}\beta_{3d}^2y_b^4+\frac{1}{16}\beta_{3l}^2y_b^2y_\tau^2-\frac{3}{4}\beta_{3u}^2y_t^4\\
&\quad+\frac{3}{8}\beta_{3u}\beta_{3d}y_b^2y_t^2,\\
(\delta m^2_{\tilde{Q}})_{12} &= (\delta m^2_{\tilde{Q}})_{21} = -\frac{3}{4\sqrt{2}}(y_t^4\beta_{3u}+y_b^4\beta_{3d}-y_t^2y_b^2(\beta_{3u}+\beta_{3d})),\\
(\delta m^2_{\tilde{u}})_{22} &= \frac{189}{8}y_t^4+\frac{9}{2}y_t^2y_b^2-6y_t^2g_{\tilde{u}}^2+\beta_{3u}^2\left(-g_{\tilde{u}}^2y_t^2+\frac{27}{4}y_t^4\right),\\
(\delta m^2_{\tilde{u}})_{33} &= \frac{45}{8}y_t^4+\frac{1}{2}y_t^2y_b^2-2y_t^2g_{\tilde{u}}^2+\beta_{3u}^2\left(-3g_{\tilde{u}}^2y_t^2+\frac{27}{4}y_t^4\right),\\
(\delta m^2_{\tilde{d}})_{22} &= \frac{189}{8}y_b^4+\frac{9}{2}y_t^2y_b^2+\frac{27}{8}y_b^2y_\tau^2-6y_b^2g_{\tilde{d}}^2+\beta_{3d}^2y_b^2\left(-g_{\tilde{d}}^2+\frac{27}{4}y_b^2+\frac{1}{8}y_\tau^2\right)+\frac{9}{8}\beta_{3l}^2y_b^2y_\tau^2,\\
(\delta m^2_{\tilde{d}})_{33} &= \frac{45}{8}y_b^4+\frac{1}{2}y_t^2y_b^2+\frac{11}{8}y_b^2y_\tau^2-2y_b^2g_{\tilde{d}}^2+\beta_{3d}^2y_b^2\left(-\frac{1}{3}g_{\tilde{d}}^2+\frac{27}{4}y_b^2+\frac{9}{8}y_\tau^2\right)+\frac{1}{8}\beta_{3l}^2y_b^2y_\tau^2,\\
(\delta m^2_{\tilde{L}})_{11} &= \frac{141}{16}y_\tau^4+\frac{81}{16}y_b^2y_\tau^2-3y_\tau^2g_{\tilde{l}}^2+\frac{27}{16}\beta_{3d}^2y_b^2y_\tau^2+\frac{9}{4}\beta_{3l}^2y_\tau^4,\\
(\delta m^2_{\tilde{L}})_{22} &= \beta_{3l}^2\left(-2g_{\tilde{l}}^2y_\tau^2+\frac{15}{8}y_b^2y_\tau^2+\frac{11}{8}y_\tau^4\right),\\
(\delta m^2_{\tilde{L}})_{33} &= \frac{17}{16}y_\tau^4+\frac{33}{16}y_b^2y_\tau^2-y_\tau^2g_{\tilde{l}}^2+\frac{3}{16}\beta_{3d}^2y_b^2y_\tau^2-\frac{7}{8}\beta_{3l}^2y_\tau^4,\\
(\delta m^2_{\tilde{L}})_{12} &= (\delta m^2_{\tilde{L}})_{21} = -\frac{3}{4\sqrt{2}}(y_\tau^4\beta_{3l})+\frac{3}{8\sqrt{2}}(\beta_{3l}^3y_\tau^4),\\
(\delta m^2_{\tilde{e}})_{22} &= \frac{135}{8}y_\tau^4+\frac{81}{8}y_b^2y_\tau^2-6y_\tau^2g_{\tilde{l}}^2+\frac{27}{8}\beta_{3d}^2y_b^2y_\tau^2+\beta_{3l}^2\left(-g_{\tilde{l}}^2y_\tau^2+\frac{3}{8}y_b^2y_\tau^2+\frac{17}{4}y_\tau^4\right),\\
(\delta m^2_{\tilde{e}})_{33} &= \frac{23}{8}y_\tau^4+\frac{33}{8}y_b^2y_\tau^2-2y_\tau^2g_{\tilde{l}}^2+\frac{3}{8}\beta_{3d}^2y_b^2y_\tau^2+\beta_{3l}^2\left(-3g_{\tilde{l}}^2y_\tau^2+\frac{27}{8}y_b^2y_\tau^2+\frac{17}{4}y_\tau^4\right),\\
\delta m^2_{H_u} &= -\frac{9}{2}y_t^4-\frac{3}{2}y_t^2y_b^2-9\beta_{3u}^2y_t^4,\\
\delta m^2_{H_d} &= -\frac{9}{2}y_b^4-\frac{3}{2}y_\tau^4-\frac{3}{2}y_t^2y_b^2-9\beta_{3d}^2y_b^4-3\beta_{3l}^2y_\tau^4,\\
(\tilde{A}_u)_{22} &= -\frac{3}{\sqrt{2}}y_t^3\beta_{3u}, \qquad (\tilde{A}_u)_{33} = -\frac{3}{2}y_t^3-\frac{1}{2}y_ty_b^2-\frac{3}{2}\beta_{3u}^2y_t^3,\\
(\tilde{A}_d)_{22} &= -\frac{3}{\sqrt{2}}y_b^3\beta_{3d}, \qquad (\tilde{A}_d)_{33} = -\frac{3}{2}y_b^3-\frac{1}{2}y_by_t^2-\frac{3}{2}\beta_{3d}^2y_b^3,\\
(\tilde{A}_e)_{22} &= -\frac{3}{\sqrt{2}}y_\tau^3\beta_{3l}-\frac{3}{2\sqrt{2}}y_\tau^3\beta_{3l}^3, \qquad (\tilde{A}_e)_{33} = -\frac{3}{2}y_\tau^3-\frac{3}{2}y_\tau^3\beta_{3l}^2.
\end{aligned}
$$

• *Ordering* $\beta_{2i} > \beta_{3i}$. Assuming the subleading $\beta_{3i} = 0$, we find the following corrections to the soft terms up to second order in β_{2i}:

$$
\begin{aligned}
(\delta m^2_{\tilde{Q}})_{22} &= \frac{195}{16}(y_t^4 + y_b^4) + \frac{15}{4}y_t^2 y_b^2 + \frac{27}{16}y_b^2 y_\tau^2 - 3y_t^2 g_{\tilde{u}}^2 - 3y_b^2 g_{\tilde{d}}^2 + \beta_{2d}^2 y_b^2 \left(-\frac{1}{2}g_{\tilde{d}}^2 + \frac{27}{8}y_b^2 + \frac{3}{16}y_t^2 + \frac{1}{16}y_\tau^2\right) \\
&\quad + \frac{9}{16}\beta_{2l}^2 y_b^2 y_\tau^2 + \beta_{2u}^2 y_t^2 \left(-\frac{1}{2}g_{\tilde{u}}^2 + \frac{27}{8}y_t^2 + \frac{3}{16}y_b^2\right) - \frac{3}{8}\beta_{2u}\beta_{2d} y_b^2 y_t^2, \\
(\delta m^2_{\tilde{Q}})_{33} &= \frac{39}{16}(y_t^4 + y_b^4) + \frac{5}{4}y_t^2 y_b^2 + \frac{11}{16}y_b^2 y_\tau^2 - y_t^2 g_{\tilde{u}}^2 - y_b^2 g_{\tilde{d}}^2 + \beta_{2d}^2 y_b^2 \left(-\frac{3}{2}g_{\tilde{d}}^2 + \frac{27}{8}y_b^2 + \frac{3}{16}y_t^2 + \frac{9}{16}y_\tau^2\right) \\
&\quad + \beta_{2u}^2 y_t^2 \left(-\frac{3}{2}g_{\tilde{u}}^2 + \frac{27}{8}y_t^2 + \frac{3}{16}y_b^2\right) - \frac{3}{8}\beta_{2u}\beta_{2d} y_b^2 y_t^2, \\
(\delta m^2_{\tilde{u}})_{11} &= \frac{189}{8}y_t^4 + \frac{9}{2}y_t^2 y_b^2 - 6y_t^2 g_{\tilde{u}}^2 + \frac{9}{4}\beta_{2d}^2 y_b^2 y_t^2 + \frac{45}{8}\beta_{2u}^2 y_t^4, \\
(\delta m^2_{\tilde{u}})_{22} &= \beta_{2u}^2 \left(-4g_{\tilde{u}}^2 y_t^2 + \frac{3}{2}y_b^2 y_t^2 + \frac{21}{4}y_t^4\right), \\
(\delta m^2_{\tilde{u}})_{33} &= \frac{45}{8}y_t^4 + \frac{1}{2}y_t^2 y_b^2 - 2y_t^2 g_{\tilde{u}}^2 - \frac{3}{4}\beta_{2d}^2 y_b^2 y_t^2 - \frac{3}{8}\beta_{2u}^2 y_t^4, \\
(\delta m^2_{\tilde{d}})_{11} &= \frac{189}{8}y_b^4 + \frac{9}{2}y_t^2 y_b^2 + \frac{27}{8}y_b^2 y_\tau^2 - 6y_b^2 g_{\tilde{d}}^2 + \frac{45}{8}\beta_{2d}^2 y_b^4 + \frac{9}{8}\beta_{2l}^2 y_b^2 y_\tau^2 + \frac{9}{4}\beta_{2u}^2 y_b^2 y_t^2, \\
(\delta m^2_{\tilde{d}})_{22} &= \beta_{2d}^2 y_b^2 \left(-\frac{1}{4}g_{\tilde{d}}^2 + \frac{21}{4}y_b^2 + \frac{3}{2}y_t^2 + \frac{5}{4}y_\tau^2\right), \\
(\delta m^2_{\tilde{d}})_{33} &= \frac{45}{8}y_b^4 + \frac{1}{2}y_t^2 y_b^2 + \frac{11}{8}y_b^2 y_\tau^2 - 2y_b^2 g_{\tilde{d}}^2 - \frac{3}{8}\beta_{2d}^2 y_b^4 + \frac{1}{8}\beta_{2l}^2 y_b^2 y_\tau^2 - \frac{3}{4}\beta_{2u}^2 y_b^2 y_t^2, \\
(\delta m^2_{\tilde{L}})_{22} &= \frac{141}{16}y_\tau^4 + \frac{81}{16}y_b^2 y_\tau^2 - 3y_\tau^2 g_{\tilde{l}}^2 + \frac{27}{16}\beta_{2d}^2 y_b^2 y_\tau^2 + \beta_{2l}^2 \left(-\frac{1}{2}g_{\tilde{l}}^2 y_\tau^2 + \frac{3}{16}y_b^2 y_\tau^2 + \frac{17}{8}y_\tau^4\right), \\
(\delta m^2_{\tilde{L}})_{33} &= \frac{17}{16}y_\tau^4 + \frac{33}{16}y_b^2 y_\tau^2 - y_\tau^2 g_{\tilde{l}}^2 + \frac{3}{16}\beta_{2d}^2 y_b^2 y_\tau^2 + \beta_{2l}^2 \left(-\frac{3}{2}g_{\tilde{l}}^2 y_\tau^2 + \frac{27}{16}y_b^2 y_\tau^2 + \frac{17}{8}y_\tau^4\right), \\
(\delta m^2_{\tilde{e}})_{11} &= \frac{135}{8}y_\tau^4 + \frac{81}{8}y_b^2 y_\tau^2 - 6y_\tau^2 g_{\tilde{l}}^2 + \frac{27}{8}\beta_{2d}^2 y_b^2 y_\tau^2 + \frac{27}{8}\beta_{2l}^2 y_\tau^4, \\
(\delta m^2_{\tilde{e}})_{22} &= \beta_{2l}^2 \left(-4g_{\tilde{l}}^2 y_\tau^2 + \frac{15}{4}y_b^2 y_\tau^2 + \frac{11}{4}y_\tau^4\right), \\
(\delta m^2_{\tilde{e}})_{33} &= \frac{23}{8}y_\tau^4 + \frac{33}{8}y_b^2 y_\tau^2 - 2y_\tau^2 g_{\tilde{l}}^2 + \frac{3}{8}\beta_{2d}^2 y_b^2 y_\tau^2 - \frac{5}{8}\beta_{2l}^2 y_\tau^4, \\
\delta m^2_{H_u} &= -\frac{9}{2}y_t^4 - \frac{3}{2}y_t^2 y_b^2 - \frac{9}{4}\beta_{2d}^2 y_b^2 y_t^2 - \frac{9}{4}\beta_{2u}^2 y_t^2 \left(2y_t^2 + y_b^2\right), \\
\delta m^2_{H_d} &= -\frac{9}{2}y_b^4 - \frac{3}{2}y_\tau^4 - \frac{3}{2}y_t^2 y_b^2 - \frac{9}{4}\beta_{2d}^2 y_b^2 (2y_b^2 + y_t^2) - \frac{9}{4}\beta_{2u}^2 y_b^2 y_t^2, \\
(\tilde{A}_u)_{22} &= -\frac{3}{2\sqrt{2}}\beta_{2u}(y_t^3 + y_t y_b^2), \qquad (\tilde{A}_u)_{33} = -\frac{3}{2}y_t^3 - \frac{1}{2}y_t y_b^2 - \frac{3}{4}\beta_{2d}^2 y_b^2 y_t - \frac{3}{4}\beta_{2u}^2 y_t^3, \\
(\tilde{A}_d)_{22} &= -\frac{3}{2\sqrt{2}}\beta_{2d}(y_b^3 + y_b y_t^2), \qquad (\tilde{A}_d)_{33} = -\frac{3}{2}y_b^3 - \frac{1}{2}y_b y_t^2 - \frac{3}{4}\beta_{2d}^2 y_b^3 - \frac{3}{4}\beta_{2u}^2 y_t^2 y_b, \\
(\tilde{A}_e)_{22} &= -\frac{3}{2\sqrt{2}}\beta_{2l} y_\tau^3 - \frac{9}{4\sqrt{2}}\beta_{2l}^3 y_\tau^3, \quad (\tilde{A}_e)_{33} = -\frac{3}{2}y_\tau^3 - \frac{3}{4}\beta_{2l}^2 y_\tau^3.
\end{aligned}
$$

Chapter 3

A Simple Portal Matter Model for Muon g-2

3.1 Introduction

Having explored the quark sector in the previous chapter of this thesis, we now turn to explorations of the lepton sector. In particular, we explore theories that involve new physics extensions that couple to the SM leptons, which can be motivated by explaining the potential discrepancy between the predicted and measured results of the anomalous magnetic moment of the muon.

To be more precise, the anomalous magnetic moment of the muon, defined as $a_\mu \equiv (g-2)_\mu/2$, has long been recognized as a potential indicator of physics beyond the SM. As introduced in Chapter 1, the first results of the FNAL measurement [5] combined with the BNL measurement [21], now place the discrepancy between the experimental measured value of a_μ and the theoretical calculation of the Standard Model [22–42] at

$$\Delta a_\mu = a_\mu^{\text{exp}} - a_\mu^{\text{SM}} = (251 \pm 59) \times 10^{-11}, \tag{39}$$

indicating a significance of 4.2σ. The question of whether this discrepancy is due to new physics or instead due to complexities of the theoretical prediction is currently an open question.[4] Under the plausible assumption at present that this discrepancy is indeed due to new physics, many BSM models have been proposed to address it.[5]

[4]Recent lattice calculations of the hadronic vacuum polarization contribution to $g-2$ [43–47]. suggest that the discrepancy can be attributed to this contribution, at the price of tension with the data-driven HVP calculation [112–114].

[5]For reviews, see e.g. [115] and the more recent [116]. Models that were of particular notice for us in this work include [117–123].

A class of models that has garnered limited attention in this context is the so-called "portal matter" models [56, 124–131]. These models address the required kinetic mixing of $O(10^{-(3-5)})$ between the Standard Model (SM) hypercharge and a hidden $U(1)_D$ symmetry, essential in vector portal/kinetic mixing scenarios for dark matter [124, 125, 132–135], by suggesting that this mixing is generated at one loop by new heavy fields - the portal matter fields, charged under both the SM hypercharge and $U(1)_D$ as described in [124, 125]. As highlighted in [56], if these fields are fermionic and are light enough to be produced at collider scales, they should be vector-like with the same SM quantum numbers as some SM fields, except that they would carry non-zero $U(1)_D$ charges. However, a minimal implementation of portal matter model was found to be insufficient to explain the observed $g-2$ discrepancy [56].

However, the field content of the portal matter construction, specifically the addition of vector-like fermions charged under a hidden $U(1)_D$, bears a striking similarity to models which address the muon $g-2$ in a well-studied fermiophobic Z' scenario [118, 136–138], in which a chirally enhanced contribution to Δa_μ is obtained by adding both isospin doublet and isospin singlet vector-like leptons, charged under the Z' gauge group, which can mix via a Yukawa coupling to the SM Higgs. In contrast to models with electroweak/TeV-scale Z' bosons, the dark matter phenomenology in portal matter models strongly motivates a *sub*-GeV dark gauge boson, and to our knowledge models with such a chirally enhanced Δa_μ value have not been explored in this region of parameter space. In this chapter, we consider the correction to Δa_μ in a simple portal matter construction with the same chiral enhancement mechanism employed in e.g. [118]. We will see that the observed value of Δa_μ can easily be accommodated and, crucially, that this scenario can trivially satisfy existing phenomenological constraints, even those that present non-trivial challenges to the analogous constructions with heavier new gauge bosons.

3.2 Model Setup

The model considered here is a simple extension of the minimal portal matter construction of [56]. The SM gauge group is extended by an Abelian dark gauge symmetry $U(1)_D$ with an $O(1)$ gauge coupling constant g_D. The SM fermion content is neutral under $U(1)_D$, but couplings to the gauge boson of the $U(1)_D$, which we shall henceforth refer to as the dark photon A_D, and the SM fields are achieved by a small kinetic mixing coefficient $\epsilon \sim O(10^{-(3-5)})$, which to an excellent approximation imparts all SM fields with a coupling

Field	$SU(2)_L$	$Y/2$	Q_D
$l_L = (\nu_L^\mu, \mu_L)^T$	$\mathbf{2}$	$-\frac{1}{2}$	0
μ_R	$\mathbf{1}$	-1	0
$L_{L,R}^+ = (\nu_{L,R}^+, D_{L,R}^+)^T$	$\mathbf{2}$	$-\frac{1}{2}$	$+1$
$E_{L,R}^+$	$\mathbf{1}$	-1	$+1$
$L_{L,R}^- = (\nu_{L,R}^-, D_{L,R}^-)^T$	$\mathbf{2}$	$-\frac{1}{2}$	-1
$E_{L,R}^-$	$\mathbf{1}$	-1	-1

Table 3.1: The representations of the portal matter leptons $D^\pm$ and $E^\pm$, and the second-generation SM leptons l_L and μ_R, with respect to $SU(2)_L \times U(1)_Y \times U(1)_D$. Note that all new fermions are vector-like under all gauge groups.

to the dark photon of ϵ times their photon coupling. The dark sector consists of the dark photon A_D, a SM singlet complex scalar S with a charge of $+1$ under $U(1)_D$ that achieves a vacuum expectation value (vev) and gives the dark photon a mass, and a dark matter field χ, which is a SM singlet charged under $U(1)_D$.

It is well known [133, 139, 140] that simplified dark matter models can generate the appropriate relic abundance consistent with other experimental constraints via s-channel annihilation of dark matter pairs into SM fermions, if the dark photon and dark matter both have masses of $O(0.01 - 1 \text{ GeV})$ and $g_D\epsilon \sim O(10^{-4})$. As the phenomenology of interest here is largely agnostic to the parameters governing the dark matter relic abundance (provided they lie broadly within the range we have discussed), we shall not specify the spin or mass of the dark matter field and only assume it is selected so that the required relic abundance is reproduced [6].

Our primary focus in this work is the heavy portal matter fermions that generate kinetic mixing between $U(1)_D$ and the SM hypercharge group $U(1)_Y$ at one loop, as in [124, 125]. In this model, these consist of two new families of vector-like leptons – two isospin doublet leptons D^+ and D^-, with $U(1)_D$ charges of $+1$ and -1, respectively, and two isospin singlet leptons E^+ and E^-, again with their $U(1)_D$ charges denoted by their superscripts. The detailed charge assignments are given in Table 3.1 [7].

For the set of vector-like fermion fields of SM hypercharges Q_{Y_i}, $U(1)_D$ charges Q_{D_i}, and

[6] See e.g. [141, 142] for alternative scenarios in which the sub-GeV vector boson is the dark matter; however, in these scenarios kinetic mixing does not play an important phenomenological role.

[7] For simplicity, we do not include any SM singlet right-handed neutrinos. A comprehensive study of options for generating neutrino masses and lepton flavor mixing angles in this context is deferred to future work.

masses m_i, the kinetic mixing coefficient ϵ is given by

$$\epsilon = c_W \frac{g_D g_Y}{12\pi^2} \sum_i Q_{Y_i} Q_{D_i} \log\left(\frac{m_i^2}{\mu^2}\right), \tag{40}$$

where μ is the renormalization scale.

The Lagrangian of this model is given by $\mathcal{L} = \mathcal{L}_G + \mathcal{L}_H + \mathcal{L}_f + \mathcal{L}_Y$, for the gauge, Higgs, fermion, and Yukawa sectors, respectively. $\mathcal{L}_G$ denotes the SM gauge Lagrangian together with the dark $U(1)$ contribution, as discussed. $\mathcal{L}_H$ includes the SM Higgs H and dark Higgs Lagrangian terms, which are

$$\mathcal{L}_H = \mathcal{L}_H^{\text{SM}} + (D_\mu S)^\dagger (D^\mu S) - V(H, S), \tag{41}$$

in which $V(H, S)$ takes the form

$$V(H, S) = -\mu_S^2 S^\dagger S + \lambda_S (S^\dagger S)^2 + \lambda_{HS} (H^\dagger H)(S^\dagger S). \tag{42}$$

Here we will assume $\lambda_{HS} \ll \lambda_S, \lambda_H$ for simplicity [8]. The fermionic kinetic terms of $\mathcal{L}_f$ are

$$\mathcal{L}_f = \mathcal{L}_f^{\text{SM}} + \sum_{F=L^\pm, E^\pm} i(\overline{F}_L \not{D} F_L + \overline{F}_R \not{D} F_R). \tag{43}$$

The Yukawa sector $\mathcal{L}_Y$ governs the mixing of portal matter fields $D^\pm$ and $E^\pm$ with the SM leptons. For simplicity, we assume here that all portal matter fields only mix with the second-generation leptons μ and ν_μ, which may be achieved via some flavor symmetry. Relaxing this assumption and allowing portal matter couplings to e.g. electrons, would introduce significant additional constraints on the model from lepton flavor-violating processes, similar to those discussed in [118]. Hence, $\mathcal{L}_Y$ is given by

$$\begin{aligned}
\mathcal{L}_Y \supset & -y_\mu \bar{l}_L H \mu_R - y_L^+ \bar{l}_L S^\dagger L_R^+ - y_L^- \bar{l}_L S L_R^- - y_E^+ \overline{E}_L^+ S \mu_R - y_E^- \overline{E}_L^- S^\dagger \mu_R \\
& - y_{LE}^+ \overline{L}_L^+ H E_R^+ - y_{EL}^+ \overline{E}_L^+ H^\dagger L_R^+ - y_{LE}^- \overline{L}_L^- H E_R^- - y_{EL}^- \overline{E}_L^- H^\dagger L_R^- \\
& - M_L^+ \overline{L}_L^+ L_R^+ - M_E^+ \overline{E}_L^+ E_R^+ - M_L^- \overline{L}_L^- L_R^- - M_E^- \overline{E}_L^- E_R^- + h.c.,
\end{aligned} \tag{44}$$

[8] In this class of models, the mixing between the SM Higgs H and a dark Higgs must be suppressed (e.g. $\lambda_{HS} \sim O(10^{-4})$) [56, 141, 143, 144] to avoid overly large corrections to the invisible branching fraction of the SM Higgs or constraints on light hidden scalar searches [145]. Thus we have assumed for simplicity that there is no mixing between the dark Higgs and SM Higgs sector. Including a small but nonzero λ_{HS} within allowed constraints does not appreciably change the phenomenology of the portal matter sector.

where the y's are Yukawa couplings and $M^{\pm}_{L,E}$ are vector-like mass parameters. Without loss of generality, we can perform phase rotations on the fields in Eq. (44) to guarantee that all M parameters, as well as $y^{\pm}_{L,E}$ and y_μ, are real and positive, but nontrivial phases can still be present in $y^{\pm}_{LE,EL}$. The fact that four complex phases in Eq. (44) are physical can be seen through parameter counting: there are 13 Yukawa couplings and 10 fermion fields that may undergo chiral phase rotations without affecting any other parameters in the action. Since a uniform rotation of all fields leaves Eq. (44) invariant, 9 complex phases can be eliminated, leaving the four physical phases in $y^{\pm}_{LE,EL}$.

After spontaneous symmetry breaking, the scalar fields S and H in the unitary gauge are $S = (v_S + h_D)/\sqrt{2}$ and $H = (0, v+h)/\sqrt{2}$, where v_S and v are the vev's of the dark and SM Higgs fields, respectively. Writing the fermion fields as $\psi^\mu_{L,R} = (\mu_{L,R},\, D^+_{L,R},\, E^+_{L,R},\, D^-_{L,R},\, E^-_{L,R})^T$, $\psi^\nu_L = (\nu_L, \nu^+_L, \nu^-_L)$, and $\psi^\nu_R = (\nu^+_R, \nu^-_R)$, Eq. (44) yields mass terms of the form $\overline{\psi}^\mu_L \mathcal{M}^\mu \psi^\mu_R$ and $\overline{\psi}^\nu_L \mathcal{M}^\nu \psi^\nu_R$, with

$$\mathcal{M}^\mu \equiv \frac{1}{\sqrt{2}} \begin{pmatrix} y_\mu v & y^+_L v_S & 0 & y^-_L v_S & 0 \\ 0 & \sqrt{2} M^+_L & y^+_{LE} v & 0 & 0 \\ y^+_E v_S & y^+_{EL} v & \sqrt{2} M^+_E & 0 & 0 \\ 0 & 0 & 0 & \sqrt{2} M^-_L & y^-_{LE} v \\ y^-_E v_S & 0 & 0 & y^-_{EL} v & \sqrt{2} M^-_E \end{pmatrix},$$
$$\mathcal{M}^\nu \equiv \frac{1}{\sqrt{2}} \begin{pmatrix} y^+_L v_S & y^-_L v_S \\ \sqrt{2} M^+_L & 0 \\ 0 & \sqrt{2} M^-_L \end{pmatrix}. \tag{45}$$

Bidiagonalizing these matrices in the usual manner, we have

$$(U^\mu)^\dagger_L \mathcal{M}^\mu U^\mu_R = \text{diag}(m_\mu, m^+_D, m^+_E, m^-_D, m^-_E). \tag{46}$$
$$(U^\nu)^\dagger_L \mathcal{M}^\nu U^\nu_R = \begin{pmatrix} 0 & 0 \\ m^+_\nu & 0 \\ 0 & m^-_\nu \end{pmatrix},$$

where the $m^\pm_\nu$ are of the order $m^\pm_D$, which further implies that the new vectorlike doublets do not contribute appreciably to the electroweak T parameter.

As seen shortly, experimental searches for leptonic portal matter generally require $M^\pm_{L,E} \gtrsim 1$ TeV. Assuming that $m_{A_D} = g_D v_S \sim O(0.01 - 1 \text{ GeV})$, this in turn suggests that $v_S/M^\pm_{L,E} \sim O(10^{-(3-4)})$. Meanwhile, $y_\mu v/M^\pm_{L,E}$ and $y^\pm_{LE,EL} v/M^\pm_{L,E}$ may in principle be

somewhat large if these Yukawa couplings saturate perturbativity bounds (in which case $yv/\sqrt{2} \sim 600$ GeV), but in practice the parameter space of interest has $y_\mu, |y^\pm_{LE,EL}| \ll 1$. Hence, we can sensibly perform our analysis perturbatively in the limit that $y_\mu v,\ |y^\pm_{LE,EL}|v,\ y^\pm_{L,E} v_S \ll M^\pm_{L,E}$. To leading order, we then have $m_\mu \approx \frac{y_\mu v}{\sqrt{2}}$, $m^\pm_D \approx M^\pm_L$, $m^\pm_E \approx M^\pm_E$,$m^\pm_\nu \approx M^\pm_L$, up to proportional corrections of $O(v^2/(M^\pm_{L,E})^2, v_S^2/(M^\pm_{L,E})^2, v_S v/(M^\pm_{L,E})^2)$. The coupling of the portal matter fields to SM matter is described in detail in [56], so we shall only summarize the critical points here: The SM isospin doublet (singlet) fermion achieves $O(v_S/M^\pm_{L,E})$ mixing with the isospin doublet (singlet) portal matter fields and, in the case of the charged leptons, $O(m_\mu v_S/(M^\pm_{L,E})^2)$ mixing with the isospin singlet (doublet) portal matter. These mixings facilitate nearly, but not entirely, chiral couplings between portal matter and SM fermions mediated by the dark photon, dark Higgs, and heavy electroweak bosons. As the dark Higgs possesses an $O(1)$ coupling between the portal matter and the SM, the portal matter overwhelmingly decays to SM fields via the emission of a dark Higgs or the longitudinal mode of a dark photon, leading to a distinctive collider signature of a high-p_T lepton and, depending on the decay of the dark photon and dark Higgs, either missing energy or a pair of highly collinear electrons, muons, or pions.

3.3 $g-2$ Calculation

In this model, there are several diagrams which yield new physics contributions at one loop to $g-2$. However, as seen in [56], the "conventional" dark photon contribution, arising from a dark photon emitted from an internal muon line in the loop (see, for example, [146, 147]) is generally between one and two orders of magnitude too small to account for the muon anomaly. In our framework, for $m_{A_D} \leq 1$ GeV, this contribution can account for $\lesssim 10\%$ of the observed anomalous muon magnetic moment and remain consistent with constraints on kinetic mixing from beam dump experiments, for example NA64 [148]. Instead, the dominant contributions to the magnetic moment must come from elsewhere – specifically, loops with a heavy vector-like fermion in the internal line. Diagrams of this class featuring the heavy electroweak bosons, the dark Higgs, and the dark photon can all contribute. However, in practice the overwhelmingly dominant contributions emerge from the dark Higgs and the longitudinal polarization of the dark photon, for the same reason that emissions of these particles dominate the decay width of the portal matter: because the dark Higgs possesses an $O(1)$ coupling between portal matter and SM states, these interactions (and by Goldstone boson equivalence, those with the longitudinal mode

of the dark photon) provide the strongest couplings of the portal matter to the SM. As $m_\mu, m_{A_D}, m_{h_D} \ll M^\pm_{L,E}$, the general results for a_μ [149] in this limit yield extremely simple expressions. More precisely, for a given heavy fermion F which couples to the muon via

$$\begin{aligned} & g_L A^\mu_D \overline{\mu}_L \gamma_\mu F_L + g_R A^\mu_D \overline{\mu}_R \gamma_\mu F_R \\ & + y_{LR} h_D \overline{\mu}_L F_R + y_{RL} h_D \overline{\mu}_R F_L + h.c., \end{aligned} \tag{47}$$

the contribution of Feynman diagrams with a dark photon loop and a dark Higgs loop with F on the internal fermion lines, as shown in Fig. 3.1, is

$$\begin{aligned} \Delta a_\mu^{A_D} &\approx \frac{m_\mu^2}{16\pi^2}\left(-\frac{5}{6}\frac{(|g_L|^2+|g_R|^2)}{m^2_{A_D}} + \frac{m_F}{m_\mu}\frac{Re[g_L^* g_R]}{m^2_{A_D}}\right), \\ \Delta a_\mu^{h_D} &\approx \frac{m_\mu^2}{16\pi^2}\left(\frac{(|y_{LR}|^2+|y_{RL}|^2)}{6m^2_F} + \frac{m_F}{m_\mu}\frac{Re[y_{LR}^* y_{RL}]}{m^2_F}\right). \end{aligned} \tag{48}$$

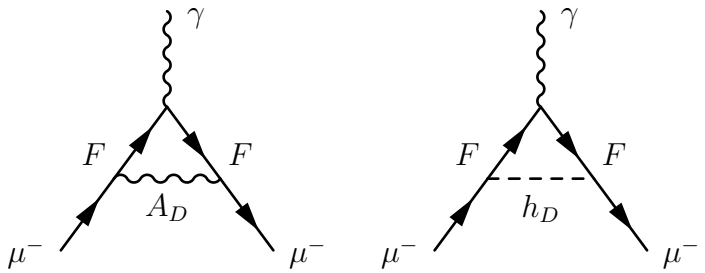

Figure 3.1: The Feynman diagrams contributing to the muon $g-2$ corrections, with $F = \{D^\pm, E^\pm\}$.

The Yukawa couplings $y_{LR,RL}$ in Eq. (48) are governed by $y^\pm_{LE,EL}$, which as we recall can be complex. However, phases in $y^\pm_{LE,EL}$ will generally also contribute to the *electric* dipole moment of the muon, which will in turn contribute to the measured anomalous magnetic dipole moment [150]. In the absence of significant tuning this contribution will be highly subleading. While the bounds on the muon EDM will be improved at the J-PARC E34 experiment [151] as well as at the FNAL Muon g-2 experiment, a direct measurement of this effect might only be reached in a dedicated muon EDM experiment, such as the planned experiment at PSI [152].

Hence, in this what follows we shall assume for simplicity that $y^\pm_{LE}$ and $y^\pm_{EL}$ are real, but may have arbitrary signs– for practical purposes the only difference between our results here and the more general case with complex Yukawa couplings (absent a direct measurement of muon EDM) would be that the dominant contributions of the new physics

to the Δa_μ would be scaled by cosines of the phase differences between these Yukawa couplings.

Of particular importance are the terms in Eq. (48) bearing the chiral enhancement factor $m_F/m_\mu \gg 1$. Without any information about the coupling constants, we would expect these terms to overwhelmingly dominate the $g-2$ correction. However, for isospin doublet (singlet) portal matter, $g_L(g_R)$ and $y_{RL}(y_{LR})$ are suppressed relative to their opposite-chirality couplings by a factor of $O(v/M^\pm_{L,E})$, so the chirally enhanced terms contribute to $g-2$ at the same order in $v/M^\pm_{L,E}, v_S/M^\pm_{L,E}$ as those which do not bear a chiral enhancement. This behavior of chirality-flipping operators in models with vector-like leptons is, of course, well-explored; it is precisely analogous to the behavior noted in [118, 119, 153, 154]. Computing the relevant dark photon and dark Higgs couplings in our model's mass basis by bidiagonalizing the mass matrices of Eq. (45), we find that

$$\Delta a_\mu^{A_D,D^\pm} = \Delta a_\mu^{h_D,D^\pm} = \frac{m_\mu^2 (y_L^\pm)^2}{192\pi^2 (M_L^\pm)^2}\left(1+\eta_L^\pm\right), \tag{49}$$
$$\eta_L^\pm \equiv \frac{6}{y_\mu}\frac{y_E^\pm}{y_L^\pm}\frac{M_L^\pm (M_E^\pm y_{LE}^\pm + M_L^\pm y_{EL}^\pm)}{(M_L^\pm)^2-(M_E^\pm)^2},$$

where the contributions from the weak isospin singlet portal matter, $\Delta a_\mu^{A_D,E^\pm}$ and $\Delta a_\mu^{h_D,E^\pm}$, are given by analogous expressions to Eq. (49), but with $L \longleftrightarrow E$ (with the caveat that $y_{LE}^\pm$ and $y_{EL}^\pm$ are not interchanged, and noting that $y_{LE}^\pm$ and $y_{EL}^\pm$ are real and can be either positive or negative). In these expressions, we have used $m_{A_D} = g_D v_S$ and $m_\mu \approx y_\mu v/\sqrt{2}$. We further note that although the individual expressions for $\Delta a^{A_D,D^\pm}$ and $\Delta a^{h_D,D^\pm}$ in Eq. (49) may appear to diverge in the limit that $M_L^\pm \to M_E^\pm$, these apparent divergences are always cancelled in the full expression for Δa_μ by the corresponding terms in $\Delta a^{A_D,E^\pm}$ and $\Delta a^{h_D,E^\pm}$.

The equivalence between the dark photon and dark Higgs contributions to $g-2$ is unsurprising. In the limit that we have taken in the unitary gauge (specifically that $m_{h_D}, m_{A_D} \ll M^\pm_{L,E}$), the only contributing part of the dark photon propagator in the loop stems from the longitudinal polarization, which in the Feynman gauge is simply the Goldstone boson part of the scalar S, of which the dark Higgs h_D forms the physical part.

More notably, the fact that the new physics $g-2$ contribution in this model is entirely dominated by the dark Higgs (and its Goldstone boson in the form of the longitudinal mode of the dark photon) means that the $g-2$ result in this model is to leading order *independent* of any of the parameters which govern the relic abundance or detection phenomenology

of the dark sector: The dark gauge coupling, kinetic mixing, and even the masses of the dark photon, dark Higgs, and dark matter fields do not enter into Eq. (49), as long as they remain within the approximate order of magnitude as specified by our parameter space. This conclusion even remains if one considers more exotic methods of generating the relic abundance than freeze-out dominated by simple s-channel annihilation to SM fermions, for example freeze-out dominated by kinematically forbidden annihilations or $3 \to 2$ processes [127, 155–157] – Eq. (49) *only* depends on the portal matter masses and their mixings with the SM fermions, and not on any of the parameters of the simplified dark matter model. This insensitivity to the specifics of the dark sector is in marked contrast to models that recreate the muon $g-2$ anomaly using lepton portal dark matter such as that of [158].

Combining all of these contributions, we arrive at the total new physics muon $g-2$ contribution in the model (up to sub-leading corrections from finite dark photon and dark Higgs masses and numerically subdominant diagrams, such as loops with the heavy electroweak bosons), which is given by

$$\begin{aligned} \Delta a_\mu^{\mathrm{PM}} &= \Delta a_\mu^{+} + \Delta a_\mu^{-}, \\ \Delta a_\mu^{\pm} &\equiv \frac{m_\mu^2}{96\pi^2}\left(\frac{(y_L^\pm)^2}{(M_L^\pm)^2} + \frac{(y_E^\pm)^2}{(M_E^\pm)^2} - \frac{6 y_L^\pm y_E^\pm}{M_L^\pm M_E^\pm}\frac{y_{LE}^\pm}{y_\mu}\right), \end{aligned} \tag{50}$$

where for clarity we have separated the contributions from the $+1$-charged portal matter, a_μ^+ from those of the -1-charged portal matter, a_μ^-. Note that while the contributions to $g-2$ from the Yukawa couplings $y_{EL}^\pm$ cancel in the summation, those corresponding to the SM Higgs Yukawa couplings with the same chiral structure as y_μ, namely $y_{LE}^\pm$, persist in the final expression for Δa_μ. Using Eq. (50), we can now perform some numerical estimates of the magnitude of the effect. As we previously discussed, collider searches for leptonic portal matter yield strong constraints, requiring $M_{L,E}^\pm \gtrsim 1$ TeV. Since perturbativity in turn requires that $y_{L,E}^\pm$ must be no greater than $O(1)$, the first two terms in the expression for $\Delta a_\mu^\pm$ in Eq. (50) can only feasibly contribute at roughly the same level as the dark photon loop with an internal muon, that is to say, they might account for $1-10\%$ of the anomalous magnetic moment. Isolating the third term, we have

$$\Delta a_\mu^\pm \approx -(\Delta a_\mu)\left(\frac{y_{LE}^\pm/y_\mu}{36}\right)\left(\frac{1\text{ TeV}}{M_E^\pm/y_E^\pm}\right)\left(\frac{1\text{ TeV}}{M_L^\pm/y_L^\pm}\right), \tag{51}$$

where Δa_μ is the measured anomaly described in Eq. (39). Hence, the observed $g-2$ anomaly can be accommodated as long as at least one of the Yukawa couplings y_{LE}^+ or

y^{-}_{LE} are negative (recall that we are working in a basis in which all Yukawa couplings are real and positive except $y^{\pm}_{LE}$ and $y^{\pm}_{EL}$), and there is a modest $O(10)$ hierarchy between whichever coupling(s) $y^{\pm}_{LE}$ dominate the $g-2$ contribution and y_μ. As y_μ is very small (roughly $O(10^{-4})$), allowing $y^{\pm}_{LE}$ to achieve a larger value is trivial – for $M^{\pm}_{L,E} \sim 1$ TeV, we expect $|y^{\pm}_{LE}|v \sim O(\text{a few GeV})$, in contrast to the $O(m_t)$ values for this quantity needed in [118], and roughly on par with the SM Yukawa couplings of the c and b quarks, or the τ lepton. These values are easily achievable with perturbative $y^{\pm}_{LE}$ values. Since these Yukawa couplings can only appear if there is a complete vector-like lepton family (with both an isospin doublet and a singlet) mixing with the muon, it is also clear why the minimal construction of [56] could not reproduce the observed $g-2$ anomaly.

As mentioned in Section 3.1, the method by which we have achieved a sizable $g-2$ correction here bears a significant similarity to models which address the muon $g-2$ anomaly with heavier $O(100-1000\text{ GeV})$ fermiophobic Z' bosons, in particular [118]. There the authors use the same chiral enhancement mechanism to generate the $g-2$ anomaly. However, our choice of a light dark photon inspired by sub-GeV kinetic mixing/vector portal dark matter, instead of a heavy hidden Z', leads to some unique characteristics: First, the contributions to the $g-2$ in Eq. (50) are entirely independent of the gauge sector parameters such as the dark photon mass and its associated gauge coupling, ultimately due to a version of Goldstone boson equivalence. Second, and perhaps more significantly, we shall see that the phenomenological constraints on this model differ markedly from the construction in [118] and similar works.

3.4 Other Constraints

It is clear from our result for Δa_μ in Eq. (50) that the principal parameters that govern Δa_μ are the Yukawa couplings $y^{\pm}_{LE}$ and the masses of the vector-like leptons, approximately given by $M^{\pm}_{L,E}$. Notably, the simplified sub-GeV dark matter model has no dependence on any of the parameters in Eq. (50), except for a logarithmic dependence of the kinetic mixing parameter ϵ on the ratios $M^{+}_{L,E}/M^{-}_{L,E}$. It is therefore trivial to find specific simplified dark matter models which reproduce the observed relic abundance and are accommodated by this construction.

Instead of the dark matter sector, we must turn to the portal matter sector directly for experimental constraints. Inspecting Eq. (51), we see that we may constrain this model by considering limits on the vector-like lepton masses. As previously stated, the current

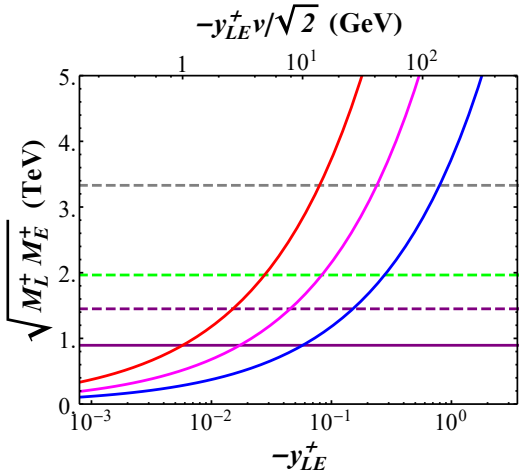

Figure 3.2: The mass scale of the $+1$-charged vector-like leptons ($\sqrt{M_L^+ M_E^+}$) to produce $\Delta a_\mu = 2.51 \times 10^{-9}$, as a function of y_{LE}^+ (assuming $|y_{LE}^+| \gg |y_{LE}^-|$), for $y_L^+ y_E^+ = 0.3$ (blue), 1 (magenta) and 3 (red). The minimum LHC mass of M_E^+ from [3] is depicted by a solid purple line, while the projected limits from [3] on M_E^+ are dashed lines for the HL-LHC (purple), HE-LHC (green), and hh-FCC (gray).

constraints on vector-like leptonic portal matter are already much stronger than the analogous limits on vector-like leptons which dominantly decay into heavier electroweak bosons, because the portal matter will overwhelmingly decay via the emission of light dark photons and dark Higgses. Assuming that these fields either decay into dark matter or are long-lived enough to escape a detector, the experimental signature for portal matter production strongly resembles that of sleptons. The study in [3] recasts the null results of an ATLAS slepton search with 139 fb^{-1} of data at 13 TeV, [159], as a limit on the mass of isospin singlet vector-like leptons, finding in our notation a limit of $M_E^\pm \geq 895$ GeV, with the mass constraints for vector-like leptons being about $16 - 20\%$ higher due to larger production cross sections [131, 160]. Assuming that $y_{L,E}^\pm \sim O(1)$, this constraint informs our estimate that $|y_{LE}^\pm| v \sim O(\text{GeV})$ to achieve the observed value of Δa_μ. While a detailed study is beyond the scope of this work, we can get a feel for the parameter space by performing some rough estimates. Fig. 3.2 shows the required mass scale of the $+1$-charged portal matter, $\sqrt{M_L^+ M_E^+}$, to reproduce $\Delta a_\mu = 2.51 \times 10^{-9}$, as a function of the Yukawa coupling y_{LE}^+, assuming that $|y_{LE}^+| \gg |y_{LE}^-|$, so that the contribution of the $+1$-charged portal matter fields to Δa_μ dominates that of the -1-charged portal matter. We have also included current and projected hadron collider constraints on isospin singlet leptonic portal matter from [3].

Notably, we see that even relatively near-term experiments, such as the HL-LHC, can probe many modest values of $|y^{\pm}_{LE}|v \sim O(\text{GeV})$. Longer term hadron collider experiments, such as hh-FCC, might be able to probe $y^{\pm}_{LE}$ values comparable to the top quark Yukawa coupling. We also note that a multi-TeV muon collider, such as discussed in [161], might permit probes of even higher portal matter lepton masses, up to roughly half of that collider's center-of-mass energy [160]. As such, even a modest 2 TeV muon collider provides comparable $y^{\pm}_{LE}$ reach to the current LHC constraints, while a muon collider with a center-of-mass energy $\gtrsim 6$ TeV will generally provide better reach than even the hh-FCC.

Several constraints that are relevant to other models that generate Δa_μ with vector-like leptons are highly suppressed in this model. For example, as the coupling between the SM muon-neutrino and the dark photon is suppressed by $v_S^2/(M^{\pm}_{L,E})^2 \lesssim 10^{-(6-8)}$, significant constraints such as neutrino trident production [162] and bounds on muon-neutrino scattering from Borexino [163] are several orders of magnitude too weak to significantly constrain this model, in marked contrast to the case of [118]. In addition, modifications to $h \to \gamma\gamma$ and $h \to \mu^+\mu^-$ are suppressed by $v_S^2/(M^{\pm}_{L,E})^2 \lesssim 10^{-(6-8)}$ and $v_S v/(M^{\pm}_{L,E})^2 \lesssim 10^{-(4-5)}$, respectively, which again are too weak to be presently constrained, though they are significant in the scenarios of [119].

3.5 Summary and Conclusions

In this letter, we have discussed a simple model of portal matter that can account for the observed muon $g-2$ anomaly via a chiral enhancement factor similar to that of [118]. However, in our model the sub-GeV mass scale of the dark photon, motivated by the kinetic mixing/vector portal dark matter scenario, has a profound influence on the $g-2$ contribution and the other phenomenological constraints. Most notably, due to the light dark photon mass in this theory, Δa_μ is to leading order independent of *any* parameters which appear in the simplified dark matter model, including the kinetic mixing, the masses of the dark photon and dark Higgs, and even the dark gauge coupling. As in [118], the contribution to Δa_μ is dominated by a SM Higgs Yukawa coupling between the isospin singlet and doublet portal matter fields, $y^{\pm}_{LE}$. However, the favored parameter range for $y^{\pm}_{LE}$ in this model is remarkably small, roughly comparable to the τ lepton Yukawa coupling, rather than $O(1)$. As Δa_μ depends on only a few parameters ($y^{\pm}_{LE}$ and the portal mass parameters $M^{\pm}_{L,E}$), large portions of the parameter space of this model can be readily explored with searches for leptonic portal matter fields at either hadron or lepton colliders;

multi-TeV muon colliders in particular represent a promising probe.

Our model is a minimal portal matter construction that addresses the muon $g-2$ anomaly, and it would be interesting to explore further extensions. A more detailed study within this framework might consider the constraints arising from mixing of the portal matter with the electron, as in [118], or how one might naturally satisfy the constraints in a more elaborate construction. Meanwhile, the similarity between our favored values for the Yukawa coupling $y_{LE}^{\pm}$ (for portal matter masses of ~ 1 TeV) and the Yukawa coupling for the τ lepton are suggestive that the order of magnitude of of $y_{LE}^{\pm}$ might be the consequence of some sort of flavor symmetry [164]. Along these lines, the next chapter of this thesis will be concerned with extending this simple model to a more complete and predictive theory based on the non-Abelian dark sector gauge group $SU(2) \times SU(2)$.

Chapter 4

An Extended Portal Matter Model with Lepton Flavor Symmetry

4.1 Introduction

Estimated to compose roughly 80% of the matter content of the universe, the presence of dark matter (DM) is clearly indicated through a plethora of cosmological and astrophysical data. However, DM's characteristics remain a mystery apart from its gravitational interactions, leading to a variety of extensions of the Standard Model (SM) featuring DM candidates [165–171]. As the parameter space for WIMP DM [165] continues to be constrained by experimental searches[9], other thermal DM paradigms have proliferated that can readily avoid these constraints and easily open up new viable parameter spaces for dark matter. For dark matter in the sub-GeV mass range (which might avoid stringent direct detection constraints from nuclear recoils [173–177]), a popular framework is that of vector portal/kinetic mixing [124, 125, 132–135]. In the simplest realization of this setup, the SM gauge group is augmented by a local Abelian $U(1)_D$ symmetry, under which an SM singlet DM candidate is charged, while the SM particle content is entirely neutral under the new group. Contact between the dark sector and the SM occurs via small kinetic mixing between $U(1)_D$ and $U(1)_Y$, the SM hypercharge, via a term in the action

$$\frac{\epsilon}{2c_w} B^{\mu\nu} X_{\mu\nu}, \tag{52}$$

where $B^{\mu\nu}$ is the usual SM hypercharge field strength tensor, $X_{\mu\nu}$ is the field strength tensor for the dark photon field, and c_w is the cosine of the Weinberg angle. For a massive

[9] See, however [172].

dark photon (where this mass might be achieved by a Higgs or Stuckelberg mechanism), this mixing then leads to a coupling between the dark photon and SM fields with non-zero hypercharge proportional to ϵ. For a sub-GeV DM candidate and a dark photon of comparable mass, this model will reproduce the *Planck* [178] observation of the DM relic abundance for $\epsilon \sim 10^{-(3-5)}$, depending on model specifics.

As noted by Holdom [124, 125], finite and calculable kinetic mixing of this magnitude can be generated at one loop if there exist additional fields in the theory which are charged under both $U(1)_D$ and $U(1)_Y$, and the $U(1)_D$ and $U(1)_Y$ charges of the additional fields are such that the ultraviolet divergence from each field's loop contribution is cancelled by the others. Recently there has been interest in the theory and phenomenology of these "portal matter" fields [55, 56, 126, 128–131, 179–182], in scenarios in which they are light enough to be kinematically accessible at present or near-future experiments. It was noted in [56] that if the portal matter is fermionic, the most phenomenologically viable scenario would be for the portal matter to be charged under $U(1)_D$, have identical SM quantum numbers to some SM field, and be vector-like under the SM gauge group and $U(1)_D$. Such fields have distinctive experimental signatures in collider experiments [3, 183], dominantly decaying into highly boosted jets (for QCD-charged portal matter) or leptons (for leptonic portal matter), plus a dark photon or dark Higgs, in contrast to channels featuring the emission of an electroweak boson that dominate vector-like fermion decay widths in scenarios without the $U(1)_D$ symmetry. Furthermore, these new portal matter fields may play a role in a variety of other unresolved questions in physics, such as the recently-observed W mass anomaly [180, 184].

One intriguing possibility is that the portal matter is purely leptonic in nature. As a concrete example, in [55] we suggested a minimal portal matter construction in which loops of portal matter fields with dark photons and dark Higgs bosons can account for the discrepancy between the experimental measurement of the anomalous magnetic moment of the muon [5, 21] and the theoretical expectation [22–42],

$$\Delta a_\mu = a_\mu^{\text{exp}} - a_\mu^{\text{SM}} = (251 \pm 59) \times 10^{-11}. \tag{53}$$

In [55] two pairs of leptonic portal matter fields (weak isospin singlets and doublets) were introduced. The weak isospin doublet and singlet fields are mixed by a Yukawa coupling to the SM Higgs field, and the dominant contribution to Δa_μ is directly proportional to this coupling, y_{LE}. Somewhat remarkably, the beyond Standard Model (BSM) contribution to Δa_μ is to an excellent approximation *independent* of the details of the sub-GeV DM sector,

and *only* dependent on the portal matter masses and their couplings to the SM and dark Higgs fields. For portal matter masses of ~ 1 TeV, the observed Δa_μ can be accommodated for intriguingly small values of y_{LE}, roughly on par with the b quark or τ lepton Yukawa couplings, and for larger $y_{LE} \sim O(1)$, portal matter masses of several TeV are potentially permitted.

While the minimality of the leptonic portal matter construction of [55] is in some respects attractive, like many minimal portal matter models, it suggests the possibility of a UV extension. As noted in [56], the $U(1)_D$ charge assignments in a minimal realization of the portal matter paradigm are essentially arbitrarily chosen to satisfy the need for finite and calculable kinetic mixing, and the fact that portal matter fields share quantum numbers with SM fields immediately suggests that both portal and SM matter might be embedded in multiplets of a larger dark sector gauge group, which, if it is semisimple, will automatically yield finite and calculable kinetic mixing. Therefore a number of more "UV-complete" models of portal matter have recently been developed to explore the model building possibilities of these types of constructions, such as [126, 128, 130, 179].

This chapter expands the work of [55] in this direction by proposing an extended dark sector gauge group. Noting that the necessary y_{LE} values to account for the observed Δa_μ in our minimal construction can be of the same magnitude as the τ Yukawa couplings, and that by restricting our model to the second and third generations we can avoid stringent precision constraints on new physics couplings to electrons, we choose as our semisimple extended dark sector the group $SU(2)_A \times SU(2)_B$ and associate it with a flavor symmetry in the second and third lepton generations. This extended construction possesses several appealing aspects: it is anomaly-free, and, because the dark gauge group is semi-simple, kinetic mixing between any $U(1)$ subgroups of it (including the group $U(1)_D$ which we identify with the group of the same name in minimal portal matter models) and the SM are finite and calculable. Furthermore, in contrast to the case of [55], the multiplet structure we choose relates some of the Higgs Yukawa couplings between isospin singlet and doublet portal matter directly with observed SM lepton masses. Constraints on flavor-changing currents are significantly mitigated with the addition of a Z_2 global discrete symmetry to the theory.

Upon analyzing the viable parameter space of this model, we find a rich phenomenology, including two qualitatively different scenarios which can both address the anomalous magnetic moment of the muon, based on the Z_2 parity of the particle that is identified as the muon. The first, which we call Scenario A, closely resembles the minimal model of [55],

with $U(1)_D$-charged portal matter that dominantly decays into muons and a contribution to the muon magnetic moment which is independent of any gauge couplings or other parameters of the underlying simplified dark matter model. In the other case, which we denote as Scenario B, the portal matter does *not* directly mix with the muons, and instead decays dominantly to τ leptons– there are meanwhile $U(1)_D$*-neutral* vector-like leptons that dominantly decay into the muons. Because loops involving heavier TeV-scale dark sector gauge fields now dominate the calculation, the $g-2$ correction in this scenario bears a greater similarity to the model of [118], in which a heavy Z' acts to generate the muon magnetic moment anomaly rather than a sub-GeV dark photon.

The remainder of the chapter is laid out as follows. In Section 4.2, we outline the construction of our model and identify various important features, as well as presenting notation that we shall use for the remainder of the work. In Section 4.3, we explore the parameter space for which the constructions of Scenario A and Scenario B can recreate the observed $g-2$ anomaly. In Section 4.4, we outline existing constraints and future prospects on both Scenario A and Scenario B, focusing on collider phenomenology and the usefulness of a multi-TeV muon collider in constraining or observing crucial model parameters. In Section 4.5, we summarize and discuss our findings and mention directions for future work.

4.2 Model Description

We will consider the augmentation of the SM gauge group $G_{SM} = SU(3)_C \otimes SU(2)_L \otimes U(1)_Y$ by a dark gauge group G_D, which we take to be of the form

$$G_D = SU(2)_A \otimes SU(2)_B, \tag{54}$$

and further augment the theory with a global Z_2 symmetry. Turning now to the fermionic matter content of the model, the SM quarks are taken to be singlets with respect to G_D and Z_2, as is one generation of the SM leptons. However, the other two generations of SM leptons will arise as the light degrees of freedom from mixing with sets of leptonic portal matter states. These states have nontrivial quantum numbers with respect to G_D and/or Z_2 as well as the electroweak gauge group, and are chosen to satisfy gauge anomaly constraints. Because G_D is semisimple, any kinetic mixing featuring the gauge fields associated with G_D will be finite and calculable. The list of these fields is given in Table [4.1].

Lepton Matter Content									
LH fields	G_{SM}	$SU(2)_A$	$SU(2)_B$	Z_2	RH Fields	G_{SM}	$SU(2)_A$	$SU(2)_B$	Z_2
L_L	$\mathbf{L}$	$\mathbf{1}$	$\mathbf{1}$	$+1$	e_R	$\mathbf{e}$	$\mathbf{1}$	$\mathbf{1}$	$+1$
Ψ_L	$\mathbf{L}$	$\mathbf{2}$	$\mathbf{2}$	$+1$	Ψ_R	$\mathbf{e}$	$\mathbf{2}$	$\mathbf{2}$	$+1$
V_L	$\mathbf{e}$	$\mathbf{1}$	$\mathbf{3}$	$+1$	V_R	$\mathbf{L}$	$\mathbf{1}$	$\mathbf{3}$	$+1$
S_L	$\mathbf{L}$	$\mathbf{1}$	$\mathbf{1}$	-1	S_R	$\mathbf{e}$	$\mathbf{1}$	$\mathbf{1}$	-1

Table 4.1: The lepton field content and corresponding representations with respect to G_D and G_{SM}. Here, $\mathbf{L}$ and $\mathbf{e}$ denote the G_{SM} charge assignments of the usual SM electroweak doublet and singlet leptons.

The breaking of G_D occurs in two stages: the first to the usual $U(1)_D$ of minimal portal matter constructions, which occurs at $O(\mathrm{T}eV)$ scales, and the second the breaking of $U(1)_D$, which occurs at sub-GeV scales. The SM Higgs boson H is taken to be a singlet with respect to G_D, and thus new scalar fields must be introduced to achieve the required symmetry breaking pattern. More precisely, we introduce the dark scalar Φ, which is a bidoublet with respect to $SU(2)_A \otimes SU(2)_B$, and two real scalar triplets $\Delta_{A,B}$, which are triplets with respect to $SU(2)_{A,B}$, respectively. In addition, Φ is even and $\Delta_{A,B}$ are odd with respect to Z_2. The dark scalar field content is summarized in Table 4.2. Writing the overall scales of

Dark Scalar Content				
Fields	G_{SM}	$SU(2)_A$	$SU(2)_B$	Z_2
Φ	$\mathbf{1}$	$\mathbf{2}$	$\mathbf{2}$	$+1$
Δ_A	$\mathbf{1}$	$\mathbf{3}$	$\mathbf{1}$	-1
Δ_B	$\mathbf{1}$	$\mathbf{1}$	$\mathbf{3}$	-1

Table 4.2: The dark scalar field content of this model. All the dark scalars are singlets under G_{SM}.

the vacuum expectation value (vevs) of Φ and $\Delta_{A,B}$ as v_Φ and $v_{\Delta_{A,B}}$, schematically, we have

$$SU(2)_A \otimes SU(2)_B \otimes Z_2 \xrightarrow[\Phi]{v_\Phi \sim 1 \text{ TeV}} U(1)_D \otimes Z_2 \xrightarrow[\Delta_A, \Delta_B]{v_{\Delta_{A,B}} \sim 1 \text{ GeV}} Z_2'$$

. We note the appearance of a residual unbroken Z_2', which arises from a combination of the unbroken part of $U(1)_D$ and the global Z_2 symmetry, as discussed in greater detail in Appendix A of [4]. We will see that while the conserved Z_2' leads to a number of intriguing features, it will ultimately need to be broken to generate viable lepton mixing. We will comment later in this chapter on possible extensions of this scenario that allow for Z_2' breaking.

As discussed in [55], we will not include terms that couple the SM Higgs boson to the dark sector at the renormalizable level, as such interactions are strongly constrained by *eg.* the invisible Higgs width (this issue is generic to portal matter constructions). In this case, the electroweak symmetry breaking and the dark symmetry breaking are decoupled. Focusing on the dark gauge group breaking, the most general renormalizable scalar potential that respects $SU(2)_A \otimes SU(2)_B \otimes Z_2$ is given by

$$\begin{aligned} V(\Phi, \Delta_{A,B}) = & -\mu_1^2 \,\mathrm{Tr}\Big(\Phi^\dagger \Phi\Big) - \frac{\mu_2^2}{2}\Big[\mathrm{Tr}\Big(\widetilde{\Phi}^\dagger \Phi\Big) + \text{h.c.}\Big] - \mu_3^2 \,\mathrm{Tr}\Big(\Delta_A^2\Big) - \mu_4^2 \,\mathrm{Tr}\Big(\Delta_B^2\Big) \\ & + \lambda_1 \,\mathrm{Tr}\Big(\Phi^\dagger \Phi\Big)^2 + \frac{\lambda_2}{2}\Big[\mathrm{Tr}\Big(\widetilde{\Phi}^\dagger \Phi\Big)^2 + \text{h.c.}\Big] + \frac{\lambda_3}{2}\Big[\mathrm{Tr}\Big(\Phi^\dagger \Phi\Big)\,\mathrm{Tr}\Big(\widetilde{\Phi}^\dagger \Phi\Big) + \text{h.c.}\Big] + \lambda_4 \,\mathrm{Tr}\Big(\Delta_B^4\Big) \\ & + \lambda_5 \,\mathrm{Tr}\Big(\Phi^\dagger \Phi\Big)\,\mathrm{Tr}\Big(\Delta_B^2\Big) + \frac{\lambda_6}{2}\Big[\mathrm{Tr}\Big(\widetilde{\Phi}^\dagger \Phi\Big)\,\mathrm{Tr}\Big(\Delta_B^2\Big) + \text{h.c.}\Big] + \lambda_7 \Big|\mathrm{Tr}\Big(\widetilde{\Phi}^\dagger \Phi\Big)\Big|^2 + \lambda_8 \,\mathrm{Tr}\Big(\Phi^\dagger \Delta_A \Phi \Delta_B\Big) \\ & + \frac{\lambda_9}{2}\Big[\mathrm{Tr}\Big(\widetilde{\Phi}^\dagger \Delta_A \Phi \Delta_B\Big) + \text{h.c.}\Big] + \lambda_{10} \,\mathrm{Tr}\Big(\Delta_A^4\Big) + \lambda_{11} \,\mathrm{Tr}\Big(\Phi^\dagger \Phi\Big)\,\mathrm{Tr}\Big(\Delta_A^2\Big) \\ & + \frac{\lambda_{12}}{2}\Big[\mathrm{Tr}\Big(\widetilde{\Phi}^\dagger \Phi\Big)\,\mathrm{Tr}\Big(\Delta_A^2\Big) + \text{h.c.}\Big] + \lambda_{13} \,\mathrm{Tr}\Big(\Delta_A^2\Big)\,\mathrm{Tr}\Big(\Delta_B^2\Big), \end{aligned} \tag{55}$$

in which $\widetilde{\Phi}_{i\alpha} = -\epsilon_{ij}\Phi^{*j\beta}\epsilon_{\beta\alpha}$.

As shown in detail in Appendix A of [4], to achieve the two-stage breaking of G_D through the minimization of Eq. (55), the vevs of the dark scalar fields Φ and $\Delta_{A,B}$ take the form:

$$\langle \Phi \rangle = v_\Phi \begin{pmatrix} \cos\theta_\Phi & 0 \\ 0 & \sin\theta_\Phi \end{pmatrix}, \qquad \langle \Delta_{A,B} \rangle = \begin{pmatrix} 0 & v_{\Delta_{A,B}} \\ v_{\Delta_{A,B}} & 0 \end{pmatrix}. \tag{56}$$

We define $v_\Delta = \sqrt{v_{\Delta_A}^2 + v_{\Delta_B}^2}$ and $\tan\theta_\Delta = v_{\Delta_A}/v_{\Delta_B}$, where $0 \leq \theta_\Delta \leq \pi/2$, and take $r_\Delta = v_\Delta/v_\Phi$. Note that $r_\Delta \sim 10^{-3} \ll 1$, and hence the symmetry breaking analysis can be performed perturbatively in r_Δ.

We begin by describing the gauge boson masses and eigenstates. Here we label the gauge fields of $SU(2)_A \otimes SU(2)_B$ as $W_{A,B}$, with coupling constants $g_{A,B}$. These gauge couplings are related to the elementary dark charge e_D of the $U(1)_D$ gauge group by $e_D = g_A \cos\theta_D = g_B \sin\theta_D$, which allows us to exchange the inputs (g_A, g_B) for (e_D, θ_D).

The mass eigenstates are given by

$$\begin{aligned} Z_D &= \cos\theta_D W_A^z + \sin\theta_D W_B^z, & M_{Z_D} &= \sqrt{2} v_\Phi e_D \csc(2\theta_D), \\ A_D &= -\sin\theta_D W_A^z + \cos\theta_D W_B^z, & m_{A_D} &= \frac{1}{\sqrt{2}} r_\Delta \sin 2\theta_D M_{Z_D}, \\ W_l^\pm &= \cos\theta_W W_A^\pm + \sin\theta_W W_B^\pm, & M_{W_l} &= \sin\theta_{lh} M_{Z_D}, \\ W_h^\pm &= -\sin\theta_W W_A^\pm + \cos\theta_W W_B^\pm, & M_{W_h} &= \cos\theta_{lh} M_{Z_D}, \end{aligned} \tag{57}$$

in which $\tan 2\theta_W = \sin 2\theta_\Phi \tan 2\theta_D$ and $\cos 2\theta_{lh} = \cos 2\theta_D \sqrt{1 + \sin^2\theta_\Phi \tan^2\theta_D}$. We note that we can exchange the inputs (e_D, θ_D) for (M_{Z_D}, θ_{lh}). The field A_D is the dark photon, which has its mass controlled by r_Δ, while the remaining gauge boson masses scale with v_Φ. We note that Z_D and A_D are even with respect to Z_2', while $W_{l,h}$ are odd.

The details of the scalar mass spectrum are provided in Appendix A of [4]; here we briefly summarize the relevant results. There are 14 real degrees of freedom in the scalar sector (8 from Φ and 6 from $\Delta_{A,B}$). 6 of these degrees of freedom are eaten via the Higgs mechanism in the breaking of $SU(2)_A \otimes SU(2)_B$, leaving 8 physical scalar fields. We denote the 8 physical scalars as

$$\{h_1, h_2, h_3, h_{deg}^1, h_{deg}^2, h_4, h_5, h_6\}, \tag{58}$$

in which (h_{deg}^1, h_{deg}^2) form a degenerate subspace. Of these scalars, all but h_3 have their masses controlled by v_Φ, while the mass of h_3 is governed by $r_\Delta v_\Phi$. We will denote the mass of $h_{deg}^{1,2}$ as $M_{h^\pm}$; this can be understood by considering the quantities $h^\pm = (h_{deg}^1 \pm i h_{deg}^2)/\sqrt{2}$, in which the "$\pm$" superscript denotes the charges with respect to the unbroken $U(1)_D$ that results after the first stage of symmetry breaking. In the forthcoming phenomenological analysis, we will use $M_{h^\pm}$ as an input parameter in the scalar sector and parameterize the remaining scalar masses as

$$M_{h_{1,2,4}} = r_{1,2,4} M_{h^\pm}, \quad m_{h_3} = r_\Delta r_3 M_{h^\pm}, \quad M_{h_5} = \cos\theta_M M_{h^\pm}, \quad M_{h_6} = \sin\theta_M M_{h^\pm}, \tag{59}$$

in which the r_i and θ_M are $O(1)$ parameters; their detailed definitions are provided in Appendix A of [4]. As the minimum is CP-conserving and Z_2'-conserving, the scalars have well-defined CP and Z_2' quantum numbers $(\mathrm{C}P, Z_2')$, as summarized in Table 4.3.

Turning now to the fermion sector, the Yukawa interactions among the $SU(2)_A \otimes SU(2)_B \otimes Z_2$-charged fermions as listed in Table 4.1 to the dark scalars Φ and Δ_B as well as

Scalars Mass Eigenstates			
Eigenstate	CP	Z_2'	Mass (In units of $M_{h^\pm}$)
h_1	$+1$	$+1$	$M_{h_1} = r_1$
h_2	$+1$	$+1$	$M_{h_2} = r_2$
h_3	$+1$	$+1$	$m_{h_3} = r_\Delta r_3$
h^1_{deg}	$+1$	$+1$	1
h^2_{deg}	-1	$+1$	1
h_4	-1	$+1$	$M_{h_4} = r_4$
h_5	$+1$	-1	$M_{h_5} = \cos\theta_M$
h_6	$+1$	-1	$M_{h_6} = \sin\theta_M$

Table 4.3: Scalar mass eigenstates listed with their CP and Z_2' quantum numbers, and their masses.

to the SM Higgs H take the form

$$\begin{aligned}-\mathcal{L}_Y =& y_H\left[\mathrm{Tr}\left(\overline{\Psi_L}H\Psi_R\right)+\text{h.c.}\right]+y_{HV}\left[\mathrm{Tr}\left(\overline{V_L}HV_R\right)+\text{h.c.}\right]+y_{HS}\left[\mathrm{Tr}\left(\overline{S_L}HS_R\right)+\text{h.c.}\right]\\ &+y_P\left[\mathrm{Tr}\left(\overline{\Psi_L}\Phi V_R\right)+\text{h.c.}\right]+\tilde{y}_P\left[\mathrm{Tr}\left(\overline{\Psi_L}\widetilde{\Phi}V_R\right)+\text{h.c.}\right]+y_{P'}\left[\mathrm{Tr}\left(\overline{V_L}\Phi^\dagger\Psi_R\right)+\text{h.c.}\right]\\ &+\tilde{y}'_P\left[\mathrm{Tr}\left(\overline{V_L}\widetilde{\Phi}^\dagger\Psi_R\right)+\text{h.c.}\right]+y_{SE}\left[\mathrm{Tr}\left(\overline{V_L}S_R\Delta_B\right)+\text{h.c.}\right]+y_{SL}\left[\mathrm{Tr}\left(\overline{S_L}V_R\Delta_B\right)+\text{h.c.}\right].\end{aligned} \tag{60}$$

For simplicity, we will take all Yukawa couplings to be real. We will further find it convenient to write the Yukawa couplings as

$$y_P = y_L\cos\theta_L,\quad \tilde{y}_P = y_L\sin\theta_L,\quad y'_P = y_E\cos\theta_E,\quad \text{and}\quad \tilde{y}'_P = y_E\sin\theta_E, \tag{61}$$

and define

$$\begin{aligned}M_L^+ &= v_\Phi y_L\cos(\theta_L-\theta_\Phi), & M_L^- &= v_\Phi y_L\sin(\theta_L+\theta_\Phi),\\ M_E^+ &= v_\Phi y_E\cos(\theta_E-\theta_\Phi), & M_E^- &= v_\Phi y_E|\sin(\theta_E+\theta_\Phi)|,\end{aligned} \tag{62}$$

where as before, both in the above and in what follows, the "$\pm$" superscripts denote charges of ±1 with respect to $U(1)_D$. Reflected above is the fact that by applying a series of chiral rotations to the fermions, we are capable of ensuring that y_L, y_E, y_{SL}, y_{SE}, y_{HS}, $\cos(\theta_L-\theta_\Phi)$, $\cos(\theta_E-\theta_\Phi)$, and $\sin(\theta_L+\theta_\Phi)$ are all positive without loss of generality, while y_H, y_{HV}, and $\sin(\theta_E+\theta_\Phi)$ can be either positive or negative– so we must take the absolute value of $\sin(\theta_E+\theta_\Phi)$ to get the physical mass M_E^-. The signs of y_H, y_{HV}, and $\sin(\theta_E+\theta_\Phi)$ will have significant phenomenological implications later, so it is important to be aware that they

remain undetermined under our conventions. For notational purposes, the electric-charged components of the matter fields will be written as

$$\Psi_{L,R} = \begin{pmatrix} \Psi_{L,R_{11}} & \Psi^{+}_{L,R} \\ \Psi^{-}_{L,R} & \Psi_{L,R_{22}} \end{pmatrix} \quad \text{and} \quad V_{L,R} = \begin{pmatrix} V^{0}_{L,R}/\sqrt{2} & V^{+}_{L,R} \\ V^{-}_{L,R} & -V^{0}_{L,R}/\sqrt{2} \end{pmatrix}, \tag{63}$$

and for the electric-neutral components we will use a similar definition, but with the inclusion of the superscript N. In the electric-charged fermion sector, we will organize the components of these fields in the following two sets: $X_{F,(L,R)} = (X^{(1)}_{F,(L,R)}, X^{(2)}_{F,(L,R)})$, in which

$$X^{(1)}_{F,(L,R)} = \left(\Psi_{(L,R)_{11}}, \Psi_{(L,R)_{22}}, V^{0}_{(L,R)}\right), \qquad X^{(2)}_{F,(L,R)} = \left(S_{(L,R)}, \Psi^{+}_{(L,R)}, V^{+}_{(L,R)}, \Psi^{-}_{(L,R)}, V^{-}_{(L,R)}\right). \tag{64}$$

The electric-charged fermion mass matrix M_F is composed of two blocks, $M^{(1)}_F$ and $M^{(2)}_F$, that do not mix with each other. These two blocks take the form

$$M^{(1)}_F = \frac{1}{\sqrt{2}} \begin{pmatrix} y_H v & 0 & M^{+}_L \\ 0 & y_H v & -M^{-}_L \\ M^{+}_E & \mp M^{-}_E & y_{HV} v \end{pmatrix} \tag{65}$$

$$M^{(2)}_F = \begin{pmatrix} \frac{y_{HS} v}{\sqrt{2}} & 0 & y^{\Delta}_{SL} r_\Delta v_\Phi & 0 & y^{\Delta}_{SL} r_\Delta v_\Phi \\ 0 & \frac{y_H v}{\sqrt{2}} & M^{+}_L & 0 & 0 \\ y^{\Delta}_{SE} r_\Delta v_\Phi & M^{+}_E & \frac{y_{HV} v}{\sqrt{2}} & 0 & 0 \\ 0 & 0 & 0 & \frac{y_H v}{\sqrt{2}} & M^{-}_L \\ y^{\Delta}_{SE} r_\Delta v_\Phi & 0 & 0 & \pm M^{-}_E & \frac{y_{HV} v}{\sqrt{2}} \end{pmatrix}, \tag{66}$$

in which v is the usual SM electroweak Higgs vev, and we have introduced the shorthanded notation $y^{\Delta}_{SL,SE} = (y_{SL,SE}/2)\cos\theta_\Delta$. Upon diagonalizing these matrices, to leading order in $r_H = v/v_\Phi \sim 10^{-2} \ll 1$ and r_Δ, the left and right-handed mass eigenstates for the Z'_2 positively charged fermions are

$$\begin{aligned} L^{b}_L &= \frac{1}{\sqrt{2}}\frac{M^{-}_L}{M^{0}_L}\Psi_{L_{11}} + \frac{1}{\sqrt{2}}\frac{M^{+}_L}{M^{0}_L}\Psi_{L_{22}}, \qquad e^{b}_R = \pm\frac{1}{\sqrt{2}}\frac{M^{-}_E}{M^{0}_E}\Psi_{R_{11}} + \frac{1}{\sqrt{2}}\frac{M^{+}_E}{M^{0}_E}\Psi_{R_{22}}, \\ L^{0}_L &= -\frac{1}{\sqrt{2}}\frac{M^{+}_L}{M^{0}_L}\Psi_{L_{11}} + \frac{1}{\sqrt{2}}\frac{M^{-}_L}{M^{0}_L}\Psi_{L_{22}}, \quad L^{0}_R = V^{0}_R, \\ E^{0}_L &= V^{0}_L, \qquad E^{0}_R = -\frac{1}{\sqrt{2}}\frac{M^{+}_E}{M^{0}_E}\Psi_{R_{11}} \pm \frac{1}{\sqrt{2}}\frac{M^{-}_E}{M^{0}_E}\Psi_{R_{22}}, \end{aligned} \tag{67}$$

with masses

$$m_b = \frac{M_E^+ M_L^+ \pm M_E^- M_L^-}{\sqrt{\left(M_E^{-2} + M_E^{+2}\right)\left(M_L^{-2} + M_L^{+2}\right)}} \frac{y_H v}{\sqrt{2}}, \quad M_L^0 = \sqrt{\frac{(M_L^-)^2 + (M_L^+)^2}{2}}, \quad M_E^0 = \sqrt{\frac{(M_E^-)^2 + (M_E^+)^2}{2}}, \quad (68)$$

respectively, while for the Z_2' negatively charged fermions, the left and right-handed mass eigenstates to leading order are

$$L_L^a = S_L, \qquad e_R^a = S_R, \qquad L_L^\pm = \Psi_L^\pm, \qquad L_R^\pm = V_R^\pm, \qquad E_L^\pm = V_L^\pm, \qquad E_R^\pm = \Psi_R^\pm, \quad (69)$$

with masses

$$m_a = \frac{y_{HS} v}{\sqrt{2}}, \qquad M_L^\pm, \qquad M_E^\pm, \quad (70)$$

respectively. The charged lepton mass eigenstates and their Z_2' charges are summarized in Table 4.4.

Lepton Mass Eigenstates					
LH fields	G_{SM}	Z_2'	RH Fields	G_{SM}	Z_2'
L_L^b	$\mathbf{L}$	$+1$	e_R^b	$\mathbf{e}$	$+1$
L_L^0	$\mathbf{L}$	$+1$	L_R^0	$\mathbf{L}$	$+1$
E_L^0	$\mathbf{e}$	$+1$	E_R^0	$\mathbf{e}$	$+1$
L_L^a	$\mathbf{L}$	-1	e_R^a	$\mathbf{e}$	-1
$L_L^\pm$	$\mathbf{L}$	-1	$L_R^\pm$	$\mathbf{L}$	-1
$E_L^\pm$	$\mathbf{e}$	-1	$E_R^\pm$	$\mathbf{e}$	-1

Table 4.4: List of charged fermion mass eigenstates and their corresponding quantum numbers with respect to G_{SM} and Z_2'.

For the electrically charge-neutral fermions, in analogy with Eq. (64), we can define

$$X_{F,L}^N = (\Psi_{L_{11}}^N, \Psi_{L_{22}}^N, S_L^N, \Psi_L^{N+}, \Psi_L^{N-}), \qquad X_{F,R}^N = (V_R^{N0}, V_R^{N+}, V_R^{N-}). \quad (71)$$

In this basis, the mass matrix for the electric charge-neutral fermions M_F^N thus takes the form

$$M_F^N = \begin{pmatrix} M_L^+/\sqrt{2} & 0 & 0 \\ -M_L^-/\sqrt{2} & 0 & 0 \\ 0 & y_{SL}^\Delta r_\Delta v_\Phi & y_{SL}^\Delta r_\Delta v_\Phi \\ 0 & M_L^+ & 0 \\ 0 & 0 & M_L^- \end{pmatrix}, \quad (72)$$

which again shows the separation into blocks according to the Z_2' charges. The electrically-neutral mass eigenstates are given by

$$\nu_{bL} = \frac{1}{\sqrt{2}}\frac{M_L^-}{M_L^0}\Psi^N_{L_{11}} + \frac{1}{\sqrt{2}}\frac{M_L^+}{M_L^0}\Psi^N_{L_{22}}, \qquad N_L^0 = -\frac{1}{\sqrt{2}}\frac{M_L^+}{M_L^0}\Psi^N_{L_{11}} + \frac{1}{\sqrt{2}}\frac{M_L^-}{M_L^0}\Psi^N_{L_{22}}, \qquad N_R^0 = V_R^{N0}, \tag{73}$$

and

$$\nu_{aL} = S_L^N, \qquad N_L^\pm = \Psi_L^{N\pm}, \qquad N_R^\pm = V_R^{N\pm}, \tag{74}$$

with masses

$$m_{\nu_a} = m_{\nu_b} = 0, \quad M_{N^0} = M_L^0, \quad M_{N^\pm} = M_L^0. \tag{75}$$

As we have not introduced right-handed neutrino singlet counterparts to balance the degrees of freedom among the left-handed and right-handed fermions, the active neutrinos ν_{aL} and ν_{bL} remain massless. For the purposes of this study, the issue of generating nonzero neutrino masses and observable mixing angles does not have a strong impact for the implications for the muon $g-2$ or the portal matter collider phenomenology, and thus we will neglect it in this work. We will comment later about the need for Z_2' breaking and its implications for the generation of neutrino masses within this framework.

A straightforward one-loop computation quickly allows us to explicitly verify that in this model, the kinetic mixing coefficient between A_D and the $U(1)_Y$ gauge field B is finite, calculable, and consistent with the $O(10^{-(3-5)})$ range we would require for a sub-GeV dark matter model. We arrive at

$$\epsilon = \frac{e_D e}{6\pi^2}\log\left(\frac{M_L^+ M_E^+}{M_L^- M_E^-}\right) \approx (5.3\times 10^{-3}) e_D \log\left(\frac{M_L^+ M_E^+}{M_L^- M_E^-}\right). \tag{76}$$

Returning to the electrically charged leptons, we see that there are two light states, which are massless in the limit that the electroweak vev $v \to 0$. These light states are e_a and e_b, with masses m_a and m_b, respectively. e_a is negatively charged with respect to Z_2', while e_b is positively charged with respect to Z_2'. The third light SM lepton is a gauge singlet with respect to G_D, and thus does not mix with the additional portal matter states; we will assume throughout this work that this state is the electron for the sake of concreteness and simplicity. We can therefore envision two general cases, depending on whether we identify e_a or e_b with the muon. To be more precise, we have the following two scenarios:

- **Scenario A**: the Z_2'-negative e_a is the muon, while e_b is the τ lepton.
- **Scenario B**: the Z_2'-positive e_b is the muon, while e_a is the τ.

We note that in Scenario B, the muon mass is controlled by the Yukawa coupling y_H and the mass eigenstate is dominated by the G_D-bidoublet fermions $\Psi_{L,R}$. In contrast, in Scenario A, the muon mass is governed by y_{HS} and the muon eigenstate is dominantly given by the $SU(2)_A \otimes SU(2)_B$ singlet $S_{L,R}$.

For our phenomenological studies of this model, it will be useful to have a compact list of parameters that we can use to uniquely specify a point in parameter space. For clarity, we shall present that here– we have selected a parameterization that maximizes the number of parameters with immediate physical interpretation (*ie* masses, relative coupling strengths) and uses entirely quantities which are explicitly defined in this Section. In the purely gauge and scalar sector, we have

$$(e_D, \lambda_1, M_{Z_D}, M_{h_{1,2,4}}, M_{h^\pm}, \theta_M, \theta_D, \theta_\Delta, \theta_{lh}), \tag{77}$$

Since we are principally concerned with the phenomenology of the theory at $O(\text{TeV})$ energy scales, there will be no need for us to uniquely specify the masses of the dark photon A_D or the dark Higgs h_3, which are both of sub-GeV scales. Furthermore, of the couplings in the potential of Eq. (55), we need only retain the quartic coupling λ_1, since all other terms are either expressible in terms of masses or the angles given above, or only enter into scalar self-coupling interactions that we shall not explore in detail in this work. To specify the fermion sector we shall have the masses and Yukawa couplings

$$(M_L^\pm, M_E^\pm, |y_{HV}|, |y_H|, |y_{SL}|, |y_{SE}|). \tag{78}$$

Finally, as mentioned earlier in this Section, there are a handful of nontrivial signs for parameters that we must specify. For a complete specification, we need only include the signs

$$\text{sign}(y_{HV}, y_H, \sin(\theta_E + \theta_\Phi), \sin(2\theta_\Phi)). \tag{79}$$

We note that although the sign of $\sin(2\theta_\Phi)$ must be independently specified, its magnitude is always determined in terms of other parameters. In all of our subsequent computations in this work, we shall employ the parameterization of Eqs.(77-79) to specify points in parameter space of this model.

4.3 Muon $g-2$

In this section, we will present the results of the computation of the new physics contribution to the anomalous magnetic moment of the muon in Scenario A and Scenario B. In both scenarios, the dominant contributions arise at the one-loop level from loops of the new scalar and gauge bosons with heavy intermediate fermions, as in [55, 118]. If the SM Higgs mediates strong enough couplings between the isosinglet and isodoublet vector-like fermions, then the resultant chirality flip in the internal heavy fermion line can give rise to a chirally-enhanced contribution to Δa_μ which can fully account for the observed discrepancy. Other contributions, such as that stemming from the coupling of the dark photon to the muon through kinetic mixing (as discussed in, *eg*, [146]), are heavily suppressed, and can generally contribute to the final result at no more than the few percent level while remaining consistent with experimental constraints.[10] In this analysis, we shall therefore focus exclusively on the dominant contributions in our analysis. While the two scenarios both exhibit a similar mechanism by which the dominant contribution to Δa_μ is realized, the specifics of the scenarios are markedly different. As the scenarios differ in which light fermion is identified with the muon, the specific diagrams that contribute to Δa_μ are in fact entirely different in the two scenarios, and they must be addressed separately.

$g-2$ in Scenario A

In Scenario A, we identify the muon with the light fermion appearing in the block $M_F^{(2)}$ of the fermion mass matrix in Eq. (65), while the τ is identified with the light mass eigenstate appearing in block $M_F^{(1)}$. In turn, this allows us to use Eqs.(68) and (70) fix the Yukawa couplings y_H and y_{HS} to

$$|y_H| = \frac{\sqrt{2}m_\tau}{v}\sqrt{\frac{(M_L^{+2}+M_L^{-2})(M_E^{+2}+M_E^{-2})}{(M_L^+M_E^+ \pm M_L^-M_E^-)^2}}, \quad y_{HS} = \frac{\sqrt{2}m_\mu}{v}, \tag{80}$$

where we note that in our sign conventions, y_{HS} is always positive, but y_H may be either positive or negative. Recalling Eq. (62) and the discussion surrounding it in Section 4.2, we recall that the $+(-)$ sign in our expression is applied when $\sin(\theta_E+\theta_\Phi)$ is positive (negative). As discussed in Section 4.2, this relative sign cannot be eliminated by chiral

[10] We find that it is in principle possible for the dark photon loop as in [146] to account for as much as $\lesssim 10\%$ while still remaining barely consistent with current limits on dark photon mass and kinetic mixing (*eg*, [148]), but this contribution in most regions of parameter space is dramatically more subdued.

phase rotations, and hence the selection of a positive or negative sign here represents a selection between two distinct points in the model parameter space.

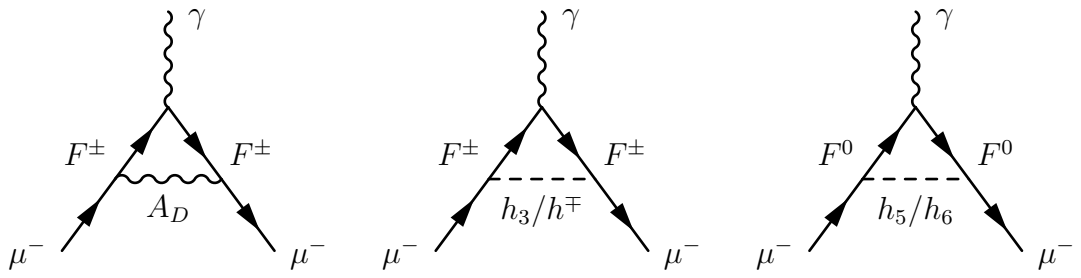

Figure 4.1: Feynman diagrams contributing to Δa_μ in Scenario A, with $F^0 = \{L^0, E^0\}$, $F^\pm = \{L^\pm, E^\pm\}$.

Scenario A features all of the same contributions to Δa_μ that our minimal construction in [55] does: Namely chirally-enhanced contributions from one-loop diagrams with dark photons and the dark Higgs, with intermediate portal matter fermions. In contrast to the minimal model presented in that work, however, the chirally enhanced contributions here feature the contributions from the exchange of heavy hidden gauge bosons and scalars, in addition to the contributions of the dark photon and dark Higgs that are associated with the $U(1)_D$ gauge group. Keeping only the chirally enhanced contribution

$$a_\mu = a_\mu^{A_D h_D} + a_\mu^{h_5 h_6} + a_\mu^{h_+, h_-}, \tag{81}$$

where a_μ^X represents the contribution to a_μ from one-loop diagrams featuring gauge or scalar bosons X. For convenience, we have also depicted the relevant diagrams in Figure 4.1. Using the general expressions of [149], we find the contributions

$$\begin{aligned}
a_\mu^{A_D h_D} &\approx \mp \sigma_\tau y_{SL} y_{SE} \frac{m_\mu m_\tau}{16\pi^2} \cos^2(\theta_\Delta) \frac{M_L^0 M_E^0}{M_L^+ M_L^- M_E^+ M_E^-}, \\
a_\mu^{h_5 h_6} &\approx \frac{y_{SL} y_{SE}}{16\pi^2} m_\mu (m_\tau \sigma_\tau a_\tau^{h5,h6} + m_{HV} a_{HV}^{h5,h6}), \\
a_\mu^{h+,h-} &\approx \frac{y_{SL} y_{SE}}{16\pi^2} m_\mu (m_\tau \sigma_\tau a_\tau^{h\pm} + m_{HV} a_{HV}^{h+,h-}), \\
\sigma_\tau &\equiv \text{sign}[y_H (M_L^+ m_E^+ \pm M_L^- M_E^-)],
\end{aligned} \tag{82}$$

where $m_{HV} \equiv y_{HV} v/\sqrt{2}$, and

$$
\begin{aligned}
a_\tau^{h5,h6} &\equiv M_L^0 M_E^0 \int_0^1 dx\, x^3 \frac{-M_{h^\pm}^2 c_\Delta^2 (1-x) P_x(M_{h^\pm}^2, M_L^{0\,2} + M_E^{0\,2}) - Q_x}{P_x(M_{h_5}^2, M_L^{0\,2}) P_x(M_{h_6}^2, M_L^{0\,2}) P_x(M_{h_5}^2, M_E^{0\,2}) P_x(M_{h_6}^2, M_E^{0\,2})}, \\
a_{HV}^{h5,h6} &\equiv \int_0^1 dx\, (1-x) x^2 \frac{M_{h_5}^2 M_{h_6}^2 (1-x) P_x(M_{h^+}^2, M_L^{0\,2} + M_E^{0\,2}) + M_{h^\pm}^2 s_\Delta^2 Q_x}{P_x(M_{h_5}^2, M_L^{0\,2}) P_x(M_{h_6}^2, M_L^{0\,2}) P_x(M_{h_5}^2, M_E^{0\,2}) P_x(M_{h_6}^2, M_E^{0\,2})}, \\
a_\tau^{h+h-} &\equiv \frac{-2 s_\Delta^2 M_L^0 M_E^0}{M_L^+ M_E^+ \pm M_L^- M_E^-} \int_0^1 dx \left(\frac{M_L^+ M_E^+}{P_x(M_{h^\pm}^2, M_L^{+\,2}) P_x(M_{h^\pm}^2, M_E^{+\,2})} \pm (M_{L,E}^+ \to M_{L,E}^-) \right), \\
a_{HV}^{h+,h-} &\equiv s_\Delta^2 \int_0^1 dx\, (1-x) x^2 \left(\frac{M_{h^+}^2}{P_x(M_{h^\pm}^2, M_L^{+\,2}) P_x(M_{h^\pm}^2, M_E^{+\,2})} + (M_{L,E}^+ \to M_{L,E}^-) \right), \\
P_x(A,B) &\equiv (1-x)A + xB, \quad Q_x \equiv M_L^{0\,2} M_E^{0\,2} x^2 - M_{h_5}^2 M_{h_6}^2 (1-x)^2, \quad (s_\Delta, c_\Delta) \equiv (\sin\theta_\Delta, \cos\theta_\Delta).
\end{aligned}
\tag{83}
$$

Notably, because these expressions are invariant under $M_{L,E}^+ \leftrightarrow M_{L,E}^-$ and $M_L^\pm \leftrightarrow M_E^\pm$, for the purposes of our numerical explorations here we can assume that the lightest portal matter field is the isodoublet with $+1$ charge under $U(1)_D$, with mass M_L^+. Numerically, we shall also find that although the various physical signs in our model, namely those of y_{HV}, y_H, and $\sin(\theta_E + \theta_\Phi)$ have physical effects, certain choices are overwhelmingly favored in order to reproduce the observed $g-2$ anomaly. First, because the signs of y_{HV} and y_H are arbitrary, we may always select them so that the y_{HV} and y_H contributions to Δa_μ interfere constructively and are of the appropriate sign to be consistent with experiment. This is, however, a physical assumption, and other possibilities exist– in particular one of the two terms may actually contribute *negatively* to Δa_μ and be compensated by a larger contribution of the other. In practice, this choice only has notable qualitative effects in the case that $y_{HV} > y_H$, where we shall explore it, and otherwise we shall assume that y_{HV} and y_H's signs are such that both terms contribute to Δa_μ in the direction consistent with the anomaly. The second physical sign selection we make, the sign of $\sin(\theta_E + \theta_\Phi)$ has a slightly more subtle effect on our results. The sign of $\sin(\theta_E + \theta_\Phi)$ leaves the y_{HV} terms of Δa_μ invariant, but if $\sin(\theta_E + \theta_\Phi) < 0$ various contributions to the y_H terms will interfere destructively, severely reducing the magnitude of this contribution relative to the $\sin(\theta_E + \theta_\Phi) > 0$ case. When applicable, we will discuss the significance of our $\sin(\theta_E + \theta_\Phi)$ sign choice.

In total, then, the chirally enhanced contributions to Δa_μ will be dependent on fixed SM parameters, plus a comparatively small subset of the model parameters that we have outlined in Eqs.(77-79): The masses of the portal matter fermions (where we always take

M_L^+ to be the lightest) and the two heavy scalars h_5 and h_6 (or equivalently, the mass of the heavy scalar $h_\pm$ and the angle θ_M, defined in Eq. (59)), the angle θ_Δ (defined below Eq. (56)), the Yukawa coupling y_{HV}, and the product of Yukawa couplings $y_{SL}y_{SE}$, plus the sign choices of $\sin(\theta_E + \theta_\Phi)$, y_H, and y_{HV}. There are several points to be made about these parameters which might guide our numerical explorations of the model's parameter space. First, as is apparent from Eqs.(81-83), when the masses of the heavy scalars are non-negligible both the Yukawa couplings $y_H \sim m_\tau/v$ and y_{HV} can play a role in the predicted value of $g-2$. This is particularly significant because while y_H is determined entirely by the value of the τ mass and the relative masses of the various portal matter fermions, y_{HV} can in principle be assigned any (perturbative) value we like– apart from affecting some branching fractions of heavier vector-like fermions to lighter ones, its only observable phenomenological consequence lies in the $g-2$ anomaly. We shall therefore consider two scenarios in our numerical investigations here: First, that $y_{HV} \ll y_H$ and so does not significantly contribute to the $g-2$ anomaly (perhaps, for example, if its value were related to the electron mass in a larger model of lepton flavor), and second that y_{HV} can take on up to $O(1)$ values.

Second, we can intuitively see that the new physics contribution to Δa_μ will be somewhat sensitive to the relative values of the masses of the portal matter fermions – if we set the lightest portal matter mass at some value, larger mass splittings between the portal matter fermions will generally suppress Δa_μ as the higher masses of the heavier portal matter fields will suppress their contributions in loops. For our numerical analysis, we shall consider a "typical" selection of $O(1)$ proportional mass splittings between portal matter fermions in most cases– $M_L^-/M_L^+ = 1.3$, $M_E^+/M_L^+ = 1.5$, and $M_E^-/M_L^+ = 1.8$ to get a sense of the numerics of a reasonable point in parameter space, as well as occasionally considering a "maximal" case in which all portal matter masses are degenerate and therefore the value of Δa_μ is maximized. Of course, the kinetic mixing between the dark and visible sectors will be weakly (logarithmically) sensitive to the mass splitting between the portal matter states, which suggests that requiring a kinetic mixing of $\gtrsim 10^{-(4-5)}$ likely merits at least an $O(1)$ mass splitting reminiscent of our typical case, and certainly renders the fully mass-degenerate scenario unfeasible for producing a viable dark matter model. The mass-degenerate numerics, where depicted, should not be considered a realistic scenario, therefore, but more of an absolute bound on the magnitude of Δa_μ that might be achieved in the model.

Finally, we note that while the new particle masses and the θ_Δ angle are both essentially

arbitrary in the absence of additional experimental evidence, we can estimate limits on the Yukawa couplings from partial wave unitarity. Following the analysis of [185] (generalized to incorporate scalars in the adjoint representations of $SU(2)$ rather than simply in the fundamental representation), we find that partial wave unitarity requires that

$$y_{SL}^2, y_{SE}^2 \leq 16\pi, \quad 3y_{SE}^2 + 5y_{SL}^2 + \sqrt{(3y_{SE}^2 + 5y_{SL}^2)^2 - 28y_{SE}^2 y_{SL}^2} < 32\pi, \tag{84}$$

such that

$$y_{SL} y_{SE} \leq \frac{16\pi}{7}(\sqrt{15} - 2\sqrt{2}) \sim 7.5, \tag{85}$$

and

$$y_{HV}^2 \leq \frac{8\pi}{3}. \tag{86}$$

While these couplings might be further constrained in future experiments, in particular from muon collider monophoton searches in the case of $y_{SL,SE}$ (see Section 4.4) and branching fractions of heavier vector-like fermions (in the event of their discovery) for y_{HV}, it is useful to keep in mind these bounds which maintain perturbative unitarity.

With the above observations in mind, we can now move on to considering a probe of some benchmark points in the model parameter space, beginning with the case in which $y_{HV} \ll y_H$, and hence the terms $a_{HV}^{h_5,h_6}$ and a_{HV}^{h+h-} do not contribute appreciably to Δa_μ. This scenario has the appealing consequence that the $g-2$ correction is specifically related to another observable quantity, namely the τ mass. In turn, this relationship significantly limits the portal matter mass range for which the model in this regime can reproduce the observed $g-2$ anomaly. In Figures 2.2 and 4.2, we have plotted the necessary value of the product $y_{SL} y_{SE}$ in order to fully account for the observed $g-2$ anomaly in the $y_{HV} \ll y_H$ scenario as a function of M_L^+, assuming that y_H is of the appropriate sign to make the resultant Δa_μ consistent with experiment, and taking $\sin(\theta_E + \theta_\Phi) > 0$ (when $\sin(\theta_E + \theta_\Phi) < 0$, the destructive interference among various Δa_μ corrections renders it unrealistic that the observed anomaly can be reproduced, so we do not consider that case here). In Figure 2.2, we consider a typical $O(1)$ mass splitting between the various portal matter masses, while in Figure 4.2, consider the case in which the portal matter masses are all degenerate (or at least have insignificant mass splitting), which will generally maximize the value of Δa_μ. In both cases, we find that for $M_L^+ \gtrsim 1$ TeV, roughly on par

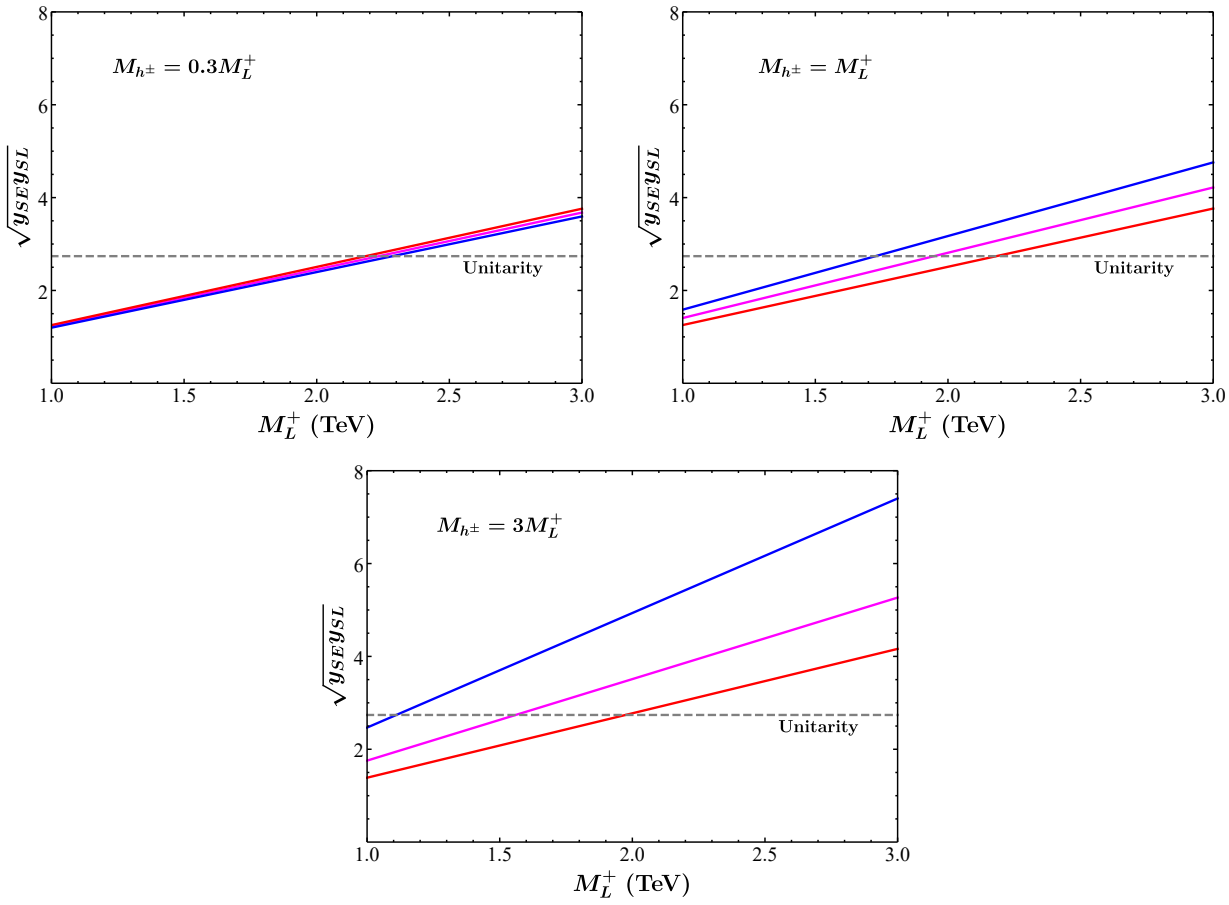

Figure 4.2: As in Figure 2.2, but with all portal masses assumed to be degenerate in order to near-maximize the new physics contribution to $g-2$ in Scenario A.

with existing LHC constraints on leptonic portal matter (we shall discuss this and other collider constraints in Section 4.4), a modest $O(1)$ enhancement of the new physics $g-2$ contribution from the product $y_{SL}y_{SE}$ is necessary. This product quickly approaches the perturbative unitarity bound on the product $y_{SL}y_{SE}$– we see for the points in parameter space considered in Figure 2.2 that M_L^+ must generally be lighter than ~ 1.5TeV in order to address the $g-2$ anomaly in this scenario, while in the more maximal case considered in Figure 4.2 we instead see that the lightest portal matter masses might be as large as ~ 2.2 TeV before the unitarity bound is saturated. Consulting the study of [3], we see that portal matter masses within this range are potentially within the reach of the $\sqrt{s} = 27$ TeV HE-LHC, and likely also within the discovery reach of a muon collider with a maximum center-of-mass energy greater than ~ 4 TeV [160].

We can get a better feel for the different parameters' effects on Δa_μ in the $y_{HV} \ll y_H$ scenario by plotting the results as functions of several different variables. In Figure 4.3, we depict contour plots of Δa_μ along several different variables. We can see several important behaviors from these plots. For example, we see that achieving the observed Δa_μ in this regime for $\gtrsim 1$ TeV portal matter will require modest $y_{SL} y_{SE} \gtrsim O(\text{a few})$ enhancements of the y_H contribution, and will generally be limited to scenarios in which the other portal matter fields and the scalars h_5 and h_6 are $\lesssim$ a few TeV, certainly not much greater than $2 - 3$ TeV. Given that these masses are all dictated in the action by the same scale v_Φ, this requirement of only modest $O(1)$ splittings between them is encouraging– it suggests that the favored parameter space for this model requires no careful tuning of the individual heavy particle masses.

Next, we consider the scenario in which the coupling y_{HV} is comparable to or greater than y_H. As noted before, because y_{HV}'s magnitude is not dictated by any other model parameter, it is feasible for it to be as large as $O(1)$, in which case $y_{HV} v/\sqrt{2} \sim 200$ GeV. In Figure 4.4, we depict contour plots of Δa_μ as a function of $m_{HV} = y_{HV} v/\sqrt{2}$ and $M_{h^+} = \sqrt{M_{h_5}^2 + M_{h_6}^2}$ for various choices of physical signs in the model, assuming that the lightest portal matter field has a mass of 1 TeV. We note that as M_{h_5} and M_{h_6} both approach 0, the required y_{HV} value to reproduce the observed Δa_μ diverges, since in the limit that these masses both vanish the y_{HV} term of the Δa_μ contribution vanishes. However, past a low-mass regime in which the observationally consistent y_{HV} value depends strongly on the particular value of M_{h^+}, which generally ends by $M_{h^+} \gtrsim 2$ TeV for all sign conventions we consider here, Δa_μ becomes only weakly dependent on the specific value of the scalar mass. Notably, we see that for $y_{SL} y_{SE} = 1$, the observed value of Δa_μ can be recreated for $m_{HV} \sim 20 - 50$ GeV as long as the h_5 and h_6 scalar bosons have masses $\gtrsim 0.5 - 1$ TeV), depending on the signs of various parameters within the model. Since these values of mass terms are well below 1 TeV, the scale of our portal matter mass, this suggests that our perturbative treatment $y_{HV} v \ll v_\Phi$ is, like our other perturbative expansions, numerically justified here.

As will be discussed later in Section 4.4, a constraint on y_{HV} may be identified by measuring the branching fractions of certain vector-like lepton decays via the emission of electroweak bosons, since this parameter contributes to the partial widths of both $U(1)_D$-uncharged and $U(1)_D$-charged vector-like leptons decaying into states which involve other vector-like leptons. However, given that these measurements are predicated on the successful discovery of not only the lightest portal matter field, but also the heavier

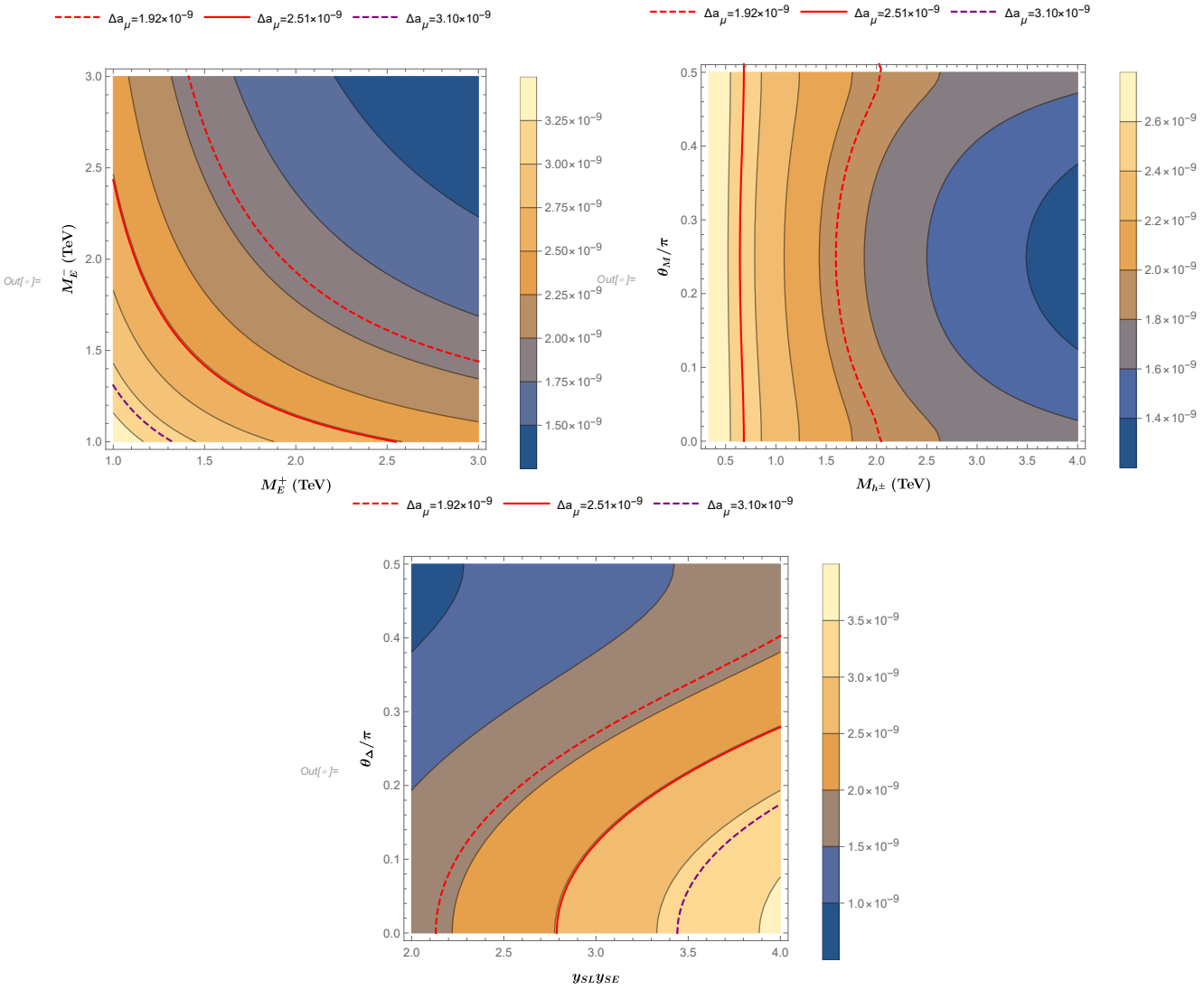

Figure 4.3: Contour plots of Δa_μ in Scenario A, with $y_{HV} \ll y_H$,$M_L^+ = 1$ TeV and $y_{SL}y_{SE} = 3$. (Top Left): contour plot as a function of M_E^+ and M_E^-, assuming $M_{h^\pm} = 1$ TeV and $\theta_M = \pi/4$, $M_L^- = 1.3$ TeV, and $\theta_\Delta = \pi/4$. (Top Right): Contour plot as a function of $M_{h^\pm}$ and θ_M, for $M_L^- = 1.3$ TeV, $M_E^+ = 1.5$ TeV, $M_E^- = 1.8$ TeV, and $\theta_\Delta = \pi/4$. (Bottom): Contour plot as a function of $y_{SL}y_{SE}$ and θ_Δ, for $M_{h^\pm} = 1$ TeV, $\theta_M = \pi/4$, and $M_L^- = 1.3$ TeV, $M_E^+ = 1.5$ TeV, $M_E^- = 1.8$ TeV. Note that points with $\theta_\Delta \neq \pi/4$ are unphysical (see Appendix A of [4]), but due to a lack of sensitivity of Δa_μ to θ_M, the plot remains illustrative of the θ_Δ behavior of Δa_μ at physical points in parameter space.

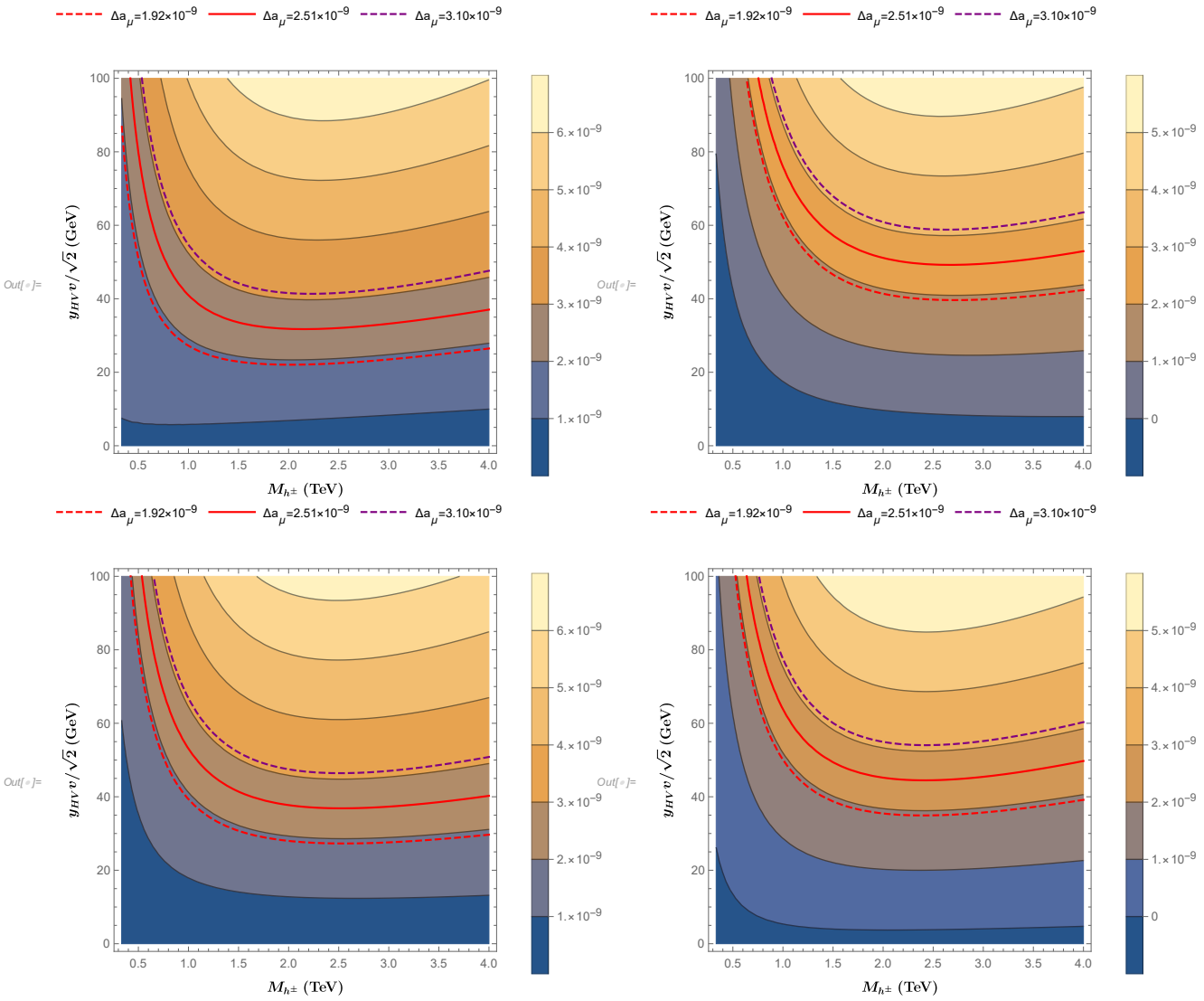

Figure 4.4: Contour plots of Δa_μ in Scenario A, for $y_{SL}y_{SE} = 1$, $M_L^+ = 1$ TeV, $M_L^- = 1.3$ TeV, $M_E^+ = 1.5$ TeV, $M_E^- = 1.8$ TeV, $\theta_\Delta = \pi/4$, and $M_{h_5} = M_{h_6} = M_{h^\pm}/\sqrt{2}$. (Top Left): Assuming the y_{HV} and y_H terms interfere constructively, and $\sin(\theta_E + \theta_\Phi) > 0$. (Top Right): the y_{HV} and y_H terms interfere destructively, and $\sin(\theta_E + \theta_\Phi) > 0$. (Bottom Left): the y_{HV} and y_H terms interfere constructively, and $\sin(\theta_E + \theta_\Phi) < 0$. (Bottom Right): the y_{HV} and y_H terms interfere destructively, and $\sin(\theta_E + \theta_\Phi) < 0$.

vector-like leptons that may possess the relevant decay channels, the principal constraint on y_{HV} currently (and for the foreseeable future) can come only from perturbative unitarity, even as the Yukawa couplings y_{SL} and y_{SE} and the mass of the lightest portal matter field can be constrained by monophoton searches at a muon collider and vector-like lepton pair production, respectively. It is therefore of some interest to explore how large the scale of the portal matter masses can be before it becomes impossible to reproduce the observed Δa_μ with perturbative y_{HV}, namely before y_{HV} saturates the partial wave unitarity bound of Eq. (86). In Figures 4.5 and 4.6, we take a sample spectrum of portal matter masses relative to one another ($O(1)$ separation in the case of Figure 4.5 and complete mass degeneracy in the case of Figure 4.6) and plot the necessary y_{HV} in order to match observation as a function of the lightest portal matter mass, for various choices of the parameters θ_Δ and $y_{SL}y_{SE}$, along with the perturbative unitarity bound on y_{HV}. We can see that for the sample spectrum of portal matter masses in Figure 4.5, the model might be disallowed for lightest portal matter masses ranging from as light as ~ 1.5 TeV, or permitted for lightest portal matter masses as large as $\gtrsim 10$ TeV– this range can be considerably narrowed by finding constraints on the Yukawa couplings y_{SL} and y_{SE} beyond those imposed by perturbative unitarity, however. The more maximal Δa_μ from assuming the portal matter masses are degenerate considered in Figure 4.6 unsurprisingly shift this portal matter mass range somewhat higher, to between ~ 2 TeV and ~ 15 TeV. Notably, the results in Figure 4.5 suggest that for $O(1)$ portal matter mass splittings and a lightest portal matter mass much above ~ 10 TeV, it is unlikely for *any* point in parameter space to be able to match the observed Δa_μ without significant fine-tuning– and hence a muon collider with a maximum center-of-mass energy of $\gtrsim 20$ TeV could likely probe the entirety of this model's viable parameter space by searching for portal matter pair production and constraining the couplings y_{SL} and y_{SE} via monophoton searches– this is roughly consistent with the behavior of the more minimal construction in [55]. Being more conservative and instead assuming that Δa_μ is maximized with degenerate portal matter masses, as in Figure 4.6, we see that the same conclusion can be reached with the upper limit on portal matter mass instead being ~ 15 TeV, which would potentially lie in the reach of a muon collider with a center-of-mass energy of $\gtrsim 30$ TeV. Of course, we remind the reader that such a high degree of portal matter mass degeneracy should be considered less realistic, and if taken literally, would lead to vanishing kinetic mixing between the photon and the dark photon A_D.

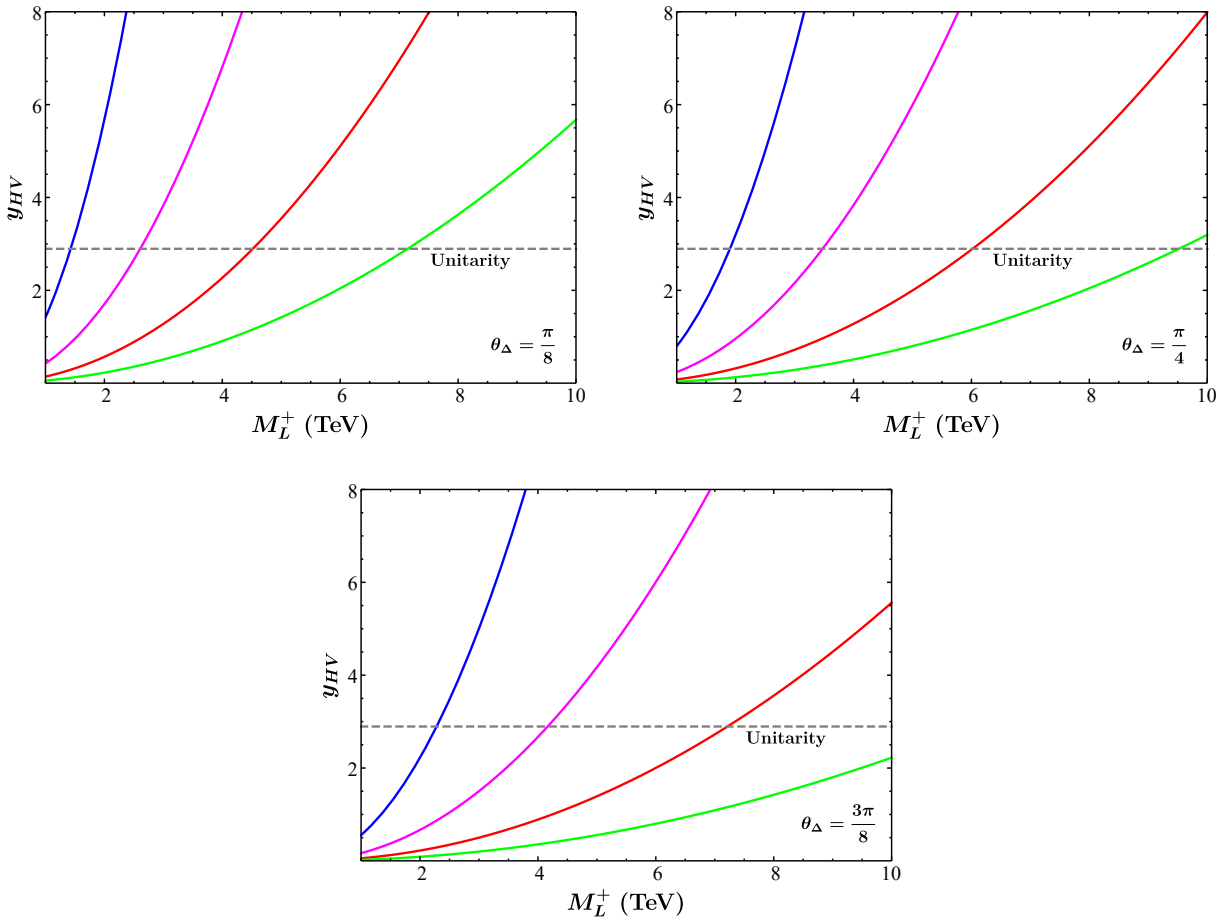

Figure 4.5: Plots of the y_{HV} coupling necessary to reproduce Δa_μ as a function of M_L^+ in Scenario A, for $M_L^-/M_L^+ = 1.3$, $M_E^+/M_L^+ = 1.5$, $M_E^-/M_L^+ = 1.3$. The perturbative unitarity bound $y_{HV}^2 = 8\pi/3$ is depicted as a gray dashed line, while we have taken $y_{SL}y_{SE} = 0.3$ (Blue), 1 (Magenta), 3 (Red), and the partial wave unitarity bound ≈ 7.5 (Green). We have also taken $\theta_\Delta = \pi/8$ (Top Left), $\pi/4$ (Top Right), and $3\pi/8$ (Bottom). Because when $y_{HV} \sim O(1)$, the y_{HV} term dominates the y_H term, this result is insensitive to choices of the sign of y_H and $\sin(\theta_E + \theta_\Phi)$.

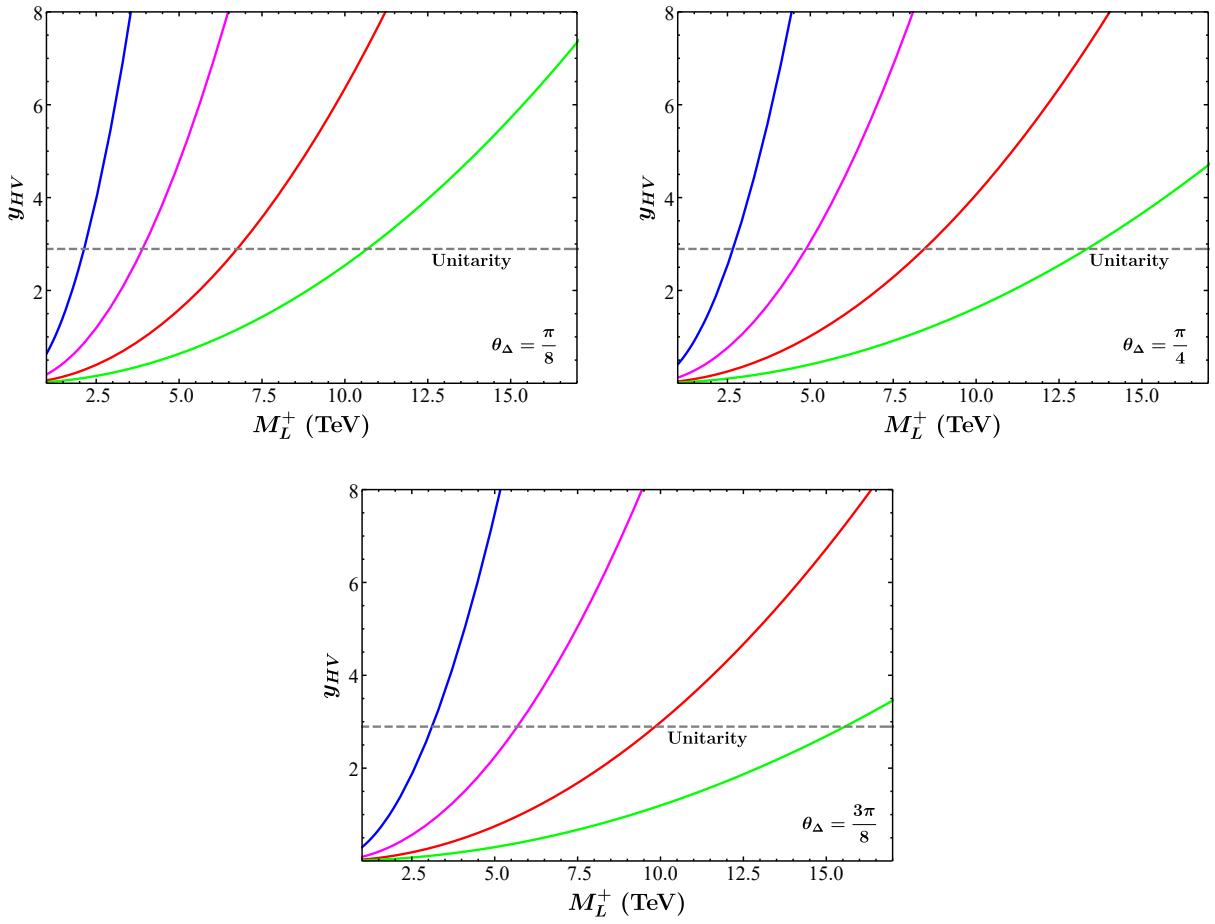

Figure 4.6: As in Figure 4.5, but assuming all portal matter masses are degenerate in order to estimate a near-maximal effect on Δa_μ.

$g-2$ in Scenario B

In Scenario B, we identify the muon with the light fermion appearing in the block $M_F^{(1)}$ of the fermion mass matrix in Eq. (65), while the τ is identified with the light fermion appearing in the block $M_F^{(2)}$. The Yukawa couplings y_H and y_{HS} then can be expressed as

$$|y_H| = \frac{\sqrt{2}m_\mu}{v}\sqrt{\frac{(M_L^{+2}+M_L^{-2})(M_E^{+2}+M_E^{-2})}{(M_L^+M_E^+ \pm M_L^-M_E^-)^2}}, \quad y_{HS} = \frac{\sqrt{2}m_\tau}{v}, \tag{87}$$

where we adopt the same sign conventions as in Scenario A, namely that y_{HS} is always positive, and y_H could be either positive or negative.

In this scenario, the muon's interactions with the new heavy gauge bosons are much stronger, appearing at leading order in r_Δ/v_Φ. Therefore, the gauge boson contributions and the scalar contributions are comparable and both should be taken into account. Fig 4.7 shows the Feynman diagrams that have dominant contributions to Δa_μ. In Scenario B, it is y_{HV} that is the most relevant coupling, unlike Scenario A in which $y_{SL}y_{SE}$ does the heavy lifting. Keeping only the chirally enhanced contribution that is numerically significant, and neglecting the term proportional to $|y_H|$, which is now far too small to contribute meaningfully to the magnetic moment anomaly, we have

$$
\begin{aligned}
a_\mu^{Z_D} &\approx \frac{5e_D^2\sigma_\mu\sigma_{E-}m_{HV}m_\mu M_E^- M_E^+ M_L^- M_L^+}{8\pi^2 s_{2D}^2 M_L^0 M_E^0}\int_0^1 dx \frac{x^2(x-1)}{P_x(M_{Z_D}^2, M_L^{0\,2})P_x(M_{Z_D}^2, M_E^{0\,2})},\\
a_\mu^{W_h,W_l} &\approx \frac{5e_D^2\sigma_\mu m_\mu m_{HV}}{16\pi^2 M_L^0 M_E^0}\left(\sigma_{E-}M_E^- M_L^-(a_-^{W_h}+a_-^{W_l}) + M_E^+ M_L^+(a_+^{W_h}+a_+^{W_l})\right),\\
a_\mu^{h_1,h_2,h_4} &\approx \frac{e_D^2\sigma_\mu m_\mu m_{HV}}{16\pi^2 M_L^0 M_E^0 M_{Z_D}^2 s_{2lh}^2}\left(2M_{h_4}^2 a^{h_4} + (M_E^{-\,2}-M_E^{+\,2})(M_L^{-\,2}-M_L^{+\,2})(M_{h_1}^2 a^{h_1}+M_{h_2}^2 a^{h_2})\right),
\end{aligned}
$$

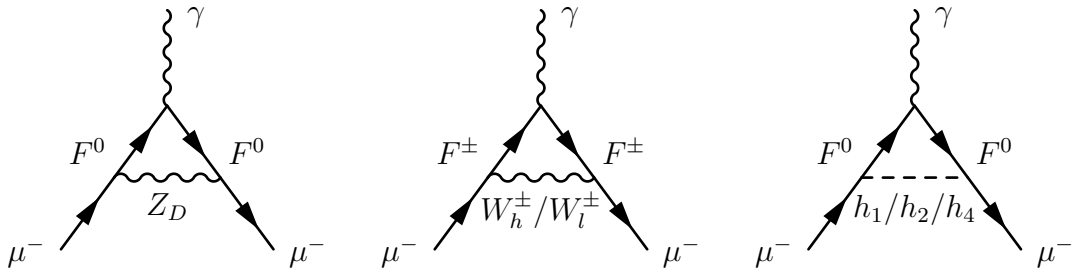

Figure 4.7: Feynman diagrams contributing to Δa_μ in Scenario B, with $F^0 = \{L^0, E^0\}$, $F^\pm = \{L^\pm, E^\pm\}$.

where

$$a_{-}^{W_h} \equiv \frac{4K_1^+(M_L^+, M_L^-, M_E^+, \sigma_{E-}M_E^-)}{s_{2D}^2}\int_0^1 dx \frac{x^2(x-1)}{P_x(c_{lh}^2 M_{Z_D}^2, M_E^{-\,2})P_x(c_{lh}^2 M_{Z_D}^2, M_L^{-\,2})},$$

$$a_{-}^{W_l} \equiv K_{-1}^-(\sigma_{E-}M_E^-, M_E^+, M_L^-, M_L^+)\int_0^1 dx \frac{x^2(x-1)}{P_x(s_{lh}^2 M_{Z_D}^2, M_E^{-\,2})P_x(s_{lh}^2 M_{Z_D}^2, M_L^{-\,2})},$$

$$a_{+}^{W_h} \equiv \frac{4K_1^+(M_L^-, M_L^+, \sigma_{E-}M_E^-, M_E^+)}{s_{2D}^2}\int_0^1 dx \frac{x^2(x-1)}{P_x(c_{lh}^2 M_{Z_D}^2, M_E^{+\,2})P_x(c_{lh}^2 M_{Z_D}^2, M_L^{+\,2})},$$

$$a_{+}^{W_l} \equiv K_{-1}^-(M_E^+, \sigma_{E-}M_E^-, M_L^+, M_L^-)\int_0^1 dx \frac{x^2(x-1)}{P_x(s_{lh}^2 M_{Z_D}^2, M_E^{+\,2})P_x(s_{lh}^2 M_{Z_D}^2, M_L^{+\,2})},$$

$$a^{h_4} \equiv 4\left(M_L^{0\,2} - M_L^+ M_L^- s_{2\Phi}\right)\left(M_E^{0\,2} - \sigma_{E-}M_E^+ M_E^- s_{2\Phi}\right)\int_0^1 dx \frac{x^2(x-1)}{P_x(2M_{h_4}^2, 2M_L^{0\,2})P_x(2M_{h_4}^2, 2M_E^{0\,2})},$$

$$a^{h_1} \equiv (1-S_h)\int_0^1 dx \frac{x^2(x-1)}{P_x(2M_{h_1}^2, 2M_L^{0\,2})P_x(2M_{h_1}^2, 2M_E^{0\,2})},$$

$$a^{h_2} \equiv (1+S_h)\int_0^1 dx \frac{x^2(x-1)}{P_x(2M_{h_2}^2, 2M_L^{0\,2})P_x(2M_{h_2}^2, 2M_E^{0\,2})},$$

and

$$M_{L,E}^{0\,2} = \frac{1}{2}\left(M_{L,E}^{+\,2} + M_{L,E}^{-\,2}\right), \quad P_x(A,B) \equiv (1-x)A + xB,$$

$$K_a^{\pm}(A,B,C,D) \equiv \frac{1}{4}\left(2ACs_D^{2a} + 2BDc_D^{2a} + (2ACs_D^{2a} - 2BDc_D^{2a} \pm (AD+BC)s_D^a c_D^a t_{2D}s_{2\Phi})\sqrt{\frac{c_{2D}^2}{c_{2lh}^2}}\right),$$

$$S_h \equiv \frac{A\left[6B - 8\left(B + As_{2\Phi}\right)\frac{s_{2lh}^2}{s_{2D}^2} - 4(M_{h_1}^2 - M_{h_2}^2)s_{2\Phi}\right] + B\left(2Bs_{2\Phi} - (M_{h_1}^2 - M_{h_2}^2)\right)\left(2 - \frac{s_{2D}^2}{s_{2lh}^2}\right)}{(M_{h_1}^2 + M_{h_2}^2)^2 + (M_{h_1}^2 - M_{h_2}^2)\left(2A - Bs_{2\Phi}\frac{s_{2D}^2}{s_{2lh}^2}\right)},$$

$$A \equiv \sqrt{-\frac{s_{2D}^2}{s_{2lh}^2}\left(M_{h_1}^2 - 2\lambda_1 e_D^{-2}s_{2lh}^2 M_{Z_D}^2\right)\left(M_{h_2}^2 - 2\lambda_1 e_D^{-2}s_{2lh}^2 M_{Z_D}^2\right)},$$

$$B \equiv M_{h_1}^2 + M_{h_2}^2 - 4\lambda_1 e_D^{-2}s_{2lh}^2 M_{Z_D}^2,$$

$$\sigma_{E-} \equiv \text{sign}[\sin(\theta_E + \theta_\Phi)], \quad \sigma_\mu \equiv \text{sign}[y_H(M_L^+ M_E^+ \pm M_L^- M_E^-)], \quad \sigma_\Phi \equiv \text{sign}[\sin 2\theta_\Phi],$$

$$(s_{nx}, c_{nx}, t_{nx}) = (\sin n\theta_x, \cos n\theta_x, \tan n\theta_x), \quad s_{2\Phi} = \sigma_\Phi\sqrt{1 - \frac{s_{2lh}^2}{s_{2D}^2}},$$

Unlike the case of Scenario A, these expressions are not invariant under $M_{L,E}^+ \leftrightarrow M_{L,E}^-$ and $M_L^\pm \leftrightarrow M_E^\pm$. Nonetheless, following the treatment in Section 4.3, we will now explore the parameter space in which we select M_L^+ to be the mass of the lightest portal matter field, and leave the exploration of the vector-like leptons' mass asymmetry to the later part of this

section. Among the choices of physical signs of various terms in our model, we find two are particularly dominant. First, the sign of the product $y_{HV}y_H$ scales all the chirally enhanced contributions to Δa_μ, and therefore in order for the observed anomaly to be generated, the sign of this product must be selected to give a positive contribution to Δa_μ. Second, the sign of the term $\sin(\theta_E + \theta_\Phi)$ alters whether certain terms will interfere destructively or constructively with one another: If we select $\sin(\theta_E + \theta_\Phi) < 0$ various contributions to the y_{HV} terms will interfere destructively, severely reducing the magnitude of this contribution relative to the $\sin(\theta_E + \theta_\Phi) > 0$ case.

Therefore, in Scenario B, the chirally enhanced contributions to Δa_μ will only be dependent on fixed SM parameters, the masses of the portal matter fermions, the masses of the heavy gauge bosons, which are parametrized as $M_{W_h} = \cos\theta_{lh} M_{Z_D}$, $M_{W_l} = \sin\theta_{lh} M_{Z_D}$, masses of the three heavy scalars $M_{h_{1,2,4}}$, the Yukawa coupling y_{HV}, the parameter λ_1 and e_D, and the angle θ_D. We find that this wealth of parameters is highly constrained by certain not immediately apparent physical consistency requirements– specifically that the mixing angle θ_λ, which parameterizes the definition of the h_1 and h_2 scalar mass eigenstates and is discussed in Appendix A of [4], must be real. In this case, we need to have the following relation between the gauge boson masses and the scalar masses:

$$M_{h_2} < \sqrt{2\lambda_1} e_D^{-1} \sin 2\theta_{lh} M_{Z_D} < M_{h_1} \tag{88}$$

where we note that $M_{h_1} > M_{h_2}$ from the definition of the h_1 and h_2 masses. This relation heavily constrains the accessible parameter space in our scenario, as 6 different input parameters need to satisfy this relation. In Fig 4.8, we plot this bound as a function of the mass of Z_D, for different θ_{lh} and fixed λ_1 and e_D. This figure is illustrative for the choice of M_{h_1} and M_{h_2} for our numerical analysis. Here we consider an $O(1)$ splitting for the gauge boson masses, which is a natural assumption since all masses of portal matter fermions and bosons are controlled by the same scale v_Φ.

Before moving on to a direct numerical probe of the $g-2$ corrections in the model, we should highlight one final crucial difference between the construction of Scenario B and that of Scenario A: In Scenario B, the muon magnetic moment correction scales quadratically with the dark gauge coupling e_D. However, unlike every other parameter here, e_D is an important parameter not just of the higher-scale, portal matter theory, but also enters into the behavior of the sub-GeV simplified dark matter models which motivate the portal matter framework. As such, the $g-2$ correction (and, as we shall see later on in Section 4.4, other collider probes of the model) can potentially have excellent complementarity with

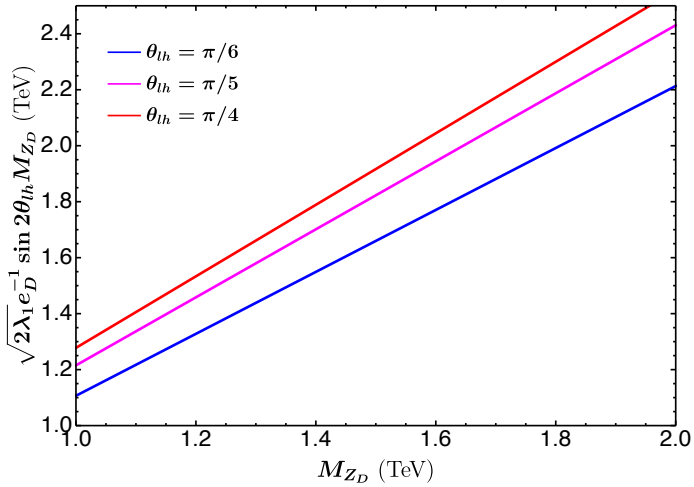

Figure 4.8: The bound $\sqrt{2\lambda_1} e_D^{-1} \sin 2\theta_{lh} M_{Z_D}$ of Eq. (88) as a function of M_{Z_D}, for $\lambda_1 = 0.4$ and $e_D = 0.7$. This bound applies in both Scenarios A and B, but is relevant for $g-2$ only in Scenario B.

limits from the dark matter sector, although the precise form of the relationship between these constraints is dependent on specifications about the nature of the sub-GeV dark matter candidate that we remain agnostic about in this work.

Similar to Scenario A, for our numerical analysis, we will always select $O(1)$ mass splittings between portal matter fermions $M_L^-/M_L^+ = 1.3$, $M_E^+/M_L^+ = 1.5$, and $M_E^-/M_L^+ = 1.8$ in most cases to get a sense of the numerics of a reasonable point in parameter space, as larger mass splittings between portal matter fermions generally lead to more suppressed loop contributions. Next, we explore the effect of the physical sign of $\sin(\theta_E + \theta_\Phi)$. In the top panels of Fig. 4.9, we depict the necessary strength of the Yukawa coupling y_{HV} in order to achieve the observed Δa_μ as a function of the lightest portal matter fermion mass M_L^+, using the benchmark values for masses of portal matter fermions. Two different physical signs of $\sin(\theta_E + \theta_\Phi)$ can give us Δa_μ with the right magnitude and sign at different regions of parameter space. For $\sin(\theta_E + \theta_\Phi) > 0$ in which various contributions mostly interfere constructively, we just need y_{HV} to be between 0.02 to 0.06 to get the observed anomaly. However, for $\sin(\theta_E + \theta_\Phi) < 0$ in which various contributions mostly interfere destructively, we need larger y_{HV}, which is around $O(0.1)$ to reproduce the observed anomaly. In the bottom panels of Fig. 4.9, we consider the case in which the portal matter masses are all degenerate, which will maximize the value of Δa_μ. For most of the θ_D values, this indeed lowers the value of y_{HV} required to generate the desired Δa_μ. Unlike Scenario A, the value

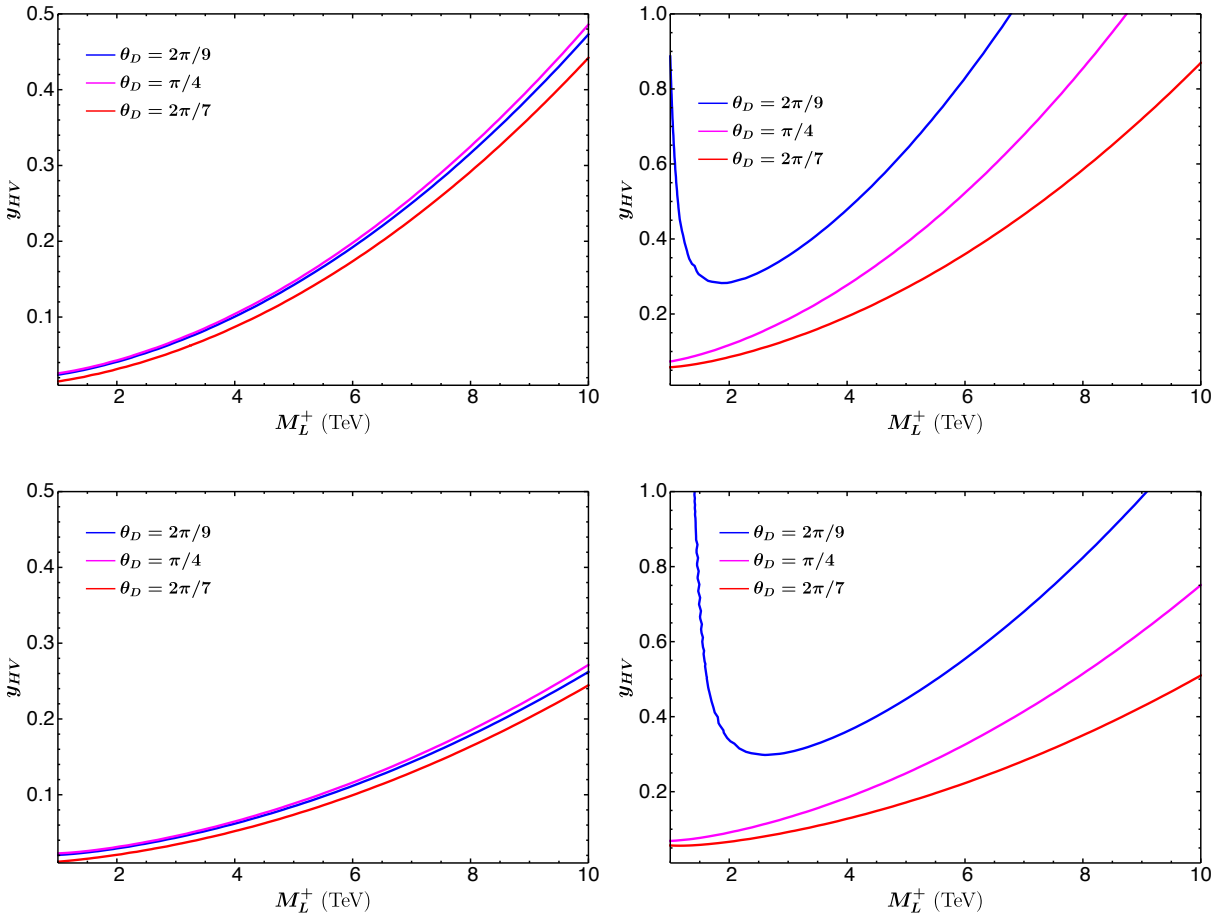

Figure 4.9: (Top): The necessary strength of y_{HV} to reproduce Δa_μ in Scenario B as a function of M_L^+, for $M_L^-/M_L^+ = 1.3$, $M_E^+/M_L^+ = 1.5$, $M_E^-/M_L^+ = 1.8$, $M_{Z_D} = 0.74$ TeV, $\theta_{lh} = \text{arccot}\,(1.7)$, $e_D = 0.8$, $\lambda_1 = 0.4$, $M_{h_2} = 1.2$ TeV, $M_{h_1} = 1.5$ TeV, $M_{h_4} = 1$ TeV. (Top left): $\sin(\theta_E + \theta_\Phi) > 0$, (top right): $\sin(\theta_E + \theta_\Phi) < 0$. (Bottom): The same as the top panels, but for degenerate portal fermion masses.

of y_{HV} required to generate the observed Δa_μ is well below the unitarity bound and thus it does not provide a meaningful constraint. However, we might be able to constrain y_{HV} from observations of the branching fractions of some vector-like leptons, as will be discussed in Section 4.4.

We now explore the asymmetry of our portal matter fermion masses with respect to $M_{L,E}^+ \leftrightarrow M_{L,E}^-$ and $M_L^\pm \leftrightarrow M_E^\pm$. Although the expressions in Eq.(88) and Eq.(88) are not manifestly symmetric under $M_L^\pm \leftrightarrow M_E^\pm$, for the parameter space of interest that is explored, Δa_μ is numerically nearly symmetric under $M_L^\pm \leftrightarrow M_E^\pm$, regardless of sign selection of

$\sin(\theta_E + \theta_\Phi)$. In Fig 4.10, we depict contour plots of Δa_μ as a function of different portal matter fermion masses, for various choices of physical signs in the model, assuming the lightest portal matter field has a mass of 1 TeV. In the case that $\sin(\theta_E + \theta_\Phi) > 0$, we observe a slight asymmetry in Δa_μ value under $M^+_{L,E} \leftrightarrow M^-_{L,E}$. In the case $\sin(\theta_E + \theta_\Phi) < 0$, the asymmetry in Δa_μ with respect to $M^+_{L,E} \leftrightarrow M^-_{L,E}$ is further amplified. In both cases, all other parameters are held constants, except y_{HV} is adjusted to access to the relevant parameter space that gives the desired Δa_μ in each case. However, this difference in y_{HV} does not contribute to the asymmetry of the portal matter masses, since it is a global constant that exists in front of all relevant corrections.

It is also of interest to explore the parameter space dependence on θ_D and e_D. As mentioned earlier, these two parameters significantly constrain the parameter space, given that they appear in the definition of the h_1, h_2 mixing angle θ_λ and the bidoublet vev angle θ_Φ in a square root form. Therefore, for the physical consistency of h_1 and h_2 mixing, θ_D and e_D can only take on certain values, after we have chosen to fix θ_{lh}, M_{Z_D} and $M_{h_{1,2}}$. For θ_D, a different sign selection of $\sin(\theta_E + \theta_\Phi)$ does affect the magnitude of Δa_μ. However, it does not change the viable region of θ_D, as this sign does not enter the definitions of θ_λ and θ_Φ. The viable θ_D range is then around $0.20 - 0.32\pi$ or $0.68 - 0.82\pi$, under the assumption that $M_{Z_D} = 0.74$ TeV, $\theta_{lh} = \text{arccot}(1.7)$, e_D=0.8, $\lambda_1 = 0.4$, $M_{h_2} = 1.2$ TeV and $M_{h_1} = 1.5$ TeV. With the same choice of θ_D and model parameters as above, we need a larger y_{HV} in the case that $\sin(\theta_E + \theta_\Phi) < 0$. Turning now to constraints on e_D, if we assume $\theta_D = 0.7$, $M_{Z_D} = 0.74$ TeV, $\theta_{lh} = \text{arccot}(1.7)$, $\lambda_1 = 0.4$, $M_{h_2} = 1.1$ TeV and $M_{h_1} = 1.9$ TeV, the viable range for e_D is then $e_D = 0.6 - 1.0$. Again for the case $\sin(\theta_E + \theta_\Phi) < 0$, with the same set of fixed parameter values as in the $\sin(\theta_E + \theta_\Phi) > 0$ case, Δa_μ always falls short by nearly an order of magnitude, and thus the relevant parameter space in cases with different sign options of $\sin(\theta_E + \theta_\Phi)$ is different. These two examples on the selection of e_D and θ_D also show that in Scenario B, although there are many parameters, the allowed range for several of them is severely limited by physical consistency. However, we are still able to realize any $O(1)$ e_D value we need without modifying anything else that affects the sub-GeV dark sector.

Another interesting feature of the muon $g-2$ anomaly in Scenario B is that the dominant contribution always arises from the contribution of heavy gauge bosons Z_D and $W_{h,l}$, regardless of the choice of signs or of the other parameters. In the case that $\sin(\theta_E + \theta_\Phi) > 0$, $W_{h,l}$ and Z_D both contribute constructively to Δa_μ, whereas $h_{1,2,4}$ contribute destructively, with a contribution which is an order of magnitude smaller than that of the heavy gauge

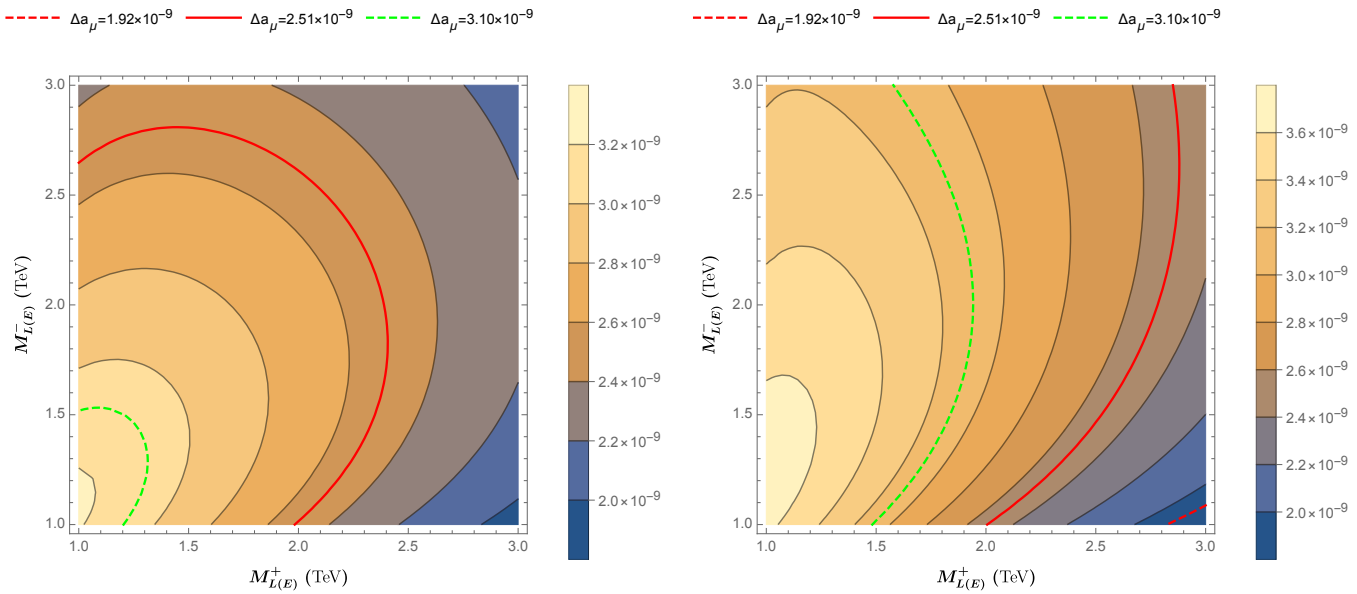

Figure 4.10: Contour plots of Δa_μ in Scenario B, for $M_{Z_D} = 0.74$ TeV, $\theta_{lh} = \operatorname{arccot}(1.7)$, $e_D = 0.8$, $\lambda_1 = 0.4$, $M_{h_2} = 1.2$ TeV, $M_{h_1} = 1.5$ TeV, $M_{h_4} = 1$ TeV, $\theta_D = \pi/4$, $M^+_{E(L)} = 1$ TeV, and $M^-_{E(L)} = 1.3$ TeV. (Left): Contour plot as a function of $M^+_{L(E)}$ and $M^-_{L(E)}$, for $y_{HV} = 0.03$, $\sin(\theta_E + \theta_\Phi) > 0$. (Right): Contour plot as a function of $M^+_{L(E)}$ and $M^-_{L(E)}$, for $y_{HV} = 0.1$, $\sin(\theta_E + \theta_\Phi) < 0$.

bosons. In the case that $\sin(\theta_E + \theta_\Phi) < 0$, the contribution of W_h and W_l is opposite in sign, causing the overall contribution from $W_{h,l}$ to be small but constructive, comparable to the size of the constructive contributions from $h_{1,2,4}$. The contribution of Z_D is dominant in this case, which is about an order of magnitude larger. This relative contributions from heavy gauge bosons and scalars hold true in all regions of parameter space explored.

4.4 Other Model Phenomenology: Constraints and Experimental Prospects

Having explored the valid parameter regimes for which this construction might address the observed muon magnetic moment anomaly, we must now consider what other observational consequences this model might lead to in both Scenario A and Scenario B, and how these compare to the more minimal construction in [55].

Fermion Collider Production

We will begin with a discussion of the segment of the theory which most resembles our minimal construction in [55], and constitute the signals which are the most characteristic of portal matter models: The direct production of the vector-like fermions. Both Scenario A and Scenario B will have extremely similar phenomenology in this sector, so we shall address both cases together. These fields are all vector-like leptons with SM quantum numbers, and so they may be pair-produced in abundance at current and future colliders through SM interactions. A distinctive characteristic of this model is the spectrum of the vector-like leptons– because the squared mass of the electroweak doublet (singlet) $U(1)_D$-neutral portal matter field is equal to the average of the squared masses of the $U(1)_D$-charged isospin doublet (singlet) portal fields, we will have

$$M_{L,E}^{\pm} \leq M_{L,E}^{0} \leq M_{L,E}^{\mp}, \tag{89}$$

that is, the weak doublet (singlet) portal matter field content consists of two $U(1)_D$-charged weak doublet (singlet) states and a $U(1)_D$-neutral weak doublet (singlet) case with a mass between them. Since a $U(1)_D$-charged state will therefore represent the lightest (and hence most likely to be kinematically accessible) new vector-like fermion, it behooves us to consider collider signatures of these states first. For brevity, when computing partial decay widths in this Section, we shall present our results in Scenario A, reminding the reader of this by applying an "A" superscript to all of our width expressions here. The corresponding results for Scenario B can be obtained by swapping the muons and τ's in all expressions.

The $U(1)_D$-charged portal matter fields will exhibit similar phenomenology to that of minimal portal matter discussed in [56]– due to their nontrivial $U(1)_D$ charge, their decay widths to SM fermions through the emission of electroweak gauge bosons are highly suppressed. These states always have far larger partial widths for decay into a muon or muon neutrino (in Scenario A) or a τ or τ neutrino (Scenario B) associated with the emission of A_D or h_D; these widths are given by

$$\Gamma^{A}_{L_{\pm},E_{\pm}\to\mu^{-}A_D} = \Gamma^{A}_{L_{\pm},E_{\pm}\to\mu^{-}h_D} = \frac{M_{L,E}^{\pm} y_{SL,SE}^{2} \cos^{2}(\theta_{\Delta})}{128\pi}. \tag{90}$$

For the lightest portal matter state, these final states will have a branching fraction of close to 100% if there are no other kinematically accessible two-body channels. In this case, the collider signature of the portal matter is simply the familiar case discussed in [56]:

A highly boosted lepton (in this case a muon or τ, depending on the scenario we have chosen) accompanied by missing energy (or a lepton-jet, if the dark photon decays visibly within the detector). For Scenario A, in which the portal matter decays into muons, the case in which both the dark photon and the dark Higgs are invisible is explored in the study of [3] by rescaling an existing ATLAS slepton search [159]. Assuming that the lightest portal matter state decays with a branching fraction of 1 through the processes outlined in Eq. (90), then if the electroweak singlet portal matter is the lightest state, $M_E^{\pm} \gtrsim 895$ GeV, while if the lightest state is an electroweak doublet, the constraint becomes $M_L^{\pm} \gtrsim 1050$ GeV (the electroweak doublet constraints are marginally stronger due to larger production cross sections [131, 160]). These are considerably stronger than the constraints on a vector-like lepton decaying dominantly through traditional channels via the emission of electroweak gauge bosons, which limit the mass of an electroweak singlet vector-like muon partner to $\gtrsim 420$ GeV [3].[11]

We can now consider the corresponding case in Scenario B, in which the lightest portal matter field will decay dominantly into τ's instead of muons. Unfortunately, a detailed study of such exotically decaying τ partners in the manner of [3] does not yet exist, but we can generally anticipate that the LHC constraints on the lightest portal matter mass will be considerably weaker than they are in the case of muons, due to the greater difficulty involved in τ reconstruction. We can most saliently see this by comparing the results of slepton searches for muon and τ partners, which provide the closest analogy to portal matter searches dominantly decaying through dark photon and dark Higgs emission: In [186], CMS finds a 95% CL lower mass bound on electroweak singlet τ sleptons of $M_{\tilde{\tau}} \gtrsim 240$ GeV from 138 fb^{-1} of data, while the ATLAS study in [187] finds a constraint of $M_{\tilde{\mu}} \gtrsim 450$ GeV in the corresponding scenario for muons. In both Scenario A and B, it should be noted that a multi-TeV muon collider will generally have a far better reach than current or future proton-proton colliders, and likely be able to constrain portal matter masses up to just below half of its center-of-mass energy.

Our considerations thus far are entirely consistent with a minimal construction of portal matter of the form discussed in [56]– we should note that any constraints from fermion production will be further modified by the fact that in our model, the dark gauge and scalar

[11] In the case of electroweak doublet vector-like fermions, constraints from such a particle decaying via electroweak gauge boson emissions can be considerably strengthened (to $\gtrsim 720$ GeV [3]) by including SM $W^{\pm}$-mediated production of a charged vector-like lepton associated with a neutral one. An analogous analysis for portal matter, in which the process $\bar{q}q \to W^{\pm} \to L^{\pm}\overline{N^{\pm}} \to \mu^- + \text{MET}$ will produce mono-lepton events, has not been performed, but might be conjectured to yield marginally stronger constraints than the $\gtrsim 1050$ GeV limit quoted for pair production of charged electroweak doublet portal matter.

sectors are no longer minimal and include a significant number of new heavy scalar and gauge bosons. Specifically, these new heavy bosons open up more decay channels for the lightest portal matter state. In particular, the $U(1)_D$-charged portal matter states may now decay into SM fields via the emission of a scalar $h_\pm$ boson, as well as a W_h and W_l bosons. For emission of a W_h boson in Scenario A, the partial width is given by

$$\Gamma^A_{L,E_\pm\to\tau^- W_h^\pm} = \frac{e_D^2 M^\pm_{L,E}}{64\pi\cos(2\theta_{lh})\cos^2\theta_{lh}}\mathcal{G}\left(\frac{M^\pm_{L,E}}{M_{Z_D}}\right)\mathcal{F}\left(\frac{M^\pm_{L,E}}{M_{Z_D}},\frac{M^\mp_{L,E}}{M_{Z_D}},\theta_{lh},\theta_D,\sigma_\Phi\right), \tag{91}$$

$$\mathcal{F}(x_A,x_B,\theta_{lh},\theta_D,\sigma_\Phi) \equiv \left[\left(1-\frac{\sin^2\theta_{lh}}{\cos^2\theta_D}\right)x_A^2 + \left(1-\frac{\sin^2\theta_{lh}}{\sin^2\theta_D}\right)x_B^2 + 2x_Ax_B\sqrt{1-\frac{\sin^2 2\theta_{lh}}{\sin^2 2\theta_D}}\sigma_\Phi\right],$$

$$\mathcal{G}(x) \equiv 1 + x^{-2} - 2x^{-4}, \quad \sigma_\Phi \equiv \text{sign}[\sin 2\theta_\Phi],$$

where θ_{lh} and θ_D are defined in Eq. (57). The corresponding width for the emission of a W_l boson is given by making the substitutions, $\theta_{lh,D} \to \theta_{lh,D} + \pi/2$. The partial widths for the corresponding neutrino-like portal matter decays into neutrinos and $W_{h,l}$ bosons are identical to those appearing in Eq. (91). Meanwhile, for emission of the $h_\pm$ scalar, the partial widths are

$$\Gamma^A_{L,E_\pm\to\mu^- h_\pm} = \frac{M^\pm_{L,E}y^2_{SL,SE}}{64\pi}\left(1-\frac{M^2_{h^\pm}}{{M^\pm_{L,E}}^2}\right)^2\sin^2\theta_\Delta. \tag{92}$$

When either $h^\pm$ or $W_{h,l}$ are too heavy to be produced on-shell via portal matter decays, channels with virtual $W^\pm_{l,h}$ and $h_\pm$ are unlikely to have significant branching fractions. In such a scenario, the lightest portal matter field will overwhelmingly decay through the emission of A_D or h_D, as in the minimal portal matter construction of [56]. If, however, any of the particles $W_{h,l}$ or $h_\pm$ are lighter than a given portal matter particle, the partial widths of Eqs.(91) and (92) can easily yield significant branching fractions into these states. These additional decay channels will in turn diminish the branching fraction of the lightest portal matter state to the final state considered in [3]. To get a sense for the scale of this effect, we plot the branching fractions of the portal matter field $L_\pm$ to $h_\pm$ and $W^\pm_{h,l}$ in Figure 4.11.

Notably, the results of Figure 4.11 demonstrate that feasible points in parameter space allow for substantial branching fractions of even the lightest portal matter field into final states other than the minimal model's dominant channels to an SM lepton and a dark photon or dark Higgs. As a result, a considerable reduction of the predicted signal in the analysis of [3], and therefore a significant weakening of constraints– if in Scenario A,

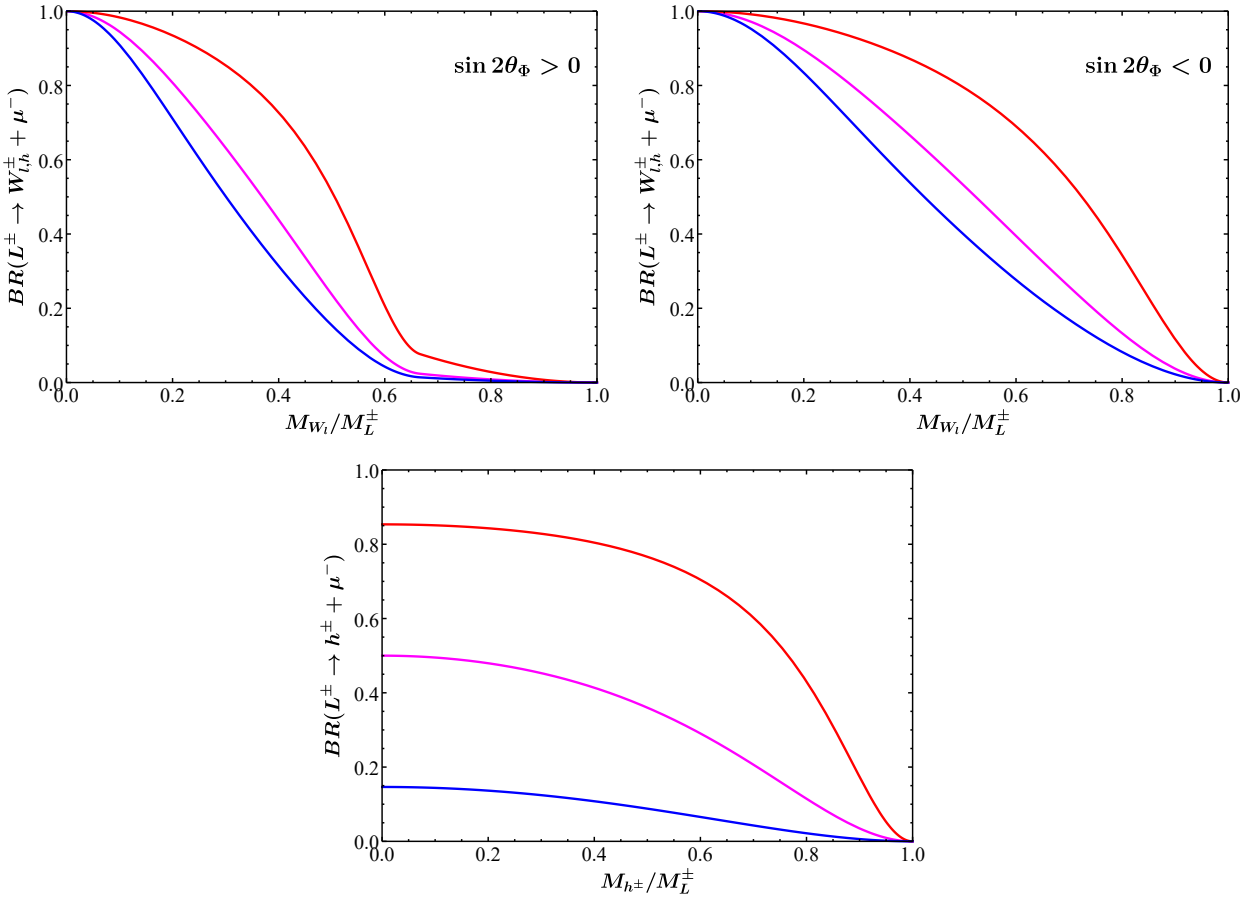

Figure 4.11: (Top): The branching fraction $BR(L_\pm \to \mu^- + W^\pm_{h,l})$, assuming that the only significant kinematically accessible decay channels are $L^\pm \to \mu^- + W^\pm_{h,l}$ and the familiar portal matter channels $L^\pm \to \mu^- + h_3, A_D$. We have taken $M_{W_h} = 1.5 M_{W_l}$, $M^-_L = 1.3 M^+_L$, $y_{SL} = 1$, $e_D = \sqrt{4\pi\alpha_{em}}$, and $\cos 2\theta_D = (\cos 2\theta_{hl})/2$ and $\theta_\Delta = \pi/8$ (Blue), $\pi/4$ (Magenta), and $3\pi/8$ (Red). The sign of $\sin 2\theta_\Phi$ is taken to be positive (left) and negative (right). (Bottom): The branching fraction $BR(L^\pm \to \mu^- + h^\pm)$, assuming that the only significant kinematically accessible decay channels are $L_\pm \to \mu^- + h^\pm$ and the familiar portal matter channels $L^\pm \to \mu^- + h_3, A_D$. Selections for θ_Δ, the only free parameter in this quantity other than the mass $M_{h^\pm}/M^\pm_L$, follow the same convention as the top figure. These charts are computed for Scenario A, but apply equally well for Scenario B by substituting all muons for τ leptons.

$BR(E_\pm \to \mu^- + A_D, h_D) \approx 0.45$, for example, then [3] finds that current LHC constraints require only that $M_E^\pm \gtrsim 600$ GeV, rather than the constraint $M_E^\pm \gtrsim 895$ GeV if $BR(E_\pm \to \mu^- + A_D, h_D) = 1$.

Of course, this diminished sensitivity could be ameliorated by including analyses with the new heavy boson final states. While a full analysis of this type is beyond the scope of this chapter, we can consider what sorts of signals might be of interest in such searches. The exact final states corresponding to the new heavy boson channels depends on the decay channel of the on-shell $W_{h,l}$ or $h_\pm$. In many regions of parameter space visible $W_{h,l}$ decays will be dominated by two-body decays featuring an SM τ (in Scenario A) or μ (in Scenario B) and a $U(1)_D$-charged portal matter field, for example $W_{h,l}^\pm \to \tau^- + \overline{L}_\mp$, if such a channel is kinematically accessible, or if no portal matter fields are lighter than $W_{h,l}$, through a three-body decay such as $W_{h,l}^\pm \to \tau^- + \mu^+ A_D, h_D$ with a virtual internal portal matter field.[12] Meanwhile, $h_\pm$ will dominantly decay into a two-body muon plus portal matter state or via bosonic interactions into a Z_D plus an h_D, if any such final states are kinematically accessible. If no two-body decays are kinematically accessible to the $h_\pm$, possible dominant three-body decays include muon-antimuon pairs from virtual portal matter $h_\pm \mu^+ \mu^- + A_D, h_D$, or somewhat more exotic channels such as $h_\pm \to 3h_D$ and $h_\pm \to h_D + Z_D^* \to \tau^+ \tau^- + h_D$. In any case, these final states are considerably more complicated than the canonical $\mu + h_D, A_D$ final states of the minimal model and invariably feature significant missing energy. In the case of pair production of the lightest portal matter fermion, the two-body decays of the on-shell gauge and scalar bosons will invariably be kinematically forbidden, and so we see that signals for these events will generally involve two nearly back-to-back lepton-jets (collimated clusters of charged particles) plus missing energy (because of the heavy on-shell intermediate particles in these processes, it is likely that the clusters of charged leptons will have some exotic event geometry which may help in tagging the signal). Such signals are likely discoverable, however it should be noted that because of the larger masses of the $W_{h,l}$ and $h_\pm$ bosons compared to the dark photon and dark Higgs, the individual leptons (in particular for pair production of the lightest portal matter fermions) will in general be significantly softer in cases with portal matter decay through the heavy boson emission than in cases where the portal matter decays through the more familiar dark photon/dark Higgs channel, making it less likely that events of this type will pass kinematic cuts [3].

[12] In the event that $W_{h,l}$ decays through on-shell portal matter emissions are kinematically inaccessible, it is also possible for the $W_{h,l}$ to decay via a two-body flavor violating decay such as $W_{h,l}^\pm \to \mu^+ \tau^-$, however this partial width will be suppressed by $O(v_\Delta^2/v_\Phi^2) \sim 10^{-6}$, and so is unlikely to exceed the partial width of the three-body channel from a virtual portal matter field, which only suffers $(2\pi)^{-3} \sim O(10)^{-3}$ relative suppression to a two-body decay from the three-body phase space.

In addition to the $U(1)_D$-charged portal matter states, one of which must constitute the lightest vector-like fermion in the model, we can also consider how the collider signatures for the $U(1)_D$-neutral vector-like leptons which appear in the model. The absence of a $U(1)_D$ charge for these fields permits these fermions to decay via the emission of electroweak bosons into SM fermions, in this case the SM τ (for Scenario A) or muon (for Scenario B), in a manner completely analogous to that of a conventional τ or μ-philic vector-like lepton. For the isodoublet, the decay widths for these processes are given by

$$\Gamma^A_{L_0\to\tau^- h} = \Gamma^A_{L_0\to\tau^- Z} = \frac{1}{2}\Gamma^A_{L_0\to\nu_\tau W^-} = \frac{M_L^0}{32\pi}\left(\frac{M_L^+ M_E^- - \sigma_{E-} M_L^+ M_E^-}{M_L^+ M_E^+ + \sigma_{E-} M_L^- M_E^-}\right)^2 \frac{m_\tau^2}{v^2}, \tag{93}$$
$$\sigma_{E-} = \text{sign}[\sin(\theta_E + \theta_\Phi)],$$

with corresponding results for the electroweak singlet portal matter, albeit without channels featuring the SM $W^\pm$ boson. Depending on the mass of the $W_{h,l}$ gauge bosons, an additional two-body decay channel may be open to the $U(1)_D$-neutral vector-like leptons of the type $L_0 \to W^\mp_{h,l} L_\pm$. Because the electroweak decay partial widths suffer substantial $m_\tau^2/v^2 \sim 10^{-5}$ suppression due to the small Yukawa coupling of the τ, the decays from $W^\mp_{h,l}$ emission will be overwhelmingly favored if they are kinematically accessible, however because $W_{h,l}$ itself tends to have a suppressed decay width (as discussed above), these channels quickly become negligible once $W_{h,l}$ becomes massive enough to kinematically forbid their on-shell emission. Therefore, there are two conceivable qualitative scenarios for the collider signature of the lightest $U(1)_D$-uncharged vector-like lepton: It may either decay like a traditional, non-portal matter vector-like lepton via emission of electroweak bosons, or it may decay dominantly into $U(1)_D$-charged portal matter and $W_{h,l}$ bosons.

In the former case, searches for these vector-like leptons will directly correspond to searches for any predominantly τ-mixed (in Scenario A) or μ-mixed (Scenario B) vector-like lepton. In Scenario A, constraints from present searches, such as that of [188] are considerably weaker than constraints on the portal matter masses– even the analysis of [188], which considers an electroweak doublet vector-like lepton, leverages the production of both charged lepton pairs and production of a single charged lepton with a vector-like neutrino, and benefits from a statistical deficit in the measured signal region events at CMS, only constrains $M_L^0 \gtrsim 790$ GeV, considerably worse than the $M_L^\pm \gtrsim 1050$ GeV constraint achieved by rescaling the constraint of [3] to limit electroweak doublet, rather than singlet, portal matter. In Scenario B, the weakened constraints on portal matter may make constraints on the $U(1)_D$-neutral fermions more important. Quantitatively, assuming

that the model's heavy gauge boson and scalar content are massive enough that the $U(1)_D$-neutral fermions decay dominantly via electroweak boson emission, the analysis of [3] finds an expected limit of $\geq 420(720)$ GeV on the isospin singlet(doublet) $U(1)_D$-neutral fermion.

The collider signature for the case in which the $U(1)_D$-neutral vector-like fermions decay dominantly via $W_{h,l}$ has been less studied. However, we can comment briefly that the preferred decay channels for the $W_{h,l}$ bosons and the $U(1)_D$-charged portal matter suggest that these channels will involve large numbers of collimated leptons (lepton-jets) and significant missing energy, and likely yield constraints similar to an analysis of the $W_{h,l}$ emission channels in the case of $U(1)_D$-charged portal matter, as mentioned earlier.

The analysis thus far has restricted our attention to the least massive portal matter fermions of that are $U(1)_D$-charged and $U(1)_D$-uncharged, but the results for the heavier portal matter fields are qualitatively quite similar, if somewhat complicated by the presence of additional possible decay channels from intermediate vector-like fermions. Notably, in both the $U(1)_D$-charged and $U(1)_D$-uncharged cases, these permit the electroweak doublet vector-like leptons to decay into the electroweak singlets (or vice versa, depending on the relative masses of the particles in question) of the same $U(1)_D$ charge via the emission of SM electroweak bosons. The partial widths of these decay channels will scale with the Yukawa couplings $y_H \sim m_{\tau,\mu}/v$ and y_{HV}, as $O(m_{\tau,\mu}^2/v^2, y_{HV} m_{\tau,\mu}/v, y_{HV}^2)$– because $m_{\tau,\mu}/v \ll 1$, this suppression will render these channels largely irrelevant for the $U(1)_D$-charged fermions unless $y_{HV} \sim 1$, but in the case of the $U(1)_D$-neutral vector-like fermions these channels can compete with the $O(m_{\tau,\mu}^2/v^2)$-suppressed decay width to SM fermions, or even dominate them when $y_{HV} \gg m_{\tau,\mu}/v$, leading to atypical signatures. In the event that the complete spectrum of vector-like fermions is discovered (likely at a multi-TeV muon collider where such a search has significantly greater reach), it may then be feasible to place limits on or even measure the coupling y_{HV} from the branching fractions of the vector-like fermions– given the central role this coupling constant can play in the generation of Δa_μ in both Scenario A and Scenario B, such a measurement would play a key role in determining if the model remains a viable explanation of the muon magnetic moment anomaly.

Boson Sector

Having discussed the fermion sector in some detail, we can now move on to the boson sector. Because the new gauge and scalar bosons are leptophilic (up to small kinetic mixing), significant production of these states (apart from in association with vector-like

fermions, as discussed in Section 4.4) is not especially feasible at the LHC, where the leptons which couple to the dark sector bosons must be produced from quark and gluon collisions. However, in both Scenario A and Scenario B, various bosons in the dark sector may be produced copiously at a multi-TeV muon collider, through t-channel exchanges of heavy vector-like leptons. The heavy gauge bosons and scalars will have visible decay channels featuring final-state charged leptons in both scenarios, while if we assume dark photons and dark Higgses decay invisibly, their production may still be measured via searches for monophoton events. Furthermore, because many of these diagrams are essentially the same as the one-loop diagrams that generate the new physics contributions to the muon magnetic moment (albeit without an external photon and with the internal scalar/gauge boson line cut), the production cross section of these bosons will necessarily be related to the same parameters which govern the muon magnetic moment correction. It is therefore of interest to consider the rate at which we might expect the dark sector bosons to be produced at a muon collider, and discuss the role that these probes might play in constraining the model's ability to address the muon $g-2$ anomaly. Because of the preserved Z_2' parity, it should be noted that there is no overlap between the bosons that can be produced at a muon collider in Scenario A and those which can be produced in Scenario B. As a result, we shall address the two scenarios separately here.

Diboson Production (Scenario A)

In Scenario A, the exotic bosons which may be produced at leading order in r_Δ/v_Φ are the dark photon A_D, the dark Higgs h_3, and the heavier scalars h_5, h_6, and $h_\pm$. Perhaps the most intriguing signatures here will be those from the production of solely A_D and h_3 states, since these both have sub-GeV masses and will always be kinematically accessible at a multi-TeV muon collider. In the event that these particles decay invisibly, it should be possible to constrain the production rate for these particles via a simple monophoton search, such as what has been considered for a WIMP dark matter model in [189, 190].[13] As these cross sections scale quartically with y_{SL} and y_{SE}, such a measurement can be used to constrain or observe these couplings, which from Eqs. (81-83) play a crucial role in generating the anomalous muon magnetic moment. The precise reach of these searches remains unclear, pending further work on the beamline background in muon colliders and, of course, knowledge of the beam energy, detector coverage, and integrated luminosity of

[13]The production of dark photons and dark Higgses from muon collisions in our model is also analogous to the corresponding case in the model of [128], in which quark portal matter mediated similar processes at the LHC and from which the authors found monojet constraints on their parameter space.

the hypothetical future machine, but we can make a rudimentary assessment by simply computing the production cross sections of the monophoton processes $\mu^+\mu^- \to \gamma A_D A_D$, $\mu^+\mu^- \to \gamma A_D h_3$, and $\mu^+\mu^- \to \gamma h_3 h_3$, and estimating their significance against the dominant background $\mu^+\mu^- \to \gamma\nu\overline{\nu}$.[14] Analytically, we find that in the limit that the muon, h_D, and A_D masses are negligible, all three LO cross sections for the signal processes here can be written as[15]

$$\sigma_{XY} = (y_{SL}^4 \sigma_{XY}^L + y_{SE}^4 \sigma_{XY}^E) \cos^4\theta_\Delta, \tag{94}$$

where X and Y can denote h_D or A_D, depending on the final state for the given signal process, and $\sigma_{XY}^{L,E}$ depend solely on SM parameters and the masses of the portal matter fermions. In turn, we can estimate the significance of the monophoton signal here for a muon collider with integrated luminosity $\mathcal{L}$ as

$$N_{SD} = \frac{\sqrt{\mathcal{L}}\cos^4\theta_\Delta}{\sqrt{\sigma_{SM}}}(y_{SL}^4\sigma^L + y_{SE}^4\sigma^E), \quad \sigma^{L,E} \equiv \sum_{XY}\sigma_{XY}^{L,E}, \quad XY = h_D h_D, A_D h_D, A_D A_D, \tag{95}$$

where σ_{SM} is the production cross section for the dominant SM background process $\mu^+\mu^- \to \gamma\nu\overline{\nu}$. For the purposes of constraining the parameter space of this model that can address the muon $g-2$ anomaly, we are primarily concerned with the value of the product $y_{SL}y_{SE}$, which scales the chirally enhanced contribution of the portal matter to Δa_μ, rather than the two Yukawa couplings' individual values. Given a spectrum of portal matter states, any given value of the product $y_{SL}y_{SE}$, will in turn have a corresponding minimum possible value for $\sum_{XY}(y_{SL}^4\sigma^L + y_{SE}^4\sigma^E)$, and hence N_{SD}. Using this minimum, we can estimate that for a given product $y_{SL}y_{SE}$, we shall achieve a significance of at least

$$N_{SD} > 2y_{SL}^2 y_{SE}^2 \cos^4\theta_\Delta \sqrt{\mathcal{L}}\sqrt{\frac{\sigma^L\sigma^E}{\sigma_{SM}}}. \tag{96}$$

[14]This estimate ignores the monophoton signature from electroweak production of the portal matter neutrino partners, which should be degenerate in mass with the charged isospin doublet portal matter, the dominant process of which is $\mu^+\mu^- \to \gamma N^\pm \overline{N}^\pm$. When the beam energy is sufficient to render these processes kinematically accessible, they produce comparable cross sections to those of the signal channels we do analyze when $y_{SL,SE} = 1$, but do not scale with these couplings. As such, generally for $y_{SL,SE} < 1$ this signal would somewhat enhance our BSM signal (and hence improve the reach of any given collider experiment), but is generally a subdominant signal contribution when $y_{SL,SE} > 1$ due to the quartic scaling of the other BSM monophoton processes with these couplings.

[15]As a $2 \to 3$ process, the monophoton cross sections are lengthy and not especially enlightening, so we do not present them in full here.

$\sqrt{s}$ (TeV)	$\mathcal{L}$ (ab^{-1})
3	1
6	4
10	10
14	20
30	90

Table 4.5: The benchmark center-of-mass energies and corresponding integrated luminosities for the study of monophoton constraints on the product $y_{SL}y_{SE}$.

We can then use Eq. (96) to estimate the 2σ exclusion and 5σ discovery reach for the product $y_{SL}y_{SE}$, given hypothetical muon collider experiments with various center-of-mass energies and integrated luminosities. We compute the signal and background cross sections using MadGraph [191], with our model implemented with Feynrules [192]. We impose kinematic cuts such that

$$E_\gamma > 50 \text{ GeV}, \quad m^2_{\text{miss}} \equiv (p_{\mu^+} + p_{\mu^-} - p_\gamma)^2 > (200 \text{ GeV})^2, \quad |\eta_\gamma| < 2.5, \tag{97}$$

where E_γ is the energy of the final-state photon, m^2_{miss} is the invariant mass of the combined four-momentum of the invisible final-state particles, and η_γ is the pseudorapidity of the photon. For the benchmark center-of-mass energies and corresponding luminosities we consider in this study, we have chosen the values displayed in Table 4.5, following those of the similar study in [189].

In Figure 4.12, we depict the 2σ exclusion and 5σ discovery reach for these benchmark muon collider experiments, assuming that the spectrum of portal matter states follows the canonical benchmark we have used thus far, namely that $M_L^- = 1.3M_L^+$, $M_E^+ = 1.5M_L^+$, and $M_E^- = 1.8M_L^+$, at various values of the angle θ_Δ in order to get a sense for the robustness of these constraints. Because the cross sections scale quartically with the couplings y_{SL} and y_{SE}, we see that even though the signal-to-background ratio in these searches is quite low (generally between 10^{-2} and 10^{-3}), the monophoton search can still present a powerful probe of the couplings, often significantly outperforming the bound on the product $y_{SL}y_{SE}$ from partial wave unitarity given in Eq. (84). Given that we have found in Section 4.3 that $\sqrt{y_{SL}y_{SE}} \gtrsim O(1)$ is generally necessary in order to achieve the desired value of Δa_μ, especially in the case where $y_{HV} \ll y_H$, it is clear that this monophoton search can potentially significantly constrain the viable parameter space in which the model can address the muon magnetic moment anomaly. Given that a multi-TeV muon collider is likely to have a discovery reach for the portal matter fermions up to half of its center-of-mass

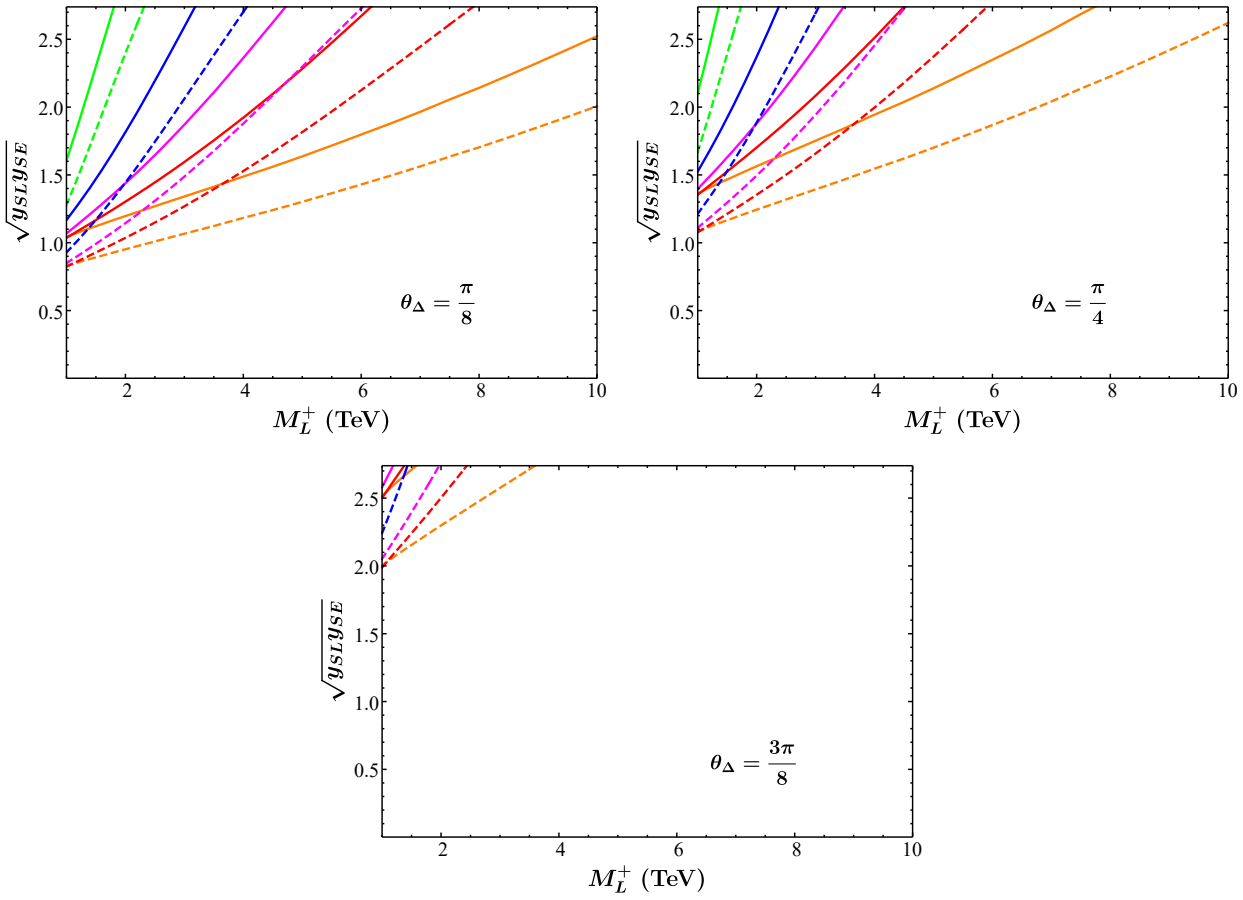

Figure 4.12: The estimated 5σ discovery (solid) and the 2σ exclusion (dashed) reach in Scenario A for $\sqrt{y_{SL}y_{SE}}$ at a potential future muon collider with center-of-mass energies $\sqrt{s} = 3$ TeV (Green), 6 TeV (Blue), 10 TeV (Magenta), 14 TeV (Red), and 30 TeV (Orange), with corresponding integrated luminosities given in Table 4.5. We have assumed that $M_L^- = 1.3M_L^+$, $M_E^+ = 1.5M_L^+$, $M_E^- = 1.8M_L^+$, and taken the θ_Δ values displayed on each chart. The y-axis at each chart terminates at the upper bound on the product $\sqrt{y_{SL}y_{SE}}$ from partial wave unitarity, given in Eq. (84), $\sqrt{y_{SL}y_{SE}} \lesssim 2.74$.

energy, it is even feasible that such a muon collider could discover all portal matter fermions in the model, and hence have their complete spectrum known in a monophoton search.The monophoton search's constraints on the product $\sqrt{y_{SL}y_{SE}}$ are potentially exceptionally powerful.

A similarly quantitative evaluation of the discriminating power of searches for other diboson processes, namely $\mu^+\mu^- \to h_{5,6}, h_{5,6}$, $\mu^+\mu^- \to h^+h^-$, $\mu^+\mu^- \to h^+h_3$, and $\mu^+\mu^- \to h^+h_D$, is considerably more complicated, and because a detailed investigation of the branch-

ing fractions of the heavy scalars in the model is highly nontrivial and dependent on the extremely complicated scalar potential terms, we will not attempt it. However, we can comment on the fermionic decay channels for these bosons which will presumably represent a sizable portion of their total decay width. The $U(1)_D$-charged scalar $h_\pm$ will invariably have open decay channels into an SM muon plus $U(1)_D$-charged portal matter fields, leading to a final state featuring a muon-antimuon pair and a dark photon or dark Higgs. Similarly, h_5 and h_6 will have open channels into an SM muon plus a virtual or on-shell $U(1)_D$-neutral vector-like lepton, L_0 or E_0, which will lead to signals featuring muons plus some electroweak boson (if the electroweak boson decays visibly, and all decay products remain hard enough to be observed by the detector, it may in fact be possible to entirely reconstruct the mass peak of the h_5 or h_6, although a detailed study of whether this is in fact feasible is not within the purview of the current work). Hence, it is feasible to suspect that in wide regions of parameter space (perhaps depending on values of scalar potential parameters, which might influence the branching fractions of the heavy scalars to other scalar states), a significant fraction of the heavy scalars will produce events with visible final state particles. Assuming that is the case, it is then useful to then get a feel for the number of events with heavy scalars that might be produced at a multi-TeV muon collider experiment. We note that for the process $\mu^+\mu^- \to XY$, where X and Y are some final-state scalars (or the dark photon), we will have a cross section given by

$$\left(\frac{d\sigma}{d\cos\theta}\right)_{\mu^+\mu^-\to XY} = \frac{1}{32\pi}\frac{1}{s}\sqrt{\left(1-\frac{m_X^2+m_Y^2}{s}\right)^2 - 4\frac{m_X^2 m_Y^2}{s^2}}|\mathcal{M}_{XY}|^2, \tag{98}$$

where s is the usual Mandelstam variable, the final-state particles X and Y have masses m_X and m_Y, respectively, and $|\mathcal{M}_{XY}|^2$ is the squared amplitude (with symmetry factors accounted for and averaged over initial spins), which for the processes involving the

production of heavy scalars will be

$$
\begin{aligned}
|\mathcal{M}_{h_5h_5}|^2 &= \frac{1}{8}\left(1-\frac{\cos(2\theta_\Delta)}{\cos(2\theta_M)}\right)^2\left(y_{SL}^4\frac{(t-u)^2(tu-M_{h^\pm}^4\cos^4\theta_M)}{(2t-M_L^{+2}-M_L^{-2})^2(2u-M_L^{+2}-M_L^{-2})^2}+(L\to E)\right),\\
|\mathcal{M}_{h_6h_6}|^2 &= \frac{1}{8}\left(1+\frac{\cos(2\theta_\Delta)}{\cos(2\theta_M)}\right)^2\left(y_{SL}^4\frac{(t-u)^2(tu-M_{h^\pm}^4\sin^4\theta_M)}{(2t-M_L^{+2}-M_L^{-2})^2(2u-M_L^{+2}-M_L^{-2})^2}+(L\to E)\right),\\
|\mathcal{M}_{h_5h_6}|^2 &= \frac{1}{4}\left(1-\frac{\cos^2(2\theta_\Delta)}{\cos^2(2\theta_M)}\right)\left(y_{SL}^4\frac{(t-u)^2(tu-M_{h^\pm}^4\sin^2\theta_M\cos^2\theta_M)}{(2t-M_L^{+2}-M_L^{-2})^2(2u-M_L^{+2}-M_L^{-2})^2}+(L\to E)\right),\\
|\mathcal{M}_{h_+h_-}|^2 &= \frac{\sin^4\theta_\Delta}{16}\left(y_{SL}^4\frac{(M_L^{-2}-M_L^{+2}+t-u)^2(tu-M_{h^+}^4)}{(t-M_L^{+2})^2(u-M_L^{-2})^2}+(L\to E)\right),\\
|\mathcal{M}_{h_Dh_+}|^2 &= |\mathcal{M}_{A_Dh_+}|^2 = \frac{\sin^2(2\theta_\Delta)}{8}\left(y_{SL}^4\frac{(M_L^{-2}-M_L^{+2}+t-u)^2tu}{(t-M_L^{+2})^2(u-M_L^{-2})^2}+(L\to E)\right),\\
|\mathcal{M}_{h_Dh_-}|^2 &= |\mathcal{M}_{A_Dh_+}|^2 = \frac{\sin^2(2\theta_\Delta)}{8}\left(y_{SL}^4\frac{(M_L^{-2}-M_L^{+2}+u-t)^2tu}{(u-M_L^{+2})^2(t-M_L^{-2})^2}+(L\to E)\right).
\end{aligned}
\tag{99}
$$

Notice that the requirement that $|\cos(2\theta_\Delta)| < |\cos(2\theta_M)|$ as shown in Appendix A of [4] is manifested in the squared amplitude for $\mu^+\mu^- \to h_5h_6$, where if it is not satisfied the cross section will become negative.

In Figures 4.13, 4.14, and 4.15, we depict the heavy scalar production cross sections at a $\sqrt{s} = 3$ TeV muon collider as functions of the portal matter mass M_L^+, again assuming our benchmark values $M_L^- = 1.3M_L^+$, $M_E^+ = 1.5M_L^+$, and $M_E^- = 1.8M_L^+$, for different values of the scalar mass scale $M_{h^\pm}$ and different choices of the angles θ_Δ and θ_M. For convenience, In Figures 4.13 and 4.15, we have combined several final states that will likely have similar or identical final-state signals, such as h_5 and h_6, h_D and A_D, and h^+ and h^-. Assuming a luminosity of $O(\text{ab}^{-1})$ for a multi-TeV muon collider, we then see that if the final states with heavy scalars are kinematically accessible, they can be produced copiously at such a machine– for M_L^+ near the current bound of ~ 1 TeV we can expect thousands of heavy scalar production events. We should also note that these processes, like the monophoton processes we inspected earlier, will scale quartically with the Yukawa couplings y_{SL} and y_{SE}, introducing possibly significant constraints on these couplings which play a key role in the new physics contribution to the anomalous muon magnetic moment.

Diboson Production (Scenario B)

In Scenario B, only heavy scalars and gauge bosons might be produced via the t-channel exchange of vector-like fermions here, since the dark photon and the dark Higgs fields both

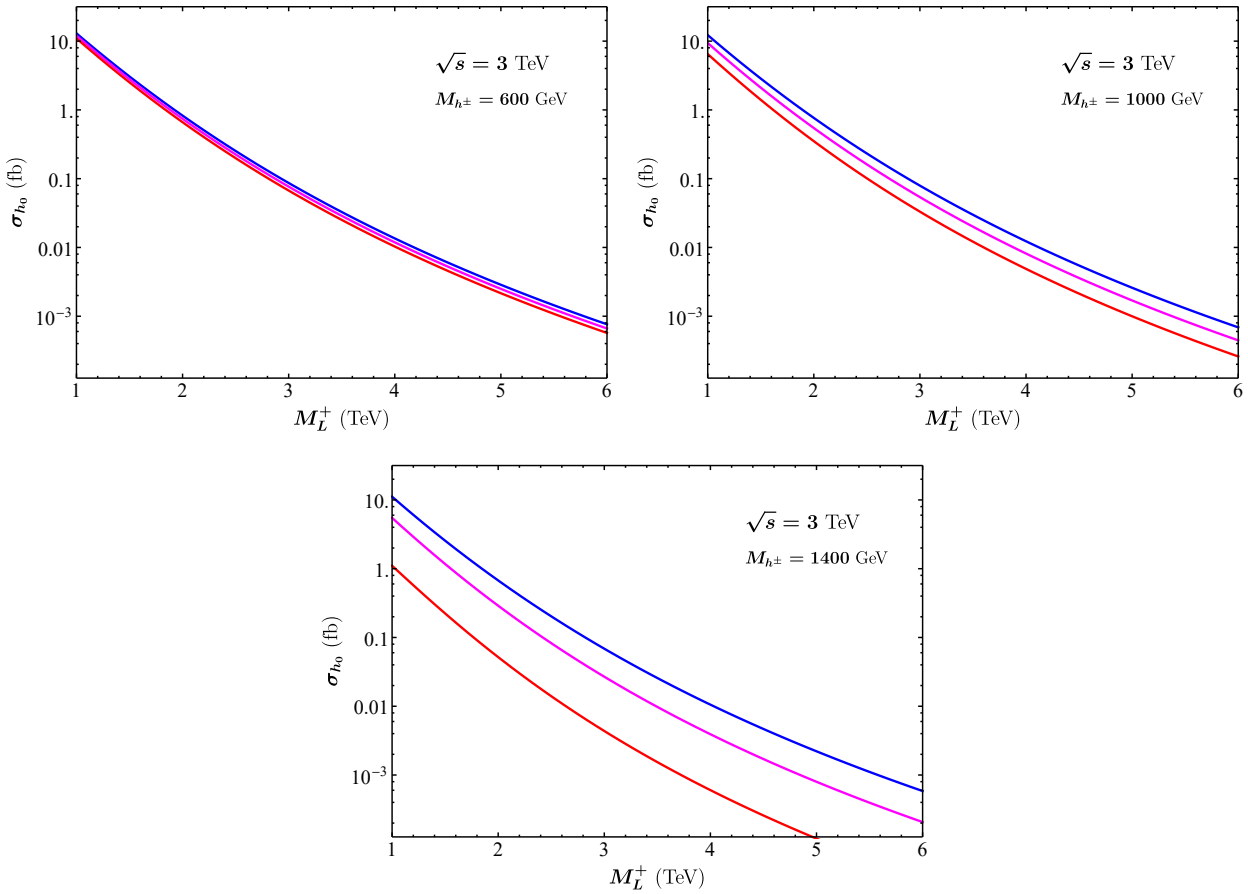

Figure 4.13: The combined total production cross section $\sigma_{h_0}\sigma_{\mu^+\mu^-\to h_5 h_5} + \sigma_{\mu^+\mu^-\to h_5 h_6} + \sigma_{\mu^+\mu^-\to h_6 h_6}$ in Scenario A as a function of the portal matter mass M_L^+ at a $\sqrt{s} = 3$ TeV muon collider for $\theta_\Delta = \theta_M = \pi/8$ (Blue), $\theta_\Delta = \theta_M = \pi/4$ (Magenta), and $\theta_\Delta = \pi/8$, $\theta_M = 3\pi/8$ (Red). We have taken $y_{SL} = y_{SE} = 1$, and assumed a benchmark portal matter mass spectrum $M_L^- = 1.3M_L^+$, $M_E^+ = 1.5M_L^+$, and $M_E^- = 1.8M_L^+$.

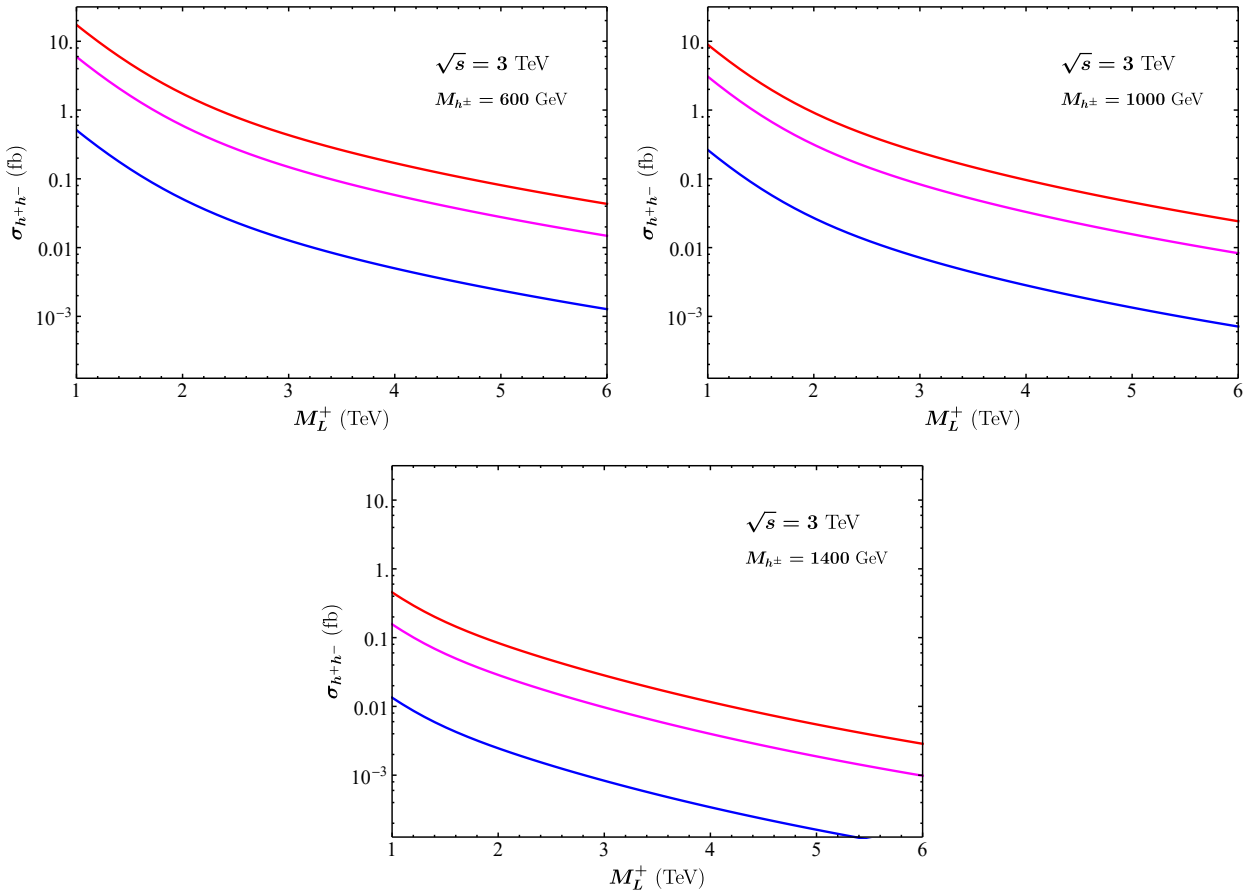

Figure 4.14: The total production cross section $\sigma_{\mu^+\mu^-\to h_+h_-}$ in Scenario A as a function of the portal matter mass M_L^+ at a $\sqrt{s} = 3$ TeV muon collider for $\theta_\Delta = \pi/8$ (Blue), $\theta_\Delta = \pi/4$ (Magenta), and $\theta_\Delta = 3\pi/8$ (Red).We have taken $y_{SL} = y_{SE} = 1$, and assumed a benchmark portal matter mass spectrum $M_L^- = 1.3M_L^+$, $M_E^+ = 1.5M_L^+$, and $M_E^- = 1.8M_L^+$.

lack appreciable fermionic couplings featuring the muon. The heavy boson production, however, might be constrained through their visible decay channels to vector-like and/or SM leptons, as with the heavy scalars in Scenario A, discussed in Section 4.4. In Scenario B, the exotic bosons that might be produced are $W_{h,l}^\pm$, Z_D, h_1, h_2, and h_4– as noted earlier, precisely those fields which may *not* be appreciably produced at a muon collider in Scenario A– final states with Z_D are likely to be of particular phenomenological interest, since it is feasible that they have an appreciable branching fraction to $\mu^+ - \mu^-$ pairs, and can therefore be easily reconstructed if their width is sufficiently narrow. The symbolic forms of the cross sections in this scenario are quite lengthy, and we do not display them here (although

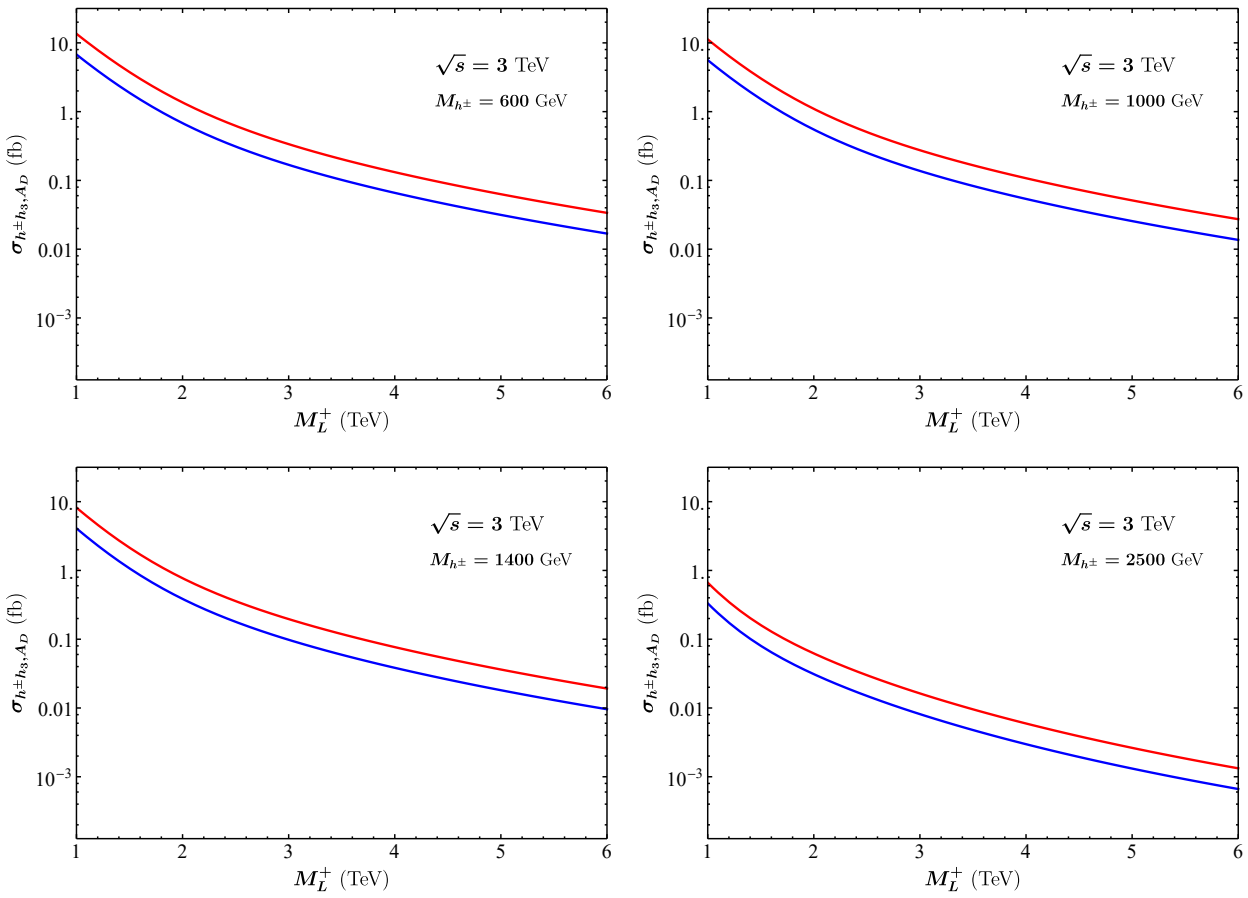

Figure 4.15: The combined total production cross section $\sigma_{h_\pm h_3, A_D} = \sigma_{\mu^+\mu^- \to h_+ h_3} + \sigma_{\mu^+\mu^- \to h_- h_3} + \sigma_{\mu^+\mu^- \to h_+ A_D} + \sigma_{\mu^+\mu^- \to h_- A_D}$ in Scenario A as a function of the portal matter mass M_L^+ at a $\sqrt{s} = 3$ TeV muon collider for $\theta_\Delta = \pi/8$ (Blue) and $\theta_\Delta = \pi/4$ (Red) (note that these cross sections are invariant under $\theta_\Delta \to \pi/2 - \theta_\Delta$). We have taken $y_{SL} = y_{SE} = 1$, and assumed a benchmark portal matter mass spectrum $M_L^- = 1.3 M_L^+$, $M_E^+ = 1.5 M_L^+$, and $M_E^- = 1.8 M_L^+$.

for those who are curious about the specific forms, they are given in Appendix 4.5. For our purposes, the salient points to be aware of are that all cross sections scale quartically with the quantity e_D/M_{Z_D}, and are otherwise dependent on the same parameters which govern the new physics correction to the muon magnetic moment here: the spectrum of vector-like fermion masses, λ_1, θ_D, θ_{lh}, the masses of the heavy scalars h_1, h_2, and h_4, and that of the gauge boson Z_D. As discussed in Section 4.3, physical consistency of the various parameters leads to a rather narrow allowed space of selections of these parameters– as in our $g-2$ analysis, then, although our space appears to have a significant number of free parameters, in practice our selections will be necessarily limited.

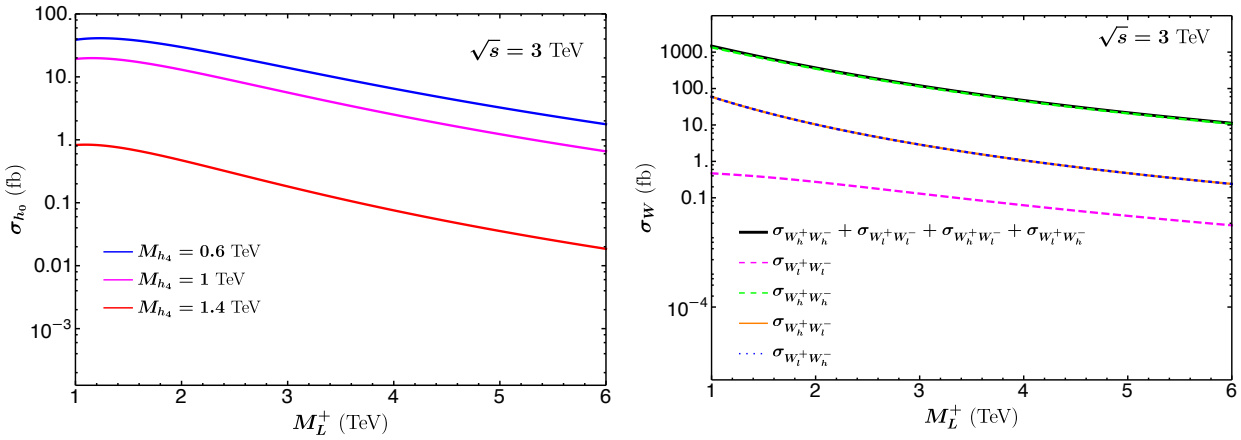

Figure 4.16: (Left): The combined total production cross section $\sigma_{h_0} = \sigma_{\mu^+\mu^-\to h_1h_1} + \sigma_{\mu^+\mu^-\to h_2h_2} + \sigma_{\mu^+\mu^-\to h_1h_2} + \sigma_{\mu^+\mu^-\to h_4h_4}$ as a function of the portal matter mass M_L^+ at a $\sqrt{s} = 3$ TeV muon collider for Scenario B, for $M_L^-/M_L^+ = 1.3$, $M_E^+/M_L^+ = 1.5$, $M_E^-/M_L^+ = 1.8$, $M_{h_1} = 1.5$ TeV and $M_{h_2} = 1.2$ TeV. (Right): The combined total and individual production cross sections $\sigma_W = \sigma_{\mu^+\mu^-\to W_l^+W_l^-} + \sigma_{\mu^+\mu^-\to W_h^+W_h^-} + \sigma_{\mu^+\mu^-\to W_h^+W_l^-} + \sigma_{\mu^+\mu^-\to W_l^+W_h^-}$ in Scenario B, for the same portal masses, but with $s_{lh}M_{Z_D} = 0.75$ TeV, $c_{lh}M_{Z_D} = 1.3$ TeV, and $\theta_D = \pi/4$.

On the left panel of Fig 4.16, we plot the combined heavy scalar production cross sections $\sigma_{h_0} = \sigma_{\mu^+\mu^-\to h_1h_1} + \sigma_{\mu^+\mu^-\to h_2h_2} + \sigma_{\mu^+\mu^-\to h_1h_2} + \sigma_{\mu^+\mu^-\to h_4h_4}$ in Scenario B at a $\sqrt{s} = 3$ TeV muon collider as functions of the portal matter mass M_L^+, with our canonical selection of benchmark values $M_L^- = 1.3M_L^+$, $M_E^+ = 1.5M_L^+$, $M_E^- = 1.8M_L^+$. Here we select $M_{h_2} = 1.2$ TeV and $M_{h_1} = 1.5$ TeV following the selection rule in Eq.(88) to ensure that the selection in parameter space is physical, and select $\theta_D = \pi/4$, which, combined with the above-mentioned bound, also ensures that the Φ vev angle θ_Φ appearing in Eq. (56) is real. The available parameter range for e_D will then also be governed by the same bound. The main channel for this process is $\sigma_{\mu^+\mu^-\to h_4h_4}$. We thus plot the combined heavy scalar

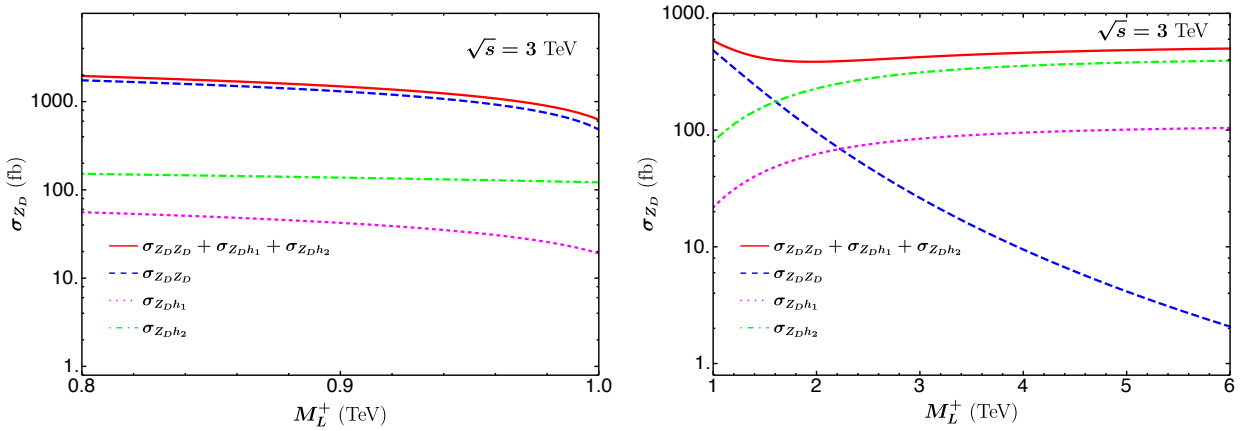

Figure 4.17: The combined total and individual production cross sections of $\sigma_{Z_D} = \sigma_{\mu^+\mu^-\to Z_D Z_D} + \sigma_{\mu^+\mu^-\to Z_D h_1} + \sigma_{\mu^+\mu^-\to Z_D h_2}$ as a function of M_L^+ at a $\sqrt{s} = 3$ TeV muon collider for Scenario B, assuming that (Left): $M_L^-/M_L^+ = 1.3$, $M_E^+/M_L^+ = 1.5$, $M_E^-/M_L^+ = 1.8$, $s_{lh} M_{Z_D}/M_L^+ = 0.75$, $c_{lh} M_{Z_D}/M_L^+ = 1.3$, $M_{h_2}/M_L^+ = 0.8$, $M_{h_1}/M_L^+ = 1.5$, $\theta_D = \pi/4$, (Right): $M_L^-/M_L^+ = 1.3$, $M_E^+/M_L^+ = 1.5$, $M_E^-/M_L^+ = 1.8$, $s_{lh} M_{Z_D} = 0.75\,\text{TeV}$, $c_{lh} M_{Z_D} = 1.3\,\text{TeV}$, $M_{h_2} = 1.2\,\text{TeV}$, $M_{h_1} = 1.5\,\text{TeV}$, and $\theta_D = \pi/4$.

production cross section σ_{h0} as a function of M_L^+ with different choice of M_{h_4}. There is a decrease in σ_{h_0} when we scale up M_{h_4}, but overall these heavy scalars can be copiously produced in a multi-TeV muon collider if they are kinematically allowed. On the right panel of Fig 4.16, we plot the combined total and individual production cross section $\sigma_W = \sigma_{\mu^+\mu^-\to W_l^+ W_l^-} + \sigma_{\mu^+\mu^-\to W_h^+ W_h^-} + \sigma_{\mu^+\mu^-\to W_h^+ W_l^-} + \sigma_{\mu^+\mu^-\to W_l^+ W_h^-}$, with the benchmark values for heavy vector-like leptons and constant heavy gauge bosons and scalars masses. The main contribution comes from $\sigma_{\mu^+\mu^-\to W_h^+ W_h^-}$, due to the choice of $\theta_D = \pi/4$. Fig 4.18 shows that the main contributing channel for σ_W actually changes with respect to θ_D. For $\theta_D = 0.7$, $\sigma_{W_h^+, W_h^-}$ dominates the total σ_W whereas for $\theta_D = 0.8$, $\sigma_{W_l^+, W_l^-}$ dominates the total σ_W. The contributions of $\sigma_{\mu^+\mu^-\to W_l^+ W_h^-}$ and $\sigma_{\mu^+\mu^-\to W_h^+ W_l^-}$ are identical, emerging in the figure as two overlapping curves, since their squared amplitudes differ by only $t \leftrightarrow u$.

In Fig 4.17, we show the combined total and individual production cross sections of Z_D, wih $\sigma_{Z_D} = \sigma_{\mu^+\mu^-\to Z_D Z_D} + \sigma_{\mu^+\mu^-\to Z_D h_1} + \sigma_{\mu^+\mu^-\to Z_D h_2}$, as a function of M_L^+, again assuming benchmark values for masses of other heavy vector-like leptons. For the masses of heavy gauge bosons and scalars, we make two different assumptions. In the right panel of Fig 4.17, we set the values of the heavy gauge bosons and scalars masses to be constants, and observe an increase in $\sigma_{\mu^+\mu^-\to Z_D h_1}$ and $\sigma_{\mu^+\mu^-\to Z_D h_2}$ as a function of M_L^+. This is because the masses of all heavy particles (scalars, vector-like leptons and gauge bosons) scale with v_Φ, the

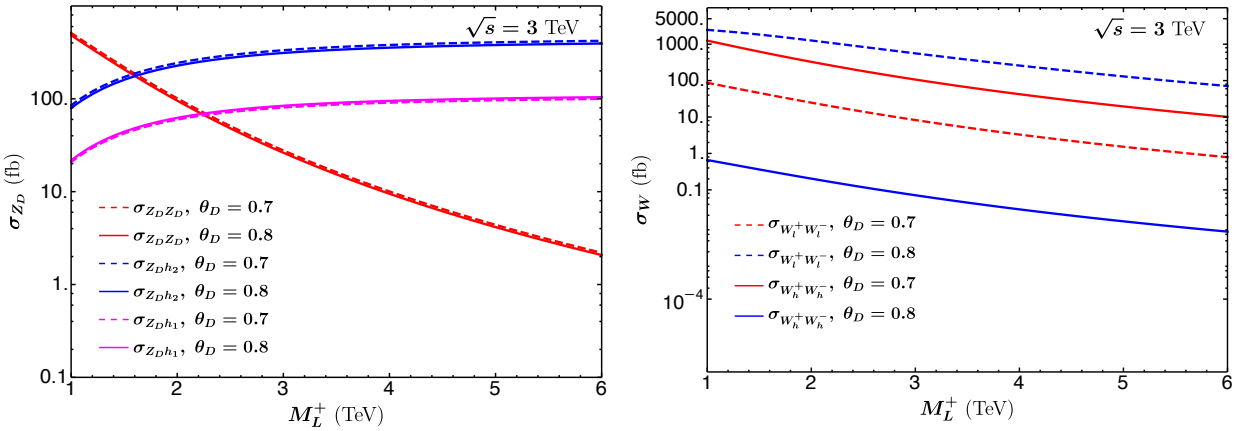

Figure 4.18: The effect of θ_D on the individual cross sections for heavy gauge bosons in Scenario B, assuming $M_L^-/M_L^+ = 1.3$, $M_E^+/M_L^+ = 1.5$, $M_E^-/M_L^+ = 1.8$, $s_{lh}M_{Z_D} = 0.75\,\text{TeV}$, $c_{lh}M_{Z_D} = 1.3\,\text{TeV}$, $M_{h_2} = 1.2\,\text{TeV}$, $M_{h_1} = 1.5\,\text{TeV}$, $e_D = 0.8$. (Left): Different channels for Z_D production are shown for $\theta_D = 0.7$ and $\theta_D = 0.8$. (Right): $\sigma_{W_l^+,W_l^-}$ are plotted in dashed curves and $\sigma_{W_h^+,W_h^-}$ are shown for $\theta_D = 0.7$ and $\theta_D = 0.8$. Note that for different values of θ_D, the main contributing channels are different.

$O(\text{TeV})$ vev of the bidoublet Φ. When we define our input parameters, v_Φ is replaced with M_{Z_D} and other proportional constants and angles. Therefore, without assuming masses of heavy scalars scale with M_L^+, we are actually assuming that the Yukawa couplings y_L and y_E, which govern the strength of the couplings of the muon to h_1 and h_2, increase when M_L^+ increases, following the relations in Eq.(62). This running of Yukawa couplings, though resulting in unexpected increase of $\sigma_{\mu^+\mu^-\to Z_D h_1}$ and $\sigma_{\mu^+\mu^-\to Z_D h_2}$ as M_L^+ increases, still respects the perturbative bound for this mass range of M_L^+. On the left panel of Fig 4.17, we fix the ratio of various heavy gauge bosons and scalars masses to M_L^+. Now, as expected, all channels of σ_{Z_D} decrease with respect to the increase of M_L^+. However, we can not show σ_{Z_D} over a larger range of M_L^+, as the masses of heavy gauge bosons and scalars become too heavy very easily, and will quickly violate the bound of Eq.(88). σ_{Z_D} also depends non-trivially on the choice of θ_D. In Fig 4.18, we plot individual cross sections with different choice of θ_D, assuming benchmark values for vector-like leptons masses, and constant heavy gauge bosons and scalars masses. Numerically, we find that larger θ_D results in larger σ_{Z_D,Z_D} and σ_{Z_D,h_2}, and vice versa for σ_{Z_D,h_1}– there is unfortunately no immediately satisfactory intuitive argument that this relation should be so, but the relationship can be ultimately observed analytically by inspection of the cross sections in Appendix 4.5.

Ultimately, we see that a TeV-scale muon collider with $O(\text{ab}^{-1})$ integrated luminosity

will readily produce thousands, if not hundreds of thousands, of potentially visible exotic diboson pairs in this model if the relevant particles are kinematically accessible. In particular, because the results scale quartically with the dark coupling e_D/M_{Z_D}, which enters into the $g-2$ calculation, searches for these particles have the potential to significantly constrain the model's ability to address the magnetic moment anomaly. Furthermore, if M_{Z_D} can be directly measured, possibly in its dimuon decay channel, constraints on the coupling e_D from physical consistency requirements with other model parameters can be determined. Because e_D directly affects the coupling strength of our conjectured dark matter candidate to the dark photon mediator, such constraints have the potential to have excellent complementarity with dark sector constraints from the relic abundance and direct and indirect detection.

Precision Constraints

In this section, we discuss the precision constraints on this model. We first note that precision electroweak observables do not provide significant constraints on this model, similar to the case of the minimal portal matter construction of [56]. As the new fermions are all vector-like with respect to the SM group, their loop-level effects on S and T are heavily suppressed. The only other potential source of corrections to the oblique parameters in this model is the kinetic mixing between the Z boson and the dark sector gauge bosons, A_D and Z_D.[16] Oblique corrections stemming from kinetic mixing scale quadratically with the kinetic mixing coefficient, however, and as such generally only constrain kinetic mixing of $O(10^{-2})$ [135, 193]. We can readily compute the kinetic mixing coefficients of both the A_D and the Z_D with Z, which due to the fact that the dark group is semisimple, will be finite and calculable. At the Z pole (the relevant scale for the precision electroweak measurements), we arrive at kinetic mixing coefficients of

$$\epsilon_{Z-A_D} = \frac{e_D e}{6\pi^2}\frac{s_w}{c_w}\log\left(\frac{M_L^+ M_E^+}{M_L^- M_E^-}\right),$$

$$\epsilon_{Z-Z_D} = \frac{e_D e}{12\pi^2\sin(2\theta_D)}\frac{s_w}{c_w}\left[\frac{M_L^{+2}-M_L^{-2}}{M_L^{+2}+M_L^{-2}}\left(\frac{5}{6}+\log\frac{M_L^0}{m_Z}\right)+(1-2\cos(2\theta_D))\log\frac{M_L^+}{M_L^-}+(L\to E)\right],$$

[16] The Z boson can also mix with the $W_{h,l}$ bosons, however due to approximate $U(1)_D$ charge conservation this mixing is highly suppressed. If we were to relax our assumption that the SM Higgs sector is not coupled to the dark scalar sector, nontrivial mass mixing between the Z boson and the scalar sector would emerge from these mixed terms in the scalar potential. However, because these couplings are under harsh phenomenological constraints, the effects of these couplings will be quite similar to those of the kinetic mixing-induced effect.

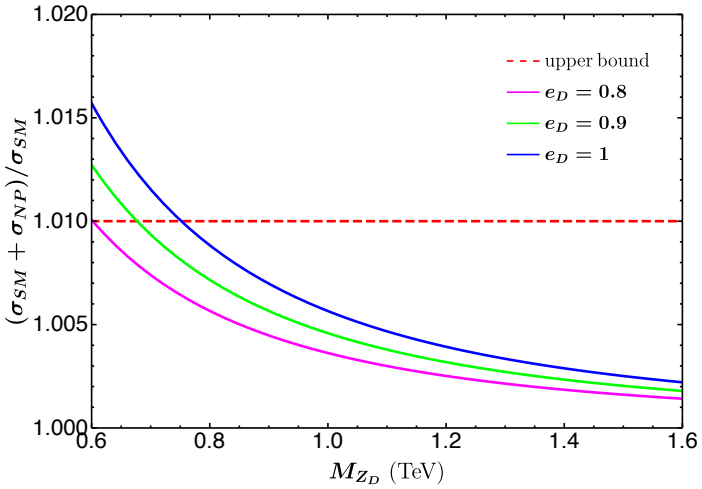

Figure 4.19: The ratio $\sigma_{SM+NP}/\sigma_{SM}$ that emerges in Scenario B from neutrino trident production. The experimental upper bound is obtained from averaging CHARM-II, CCFR and NuTEV.

to leading order in $m_Z^2/{M_{L,E}^{\pm}}^2$ and $m_{\tau,\mu}^2/m_Z^2$. Following the analysis of [194], because Z_D interacts at leading order with SM fields (the τ or μ, depending on whether we consider Scenario A or Scenario B, and its corresponding neutrino), we have included the effects of both the kinetic mixing of the Z_D with the $U(1)_Y$ *and* $SU(2)_L$ gauge fields. Given that the coefficient $es_w/(12\pi^2 c_w) \approx 1.4 \times 10^{-3}$, it is trivial to see that both kinetic mixing coefficients trivially satisfy precision electroweak constraints from, *eg.*, [135], as long as $M_{Z_D} - m_Z \gtrsim 10$ GeV. Since it is unlikely that Z_D would be so light while the portal matter (which presumably has masses of the same magnitude) would remain undetected, we can reasonably conclude that precision electroweak observables play no serious role in constraining the parameter space.

In Scenario B, the fact that Z_D couples to muons, rather than τ's, requires us to consider further precision constraints, emerging from four-lepton operators featuring muons and muon neutrinos. The strongest of these constraints comes from the neutrino trident production process $\nu_\mu N \to \nu_\mu \mu^+ \mu^- N$. Following the results of [195] for chiral Z_D couplings, we have

$$\frac{\sigma_{SM+NP}}{\sigma_{SM}} = 1 + 8\frac{(1+4s_W^2)\frac{g^L_{\mu\mu}(g^L_{\mu\mu}+g^R_{\mu\mu})}{g_2^2}\frac{m_W^2}{M_{Z_D}^2} - \frac{g^L_{\mu\mu}(g^L_{\mu\mu}-g^R_{\mu\mu})}{g_2^2}\frac{m_W^2}{M_{Z_D}^2}}{1+(1+4s_W^2)^2}, \tag{100}$$

where s_W, m_W and g_2 are the usual Standard Model parameters, and $g^{L,R}_{\mu\mu}$ describe left and

right $\bar{\mu}\mu Z_D$ couplings. In Scenario B, they take the forms

$$g^L_{\mu\mu} = \frac{e_D(M_L^{-2} - M_L^{+2})}{\sin 2\theta_D(M_L^{-2} + M_L^{+2}))}, \qquad g^R_{\mu\mu} = \frac{e_D(M_E^{-2} - M_E^{+2})}{\sin 2\theta_D(M_E^{-2} + M_E^{+2})}, \tag{101}$$

Average results from CHARM-II [196], CCFR [197] and NuTEV [198] places a bound on this ratio

$$\frac{\sigma_{SM}\sigma_{NP}}{\sigma_{SM}} = 0.83 \pm 0.18 \tag{102}$$

We plot this ratio as a function of Z_D mass in Fig 4.19, for 3 different values of e_D. We find that for reasonable ranges of the choice of e_D, for $M_{Z_D} > 0.8\,\text{TeV}$, this ratio is always well bounded. For smaller values of e_D, the lower bound on M_{Z_D} could be further pushed down to around 0.6 TeV.

Turning now to bounds from flavor violation, we first note that charged lepton flavor constraints also do not provide significant constraints on this model. More precisely, because the dark gauge symmetry breaking preserves a residual Z_2', as discussed in Section 4.2, the muon and τ lepton flavors are to excellent approximation isolated from one another, and charged lepton flavor-violating couplings are so suppressed that constraints, from, *eg.*, flavor-violating τ decays are trivially satisfied in both Scenario A and Scenario B. Flavor-violating couplings between SM fermions mediated by the W_h and W_l gauge bosons do exist, but they are heavily suppressed. Note also that since the electron is taken to be a singlet with respect to G_D and Z_2 (and thus even with respect to Z_2'), charged lepton flavor violation involving the first generation would necessarily be absent at tree level in this model.

That said, we note that if the model is taken literally in the neutrino sector, the preserved Z_2', which conveniently insulates the model from large flavor-changing neutral currents in the charged lepton sector, also prevents mixing among the ν_τ and ν_μ, in conflict with current best-fits for the parameters of the PMNS matrix (see *eg.* [199] and references therein). Hence, the Z_2' must not be an exact symmetry, which ultimately means that this model needs to be extended. The Z_2' breaking might be introduced solely into the neutrino sector via, for example, sterile neutrinos with Z_2'-violating Majorana mass terms, or the underlying global Z_2 we originally introduced into the model might be removed or softly broken in the scalar sector, leading to additional non-trivial constraints on the model from charged lepton flavor-violation searches. As a detailed exploration of the neutrino flavor physics within this general framework is beyond the scope of this chapter, we shall defer such an analysis to future work.

4.5 Conclusions and Outlook

In this work, we have presented an extension to a minimal framework of leptonic portal matter inspired by the model presented in [55] to address the muon magnetic moment anomaly. By augmenting the SM gauge group with a semisimple symmetry that contains a dark $U(1)_D$, in our case $SU(2)^2$ augmented by a global Z_2, we are able to accommodate both portal and SM matter as constituents of single multiplets such that any kinetic mixing between Abelian factors of the new dark gauge group and SM gauge fields are finite and calculable. Compared to the minimal construction, this extended dark gauge group presents a far richer parameter space in which the observed correction to the muon magnetic moment can be recreated, including a number of nontrivial physical phase differences (or, in our simplifying assumption that the parameters are real, signs) between parameters, contributions to the magnetic moment involving an extended scalar and gauge sector, and even an implementation of the model in which the muon does not directly mix with the portal matter fields, but still experiences a sizable correction to $g-2$ arising from loops involving both the portal matter fields and new $U(1)_D$-neutral vector-like leptons.

We have explored other possible experimental signatures of the model, noting that the model presents rich collider phenomenology. In the fermion sector, we found that the extended dark gauge group gives rise to the possibility of non-trivial additional decay channels for the portal matter fields *and* the $U(1)_D$-neutral vector-like leptons, which can lead to atypical experimental signatures for these fields. We have also seen that a multi-TeV muon collider offers excellent prospects to discover the model's new vector-like leptons as well as the TeV-scale scalar and vector boson content arising from the extended dark gauge group. Additionally, the similarity between the Feynman diagrams contributing to the production of the model's new scalars and gauge bosons at such a machine and those diagrams which contribute to the anomalous magnetic moment of the muon make searches for these particles a potentially useful method of constraining or measuring various critical parameters governing the magnitude of the $g-2$ correction.

There are several immediate directions in which this work might be extended. As mentioned in Section 4.4, implementing a phenomenologically realistic model for neutrinos within this framework presents challenges, including relaxing the Z_2 symmetry which offers flavor protection in the charged lepton sector. As a result, a detailed exploration of the feasibility of preserving this Z_2 for the charged leptons and violating it in the neutrino sector, or the degree to which recreating realistic neutrino mixing would require explicit

Z_2 breaking in the charged sector, would be of interest. Additionally, inspired by the idea of interrelating the muon $g-2$ contribution in this framework to the τ lepton Yukawa coupling and avoiding experimental constraints on new physics coupled to electrons, we have limited the discussion of this lepton flavor symmetry to involve only the second and third generations. Because both the electron and muon anomalous magnetic moments have been measured, a study of the kind given in, *eg.* [118, 200] of an analogous framework to the model presented here, featuring a flavor symmetry of the first two lepton generations instead of the last two could be an enlightening additional regime of the model to consider. More broadly, the model we have presented here represents a reasonable "proof of concept" in incorporating the muon $g-2$ paradigm of [55] into a more UV complete portal matter construction, and in the process has demonstrated a rich nontrivial phenomenology descending from the extended dark gauge group. In principle a broad number of similar frameworks, perhaps associated with an extended dark gauge group containing other phenomenologically significant BSM symmetries, can be developed.

Appendix B: Diboson Cross Sections in Scenario B

Here, we reproduce the full set of squared amplitudes for the diboson production processes considered in Section 4.4. In keeping with the notation of Section 4.4, we shall denote each cross section by as $|\mathcal{M}_{XY}|$, where X, Y shall denote the two bosons being produced. We shall group these cross sections into three categories: Those which feature only the scalar bosons h_1, h_2, and h_4, those which feature the dark gauge boson Z_D, and finally those which feature the dark gauge bosons $W^{\pm}_{h,l}$. In the first category, we have

$$
\begin{aligned}
|\mathcal{M}_{h_1h_1}|^2 &= \frac{e_D^4(1-S_h)^2}{256M_{Z_D}^4 s_{2D}^4 c_{2\phi}^4}\left(\frac{(M_L^{-2}-M_L^{+2})^4(t-u)^2(tu-M_{h_1}^4)}{M_L^{0\,4}(M_L^{0\,2}-t)^2(M_L^{0\,2}-2u)^2}+(L\to E)\right),\\
|\mathcal{M}_{h_2h_2}|^2 &= \frac{e_D^4(1+S_h)^2}{256M_{Z_D}^4 s_{2D}^4 c_{2\phi}^4}\left(\frac{(M_L^{-2}-M_L^{+2})^4(t-u)^2(tu-M_{h_2}^4)}{M_L^{0\,4}(M_L^{0\,2}-t)^2(M_L^{0\,2}-2u)^2}+(L\to E)\right),\\
|\mathcal{M}_{h_4h_4}|^2 &= \frac{e_D^4}{4M_{Z_D}^4 s_{2D}^4 c_{2\phi}^4}\left(\frac{M_L^{0\,4}(t-u)^2(tu-M_{h_4}^4)}{(M_L^{0\,2}-t)^2(M_L^{0\,2}-u)^2}+(L\to E)\right),\\
|\mathcal{M}_{h_1h_2}|^2 &= \frac{e_D^4(1-S_h^2)}{256M_{Z_D}^4 s_{2D}^4 c_{2\phi}^4}\left(\frac{(M_L^{-2}-M_L^{+2})^4(t-u)^2(tu-M_{h_1}^2M_{h_2}^2)}{M_L^{0\,4}(M_L^{0\,2}-t)^2(M_L^{0\,2}-u)^2}+(L\to E)\right),
\end{aligned}
$$

where we follow the notation outlined in Eq. (88). Squared amplitudes for processes featuring final-state Z_D are given by

$$
\begin{aligned}
|\mathcal{M}_{Z_DZ_D}|^2 &= \frac{e_D^4 M_L^{-4}M_L^{+4}}{4M_{Z_D}^4 s_{2D}^4 M_L^{0\,8}}\left(\frac{4C_{Z_DZ_D,1}}{(M_L^{0\,2}-t)^2}+\frac{4C_{Z_DZ_D,2}}{(M_L^{0\,2}-u)^2}+\frac{C_{Z_DZ_D,3}}{(M_L^{0\,2}-u)^2(M_L^{0\,2}-t)^2}\right)+(L\to E),\\
|\mathcal{M}_{Z_Dh_1}|^2 &= \frac{e_D^4 C_{\lambda\phi-}^2 M_L^{-2}M_L^{+2}(M_L^{-2}-M_L^{+2})^2(2M_L^{0\,2}-t-u)^2C_{Z_Dh_1,1}}{32M_{Z_D}^4 s_{2D}^4 c_{2\phi}^4 M_L^{0\,8}(M_L^{0\,2}-t)^2(M_L^{0\,2}-u)^2}+(L\to E),\\
|\mathcal{M}_{Z_Dh_2}|^2 &= \frac{e_D^4 C_{\lambda\phi+}^2 M_L^{-2}M_L^{+2}(M_L^{-2}-M_L^{+2})^2(2M_L^{0\,2}-t-u)^2C_{Z_Dh_2,1}}{32M_{Z_D}^4 s_{2D}^4 c_{2\phi}^4 M_L^{0\,8}(M_L^{0\,2}-t)^2(M_L^{0\,2}-u)^2}+(L\to E),
\end{aligned}
$$

where

$$
\begin{aligned}
C_{Z_DZ_D,1} &= -\frac{1}{4}\Big(4M_{Z_D}^8-t^3u+4t^2(t+u)M_{Z_D}^2-t(7t+4u)M_{Z_D}^4\Big),\\
C_{Z_DZ_D,2} &= -\frac{1}{4}\Big(4M_{Z_D}^8-tu^3+4u^2(t+u)M_{Z_D}^2-u(7u+4t)M_{Z_D}^4\Big)\\
C_{Z_DZ_D,3} &= \frac{1}{2}\Big(16M_{Z_D}^8-8(t+u)M_{Z_D}^6-7tuM_{Z_D}^4+4tu(t+u)M_{Z_D}^2-t^2u^2\Big)\\
C_{Z_Dh_1,1} &= 2M_{Z_D}^4+M_{h_1}^2M_{Z_D}^2-2(t+u)M_{Z_D}^2+tu,\\
C_{Z_Dh_2,1} &= 2M_{Z_D}^4+M_{h_2}^2M_{Z_D}^2-2(t+u)M_{Z_D}^2+tu.
\end{aligned}
$$

Finally, the squared amplitudes for final states featuring $W^{\pm}_{h,l}$ are given by

$$|\mathcal{M}_{W_l^+W_l^-}|^2 = -\frac{e_D^4}{128M_{Z_D}^4 s_{lh}^4 M_L^{0\,4}}\left(\frac{2C_{W_l^+W_l^-,1}}{(M_L^{+\,2}-t)^2}+\frac{2C_{W_l^+W_l^-,2}}{(M_L^{-\,2}-u)^2}+\frac{C_{W_l^+W_l^-,3}}{(M_L^{+\,2}-t)(M_L^{+\,2}-u)}\right)+(L\to E)$$

$$|\mathcal{M}_{W_h^+W_h^-}|^2 = -\frac{e_D^4}{128M_{Z_D}^4 c_{lh}^4 M_L^{0\,4}}\left(\frac{2C_{W_h^+W_h^-,1}}{(M_L^{+\,2}-t)^2}+\frac{2C_{W_h^+W_h^-,2}}{(M_L^{-\,2}-u)^2}+\frac{C_{W_h^+W_h^-,3}}{(M_L^{+\,2}-t)(M_L^{+\,2}-u)}\right)+(L\to E)$$

$$|\mathcal{M}_{W_h^+W_l^-}|^2 = -\frac{e_D^4}{64M_{Z_D}^4 c_{lh}^2 s_{lh}^2 M_L^{0\,4}}\left(\frac{C_{W_h^+W_l^-,1}}{(M_L^{+\,2}-u)^2}+\frac{2C_{W_h^+W_l^-,2}}{(M_L^{-\,2}-t)(M_L^{+\,2}-u)}+\frac{C_{W_h^+W_l^-,3}}{(M_L^{-\,2}-t)^2}\right)+(L\to E)$$

$$|\mathcal{M}_{W_l^+W_h^-}|^2 = |\mathcal{M}_{W_h^+W_l^-}|^2\Big|_{t\leftrightarrow u},$$

where

$$C_{W_l^+W_l^-,1} = \left(4s_{lh}^8M_{Z_D}^8 - t(7t+4u)s_{lh}^4M_{Z_D}^4 + 4t^2(t+u)s_{lh}^2M_{Z_D}^2 - t^3u\right)\left(H^-_{-1,-1}(M_L^+,M_L^-)\right)^4,$$

$$C_{W_l^+W_l^-,2} = \left(4s_{lh}^8M_{Z_D}^8 - u(7u+4t)s_{lh}^4M_{Z_D}^4 + 4u^2(t+u)s_{lh}^2M_{Z_D}^2 - tu^3\right)\left(H^-_{-1,-1}(M_L^-,M_L^+)\right)^4,$$

$$C_{W_l^+W_l^-,3} = \left(16s_{lh}^8M_{Z_D}^8 - 8(t+u)s_{lh}^6M_{Z_D}^6 - 7tus_{lh}^4M_{Z_D}^4 + 4tu(t+u)s_{lh}^2M_{Z_D}^2 - t^2u^2\right)C'_{W_l^+W_l^-,3},$$

$$C'_{W_l^+W_l^-,3} = \left(\frac{M_L^+M_L^-(c_{2\pm}+4)}{s_{2D}^2} - \frac{1}{c_D}\left(\frac{2M_L^{0\,2}s_{2\pm}}{s_D} + M_L^+M_L^-\left(\frac{c_\pm^2}{c_D}-\frac{s_\pm^2}{c_D}\right)\right)\right)^2,$$

$$C_{W_h^+W_h^-,1} = \left(4c_{lh}^8M_{Z_D}^8 - t(7t+4u)c_{lh}^4M_{Z_D}^4 + 4t^2(t+u)c_{lh}^2M_{Z_D}^2 - t^3u\right)\left(J^+_{-1,-1}(M_L^-,M_L^+)\right)^4,$$

$$C_{W_h^+W_h^-,2} = \left(4c_{lh}^8M_{Z_D}^8 - u(7u+4t)c_{lh}^4M_{Z_D}^4 + 4u^2(t+u)c_{lh}^2M_{Z_D}^2 - tu^3\right)\left(J^+_{-1,-1}(M_L^+,M_L^-)\right)^4$$

$$C_{W_h^+W_h^-,3} = \left(16c_{lh}^8M_{Z_D}^8 - 8(t+u)c_{lh}^6M_{Z_D}^6 - 7tuc_{lh}^4M_{Z_D}^4 + 4tu(t+u)c_{lh}^2M_{Z_D}^2 - t^2u^2\right)C'_{W_h^+W_h^-,3}$$

$$C'_{W_h^+W_h^-,3} = \left(\frac{M_L^+M_L^-(-c_{2\pm}+4)}{s_{2D}^2} + \frac{1}{c_D}\left(\frac{2M_L^{0\,2}s_{2\pm}}{s_D} + M_L^+M_L^-\left(\frac{c_\pm^2}{c_D}-\frac{s_\pm^2}{c_D}\right)\right)\right)^2,$$

$$C_{W_h^+W_l^-,1} = \frac{(1-c_{8lh})M_{Z_D}^8 + 8u(c_{4lh}-1)M_{Z_D}^6 + \left(4t^2(c_{4lh}-1)+16tu(3-c_{4lh})\right)M_{Z_D}^4 - 64t^2uM_{Z_D}^2 + 32t^3u}{32C'^{-1}_{W_h^+W_l^-,1}},$$

$$C'_{W_h^+W_l^-,1} = \left(J^+_{-1,-1}(M_L^-,M_L^+)\right)^2\left(H^-_{-1,-1}(M_L^+,M_L^-)\right)^2$$

$$C_{W_h^+W_l^-,2} = \frac{(1-c_{4lh})M_{Z_D}^8 + (t+u)(c_{4lh}-1)M_{Z_D}^6 + tu(9-c_{4lh})M_{Z_D}^4 - 8tu(t+u)M_{Z_D}^2 - 8t^2u^2}{8C'^{-1}_{W_h^+W_l^-,2}},$$

$$C'_{W_h^+W_l^-,2} = H^-_{-1,-1}(M_L^+,M_L^-)\,H^-_{-1,-1}(M_L^-,M_L^+)\,J^+_{-1,-1}(M_L^-,M_L^+)\,J^+_{-1,-1}(M_L^+,M_L^-)$$

$$C_{W_h^+W_l^-,3} = \frac{(1-c_{8lh})M_{Z_D}^8 + 8t(c_{4lh}-1)M_{Z_D}^6 + \left(4u^2(c_{4lh}-1)+16tu(3-c_{4lh})\right)M_{Z_D}^4 - 64u^2tM_{Z_D}^2 + 32u^3t}{32C'^{-1}_{W_h^+W_l^-,3}},$$

$$C'_{W_h^+W_l^-,3} = \left(J^+_{-1,-1}(M_L^+,M_L^-)\right)^2\left(H^-_{-1,-1}(M_L^-,M_L^+)\right)^2$$

and

$$H^{\pm}_{a,b}(A,B) \equiv Ac_{\pm}s^{a}_{D} \pm Bs_{\pm}c^{b}_{D}, \tag{103}$$
$$J^{\pm}_{a,b}(A,B) \equiv Ac_{\pm}c^{a}_{D} \pm Bs_{\pm}s^{b}_{D},$$

Chapter 5

Model Building of Leptonic Portal Matter Models Using Graph Reinforcement Learning

5.1 Introduction

In the current era in which models of physics beyond the Standard Model (BSM) have been experimentally constrained at unprecedented levels, identifying means for more comprehensive explorations of the space of potentially viable BSM theories, which encompasses all theories which contain the Standard Model effective field theory and possess only additions which avoid present experimental constraints, is of increasing importance. Reinforcement learning (RL) provides one such method for an automated exploration of such large spaces for which viable points are sparsely distributed. In a reinforcement learning scan, an agent is trained to recommend actions to modify a model in ways that maximize its expected reward. In our case, this reward is by design correlated to some metric of the theoretical or phenomenological viability of the model.

RL has already demonstrated promise in the field of BSM model building for frameworks that have a finite number of discrete parameters, for example in probing large spaces in string theory [201], and identifying viable Froggatt-Nielsen charges [202, 203]. However, if reinforcement learning scans are to be generalized effectively to a broader class of BSM model building problems, it is crucial that the procedure be adapted to scanning over spaces of models where the BSM particle content, and therefore the feature dimensionality of the subspace, is variable.

To this end, we present a procedure in which BSM theories are represented as graphs and use graph neural networks. Our procedure can be used to explore any class of four-dimensional BSM theories with a finite but otherwise arbitrary and not pre-specified

number of fields, essentially only excluding theories with infinite towers of states such as Kaluza-Klein theories. The theorist would then just need to specify the symmetry group and the possible group representations of the particles in the theory.

To explore this idea, we return to our previously-studied framework of lepton portal matter theories [56, 130], as discussed in Chapters 3 and 4. In this chapter, we apply our reinforcement learning method based on graph representations to the class of models partially based on [55] presented in Chapter 3, but also allowing for vectorlike leptons that are uncharged under $U(1)_D$, for greater generality. We impose a minimal set of a priori assumptions on this model space, including making no prior stipulations enforcing flavor conservation. Upon imposing experimental constraints, including the muon anomalous magnetic moment discrepancy [5, 21–42, 204], and flavor and electroweak precision constraints, and incentivizing simplicity, our procedure yields not only minimal constructions that have already been explored [55], but also alternatives that have not to our knowledge been previously studied in the literature.

This chapter, which is based on the works [57, 58], is structured as follows. In Section 5.2, we describe the representation of BSM theories as graphs and discuss graph neural networks. We turn in Section 5.3 to a discussion of our reinforcement learning environment. In Section 5.4, we present the results of the RL scan for the leptonic portal matter theories considered. The discussion and conclusions are provided in Section 5.5. We also present an appendix on the details of the hybrid Proximal Policy Optimization (H-PPO) algorithm used in this study.

5.2 BSM Graph Representations

Our procedure is based on leveraging the utility of using graphs in representing arbitrary BSM theories, with learning tasks accomplished through a graph neural network. Mathematically, a graph consists of nodes and the edges which connect them, where each node is described by a feature vector, and each edge consists of the pair of connected nodes and a corresponding feature vector for the edge that characterizes the coupling. In our BSM graph grammar, each node in a graph will represent either a field or an interaction term. Edges connect field nodes to coupling terms, allowing interaction terms with arbitrary numbers of different fields to be represented with edges that connect only pairs of particles.

Here we are interested in four-dimensional BSM theories with an arbitrary but finite number of different fields, which have representations under Lorentz symmetry and any

proposed internal symmetries. With the assumption that there is a finite number of distinct group representations appearing in the model, and that there is a finite maximum mass dimension for the allowed interaction terms that are written down, it can be shown that the full set of nodes and edges, including the elements of their feature vectors, is finite [58].

For the class of models we consider here, the new states are electroweak doublet or singlet vector-like leptons with $U(1)_D$ charges of ± 1 or 0. We denote these states by L_q and E_q, respectively, where q is its $U(1)_D$ charge, with mass parameters $M^{L(E),0(\pm)}$ (we choose to work in a basis where there are no mixed mass parameters between the SM leptons and the new vector-like leptons). These states interact with the SM leptons via Yukawa couplings to the SM Higgs h or to a dark Higgs field h_D, which breaks the $U(1)_D$. Since the $U(1)_D$ breaking is at the sub-GeV scale in portal matter models, we will not need to include the dark Higgs or the dark photon explicitly as nodes in our BSM graphs, since for observable quantities of interest for the vector-like leptons these sub-GeV mass scales do not directly appear.

The vector-like leptons couple to the SM leptons through the Yukawa couplings $\lambda^{\pm}_{L(E)}$, which couple $L_{\pm}$ ($E_{\pm}$) to the SM leptons via h_D, and $y^0_{L(E)}$, which couple L^0 (E^0) to the SM leptons via h. The vector-like leptons can also have Yukawa interactions with each other in various ways: $y^{\alpha}_{LE,EL}$ denotes the Yukawa couplings of L_q and E_q with the SM Higgs ($\alpha = \{0, \pm\}$), and $\lambda^{0\pm,\pm 0}_{L(E)}$ are the Yukawa couplings of vector-like doublets (singlets) of dark charge ± 1 to those with dark charge 0.

In our graph construction, theories are represented as a heterogeneous graphs, which have differing node types.[17] There can be multiple ways to construct graph grammars, depending on how we encode information in different node types. As we will see, while the choice of graph grammar is by no means unique, it can have a nontrivial impact on the reinforcement learning results. For the leptonic portal matter model framework considered in this study, we explored two possibilities: graph grammar A and graph grammar B.

These two graph grammars handle particles with different electroweak representations differently. In graph grammar A, which is shown in Table 5.1, theories are represented as a heterogeneous graph with two node types of different feature dimensionality: particles and couplings. Discrete node features are used to identify the electroweak representation and dark $U(1)$ charge of particle nodes, and a discrete node feature is used to distinguish between dark Higgs and SM Higgs Yukawa couplings among the coupling nodes. Note that the Yukawa coupling terms between two vector-like fields must treat the two incoming fields

[17] It is in principle possible to construct graph grammars using a traditional homogeneous graph, without differing node types. For more details on the subtleties of this construction we refer the reader to [58].

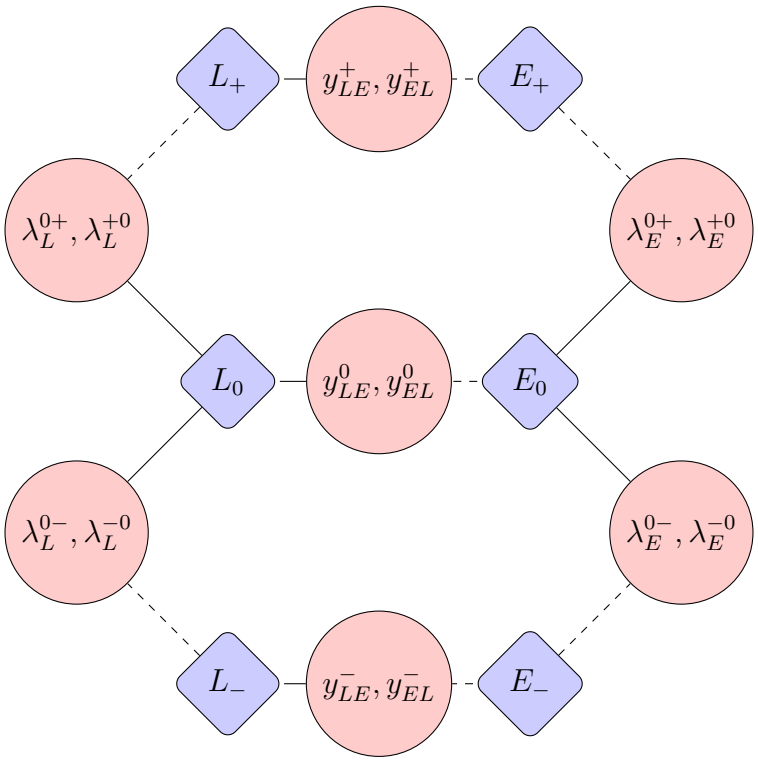

Figure 5.1: A visual depiction of a graph in the class of theories explored with six total BSM fermions (an isospin singlet and a doublet that are uncharged under $U(1)_D$, and two isospin singlets and doublets that have a dark charge of ± 1), following graph grammar A of Table 5.1. Diamonds denote particle nodes, which contain the particle mass and Yukawa couplings to SM particles as features, and circles denote Yukawa couplings. A solid line denotes an edge of type e_1, while a dashed line denotes an edge type of e_2.

differently, otherwise terms such as the y_{EL} couplings would not be distinguished from the y_{LE} couplings. Therefore, for each different type of interaction node we consider, we must have two different edge types, as shown. The relations between various Yukawa couplings among different particles is shown graphically in Figure 5.1. In graph grammar B, instead of coding electroweak representation as a discrete node features, particles with different electroweak representations (singlets and doublets) are identified as separate node types, as shown in Table 5.2. The relations between various Yukawa couplings among different particles is shown graphically in Figure 5.2. Since representation A encodes electroweak singlets and doublets within a single node type, continuous parameters are shared between these two types of vector-like leptons and hence the agent has more information and fewer separate weights to learn. In contrast, electroweak doublets and singlets are expressed in different node types in representation B and hence the knowledge is not shared among

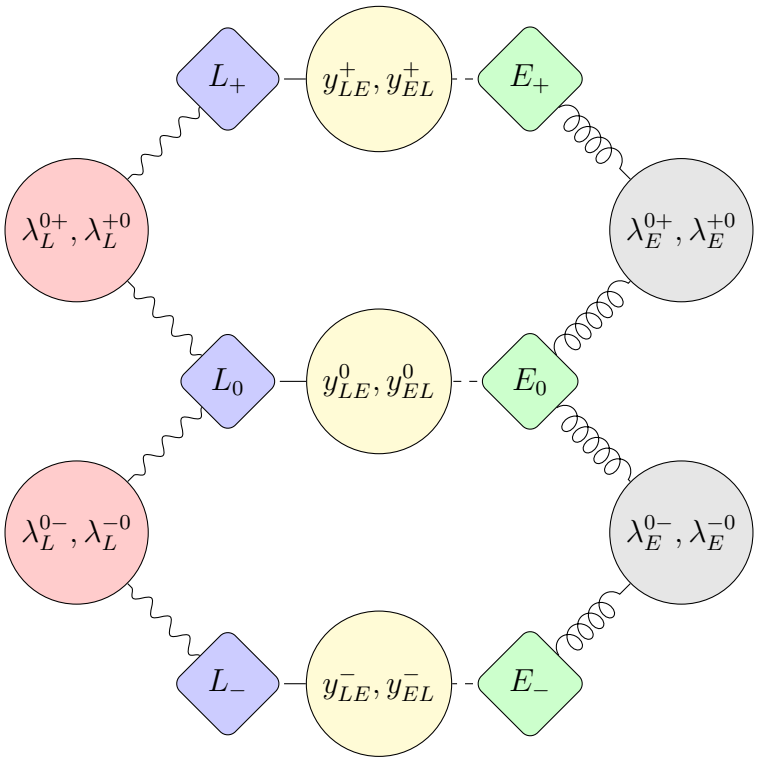

Figure 5.2: A visual depiction of a graph in the class of theories with six total BSM fermions, following the graph grammar B summarized in Table 5.2. Diamonds denote particle nodes, which contain the particle mass and Yukawa couplings to SM particles as features. Circles denote Yukawa couplings. Different heterogeneous node types are denoted by different colors. For couplings: Yellow denotes an h Yukawa, red denotes h_D doublet Yukawa, gray denotes h_D singlet Yukawa. For particles: Blue denotes an electroweak doublet vector-like lepton, while green denotes an electroweak singlet. A solid line denotes an edge of type e_D, while a dashed line e_S, a wavy line e_{DD}, and a coiled line e_{SS}.

them and the agent has to learn two independent sets of separate weights. We will further explore in the results section how this choice of graph grammar could potentially affect the outcome of the agent's search.

5.3 Reinforcement Learning Environment

We now turn to the construction of the reinforcement learning environment. Reinforcement learning is modelled as a Markov decision process, consisting of a state space $\mathcal{S}$, a space of actions $\mathcal{A}$, and a policy π_θ. Given a state $s \in \mathcal{S}$, the policy π_θ will assign probabilities to different actions $a \in \mathcal{A}$ which transform a given state into a new one. The parameters θ, here the weights of a neural network, define the behavior of this policy. Desirable

Nodes		
Node Type	Field/Coupling	Feature Vector
Particle	L_0	$\{M^{L,0}, \vec{y}_L^0, 0, 0\}$
	$L_\pm$	$\{M^{L,\pm}, \vec{\lambda}_L^\pm, \pm 1, 0\}$
	E_0	$\{M^{E,0}, \vec{y}_E^0, 0, 1\}$
	$E_\pm$	$\{M^{E,\pm}, \vec{\lambda}_E^\pm, \pm 1, 1\}$
Coupling	$y_{LE}^0,\ y_{EL}^0$	$\{y_{LE}^0, y_{EL}^0, 0\}$
	$y_{LE}^\pm,\ y_{EL}^\pm$	$\{y_{LE}^\pm, y_{EL}^\pm, 0\}$
	$\lambda_L^{0\pm},\ \lambda_L^{\pm 0}$	$\{\lambda_L^{0\pm}, \lambda_L^{\pm 0}, 1\}$
	$\lambda_E^{0\pm},\ \lambda_E^{\pm 0}$	$\{\lambda_E^{0\pm}, \lambda_E^{\pm 0}, 1\}$
Edges		
Edge Type	Particle F to Coupling $\{g_1, g_2\}$	
e_1	$g_1 \overline{F} P_R \Box + g_2 \overline{\Box} P_R F$	
e_2	$g_1 \overline{\Box} P_R F + g_2 \overline{F} P_R \Box$	

Table 5.1: The graph grammar A used to represent models of the class explored. $\vec{y}$ and $\vec{\lambda}$ are three-component vectors which describe the Yukawa couplings between vector-like fermions and the SM fields.

states for the model are given positive numerical values known as rewards; following a training algorithm the parameters θ are optimized to maximize the accumulated reward that the agent will achieve over some trajectory of actions. These trajectories are "episodes," and they consist of the set of states produced by a series of modifications of an original randomly-sampled model, until either a viable model (which will be called a "terminal" state) is produced or the agent has taken 250 actions.

Here the state space consists of a graph representing a BSM model, in addition to graph metadata counting the number of vector-like leptons of each species that are present in the model. The agent is rewarded based on producing models with a larger log-likelihood than the SM given the experimental inputs summarized in Table 5.3, and for achieving this likelihood with a minimal number of BSM particles. We find good results for a model

Nodes		
Node Type	Field/Coupling	Feature Vector
Doublet	L_0	$\{M^{L,0}, \vec{y}_L^0, 0\}$
	$L_\pm$	$\{M^{L,\pm}, \vec{\lambda}_L^\pm, \pm 1\}$
Singlet	E_0	$\{M^{E,0}, \vec{y}_E^0, 0\}$
	$E_\pm$	$\{M^{E,\pm}, \vec{\lambda}_E^\pm, \pm 1\}$
h Yukawa	y_{LE}^0, y_{EL}^0	$\{y_{LE}^0, y_{EL}^0\}$
	$y_{LE}^\pm$, $y_{EL}^\pm$	$\{y_{LE}^\pm, y_{EL}^\pm\}$
h_D Doublet Yukawa	$\lambda_L^{0\pm}$, $\lambda_L^{\pm 0}$	$\{\lambda_L^{0\pm}, \lambda_L^{\pm 0}\}$
h_D Singlet Yukawa	$\lambda_E^{0\pm}$, $\lambda_E^{\pm 0}$	$\{\lambda_E^{0\pm}, \lambda_E^{\pm 0}\}$
Edges		
Edge Type	Connects	F-$\{g_1, g_2\}$ Coupling
e_D	Doublet-h Yukawa	$y_{LE}^{0,\pm}\overline{F}P_R\square + y_{EL}^{0,\pm}\overline{\square}P_R F$
e_S	Singlet-h Yukawa	$y_{LE}^{0,\pm}\overline{\square}P_R F + y_{EL}^{0,\pm}\overline{F}P_R\square$
e_{DD}	Doublet-h_D Doublet Yukawa	$\lambda_L^{0\pm}\overline{F}P_R\square + \lambda_L^{\pm 0}\overline{\square}P_R F, \;\; Q_D = 0$
		$\lambda_L^{0\pm}\overline{\square}P_R F + \lambda_L^{\pm 0}\overline{F}P_R\square, \;\; Q_D = \pm 1$
e_{SS}	Singlet-h_D Singlet Yukawa	$\lambda_E^{0\pm}\overline{F}P_R\square + \lambda_E^{\pm 0}\overline{\square}P_R F, \;\; Q_D = 0$
		$\lambda_E^{0\pm}\overline{\square}P_R F + \lambda_E^{\pm 0}\overline{F}P_R\square, \;\; Q_D = \pm 1$

Table 5.2: As Table 5.1, except depicting the graph grammar for graph representation B. There are 5 different node types, denoting vector-like doublets, vector-like singlets, SM Higgs Yukawa interactions, and dark Higgs Yukawa interactions that couple either vector-like singlets or vector-like doublets. Edges follow the pattern outlined in the Table, with 4 edge types. Note that even though two edge types, e_{DD} and e_{SS}, denote two different possible places for the fermion F to be inserted in the contraction, the graph representation is unambiguous because the particles connected to the h_D Yukawa nodes are distinguished by their dark charge Q_D.

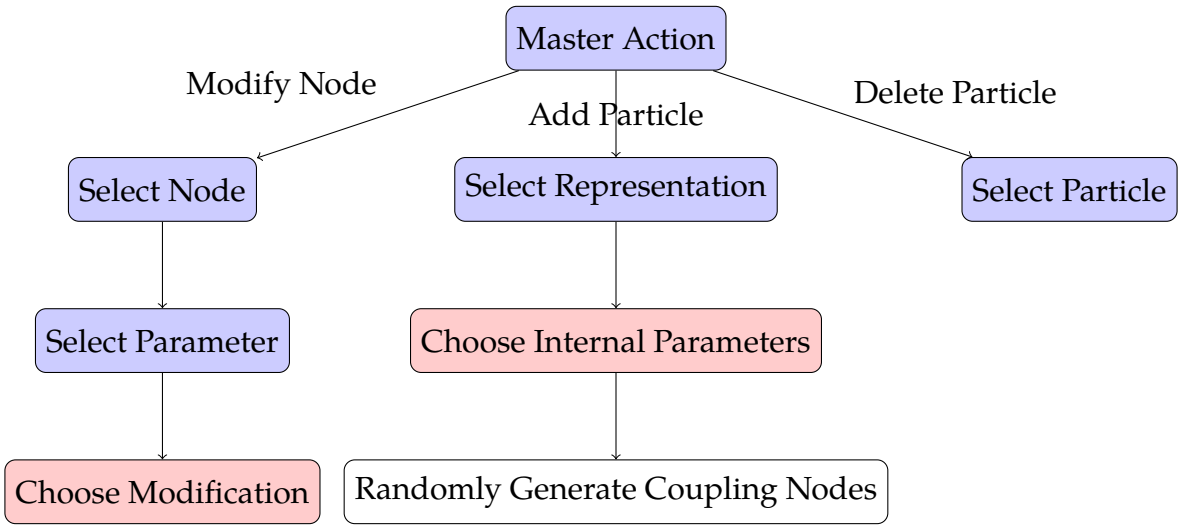

Figure 5.3: A visual summary of the structure of the action space in our reinforcement learning environment. Each blue box represents a discrete action, while red particles denote continuously-parameterized actions. The sole white box denotes random sampling with a uniform prior (thus not informed by a learned policy).

evaluation metric inspired by the Akaike Information Criterion (AIC), given as

$$K(s) \equiv \log\left(\frac{L(\text{Data}|s)}{L(\text{Data}|\text{SM})}\right) - k \times n_{\text{particles}}, \tag{104}$$

where $L(\text{Data}|s)$ is the likelihood of the model state s given the precision observables of Table 5.3, $L(\text{Data}|\text{SM})$ is the same for the SM, $n_{\text{particles}}$ is the total number of vector-like leptons which are present in the model, and k is a constant, which for our trials we take to be $k = 0.5$. At each step, the agent receives rewards based on improving on the highest score that it has received so far in the episode. In this analysis, we explore three different reward functions. The first one takes the form:

$$R_{\text{I}}(K_t, K_{\text{max}}) = \begin{cases} 0 & K_t \leq K_{\text{max}} \\ \log(K_{\text{max}}/K(s_t))/\text{max}(\log|K_t|, \log|K_{\text{max}}) & K_{\text{max}} < K_t < 0 \\ K_t + (K_t - \theta(K_{\text{max}})) & K_t > K_{\text{max}}, K_t > 0 \end{cases}, \tag{105}$$
$$K_{\text{max}} \equiv \max_{\tau<t} K_\tau,$$

where K_t is the score K of the model, as defined in Eq.(104) at timestep t. For positive K, this reward function is straightforward: For each time step where it achieves a new

maximum score, the function gives a base reward of the new score K_t, plus an additional reward equal to the difference between the current score and the maximum score achieved so far during the episode. However, as the exceptionally strong constraints on lepton flavor violation will result in potentially enormous negative K for models which don't respect lepton flavor conservation, using the same reward metric for negative K values can result in very large rewards that undermines critic network's performance. For example, eliminating a single vector-like lepton from the model which has significant mixing with both muons and electrons might result in a log-likelihood difference of more than 10^{20}. Therefore, for negative K values a proportional difference in the logs of these values are used, to reduce the rewards received while still allowing the reward function to significantly differentiate between improvements of very different magnitudes.

The second and third reward functions considered here are within a class of reward functions that reward the agent for passing certain "milestone" values instead of directly rewarding the improvement at each step. More precisely, the agent rewarded when it first exceeds certain K values in the episode. These reward functions take the following forms:

$$\begin{aligned}
&R_{IIa}(K_t, K_{\text{max}}) = \theta(K_t - K_{\text{max}}) \sum_j [j\theta(K_t - m_i) - j\theta(K_{\text{max}} - m_i)], \\
&R_{IIb}(K_t, K_{\text{max}}) = \theta(K_t - K_{\text{max}}) \sum_j [j\theta(K_t - m'_i) - j\theta(K_{\text{max}} - m'_i)], \\
&\vec{m} \equiv [-10, -5, -2, 1, 2, 3, 4, 5, 6, 7, 8]. \\
&\vec{m}' \equiv [-10^{15}, -10^{10}, -10^5, -100, \vec{m}].
\end{aligned} \tag{106}$$

R_{IIa} and R_{IIb} share the same philosophy for assigning rewards, but R_{IIb} is more generous, rewarding improvements even to models with poor scores.

To ensure that our expected rewards follow the Markov property, the state space is supplemented with K_{max} at each step. As the number of steps in an episode is truncated, we also include the number of steps that the agent has already taken as a state variable. In addition to the intermediate rewards, the agent receives a reward of $+100$ for achieving a sufficiently viable terminal state to conclude the episode early. We define a terminal state as

$$\begin{aligned}
&K(s_{\text{terminal}}) \geq 9 - 2k, \\
&k = 0.5 \rightarrow K(s_{\text{terminal}}) \geq 8.
\end{aligned} \tag{107}$$

Observable	Definition	Value	Source
M_W	W boson mass	80.377 ± 0.012 GeV	[15, 184, 205–214]
$BR(W \to e\nu)$	W partial width	0.1071 ± 0.0016	[15, 215–219]
$BR(W \to \mu\nu)$		0.1063 ± 0.0015	
$BR(W \to \tau\nu)$		0.1138 ± 0.0021	
R_e	Z partial width ratio (hadrons to leptons)	20.804 ± 0.050	[15, 220–223]
R_μ		20.784 ± 0.034	
R_τ		20.764 ± 0.045	
A_e	Z pole electron asymmetry parameter	0.1515 ± 0.0019	[15, 224–230]
A_μ		0.142 ± 0.015	[15, 225]
A_τ		0.143 ± 0.004	[15, 224–228]
$A_{FB}^{(0,e)}$	Z pole forward-backward asymmetry	0.0145 ± 0.0025	[15, 220–223]
$A_{FB}^{(0,\mu)}$		0.0169 ± 0.0013	
$A_{FB}^{0,\tau}$		0.0188 ± 0.0017	
Δa_e	lepton anomalous magnetic moment	$(-8.8 \pm 3.6) \times 10^{-13}$	[231]
Δa_μ		$(2.51 \pm 0.59) \times 10^{-9}$	[5, 21–42]
y_μ	muon Yukawa coupling	1.12 ± 0.2	[15, 232, 233]
y_τ	τ Yukawa coupling	0.94 ± 0.07	
$BR(\mu \to e\gamma)$	$\mu \to e\gamma$ branching fraction	$< 4.2 \times 10^{-13}$	[234]
$BR(\tau \to e\gamma)$	$\tau \to e\gamma$ branching fraction	$< 3.3 \times 10^{-8}$	[235]
$BR(\tau \to \mu\gamma)$	$\tau \to \mu\gamma$ branching fraction	$< 4.2 \times 10^{-8}$	[236]
$\Gamma_{\text{Au}}^{\text{conv}}/\Gamma_{\text{Au}}^{\text{capt}}$	$\mu - e$ conversion in gold nuclei	$< 7 \times 10^{-13}$	[237]

Table 5.3: The physical observables used in our analysis. Upper limits are quoted as 90% CL bounds.

The action space $\mathcal{A}$ consists of a series of hierarchical actions, in which top-level decisions about modifications that the agent can make are parameterized by a number of sub-decisions. The detailed construction of the action space is dependent on the graph grammar (A or B) chosen. While the structure of action space of the two graph grammars are quite different, we can generally summarize the three classes of actions as follows:

- **Delete a particle:** If selected, the agent has the associated sub-action of specifying particle to delete. Once the particle is deleted, all coupling nodes that are associated with it are also automatically deleted.

- **Add a particle:** If selected, the agent must make discrete decisions about the electroweak representation (singlet or doublet) of the new particle and its $U(1)_D$ charge (-1, 0, or $+1$). The agent must select the four continuous features describing a particle

node (its mass and its Yukawa couplings to the SM leptons). The Yukawa couplings between the new particle and the BSM particles already in the model are sampled randomly from $O(1)$ parameters, and may be modified by agent actions.

- **Modify a continuous feature on an existing node:** If selected, the agent first selects a node (either coupling or particle) to modify, and then the parameter of that node to modify. Finally, it selects a numerical modification to be made to that parameter.

The structure of the action space of these three classes of actions is shown in Figure 5.3. The action space is highly hierarchical, a structure which is not supported by all reinforcement learning algorithms. However, the H-PPO reinforcement learning algorithm [238] is expressly designed to learn policies over such an action space, and so we select it in implementing our environment. Details on H-PPO are presented in Appendix C.

Our policy π_θ over these actions is parameterized by a neural network which takes the environment state as an input, and outputs a prediction for the long-term rewards that the agent can expect from the state over the course of the episode and probability distributions from which actions can be sampled. For each continuous action parameter, the agent must output both a mean and a variance, which together define a normal distribution from which a continuous action parameter is sampled. For each discrete action parameter, the agent must output a log-probability associated with each choice, which defines a probability over the discrete options from which the action is sampled. In the terminology of graph neural networks, different action parameters are node-level and graph-level outputs, depending on the action parameter in question. To accommodate large hierarchies between parameters while allowing the neural network to process only $O(1)$ inputs, we represent magnitudes such as the model evaluation score and the various Yukawa couplings in scientific notation to the agent's neural network (for example, a feature with a value 0.02 will be passed as a length-two vector $\{2., -2\}$, where the first parameter is a continuous $O(1)$ value and the second is a discrete exponent). This scientific notation representation allows the action space to include modifications of either the exponential or continuous part of model parameters. Further details involving our neural network implementation, including the manner in which supplementary state data (such as the current maximum episode score and the number of steps the agent has already taken) are handled are discussed in [58].

5.4 Results

We implement a customized learning environment built with the Python library gymnasium [239] and the graph neural network using the library Pytorch Geometric [240]. To obtain RL trajectories, we randomly sample 32 parallel environments from the model space. We limit our model space by requiring all vector-like leptons to have a mass of ≥ 1.5 TeV (easily consistent with current LHC constraints on vector-like leptons [3, 160, 241–244]) and require that these particles be no heavier than 7 TeV (which might be achievable via pair production at a $\sqrt{s} \sim 14$ TeV future lepton collider). For simplicity, we assume that all Yukawa coupling constants are real, but may have either positive or negative sign, and, we generally restrict them to have a magnitude between 10^{-10} and 10. The SM Higgs Yukawa coupling constants which mix the SM leptons with zero dark-charge vector-like leptons are required to have magnitudes between 10^{-12} and 0.1 to avoid parameter regimes in which the SM leptons' mixing with the BSM states can become large. Though our graph architecture allows for arbitrarily large particle content in principle, we limit the number of additional BSM particles because the complexity of the numerical likelihood calculation will increase polynomially with larger numbers of such particles, simply in order to slightly accelerate computation time. We also incentivize simplicity by defining the terminal state to have the minimal number of BSM states, which here will be at most two new vector-like states, consistent with Eq. (107).

The agent then evolves the model according to its policy for 50 time steps before being trained according to the H-PPO algorithm, after which point it will continue. Episodes that have not attained a terminal state will end after 250 total steps. Each agent is trained simultaneously over the 32 parallel environments, and continued until 1000 rounds of 50 steps each have been completed– the agent therefore samples 1.6 million models over the course of its training. We record all terminal states that the agent produces over the course of its training. To reduce tje significant variance in performance due to initial trajectories (which depend on the initial training model states, the agent's initial weight parameters, and the random sampling from the agent's policy probabilities early in training), we also perform each run 10 independent times with 10 independent initializations.

To qualitatively assess the agent's sensitivity to various training factors, the agent's performance is compared with different choices across the following six factors:

- **Graph Representation:** We consider both graph grammar A and B, as described in Section 5.2.

- **Skip Layers:** A potential concern in multi-layer graph neural networks is the loss of any difference between graph nodes after several layers of message-passing. To assess this effect, we compare the performance of agents with and without what are known as "skip layers." In implementing these skip layers, we supplement the existing neural network architecture by appending each node's original feature vectors to their transformed feature vectors at certain layers. These skips are performed at two points: (i) immediately after the neural network's shared message-passing layers complete their transformations, and (ii) onto the final node feature vectors.

- **Training Epochs:** As discussed in Appendix C, this hyperparameter controls the number of training epochs performed at each step of the H-PPO algorithm. A larger number of training epochs allows the agent to extract a greater amount of information out of each set of sampled trajectories that it collects, at the cost of potentially biasing the agent toward overtraining on its latest training sample, which may suffer from statistical errors in the algorithm's estimation of expected reward.

- **Intermediate Rewards:** The agent always receives a reward of $+100$ for finding a terminal state and a reward of -1 for taking a forbidden action (an action that cannot be executed sensibly in the model space, such as reducing a parameter when it is already at its minimum value or removing a particle when only one BSM particle remains in the model). The structure of intermediate rewards varies following the the forms given in Eqs.(105) and (106).

- **Entropy Regularization:** The coefficient β, discussed in Appendix C, is a training hyperparameter that controls the degree to which the agent is incentivized to explore new parameter spaces or exploit already useful parameter spaces. A higher value of β provides a larger reward for agent outputs with higher entropy, so higher β incentivizes greater exploration over exploitation. We scan over the values $\beta = 0.001, 0.01, 0.05, 0.1, 0.2, 0.5$.

- **Reward Normalization:** Since rewards can attain large magnitudes, in other tasks it is useful to limit the magnitude of the rewards that the agent receives [245]. We compare the results of running trials without a reward normalization scheme to trials in which we include a normalization on both the immediate rewards that the agent receives and the critic's estimates of the cumulative total reward that the agent expects over the course of a single episode.

Other hyperparameters not mentioned are kept constant for all scans. Although this scan does not comprehensively explore all possible choices, it sufficiently helps to probe several factors of interest. The first three choices focus on how altering the neural network's architecture and learning process affects outcomes. Graph representation A is simpler than B, allowing us to explore the benefits of grouping similar parameters as the same features in a BSM model graph. Implementing skip layers helps us understand the impact of possible information loss over the course of our message-passing layers. The number of training epochs indicates the advantages and disadvantages of extracting more information from each training example in our action space. The latter three choices alter the loss function that the agent optimizes rather than the neural network directly. Modifying the intermediate reward structure and entropy regularization constant reveals the sensitivity of the agent's performance to different reward structures. Examining the effects of normalizing the environment's rewards allows us to assess whether our task benefits from calibrating reward magnitudes to values more suitable for a neural network.

We now present the results of our reinforcement learning scans. We find that our technique proves to be effective in generating viable models. Depending on hyperparameter selections, agents may achieve as few as several terminal states or as many as several thousand over the course of their training. The detailed analysis of our results is discussed in the following three sections. First, as a simple elucidation of our techniques' utility, we discuss the space of viable models that the agents collectively identify, and discuss what physical insights we can glean from the results of our scans. To further explore the utility of our frameworks, we discuss the performance of two of our hyperparameter sets that were highly successful in generating a large number or diversity of viable models, and explore what further understanding of the parameter space can be extracted from the data of these scans. Finally, we explore the relative importance of the various training hyperparameters to the agent's performance.

Models Identified by the Agents

As shown in Table 5.4, our reinforcement learning agents have identified six distinct sets of new physics particle content, each with two BSM particles, which achieve a high enough evaluation score by the standard given in Eq.(107) to be labeled as terminal states.

Of the models listed in Table 5.4, we see that models 'a' and 'b' each have two vector-like leptons sharing the same (non-zero) dark charge, one being an electroweak singlet and the other being an electroweak doublet. As studied previously in [55], such scenarios are

	Number of particles					
Label	L_0	L_+	L_-	E_0	E_+	E_-
a	0	1	0	0	1	0
b	0	0	1	0	0	1
c	1	1	0	0	0	0
d	1	0	1	0	0	0
e	0	0	0	1	1	0
f	0	0	0	1	0	1

Table 5.4: The BSM particle contents for distinct chiral models.

capable of providing chirally-enhanced one-loop dark photon and dark Higgs contributions to the muon anomalous magnetic moment from the SM Higgs coupling between the two vector-like lepton representations. The sole discrepancy between 'a' and 'b' is whether the BSM fermions have dark charges of $+1$ or -1, the only two nontrivial dark charge values that we consider in this analysis. Models 'c'-'f', however, identify a new chiral enhancement mechanism. In these models, the vector-like leptons are of a single electroweak representation (either singlet or doublet), and instead differ by one unit of dark charge (one with $Q_D = 0$ and one with $Q_D = \pm 1$). Constructing a toy model representative of classes 'e' and 'f' based on electroweak singlet vector-like leptons, it is straightforward to see that the correction to the SM prediction for the muon magnetic moment is of the form:

$$a_\mu^{e,f} \approx -\frac{m_\mu^2}{16\sqrt{2}\pi^2}\frac{M^{L,\pm}}{m_\mu}\frac{\lambda_{E,\mu}^{\pm}\lambda_E^{\pm 0}v_D^2}{(M^{E,\pm})^2}\frac{y_{E,\mu}^0 v}{M^{E,0}}. \tag{108}$$

Intuitively, this chiral enhancement occurs in models 'e' and 'f' because the left-handed SM leptons mix primarily with the $Q_D = 0$ vector-like lepton, through couplings with the SM Higgs, while right-handed SM leptons mix primarily with the $Q_D = \pm 1$ vector-like lepton. A chirality-flipping operator that generates a magnetic moment appears at leading order from the mixing between the two vector-like lepton species, from the dark Higgs Yukawa coupling $\lambda_E^{\pm 0}$. Similar constructions with electroweak doublet vector-like leptons such as models 'c' and 'd' have an analogous chiral enhancement mechanism.

The differences between these chiral enhancement mechanisms have significant implications to the model builder. Different electroweak representations of vector-like leptons will have differing production cross-sections, with vector-like electroweak doublets somewhat more tightly constrained by collider searches [130, 160]. It is known that the production of vector-like leptons with $Q_D = \pm 1$ is dominated by channels featuring a dark photon

Configuration	Graph	Skip Layers	Epochs	Reward	β	Reward Normalization
Optimal Terminal States	A	No	5	R_{IIa}	0.05	No
Optimal Distinct States	A	Yes	5	R_{IIa}	0.2	Yes

Table 5.5: The various hyperparameter selections for the two optimal configurations that we find in our analysis.

emission, rather than the emission of an SM gauge boson, and as a result have different (and generally stronger) experimental constraints than standard vector-like leptons with $Q_D = 0$. These models suggest different UV completions: Models 'a' and 'b' may arise in left-right symmetric models, where the BSM particle content possesses states in both the electroweak singlet and doublet representations. Models 'c'-'f', which have vector-like leptons in the same electroweak representations, might arise within grand unified theories such as E_6.

Scan Performance: Optimal Configurations

We now turn to discussions of scan performance. We start by deferring a detailed discussion of our various hyperparameter selections and instead consider two specific "optimal" (by different metrics) configurations: (i) one which, averaged over ten independent trials, produces the largest total number of terminal states ("optimal terminal states"), and (ii) one which achieves the largest number of models with distinct particle content ("optimal distinct states") over the course of a single run (averaged, again, over ten independent trials). In Table 5.5, we summarize the selections for the various training hyperparameters for both scans. The results of all ten independent scans for each configuration are then summarized in Table 5.6.

Table 5.6 clearly shows that there is a significant trade-off in the scan hyperparameters between configurations that maximize the number of terminal states that are generated and those that maximize the number of distinct particle contents that are found. The optimal terminal states configuration produces on average two orders of magnitude more terminal states than the optimal distinct states configuration, however the optimal distinct states configuration either finds all 6 viable particle contents that are represented collectively in the scan, or finds 5 of them– in stark contrast to the optimal terminal states configuration which never identifies more than 4.

Apart from identifying the number of distinct models that both configurations produce, we can also extract how the different viable particle contents are distributed among the terminal states that each model produces. In Figure 5.4, we show stacked histograms over

	Optimal Terminal States		Optimal Distinct States	
	Terminal States	Distinct States	Terminal States	Distinct States
Trial 1	9559	2	131	6
Trial 2	10246	4	69	5
Trial 3	5578	3	33	6
Trial 4	8182	2	150	5
Trial 5	4377	3	57	6
Trial 6	5750	3	49	6
Trial 7	8917	2	29	6
Trial 8	4473	4	89	6
Trial 9	10171	2	82	5
Trial 10	3591	2	17	6
Mean	7100 ± 2600	2.7 ± 0.8	71 ± 44	5.7 ± 0.5

Table 5.6: The performance, including the number of terminal states identified and the number of models with distinct particle content, achieved by the two optimal agents across ten independent trials.

our 10 independent trials which show the number of viable models of each of the types outlined in Table 5.4 that the agents produce. Although individual trials in the optimal terminal states configuration invariably fail to produce all possible models, all are ultimately represented among the aggregate of all 10 independent trials. This suggests that some of the disadvantage in model diversity that the optimal terminal states configuration exhibits in comparison to the optimal distinct states configuration can be mitigated simply by repeated scans. However, this technique is not perfect. In particular, we see that across both configurations, the agents preferentially sample models 'c'-'f' (namely, those which have one $Q_D = 0$ and one $Q_D = \pm 1$ vector-like lepton of the same electroweak representation) over models 'a' and 'b' (those models which rely on one electroweak doublet lepton and one electroweak singlet, which share a dark charge of $Q_D = \pm 1$). The hierarchy is far more pronounced in the case of the optimal terminal states configuration, however, where for example only a single terminal state of configuration 'b' is produced across all 10 scans.

We now discuss the parameter space of terminal states. Since the number of total terminal states in the optimal distinct states configuration is limited, for this component of our analysis we shall restrict ourselves to the optimal terminal states configuration, where thousands of models have been sampled. In Figure 5.5 we show a histogram of the corrections to Δa_μ which appear in the terminal states for our "optimal terminal states" configuration. We see that the terminal states of the model roughly uniformly sample an area that is around $1/3$ of a standard deviation from the central value of the anomaly. This

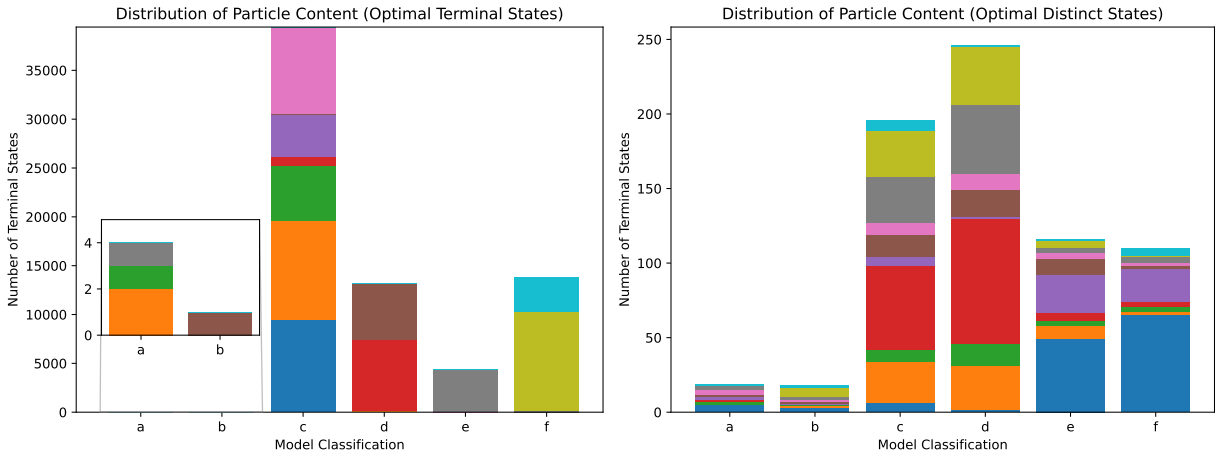

Figure 5.4: Stacked histograms of the different models, following the naming convention in Table 5.4, achieved by the agent over 10 independent trials for the optimal terminal states configuration (left) and the optimal distinct states configuration (right). Different colors denote the contributions of individual trials.

range coincides quite precisely with the model score cutoff of Eq.(107) that we use to define terminal states. Calculating the change in the model score from addressing the muon magnetic moment anomaly exactly, and ignoring the effects of all other observables, we find that a two-particle theory will produce a model score above the cutoff value for a model which recreates the observed muon anomalous magnetic moment to within $\sim 0.31\sigma$. The fact that the number of terminal states drops off sharply outside of this range suggests that the agent is not capable of precisely recreating the observed anomalous magnetic moment correction to within this precision, since it does not appear to have a strong preference for producing states near the central value, as would be anticipated given the fact that various model parameters are selected stochastically, and the agent is incentivized to maximize the probability of sampling within the desired range for Δa_μ. Instead, a much broader range of values for Δa_μ are likely achieved by the agent's actions, which are then subject to a sharp cutoff when we collect only the terminal states.

Inspecting individual parameter values, we can learn about the constraints on these models from the distributions of continuous parameters. As an example, we consider the BSM leptons' Yukawa couplings with the electron, which in theory need only be below a particular order of magnitude to avoid lepton flavor violation constraints. In Figure 5.6, we depict histograms of the various BSM leptons' Yukawa couplings with the electron in the terminal states, which are visually consistent with normally distributed sampling of the $O(1)$ value around a value with a *fixed* order of magnitude. The sharp cutoffs in

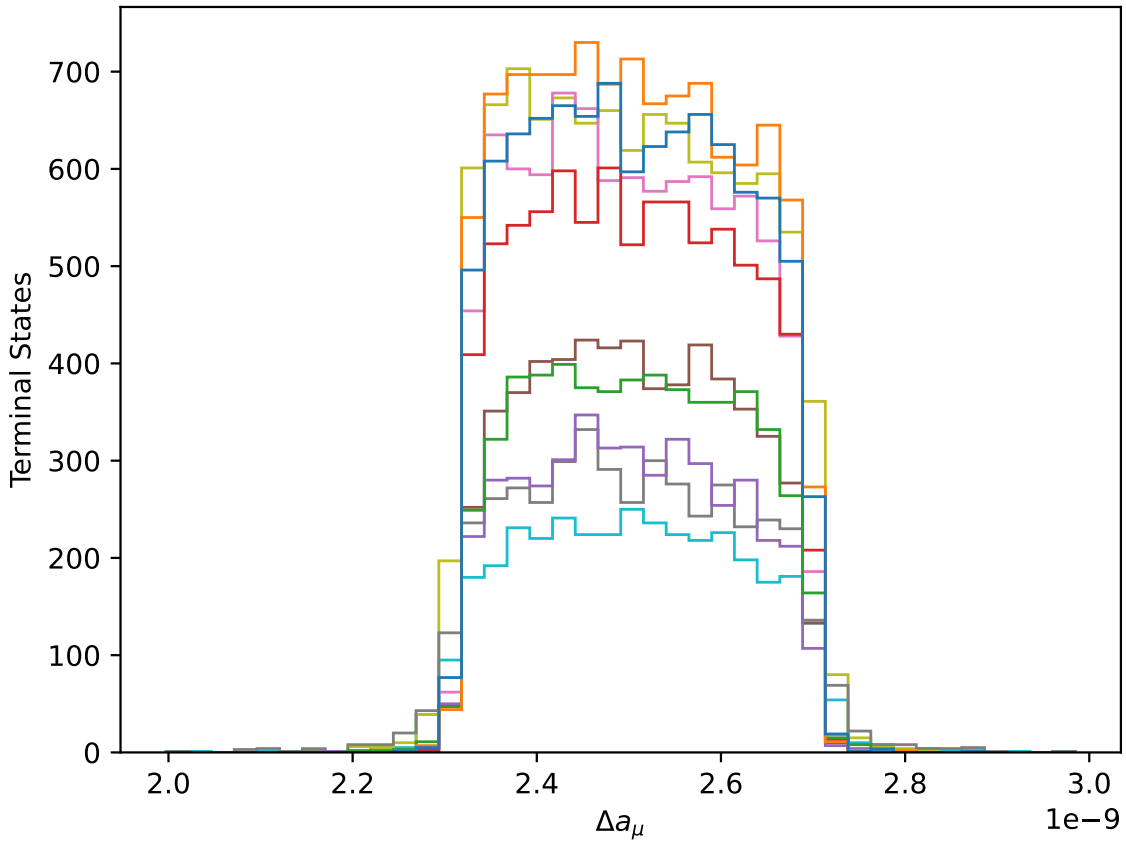

Figure 5.5: A histogram of the correction to the muon anomalous magnetic moment, Δa_μ, in different models generated as terminal states from the "optimal terminal states" configuration of our reinforcement learning scan, described in Table 5.5. Different colors denote the results of different independent trials using the same hyperparameters. Recall that our numerical likelihood calculations use the experimental data up through [5], which suggests $\Delta a_\mu = (2.51 \pm 0.59) \pm 10^{-9}$.

the distributions for two of the trials suggest that a higher order-of-magnitude parameter, near the boundary of the experimental constraints, is preferred in these scans. The fact that such a sharp cutoff exists for these trials indicates that the agent still has difficulty estimating parameters beyond the $O(1)$ level, but it also does provide a numerical sense of the constraints on these couplings.

A further lesson from Figure 5.6 is that the form of the distribution of model parameters depends strongly on the design of the action space. For example, we note that consistently across independent trials, the agent selects (for its terminal states) BSM-to-electron Yukawa couplings on the order of 10^{-7} for those to the SM Higgs, and 10^{-5} for those to the dark Higgs, in spite of the fact that significantly lower (indeed, down to the model space's

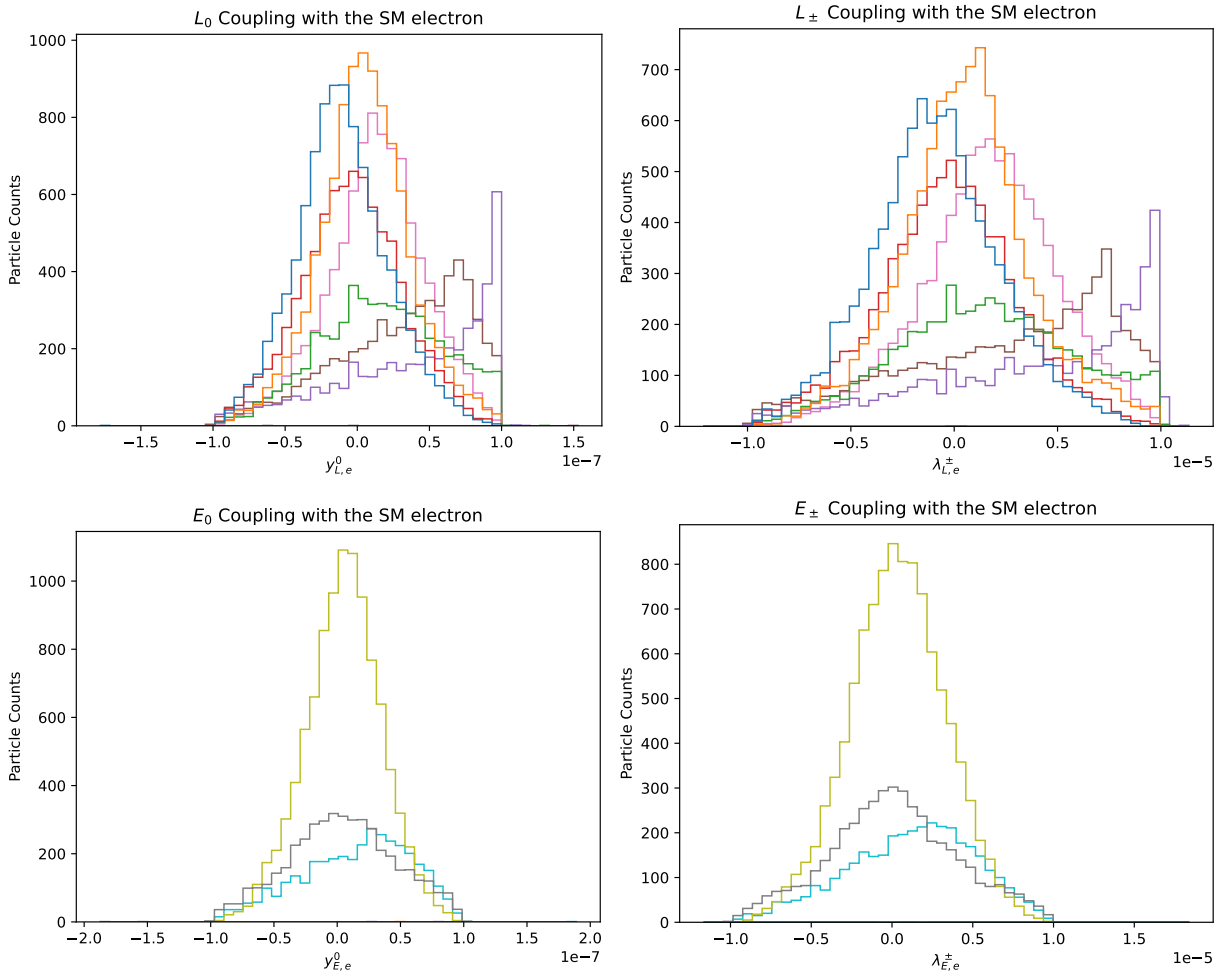

Figure 5.6: Histograms of vector-like leptons' Yukawa couplings with electrons for different trials in the optimal terminal states hyperparameter configuration. The histograms depict $y^0_{L,e}$ (top left), $\lambda^\pm_{L,e}$ (top right), $y^0_{E,e}$ (bottom left), and $\lambda^\pm_{E,e}$ (bottom right). Different colors denote different independent trials.

magnitude cutoffs of 10^{-12} and 10^{-10}, respectively) orders of magnitude are phenomenologically viable. The reason for the agent selecting these magnitudes, as opposed to lower ones, is unclear, and is likely an artifact of specifics of our implementation. The broader implication is that the population of terminal states from a reinforcement learning scan represents a nontrivially distributed sample of the viable model parameter space which may not readily match a theorist's priors on a given parameter (such as the expectation that a Yukawa coupling might be zero or loop-suppressed). The reinforcement learning agent can readily produce examples of viable models that a theorist might use as inspiration, but the distribution of terminal states in the parameter space that it finds can be subject to a number of factors unrelated to the underlying physics of the problem. It may be that the more valuable metric for the model builder is the number of distinct models (with different particle content) that a scan produces, i.e., a model builder is more likely to value the optimal *distinct* states hyperparameter configuration over the optimal *terminal* states configuration.

Scan Performance: Comparing Hyperparameter Choices

We shall now discuss the impact of different training factors on the agent's performance. Again, we will evaluate the agent's performance using the two introduced performance metrics: "optimal terminal states" and "optimal distinct states." As discussed in Section 5.4, for practical use cases maximizing the total number of terminal states is less useful as a performance target than maximizing the number of distinct states, but the number of terminal states is still important, since reaching a terminal state in our context is equivalent to finding a viable BSM model. Although this metric cannot measure the diversity of the terminal states, it measures the frequency at which these states are attained and can thus serve as a measure of the agent's ability to explore the continuous part of the parameter space and therefore learn effectively. As shown in Table 5.4, the distinct states here are defined as distinct combinations of 2 isospin singlet or doublet particles that carry different dark $U(1)$ charges and have significant chiral enhancements contributing to the muon anomalous magnetic moment. There are only 6 such combinations for this simple vector-like lepton model, given that we want our terminal states to be models with at most two BSM fermions. Qualitatively this metric serves as a measure of the agent's ability to explore the discrete action space and identify distinct promising models which might be further explored through other means.

In Figure 5.7, the total number of terminal states and distinct states, averaged over

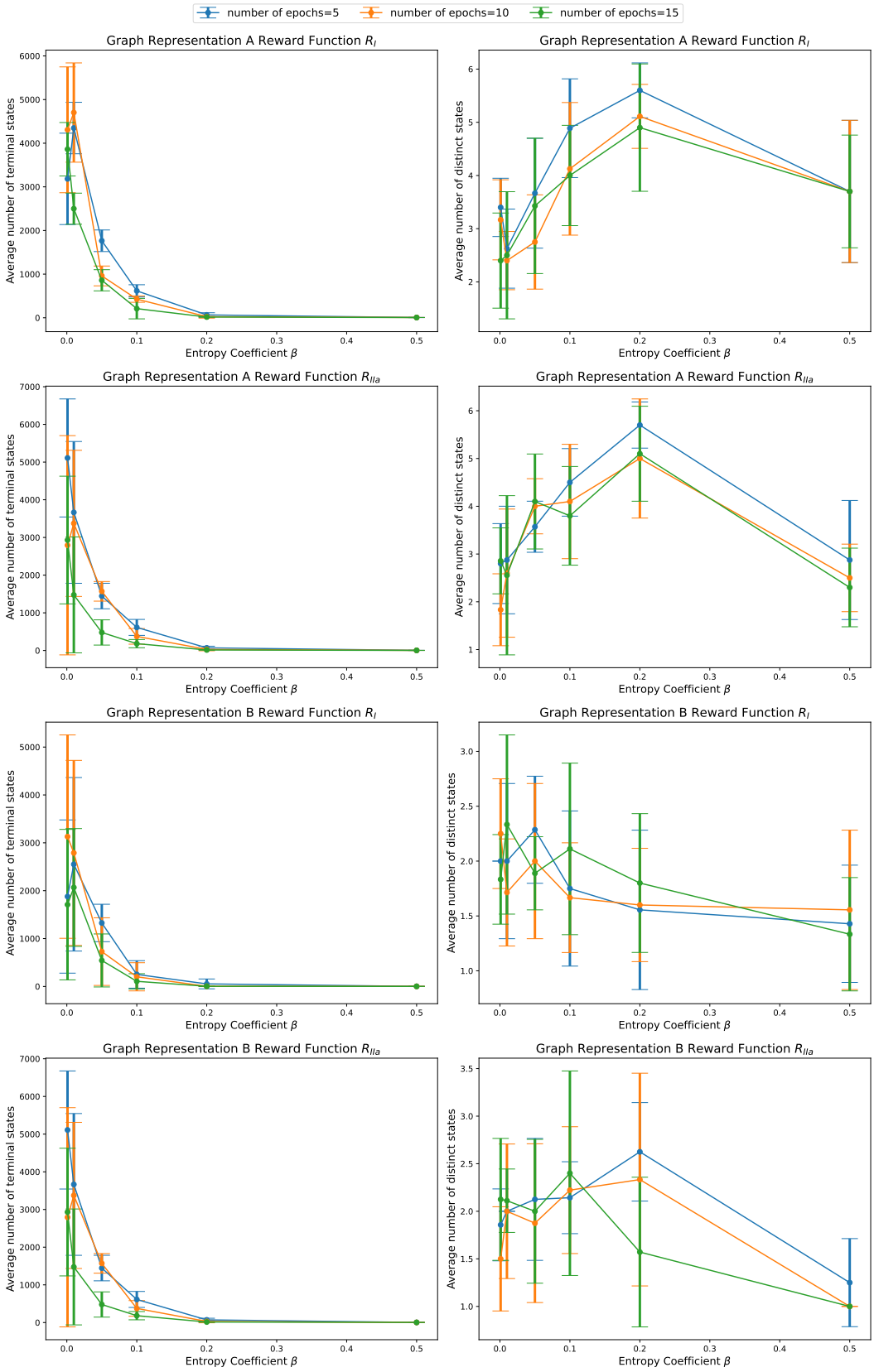

Figure 5.7: The number of terminal states (left) and distinct states (right), obtained as the mean of 10 independent trials for each data point, with standard deviation as a function of the entropy coefficient β for both graph representations A and B and reward functions R_I and R_{II}

10 independent identical trials for each hyperparameter configuration, are plotted for both graph representation A and B and reward function R_I and R_{IIa}, as a function of a scan of entropy coefficient $\beta = 0.001$, 0.01, 0.05, 0.1, 0.2, 0.5. These values are taken for experiments with different numbers of training epochs, and with skip layers and reward normalization implemented. Out of the 10 different independent experiments for each number of epochs, the experiments that return null results are excluded – this principally affects the results of trials with graph representation B. It is clear that both performance metrics depend on the choice of entropy coefficient β. This dependency is particularly strong for the average total number of terminal states. For both graph representation with both reward functions, we can see that the average total number of terminal states peaks at around $O(0.001 - 0.01)$. This is unsurprising: If it has a low entropy coefficient, an agent will have a strong incentive to output probability distributions that are heavily weighted toward states which it has previously seen yield high rewards, and therefore will be likely to produce a large number of terminal states, as long as it finds at least one before its training is completed. Despite being the optimal range for finding maximum average total number of terminal states, this range is not optimal for finding the average total number of distinct states, a metric which clearly favors exploration of the model space over exploitation of known regions. For graph representation A, $\beta \sim 0.2$ seems to be optimal for both reward functions. In contrast, for graph representation B, the performance is comparable for $\beta = 0.001, 0.01, 0.05, 0.1, 0.2$– we might attribute this to the fact that the total magnitude of the number of discrete states is somewhat smaller for trials in representation B and may therefore be more sensitive to statistical fluctuations. An important message is that depending on the task and performance metric to be optimized, we should always tune on the entropy coefficient β. For the remainder of this section, we always optimize the entropy coefficient while presenting results and discussing the roles of other factors.

In Figure 5.7, we can also see that both the average total number of terminal states and distinct states possess a large standard deviation over the trials, as depicted in the error bars around each point. This indicates that the results are very sensitive to the initial starting conditions, and hence each experiment with the same set of hyperparameters selection can return very different results.[18] For the total number of distinct states, graph

[18]For practical implementations of this graph-based reinforcement learning strategy, this sensitivity means that ensuring reproducibility between runs can be difficult. In particular, the PyTorch machine learning library's random number generation utilities will produce different random sequences even when passed the same seed when operating on different machines, even when computations are not performed on a CPU. For best practices, we recommend maximizing the number of independent trials when exploring a model space in order to defray this sensitivity.

representation B generally has a larger standard deviation than graph representation A, which indicates that the agent's performance is even more sensitive to the starting condition. This is probably due to the fact that in representation B, different particles (electroweak isospin doublets and singlets) are represented as different node types, resulting in more separate weights to be learned. From the figure, it is also clear that graph representation A generally finds more terminal states and distinct states than graph representation B, regardless of the type of reward function used.

Table 5.7 shows the total number of terminal states and distinct states with or without the implementation of skip layers and/or reward normalization, averaged across 10 independent trials with non-null results, when the optimal value of entropy coefficient β is chosen across each metric. Here we neglect the fact that results for different β are very different, as our aim is just to examine the overall effects of the implementation of skip layers and reward normalization. An immediate observation is that these parameters (skip layers, reward normalization) can have an impact on the results, but the amount of impact depends non-trivially on the global selection of other discrete hyperparameters. For example, looking at the total number of terminal states for the optimal case, the agents always found more terminal states when there was no reward normalization. However, depending on the choice of reward function and the number of epochs, the implementation of skip layers may be favorable or not, so again different performance metrics are sensitive to different choices of hyperparameters. If we instead consider the optimal total number of distinct states, graph representation A always found the most number of distinct models when skip layers and reward normalization were both implemented, while for graph representation B, the optimal result varies non-trivially with different choices of the number of epochs and the reward function.

In addition to showing the results of selecting different optimal β for each set of experiments with different hyperparameter settings, we also present Table 5.8, in which the number of training epochs is 10, and the entropy coefficient $\beta = 0.2$ is selected for representation A and $\beta = 0.001$ is selected for representation B, averaged over 10 independent identical trials with null results excluded. For this set of data with a fixed β value chosen across the four architecture choices (with/without skip layers and/or reward normalization), it clearly shows no consistent behavior in the dependency on skip layers and reward normalization for different choices of graph representations and reward functions, except that for reward function R_I and R_{IIa}, representation A performs the best when both are implemented. This further justifies our claim that these two architecture choices are very

				Number of terminal states		Number of distinct states	
Epochs	Reward	Skip Layers	Reward Normalization	Representation A	Representation B	Representation A	Representation B
5	R_I	No	No	7756.0	6368.3	3.5	2.3
		Yes	No	6101.8	4827.2	3.7	2.0
		No	Yes	5690.4	3847.0	4.7	2.0
		Yes	Yes	4348.1	2551.4	5.6	2.3
	R_{IIa}	No	No	8229.3	6453.3	2.9	2.3
		Yes	No	6345.0	6314.4	3.7	2.1
		No	Yes	5715.0	2201.3	3.8	1.9
		Yes	Yes	5109.6	3540.9	5.7	2.6
	R_{IIb}	No	No	4932.0	4477.0	3.3	2.3
		Yes	No	6322.1	6011.0	3.9	2.2
		No	Yes	4376.0	1294.4	3.6	1.7
		Yes	Yes	4230.2	3361.5	5.2	2.0
10	R_I	No	No	4691.8	5866.0	4.5	2.0
		Yes	No	6975.7	3929.3	3.0	1.9
		No	Yes	3734.2	3189.0	4.3	2.2
		Yes	Yes	4702.8	3129.5	5.1	2.3
	R_{IIa}	No	No	5423.9	3086.7	3.1	2.3
		Yes	No	4922.4	5271.8	4.3	2.1
		No	Yes	3478.2	3344.0	4.0	2.2
		Yes	Yes	3373.6	2230.4	5.0	2.3
	R_{IIb}	No	No	3960.1	4240.2	4.1	2.0
		Yes	No	4842.0	4216.4	4.3	2.4
		No	Yes	1018.2	794.0	4.0	2.0
		Yes	Yes	4647.0	2698.7	4.4	2.0
15	R_I	No	No	4154.3	3718.0	3.9	2.0
		Yes	No	4359.2	3310.9	3.7	2.0
		No	Yes	3440.9	1642.0	4.1	2.0
		Yes	Yes	3861.8	2067.2	4.9	2.3
	R_{IIa}	No	No	4510.3	2315.9	3.5	2.2
		Yes	No	3746.3	3160.5	4.0	2.2
		No	Yes	1557.2	1970.2	3.9	2.0
		Yes	Yes	2931.7	1813.0	5.1	2.4
	R_{IIb}	No	No	3034.1	2262.0	3.3	2.3
		Yes	No	2304.9	2576.3	4.3	2.2
		No	Yes	2432.8	821.3	3.5	2.0
		Yes	Yes	1740.1	2015.3	3.8	2.0

Table 5.7: The number of terminal states and distinct models with/without the implementation of skip layers and/or reward normalization, for different number of epochs and reward functions, when the optimal value of entropy coefficient β is picked across each metric, in graph representations A and B.

model-dependent. Therefore, any other model building and analysis similar to this project should experiment with these techniques to see if they truly improve the results before deploying them.

From Tables 5.7–5.8, if we compare the performance of the agent with the same hyperparameter settings but different choices of reward functions, we see that the results are insensitive to the selection of the reward function. In fact, comparing all the results, we

find that each reward function might have its own set of optimal hyperparameters that maximize both or one of the performance metrics. However, for most of the hyperparameter ranges that we have covered, both graph representations has reasonable performance under all three reward functions, so fine-tuning is not necessary.

			Number of terminal states		Number of distinct states	
Reward	Skip Layers	Reward Normalization	Representation A ($\beta = 0.2$)	Representation B ($\beta = 0.001$)	Representation A ($\beta = 0.2$)	Representation B ($\beta = 0.001$)
R_I	No	No	11.7	5866.0	4.5	2.0
	Yes	No	1828.4	3929.3	3.0	1.8
	No	Yes	8.6	2623.7	4.3	2.2
	Yes	Yes	24.8	3129.5	5.1	2.3
R_{IIa}	No	No	1429.9	2588.9	3.0	2.3
	Yes	No	3608.8	5271.8	3.4	2.0
	No	Yes	7.9	2559.6	4.0	2.2
	Yes	Yes	29.0	2093.2	5.0	1.5
R_{IIb}	No	No	1634.7	3105.2	4.1	1.8
	Yes	No	1914.7	4216.4	2.7	2.4
	No	Yes	3.5	794.0	2.3	1.4
	Yes	Yes	8.8	2698.7	3.9	2.0

Table 5.8: The average total number of terminal states and distinct models with/without the implementation of skip layers and/or reward normalization, for 10 epochs, and $\beta = 0.2$ for graph representation A and $\beta = 0.001$ for graph representation B.

The last factor to be discussed, and potentially the most important one, is the choice of the graph representation and how it affects the agent's performance. In Table 5.9, we select the "optimal terminal states" and "optimal distinct states" hyperparameter configurations as discussed in Section 5.4, and compare the results of these trials to trials with the same hyperparameter configurations using graph representation B. Comparing these results, it is apparent that graph representation A always outperforms graph representation B; however, this could simply be a product of the fact that our other hyperparameters have optimized the results for graph representation A. To examine the robustness of this finding, we present Table 5.10, in which we select the optimal set of hyperparameter configurations for graph representation B. We can see that for the optimal total number of terminal states, the best set of results for graph representation B slightly outperforms graph representation A, but the values final averages are easily statistically identical (albeit with graph representation B's result having a substantially lower variance). However, in terms of finding distinct states, graph representation A is always better. The best performance of the agent with graph representation B finds 5 distinct states in one out of the ten trials, while A easily finds 5-6 distinct states for all trials under its optimal hyperparameter setting. Even when

	Optimal Terminal States (A)				Optimal Distinct States (A)			
	Terminal States		Distinct States		Terminal States		Distinct States	
	A	B	A	B	A	B	A	B
Trial 1	9559	7797	2	2	131	29	6	2
Trial 2	10246	1	4	1	69	12	5	3
Trial 3	5578	0	3	0	33	7	6	2
Trial 4	8182	6620	2	2	150	0	5	0
Trial 5	4377	5069	3	2	57	6	6	3
Trial 6	5750	7600	3	2	49	0	6	0
Trial 7	8917	0	2	0	29	28	6	3
Trial 8	4473	2525	4	2	89	2	6	2
Trial 9	10171	6816	2	2	82	3	5	3
Trial 10	3591	6540	2	2	17	128	6	3
Mean	7100 ± 2600	4297 ± 3147	2.7 ± 0.8	1.5 ± 0.9	71 ± 44	22 ± 37	5.7 ± 0.5	2.1 ± 1.2

Table 5.9: The optimal performance of the agent in graph representation A, including the number of terminal states identified and the number of models with distinct particle content and the comparison between results for graph representations A and B, across 10 independent trials.

	Optimal Terminal States (B)				Optimal Distinct States (B)			
	Terminal States		Distinct States		Terminal States		Distinct States	
	A	B	A	B	A	B	A	B
Trial 1	6268	5045	2	3	14	8	4	1
Trial 2	5973	6449	3	2	41	3	4	2
Trial 3	8669	3468	2	2	217	136	2	2
Trial 4	4872	5733	3	2	115	28	5	2
Trial 5	5825	4260	2	2	100	10	4	5
Trial 6	8179	6791	5	2	203	18	5	3
Trial 7	0	4858	0	2	322	4	4	2
Trial 8	0	4684	0	2	321	6	4	2
Trial 9	5407	4814	2	2	230	7	4	3
Trial 10	5567	6467	2	2	260	4	2	2
Mean	5076 ± 2930	5257 ± 1019	2.1 ± 1.4	2.1 ± 0.3	182 ± 110	22 ± 39	3.8 ± 1.0	2.4 ± 1.1

Table 5.10: The optimal performance of agent with representation B, including the number of terminal states identified and the number of models with distinct particle content and the comparison between results for representation A and B, across ten independent trials.

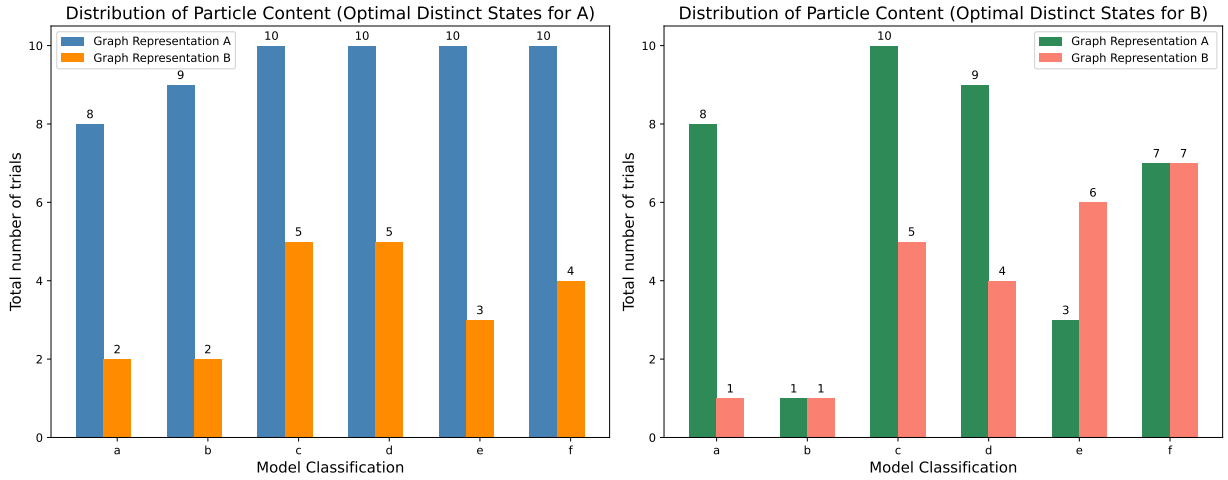

Figure 5.8: The number of times each model was achieved by the agent over 10 independent trials for the optimal distinct states configuration of graph representation A and its comparison to the results of graph representation B with the same hyperparameter settings (left). The number of times each model was achieved by the agent over 10 independent trials for the optimal distinct states configuration of graph representation B and its comparison to the results of graph representation A with the same hyperparameter settings (right).

working with B's optimal hyperparameters, the average number of distinct states that the graph representation A agent finds significantly outpaces that of the graph representation B.

The fact that graph representation A outperforms B is not surprising, as A shares weights between related parameters of isospin singlet and isospin doublet leptons, such that the agent has more information and fewer separate weights to learn. To see this, we plot the total number of trials (out of 10) in which each model appears in both representations for the hyperparameter setting that returns the optimal number of distinct states for A (left subplot) and B (right subplot) in Figure 5.8. Looking at the optimal configuration for graph representation B, the agent of B has a clear preference for models 'c'-'f', while graph representation A's agent does not. Meanwhile the difference is somewhat slighter in the optimal configuration of graph representation A, but the agent of B still somewhat favors 'c'-'f'. To further justify this finding, we show the total number of times our agents produced 'a' and 'b' terminal states compared to 'c'-'f' ones over all trials with all different hyperaparameter configurations probed with graph representation A and graph representation B in Figure 5.9. Clearly, both the A and B agents favor 'c'-'f', but the difference is much significant in graph representation B. Recalling the particle content for these models in Table 5.4, models 'c'–'f' consist of one charged and one uncharged particle under the

dark gauge group, but with the same electroweak representation, while models 'a' and 'b' consists of one doublet and one singlet that are both charged under the dark gauge group. This discrepancy between the two graph representations in the favoritism of specific models can likely be explained by the sharing of weights between isospin doublets and singlets in graph representation A. Unlike in graph representation B, the agent does not need to learn the weight for these two types of particles independently, which helps to better identify the possible connections between them.

From all the discussions and results presented with varying factors and hyperparameter settings, we conclude that the performance of the agent is strongly influenced by the graph representation and the entropy coefficient β. If a suitable graph representation that contains appropriate amount of information about the underlying physics is chosen, the agent can achieve good performance with little dependence on the other hyperparameter settings that we have probed. In this case, we can see that agent with graph representation A nearly always outperforms agent with graph representation B, regardless of the hyperparameters chosen, including regarding the choices of environment or agent architecture, such as the implementation of reward normalization or skip layers. These additional settings might help improve performance, but only with subleading effects in our study. In the case of the entropy parameter β, it is reasonably straightforward to tune this parameter via a simple scan over various values. However, choosing an appropriate graph representation for a class of BSM models is somewhat nontrivial and involves discretionary choices informed by the physics of the system. That said, in spite of the graph representation's apparent primacy, it is worth mentioning that our suboptimal graph representation (B) still successfully identified a multitude of terminal states and was capable of identifying all 6 distinct models over the course of 10 trials for multiple hyperparameter configurations. This suggests that while an effective choice of graph representation can provide a significant benefit to the agent's performance, the procedure we have outlined can achieve success without necessarily finding an optimal representation, at least for the simple model building task we have analyzed in this paper.

5.5 Summary and Conclusions

We have presented a method by which reinforcement learning can be used to explore virtually arbitrary spaces of BSM theories, defined only by the theory's symmetry group and the representations that the BSM particles might take, by leveraging the capabilities of

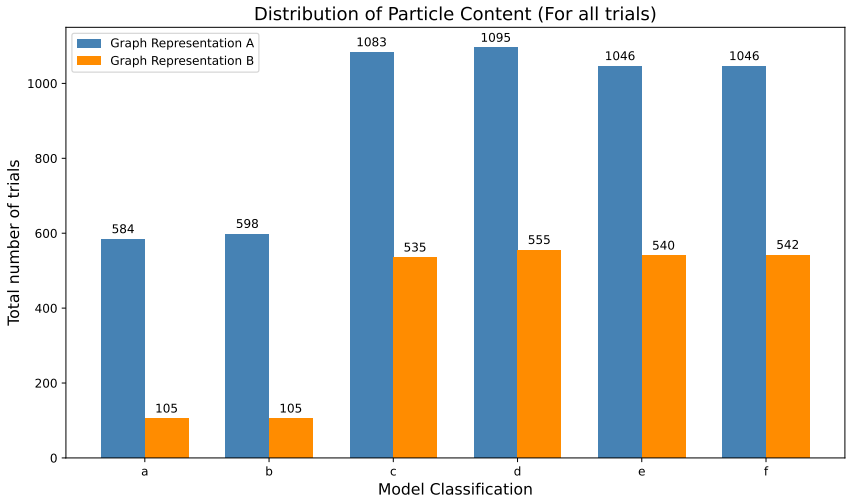

Figure 5.9: The number of times each model was achieved by the agent over all independent trials with different hyperparameter configurations we probed, for graph representations A and B.

graph neural networks. As a case study, we performed an exploration of a simple space of models described by vector-like leptons, inspired by the portal matter framework of [56, 130]. By evaluating models based on their log-likelihood difference with the SM, the agent was capable of generating both known and novel constructions which addressed the most significant experimental tension with the SM in our input data, which is the anomalous magnetic moment of the muon. The agent proved capable of generating a significant variety of these constructions, with all six feasible sets of particle content being generated in a single scan. Furthermore, the agent managed to accomplish this task in a somewhat simple, but hardly trivial environment: to identify viable parameter space points, the agent determined both discrete and continuous model parameters, and even learned hierarchical differences between model parameters in order to remain consistent with lepton flavor violation observables.

We analyzed various training hyperparameters, noting configurations that significantly influence agent performance, and proposed “best practices" for more complex tasks. Consistent with similar tasks [246, 247], intermediate rewards for improving a score over the episode maximum are effective, though the agent’s sensitivity to the specific reward function form is limited. Among the hyperparameters, the entropy regularization constant β and the graph grammar used had the most impact on scan quality, while others had limited effects. Graph representation A, with combined features (masses and SM coupling parameters of electroweak singlet and doublet vector-like leptons), outperformed representation

B by allowing greater transfer learning. Entropy coefficient β significantly influenced the number and diversity of viable models by balancing exploration and exploitation. Best practices include scanning various values and designing a graph grammar that uses the same node features for similar parameters, keeping other hyperparameters fixed. The agent's bias in sampling continuous parameters suggests that this technique may not be optimal for probing specific models' parameter spaces but excels in identifying viable particle content, offering inspiration for model-builders to consider a wider diversity of constructions.

We emphasize that although our case study is performed for a reasonably simple model, virtually any class of BSM theories might be explored through this technique, without specifying *a priori* the particle content of the model. Therefore, our graph-based approach represents a significant step in automating the process of BSM model building through reinforcement learning. As discussed in our work [58], the techniques we have outlined here also leave significant possibilities for future refinement and exploration. For example, developing an understanding of the scaling of this procedure's efficacy with more elaborate model spaces requires further experimentation, and various significant refinements, such as implementing scans of continuous parameter spaces with Monte Carlo techniques once the reinforcement agent has specified parameters' orders of magnitude, might radically improve the methodology's efficiency.

Given its generality, the development of this procedure into an automated model-building tool is a significant, but feasible, undertaking. In particular, if the generation of graph grammars for different classes of models can be automated, the large variety of automatic computing tools for BSM observables [191, 248–251] could be readily incorporated into a pipeline which rapidly implements an environment and performs these reinforcement learning scans.

Appendix C: Details on PPO and H-PPO

This Appendix discusses the mathematical details of the PPO reinforcement learning algorithm, and those of its generalization H-PPO. Leveraging a policy gradient strategy, PPO trains an agent's policy network with a constrained step size (policy updates) to find a balance between efficiency and stability. The goal of policy-gradient strategy is to find parameters θ that maximize the expected return. In the context of neural network, this parameter θ is the weights and biases of the neural network that maps actions to probability distributions. The policy will then be tuned so that "good" actions that maximize the return are sampled more frequently in the future. This goal is achieved by maximizing an objective function:

$$L^{PG}(\theta) = \hat{\mathbb{E}}_\tau\Big[R(\tau)] = \sum_\tau P(\tau;\theta)R(\tau) = \sum_\tau \left[\prod_{t=0} P(s_{t+1}|s_t, a_t)\pi_\theta(a_t|s_t)\right] R(\tau). \tag{109}$$

where the expected return $\hat{\mathbb{E}}_\tau\Big[R(\tau)]$ is the weighted average of all possible values that the return $R(\tau)$ can get. $P(\tau;\theta)$ is the probability of each possible trajectory τ as a function of parameter θ. It is determined by the state distribution, namely the possibility of state s_{t+1} getting selected from state s_t if action a_t is selected, and the policy $\pi_\theta(a_t|s_t)$, which is just the probability of the agent selecting action a_t from state s_t given our policy. Instead of calculating the actual gradient of this objective function, which requires calculating the probability of each possible trajectory, a gradient estimation is performed instead with a sample-based estimate. This objective function is also not directly differentiable since it involves differentiation of state distribution that might be unknown. Using the Policy Gradient Theorem, it can be shown that the gradient of the objective function can be re-expressed into this form:

$$\boldsymbol{\nabla}_\theta L^{PG}(\theta) = \hat{\mathbb{E}}_t\Big[\boldsymbol{\nabla}_\theta \log \pi_\theta(a_t|s_t)R(\tau)\Big]. \tag{110}$$

where the expectation $\hat{\mathbb{E}}_t$ is the empirical average over a finite batch of samples. Now the weight of the policy is updated following the direction of $\boldsymbol{\nabla}_\theta \log \pi_\theta(a_t|s_t)$; this is the direction of steepest increase of the log probability of selecting action a_t at state s_t scored by the return.

In an actor-only method that depends solely on policy gradient, the gradient estimator may have a large variance. This is due to the fact that the return (long-term cumulative

reward) used to score the log-probability of state-action pair can have very different values in a stochastic environment with a stochastic policy. In this case, an actor-critic approach could be employed to mitigate this large variance problem, and could thus lead to faster convergence of the algorithm. To demonstrate this, let's start by introducing a function $V(s_t)$, which is the state value that estimate the expected return of being in state s_t:

$$V(s_t) = \hat{\mathbb{E}}_\tau \Big[R_t | s_t \Big] \tag{111}$$

A critic network can, if passed a state s_t, be trained to estimate this value function. Then to compute the policy gradient, we can define a state action value $Q(s_t, a_t)$, also known as Q-function, which is the expected return of taking action a_t in state s_t under the current policy. If the trajectory of agent interacting with its environment is recorded over T time steps, $Q(s_t, a_t)$ takes the following form:

$$Q(s_t, a_t) = \hat{\mathbb{E}}_\tau \Big[R_t | s_t, a_t \Big] = r_t + \gamma r_{t+1} + \cdots + \gamma^{T-t-1} r_{T-1} + \gamma^{T-t} V(s_T) \tag{112}$$

where $\gamma \leq 1$ is the discount factor that gauge the importance between immediate and future rewards – if γ is small, the agent will prioritize immediate rewards, since far-future rewards will contribute less to Q, while if γ is large, the agent will be more responsive to longer-term rewards. $V(s_T)$ is the state value estimated at the terminal state s_T of the trajectory. Introducing Q-function of this form with the discount factor enables us to look a finite number of steps ahead and still anticipate long-term rewards, yet reduce variance by down-weighting future rewards that corresponds to delayed effects (at the expense of introducing bias into our estimator of cumulative rewards over an episode, which increases with smaller γ) [252]. We can reduce the variance even further by introducing the advantage function, which is a measure of the relative advantage for taking action a_t at state s_t compared to taking other possible actions at that state. This relative advantage is quantified by measuring the extra reward we get if we choose certain action at that state compared to the mean reward we get at that state:

$$A(s_t, a_t) = Q(s_t, a_t) - V(s_t), \tag{113}$$

Since this is the difference between the estimated target value for a state-action pair and the value function of the state itself, $A(s_t, a_t)$ measure the benefit of taking a particular action a_t at state s_t over the expected value of following the current policy from state s_t. Subtracting

out $V(s_t)$ does not alter the maximum of the expected return since it is a constant as a function of the action a_t.

In the actor-critic approach, both the action network and critic network are trained together. The critic learns to approximate the advantage function (or more precisely, the value function) which is then used to update the actor's policy parameters. Conceptually, the actor network learns the policy that controls how our agent acts and the critic network learns the value function to assist the policy update by evaluating how good the action taken is. Because smaller sample trajectories rather than an entire episode, are used to evaluate the expected rewards, the variance of these expectation values is dramatically reduced. This approach also allows the agent to learn tasks with longer, or even infinite-length, episodes.

PPO is essentially an architecture with an actor-critic mechanism that also improves the agent's training stability by controlling the step size of the policy update. With appropriately-sized small policy updates during the training, we can avoid having step size that is too small that slows down the training significantly, while also avoid having a step size that is so large that the policy might be updated to a state so far from optimality that convergence to a good policy again might be severely delayed or prevented entirely. PPO possesses several advantages which we can leverage in this task: It is capable of learning policies with a long time horizon, its stability allows agents to be trained for multiple epochs on a single episode's training data, and it can readily be adapted to train simultaneously on multiple episodes in parallel, which is essential to maximize the exploration of our space of theories.

Using gradient ascent, PPO maximizes the overall objective functions for policy and value functions, which have the same local extremum as the parameter θ, supplemented by an entropy bonus term to ensure sufficient exploration:

$$L = L_{PPO} - L_{\text{critic}} + \beta S[\pi_\theta] \tag{114}$$

where L_{PPO} denotes the clipped surrogate objective function used to train the policy network. L_{critic} is the loss function for training the critic network and $S[\pi_\theta]$ is the mean entropy of the policy's output distributions over the sampled trajectory, scaled by a hyperparameter β. β plays the role as a regularizer during policy training and also tuning it allows us to adjust the degree of exploration of the state space versus exploitation of a single optimal strategy. The Adam optimizer is used to perform this stochastic gradient ascent.

The clipped surrogate objective function takes the form

$$L_{PPO}(\theta) = \hat{\mathbb{E}}_t\Big[\min(r_t(\theta)\hat{A}_t, \text{clip}(r_t(\theta), 1-\epsilon, 1+\epsilon)\hat{A}_t)\Big], \tag{115}$$
$$r_t(\theta) = \frac{\pi_\theta(a_t|s_t)}{\pi_{\theta,\text{old}}(a_t|s_t)}.$$

Here, $\pi_\theta(a_t|s_t)$ represents the policy's (given by the set of parameters θ) probability of selecting action a_t given an input state of s_t, while $\pi_{\theta,\text{old}}(a_t|s_t)$ represents the probability of the same action given the model *before* its current round of training. The ratio function $r_t(\theta)$ denotes the probability ratio between the current and old policy, that tells us whether an action a_t is more or less likely in the current policy than the old one. ϵ is a hyperparameter that defines the clip range of the probability ratio, so that we can avoid a policy update that is too large: if the current network's probability for a given action differs too much from that of the policy when the action is sampled (which can occur if the agent is trained on a given trajectory for multiple epochs), this ratio is clipped and becomes independent of the policy parameters, and therefore that action becomes irrelevant to training the network further. $\hat{A}_t$ is the advantage estimator.

The objective function of the critic network takes the form

$$L_{\text{critic}}(\theta) = \hat{\mathbb{E}}_t\Big[\big(V_\theta(s_t) - Q(s_t, a_t)\big)^2\Big] \tag{116}$$

where $V_\theta(s_t)$ is the state value output by the critic network and $Q(s_t, a_t)$ is the state action value computed based on the observations throughout a trajectory, as defined in Eq.(112).

Following the program flow of training described in the main text, with these formulas provided for various objective functions and advantage function, PPO can be trained accordingly. As noted in the main text, in our constructed model our task includes both discrete and continuous actions, so we use the HPPO algorithm [238] to learn the hybrid action space. H-PPO works similarly to conventional PPO, except that the action space is now hierarchically structured, consisted of multiple actors representing policies for various discrete and continuous actions. The actions in our model are also hierarchical, in the sense that certain discrete action (such as which particle to be modified) must necessarily be accompanied by continuous actions that parameterize it (such as the mass and coupling of that particle). In addition to the multiple-actor networks, there is one global critic network that updates the policy parameter θ of all sub-actor networks.

To describe the action space in a mathematical way, we follow the method presented in [238]: we have a finite set of discrete action $\mathcal{A}_d = \{a_1, a_2, \cdots, a_k\}$ and for each action $a \in \mathcal{A}_d$, there are multiple sets of real-valued continuous parameters $x^i \in \mathcal{X}_a^i$ associated with a to be specified. A complete action $(a, x^1, x^2, \cdots, x^i)$ is then composed of a discrete action and continuous parameters to be executed with that action. The whole hybrid action space $\mathcal{A}$ then takes the form:

$$\mathcal{A} = \bigcup_{\substack{a \in \mathcal{A}_d \\ i \in \{1,2,\ldots,n\}}} \{(a, x^1, \cdots, x^n) | x^i \in \mathcal{X}_a^i\}. \tag{117}$$

To deal with this action space, there are two actors: A discrete actor, which will learn a policy over the discrete actions $\mathcal{A}_d$, and a continuous actor, which will learn policies over all the continuous parameters in $\mathcal{X}_a^i$ for each discrete action a. The two actors' objective functions are evaluated separately according to the PPO objective function following Eq. (115), and added together to compute the full H-PPO objective function. Crucially, in H-PPO the network will generate probability distributions over *all* the parameters for all possible actions, even those which aren't ultimately chosen by the top-level discrete action. When computing the objective function, however, only those outputs which are actually used in parameterizing the action at each step are included. Our action space has a tree structure that describes multiple layers of actions. For example, as discussed in the main text, if we select that a particle's parameters should be modified, we would then have to select which particle should be modified, which parameter of that particle should be modified, and finally what modification we should make to that parameter. In this hierarchical action space, the hybrid actor-critic architecture contains multiple actor networks and one critic network. There is one actor network for each discrete or continuous action-selection sub-problems. The critic network follows the same virtue as the one in PPO. Each of the actor networks generates either a stochastic discrete policy or a stochastic continuous policy, and these actors are updated separately as independent policies using PPO during training.

With the hybrid actor-critic architecture, H-PPO uses PPO as the policy optimization method for all of its discrete policy π_{θ_d} and continuous policy π_{θ_c}. The policies are updated separately and independently for each actor by maximizing their individual clipped surrogate objective function. For each actor with discrete policy $\pi_{\theta_d}^i$, with i denotes the i-th actor,

the objective takes the form

$$L^i_{PPO,d}(\theta_{d,i}) = \hat{\mathbb{E}}_t\Big[\min(r^{d,i}_t(\theta_{d,i})\hat{A}_t, \text{clip}(r^{d,i}_t(\theta_{d,i}), 1-\epsilon, 1+\epsilon)\hat{A}_t)\Big], \tag{118}$$

$$r_t(\theta_{d,i}) = \frac{\pi^i_{\theta_{d,i}}(a_t|s_t)}{\pi^i_{\theta_{d,i},\text{old}}(a_t|s_t)}. \tag{119}$$

Whereas for each actor i with continuous policy $\pi^i_{\theta_c}$, the objective function is:

$$L^i_{PPO,c}(\theta_{c,i}) = \hat{\mathbb{E}}_t\Big[\min(r^{c,i}_t(\theta_{c,i})\hat{A}_t, \text{clip}(r^{c,i}_t(\theta_{c,i}), 1-\epsilon, 1+\epsilon)\hat{A}_t)\Big], \tag{120}$$

$$r_t(\theta_{c,i}) = \frac{\pi^i_{\theta_{c,i}}(x^i_t|s_t)}{\pi^i_{\theta_{c,i},\text{old}}(x^i_t|s_t)}. \tag{121}$$

Here we can see that even if multiple discrete and continuous policies work together to specify a complete action, their objective functions are independent and their policies are viewed as separate distributions.

Chapter 6

Conclusion

In this thesis, we have explored two general types of BSM model building possibilities. In the quark sector, we have investigated flavored gauge mediation models in which the Higgs and messenger doublets are embedded in multiplets of the discrete non-Abelian symmetry $\mathcal{S}_3$. In these theories, this symmetry correlates the flavor structure of the quark and lepton Yukawa couplings with the structure of the messenger Yukawa couplings that contribute to the soft supersymmetry breaking mass parameters. We provided a systematic exploration of possible scenarios within this framework that can accommodate hierarchical quark and charged lepton masses, and examined the resulting phenomenological implications in each case. These theories exhibit a heavier spectrum for the superpartner masses compared to flavored gauge mediation models controlled by Abelian symmetries, which can be directly traced back to the need in our scenarios for two vectorlike pairs of messenger fields for viable electroweak symmetry breaking.

In the lepton sector, we have first explored a minimal construction within the framework of lepton portal matter models with kinetic mixing that address the muon $g-2$ anomaly. We found that with the addition of several portal matter particle species, and thus additional mass scales in the system (reminiscent of how more particle species and mass scales in the FGM model solves the μ/B_μ problem), the chiral enhancement contributing from the SM Higgs coupling between the different portal matter species can have sufficient contribution to the anomalous muon magnetic moment. Although this chiral enhancement mechanism is reminiscent of that of fermiophobic Z' gauge models, the parameter space is vastly different. We then attempted to extend this simple model to a more UV-complete model, with an extended dark gauge sector $SU(2) \times SU(2)$, in which SM and portal matter fields exist as members of the same dark gauge multiplets. We found that there is a rich collider phenomenology in this extended model, which is particularly well-suited to explorations

at a future muon collider.

Equipped with our knowledge about the leptonic portal matter framework, we also took a step forward towards automating the model-building process for BSM physics using reinforcement learning. Using the graph grammar method developed to represent BSM models, we created a RL environment for this well-studied simple leptonic portal matter framework. The RL agent successfully explored a model space consisting of both continuous and discrete parameters and identified consistent theories. The models found include both known and previously unstudied examples that can accommodate the muon anomalous magnetic moment and satisfy precision electroweak and flavor constraints. The approach set the stage for future explorations that harness the power of machine learning techniques to explore fundamental physics.

BIBLIOGRAPHY

[1] S. N. et al. (Particle Data Group), Physical Review D **110**, 030001 (2024).

[2] CKMfitter Group (J. Charles et al.), European Physical Journal C **41**, 1 (2005), updated results and plots available at: `http://ckmfitter.in2p3.fr`, hep-ph/0406184 .

[3] G. Guedes and J. Santiago, JHEP **01**, 111, arXiv:2107.03429 [hep-ph] .

[4] G. N. Wojcik, L. L. Everett, S. T. Eu, and R. Ximenes, Phys. Rev. D **108**, 055033 (2023), arXiv:2303.12983 [hep-ph] .

[5] B. Abi *et al.* (Muon g-2), Phys. Rev. Lett. **126**, 141801 (2021), arXiv:2104.03281 [hep-ex] .

[6] S. L. Glashow, Nucl. Phys. **22**, 579 (1961).

[7] S. Weinberg, Phys. Rev. Lett. **19**, 1264 (1967).

[8] A. Salam, Conf. Proc. C **680519**, 367 (1968).

[9] N. Cabibbo, Phys. Rev. Lett. **10**, 531 (1963).

[10] M. Kobayashi and T. Maskawa, Prog. Theor. Phys. **49**, 652 (1973).

[11] L. Wolfenstein, Phys. Rev. Lett. **51**, 1945 (1983).

[12] R. W. et al. (Particle Data Group), Progress of Theoretical and Experimental Physics **2022**, 083C01 (2022).

[13] Z. Maki, M. Nakagawa, and S. Sakata, Progress of Theoretical Physics **28**, 870 (1962), https://academic.oup.com/ptp/article-pdf/28/5/870/5258750/28-5-870.pdf .

[14] B. Pontecorvo, Zh. Eksp. Teor. Fiz. **34**, 247 (1957).

[15] R. L. Workman and Others (Particle Data Group), PTEP **2022**, 083C01 (2022).

[16] P. Salucci, The Astronomy and Astrophysics Review **27**, 10.1007/s00159-018-0113-1 (2019).

[17] N. A. Bahcall, R. Cen, R. Dave, J. P. Ostriker, and Q. Yu, The Astrophysical Journal **541**, 1–9 (2000).

[18] S. W. Randall, M. Markevitch, D. Clowe, A. H. Gonzalez, and M. Bradač, The Astrophysical Journal **679**, 1173–1180 (2008).

[19] A. J. S. Hamilton and M. Tegmark, Monthly Notices of the Royal Astronomical Society **330**, 506–530 (2002).

[20] N. Aghanim, Y. Akrami, M. Ashdown, J. Aumont, C. Baccigalupi, M. Ballardini, A. J. Banday, R. B. Barreiro, N. Bartolo, S. Basak, R. Battye, K. Benabed, J.-P. Bernard, M. Bersanelli, P. Bielewicz, J. J. Bock, J. R. Bond, J. Borrill, F. R. Bouchet, F. Boulanger, M. Bucher, C. Burigana, R. C. Butler, E. Calabrese, J.-F. Cardoso, J. Carron, A. Challinor, H. C. Chiang, J. Chluba, L. P. L. Colombo, C. Combet, D. Contreras, B. P. Crill, F. Cuttaia, P. de Bernardis, G. de Zotti, J. Delabrouille, J.-M. Delouis, E. Di Valentino, J. M. Diego, O. Doré, M. Douspis, A. Ducout, X. Dupac, S. Dusini, G. Efstathiou, F. Elsner, T. A. Enßlin, H. K. Eriksen, Y. Fantaye, M. Farhang, J. Fergusson, R. Fernandez-Cobos, F. Finelli, F. Forastieri, M. Frailis, A. A. Fraisse, E. Franceschi, A. Frolov, S. Galeotta, S. Galli, K. Ganga, R. T. Génova-Santos, M. Gerbino, T. Ghosh, J. González-Nuevo, K. M. Górski, S. Gratton, A. Gruppuso, J. E. Gudmundsson, J. Hamann, W. Handley, F. K. Hansen, D. Herranz, S. R. Hildebrandt, E. Hivon, Z. Huang, A. H. Jaffe, W. C. Jones, A. Karakci, E. Keihänen, R. Keskitalo, K. Kiiveri, J. Kim, T. S. Kisner, L. Knox, N. Krachmalnicoff, M. Kunz, H. Kurki-Suonio, G. Lagache, J.-M. Lamarre, A. Lasenby, M. Lattanzi, C. R. Lawrence, M. Le Jeune, P. Lemos, J. Lesgourgues, F. Levrier, A. Lewis, M. Liguori, P. B. Lilje, M. Lilley, V. Lindholm, M. López-Caniego, P. M. Lubin, Y.-Z. Ma, J. F. Macías-Pérez, G. Maggio, D. Maino, N. Mandolesi, A. Mangilli, A. Marcos-Caballero, M. Maris, P. G. Martin, M. Martinelli, E. Martínez-González, S. Matarrese, N. Mauri, J. D. McEwen, P. R. Meinhold, A. Melchiorri, A. Mennella, M. Migliaccio, M. Millea, S. Mitra, M.-A. Miville-Deschênes, D. Molinari, L. Montier, G. Morgante, A. Moss, P. Natoli, H. U. Nørgaard-Nielsen, L. Pagano, D. Paoletti, B. Partridge, G. Patanchon, H. V. Peiris, F. Perrotta, V. Pettorino, F. Piacentini, L. Polastri, G. Polenta, J.-L. Puget, J. P. Rachen, M. Reinecke, M. Remazeilles, A. Renzi, G. Rocha, C. Rosset, G. Roudier, J. A. Rubiño-Martín, B. Ruiz-Granados, L. Salvati, M. Sandri, M. Savelainen, D. Scott, E. P. S. Shellard, C. Sirignano, G. Sirri, L. D. Spencer, R. Sunyaev, A.-S. Suur-Uski, J. A. Tauber, D. Tavagnacco, M. Tenti, L. Toffolatti, M. Tomasi, T. Trombetti, L. Valenziano, J. Valiviita, B. Van Tent, L. Vibert,

P. Vielva, F. Villa, N. Vittorio, B. D. Wandelt, I. K. Wehus, M. White, S. D. M. White, A. Zacchei, and A. Zonca, Astronomy and Astrophysics **641**, A6 (2020).

[21] G. W. Bennett *et al.* (Muon g-2), Phys. Rev. D **73**, 072003 (2006), arXiv:hep-ex/0602035 .

[22] T. Aoyama *et al.*, Phys. Rept. **887**, 1 (2020), arXiv:2006.04822 [hep-ph] .

[23] T. Aoyama, M. Hayakawa, T. Kinoshita, and M. Nio, Phys. Rev. Lett. **109**, 111808 (2012), arXiv:1205.5370 [hep-ph] .

[24] T. Aoyama, T. Kinoshita, and M. Nio, Atoms **7**, 28 (2019).

[25] A. Czarnecki, W. J. Marciano, and A. Vainshtein, Phys. Rev. **D67**, 073006 (2003), [Erratum: Phys. Rev. **D**73, 119901 (2006)], arXiv:hep-ph/0212229 [hep-ph] .

[26] C. Gnendiger, D. Stöckinger, and H. Stöckinger-Kim, Phys. Rev. **D88**, 053005 (2013), arXiv:1306.5546 [hep-ph] .

[27] M. Davier, A. Hoecker, B. Malaescu, and Z. Zhang, Eur. Phys. J. **C77**, 827 (2017), arXiv:1706.09436 [hep-ph] .

[28] A. Keshavarzi, D. Nomura, and T. Teubner, Phys. Rev. **D97**, 114025 (2018), arXiv:1802.02995 [hep-ph] .

[29] G. Colangelo, M. Hoferichter, and P. Stoffer, JHEP **02**, 006, arXiv:1810.00007 [hep-ph] .

[30] M. Hoferichter, B.-L. Hoid, and B. Kubis, JHEP **08**, 137, arXiv:1907.01556 [hep-ph] .

[31] M. Davier, A. Hoecker, B. Malaescu, and Z. Zhang, Eur. Phys. J. **C80**, 241 (2020), [Erratum: Eur. Phys. J. **C**80, 410 (2020)], arXiv:1908.00921 [hep-ph] .

[32] A. Keshavarzi, D. Nomura, and T. Teubner, Phys. Rev. **D101**, 014029 (2020), arXiv:1911.00367 [hep-ph] .

[33] A. Kurz, T. Liu, P. Marquard, and M. Steinhauser, Phys. Lett. **B734**, 144 (2014), arXiv:1403.6400 [hep-ph] .

[34] K. Melnikov and A. Vainshtein, Phys. Rev. **D70**, 113006 (2004), arXiv:hep-ph/0312226 [hep-ph] .

[35] P. Masjuan and P. Sánchez-Puertas, Phys. Rev. **D95**, 054026 (2017), arXiv:1701.05829 [hep-ph] .

[36] G. Colangelo, M. Hoferichter, M. Procura, and P. Stoffer, JHEP **04**, 161, arXiv:1702.07347 [hep-ph] .

[37] M. Hoferichter, B.-L. Hoid, B. Kubis, S. Leupold, and S. P. Schneider, JHEP **10**, 141, arXiv:1808.04823 [hep-ph] .

[38] A. Gérardin, H. B. Meyer, and A. Nyffeler, Phys. Rev. **D100**, 034520 (2019), arXiv:1903.09471 [hep-lat] .

[39] J. Bijnens, N. Hermansson-Truedsson, and A. Rodríguez-Sánchez, Phys. Lett. **B798**, 134994 (2019), arXiv:1908.03331 [hep-ph] .

[40] G. Colangelo, F. Hagelstein, M. Hoferichter, L. Laub, and P. Stoffer, JHEP **03**, 101, arXiv:1910.13432 [hep-ph] .

[41] T. Blum, N. Christ, M. Hayakawa, T. Izubuchi, L. Jin, C. Jung, and C. Lehner, Phys. Rev. Lett. **124**, 132002 (2020), arXiv:1911.08123 [hep-lat] .

[42] G. Colangelo, M. Hoferichter, A. Nyffeler, M. Passera, and P. Stoffer, Phys. Lett. **B735**, 90 (2014), arXiv:1403.7512 [hep-ph] .

[43] S. Borsanyi *et al.*, Nature **593**, 51 (2021), arXiv:2002.12347 [hep-lat] .

[44] C. Lehner and A. S. Meyer, Phys. Rev. D **101**, 074515 (2020), arXiv:2003.04177 [hep-lat] .

[45] M. Cè *et al.*, (2022), arXiv:2206.06582 [hep-lat] .

[46] C. Alexandrou *et al.*, (2022), arXiv:2206.15084 [hep-lat] .

[47] G. Colangelo, A. X. El-Khadra, M. Hoferichter, A. Keshavarzi, C. Lehner, P. Stoffer, and T. Teubner, Phys. Lett. B **833**, 137313 (2022), arXiv:2205.12963 [hep-ph] .

[48] S. T. Eu, L. L. Everett, T. Garon, and N. Leonard, Phys. Rev. D **105**, 055019 (2022), arXiv:2110.05599 [hep-ph] .

[49] S. P. MARTIN, A supersymmetry primer, in *Advanced Series on Directions in High Energy Physics* (WORLD SCIENTIFIC, 1998) p. 1–98.

[50] D. J. H. Chung, L. L. Everett, G. L. Kane, S. F. King, J. D. Lykken, and L.-T. Wang, Phys. Rept. **407**, 1 (2005), arXiv:hep-ph/0312378 .

[51] D. Bertolini, J. Thaler, and Z. Thomas, in *Searching for New Physics at Small and Large Scales* (WORLD SCIENTIFIC, 2013).

[52] L. Girardello and M. Grisaru, Nuclear Physics B **194**, 65 (1982).

[53] S. Krippendorf, F. Quevedo, and O. Schlotterer, Cambridge lectures on supersymmetry and extra dimensions (2010), arXiv:1011.1491 [hep-th] .

[54] G. Dvali, G. Giudice, and A. Pomarol, Nuclear Physics B **478**, 31 (1996).

[55] G. N. Wojcik, L. L. Everett, S. T. Eu, and R. Ximenes, Phys. Lett. B **841**, 137931 (2023), arXiv:2211.09918 [hep-ph] .

[56] T. G. Rizzo, Phys. Rev. D **99**, 115024 (2019), arXiv:1810.07531 [hep-ph] .

[57] G. N. Wojcik, S. T. Eu, and L. L. Everett, (2024), arXiv:2407.07184 [hep-ph] .

[58] G. N. Wojcik, S. T. Eu, and L. L. Everett, (2024), arXiv:2407.07203 [hep-ph] .

[59] M. Dine, W. Fischler, and M. Srednicki, Nucl. Phys. B **189**, 575 (1981).

[60] L. Alvarez-Gaumé, M. Claudson, and M. B. Wise, Nuclear Physics B **207**, 96 (1982).

[61] S. Dimopoulos and S. Raby, Nuclear Physics B **192**, 353 (1981).

[62] S. Dimopoulos and S. Raby, Nuclear Physics B **219**, 479 (1983).

[63] M. Dine and W. Fischler, Physics Letters B **110**, 227 (1982).

[64] C. R. Nappi and B. A. Ovrut, Phys. Lett. B **113**, 175 (1982).

[65] M. Dine and A. E. Nelson, Physical Review D **48**, 1277–1287 (1993).

[66] M. Dine, A. E. Nelson, and Y. Shirman, Physical Review D **51**, 1362–1370 (1995).

[67] M. Dine, A. E. Nelson, Y. Nir, and Y. Shirman, Physical Review D **53**, 2658–2669 (1996).

[68] M. Dine, Y. Nir, and Y. Shirman, Physical Review D **55**, 1501–1508 (1997).

[69] G. Giudice and R. Rattazzi, Physics Reports **322**, 419–499 (1999).

[70] P. Draper, P. Meade, M. Reece, and D. Shih, Physical Review D **85**, 10.1103/physrevd.85.095007 (2012).

[71] A. Arbey, M. Battaglia, A. Djouadi, F. Mahmoudi, and J. Quevillon, Physics Letters B **708**, 162–169 (2012).

[72] M. Adeel Ajaib, I. Gogoladze, F. Nasir, and Q. Shafi, Physics Letters B **713**, 462–468 (2012).

[73] W. Fischler and W. Tangarife, Journal of High Energy Physics **2014**, 10.1007/jhep05(2014)151 (2014).

[74] L. Calibbi, P. Paradisi, and R. Ziegler, The European Physical Journal C **74**, 10.1140/epjc/s10052-014-3211-x (2014).

[75] P. Meade, N. Seiberg, and D. Shih, Prog. Theor. Phys. Suppl. **177**, 143 (2009), arXiv:0801.3278 [hep-ph] .

[76] Z. Chacko and E. Pontón, Physical Review D **66**, 10.1103/physrevd.66.095004 (2002).

[77] Y. Shadmi and P. Z. Szabo, Journal of High Energy Physics **2012**, 10.1007/jhep06(2012)124 (2012).

[78] J. L. Evans, M. Ibe, and T. T. Yanagida, Physics Letters B **705**, 342–348 (2011).

[79] J. L. Evans, M. Ibe, and T. T. Yanagida, Probing extra matter in gauge mediation through the lightest higgs boson mass (2011), arXiv:1108.3437 [hep-ph] .

[80] J. L. Evans, M. Ibe, S. Shirai, and T. T. Yanagida, Physical Review D **85**, 10.1103/physrevd.85.095004 (2012).

[81] Z. Kang, T. Li, T. Liu, C. Tong, and J. M. Yang, Physical Review D **86**, 10.1103/physrevd.86.095020 (2012).

[82] N. Craig, S. Knapen, D. Shih, and Y. Zhao, Journal of High Energy Physics **2013**, 10.1007/jhep03(2013)154 (2013).

[83] A. Albaid and K. S. Babu, Physical Review D **88**, 10.1103/physrevd.88.055007 (2013).

[84] M. Abdullah, I. Galon, Y. Shadmi, and Y. Shirman, Journal of High Energy Physics **2013**, 10.1007/jhep06(2013)057 (2013).

[85] M. J. Pérez, P. Ramond, and J. Zhang, Physical Review D **87**, 10.1103/physrevd.87.035021 (2013).

[86] P. Byakti and T. S. Ray, Journal of High Energy Physics **2013**, 10.1007/jhep05(2013)055 (2013).

[87] J. A. Evans and D. Shih, Journal of High Energy Physics **2013**, 10.1007/jhep08(2013)093 (2013).

[88] L. Calibbi, P. Paradisi, and R. Ziegler, Journal of High Energy Physics **2013**, 10.1007/jhep06(2013)052 (2013).

[89] J. A. Evans, D. Shih, and A. Thalapillil, Chiral flavor violation from extended gauge mediation (2015), arXiv:1504.00930 [hep-ph] .

[90] I. Galon, G. Perez, and Y. Shadmi, Journal of High Energy Physics **2013**, 10.1007/jhep09(2013)117 (2013).

[91] F. R. Joaquim and A. Rossi, Nucl. Phys. B **765**, 71 (2007), arXiv:hep-ph/0607298 .

[92] F. R. Joaquim and A. Rossi, Phys. Rev. Lett. **97**, 181801 (2006), arXiv:hep-ph/0604083 .

[93] N. Ierushalmi, S. Iwamoto, G. Lee, V. Nepomnyashy, and Y. Shadmi, Journal of High Energy Physics **2016**, 10.1007/jhep07(2016)058 (2016).

[94] T. Jeliński and J. Gluza, Physics Letters B **751**, 541–547 (2015).

[95] L. L. Everett and T. S. Garon, Physical Review D **97**, 10.1103/physrevd.97.095028 (2018).

[96] L. L. Everett, T. S. Garon, and A. B. Rock, Physical Review D **100**, 10.1103/physrevd.100.015039 (2019).

[97] W. Ahmed, L. Calibbi, T. Li, A. Mustafayev, and S. Raza, Physical Review D **95**, 10.1103/physrevd.95.095031 (2017).

[98] Z.-z. Xing, Journal of Physics G: Nuclear and Particle Physics **23**, 1563–1578 (1997).

[99] H. Fritzsch and D. Holtmannspötter, Physics Letters B **338**, 290–294 (1994).

[100] H. Fritzsch and Z.-Z. Xing, Progress in Particle and Nuclear Physics **45**, 1–81 (2000).

[101] L. L. Everett, T. S. Garon, and A. B. Rock, Physical Review D **101**, 10.1103/physrevd.101.115003 (2020).

[102] R. Barbieri and G. Giudice, Nuclear Physics B **306**, 63 (1988).

[103] B. C. Allanach, Comput. Phys. Commun. **143**, 305 (2002), arXiv:hep-ph/0104145 [hep-ph] .

[104] P. A. Zyla *et al.* (Particle Data Group), PTEP **2020**, 083C01 (2020), and 2021 updates.

[105] G. Raz, Physical Review D **66**, 10.1103/physrevd.66.037701 (2002).

[106] M. Misiak, S. Pokorski, and J. Rosiek, Advanced Series on Directions in High Energy Physics , 795–828 (1998).

[107] B. Abi *et al.* (Muon $g-2$ Collaboration), Phys. Rev. Lett. **126**, 141801 (2021).

[108] A. M. Sirunyan *et al.* (CMS), Phys. Lett. B **790**, 140 (2019), arXiv:1806.05264 [hep-ex] .

[109] F. D. Steffen, JCAP **09**, 001, arXiv:hep-ph/0605306 .

[110] J. L. Feng, S.-f. Su, and F. Takayama, Phys. Rev. D **70**, 063514 (2004), arXiv:hep-ph/0404198 .

[111] T. Asaka, K. Hamaguchi, and K. Suzuki, Physics Letters B **490**, 136 (2000).

[112] A. Crivellin, M. Hoferichter, C. A. Manzari, and M. Montull, Phys. Rev. Lett. **125**, 091801 (2020), arXiv:2003.04886 [hep-ph] .

[113] A. Keshavarzi, W. J. Marciano, M. Passera, and A. Sirlin, Phys. Rev. D **102**, 033002 (2020), arXiv:2006.12666 [hep-ph] .

[114] G. Colangelo, M. Hoferichter, and P. Stoffer, Phys. Lett. B **814**, 136073 (2021), arXiv:2010.07943 [hep-ph] .

[115] F. Jegerlehner and A. Nyffeler, Physics Reports **477**, 1 (2009), arXiv:0902.3360 [hep-ph] .

[116] P. Athron, C. Balázs, D. H. J. Jacob, W. Kotlarski, D. Stöckinger, and H. Stöckinger-Kim, JHEP **09**, 080, arXiv:2104.03691 [hep-ph] .

[117] A. de Giorgi, L. Merlo, and S. Pokorski, (2022), arXiv:2211.03797 [hep-ph] .

[118] A. E. Cárcamo Hernández, S. F. King, H. Lee, and S. J. Rowley, Phys. Rev. D **101**, 115016 (2020), arXiv:1910.10734 [hep-ph] .

[119] R. Dermisek and A. Raval, Phys. Rev. D **88**, 013017 (2013), arXiv:1305.3522 [hep-ph] .

[120] A. Bodas, R. Coy, and S. J. D. King, Eur. Phys. J. C **81**, 1065 (2021), arXiv:2102.07781 [hep-ph] .

[121] P. Agrawal, D. E. Kaplan, O. Kim, S. Rajendran, and M. Reig, (2022), arXiv:2210.17547 [hep-ph] .

[122] M. Endo, K. Hamaguchi, S. Iwamoto, and T. Kitahara, JHEP **07**, 075, arXiv:2104.03217 [hep-ph] .

[123] G. Arcadi, L. Calibbi, M. Fedele, and F. Mescia, Phys. Rev. Lett. **127**, 061802 (2021), arXiv:2104.03228 [hep-ph] .

[124] B. Holdom, Phys. Lett. B **166**, 196 (1986).

[125] B. Holdom, Phys. Lett. B **178**, 65 (1986).

[126] G. N. Wojcik and T. G. Rizzo, Phys. Rev. D **105**, 015032 (2022), arXiv:2012.05406 [hep-ph] .

[127] G. N. Wojcik and T. G. Rizzo, JHEP **04**, 033, arXiv:2109.07369 [hep-ph] .

[128] T. D. Rueter and T. G. Rizzo, Phys. Rev. D **101**, 015014 (2020), arXiv:1909.09160 [hep-ph] .

[129] T. D. Rueter and T. G. Rizzo, (2020), arXiv:2011.03529 [hep-ph] .

[130] T. G. Rizzo, (2022), arXiv:2209.00688 [hep-ph] .

[131] T. G. Rizzo, in *2022 Snowmass Summer Study* (2022) arXiv:2202.02222 [hep-ph] .

[132] M. Pospelov, A. Ritz, and M. B. Voloshin, Phys. Lett. B **662**, 53 (2008), arXiv:0711.4866 [hep-ph] .

[133] E. Izaguirre, G. Krnjaic, P. Schuster, and N. Toro, Phys. Rev. Lett. **115**, 251301 (2015), arXiv:1505.00011 [hep-ph] .

[134] R. Essig *et al.*, in *Community Summer Study 2013: Snowmass on the Mississippi* (2013) arXiv:1311.0029 [hep-ph] .

[135] D. Curtin, R. Essig, S. Gori, and J. Shelton, JHEP **02**, 157, arXiv:1412.0018 [hep-ph] .

[136] S. F. King, JHEP **08**, 019, arXiv:1706.06100 [hep-ph] .

[137] H. Lee and A. E. Cárcamo Hernández, (2022), arXiv:2207.01710 [hep-ph] .

[138] H. M. Lee and K. Yamashita, Eur. Phys. J. C **82**, 661 (2022), arXiv:2204.05024 [hep-ph] .

[139] L. Darmé, S. Rao, and L. Roszkowski, JHEP **03**, 084, arXiv:1710.08430 [hep-ph] .

[140] T. G. Rizzo, JHEP **07**, 118, arXiv:1801.08525 [hep-ph] .

[141] K.-C. Yang, (2022), arXiv:2209.10827 [hep-ph] .

[142] A. Amiri, B. Díaz Sáez, and K. Ghorbani, (2022), arXiv:2209.11723 [hep-ph] .

[143] M. Aaboud *et al.* (ATLAS), Phys. Rev. Lett. **122**, 231801 (2019), arXiv:1904.05105 [hep-ex] .

[144] T. G. Rizzo and G. N. Wojcik, JHEP **03**, 173, arXiv:2006.06858 [hep-ph] .

[145] M. W. Winkler, Phys. Rev. D **99**, 015018 (2019), arXiv:1809.01876 [hep-ph] .

[146] M. Pospelov, Phys. Rev. D **80**, 095002 (2009), arXiv:0811.1030 [hep-ph] .

[147] H. Davoudiasl, H.-S. Lee, and W. J. Marciano, Phys. Rev. D **89**, 095006 (2014), arXiv:1402.3620 [hep-ph] .

[148] Y. M. Andreev *et al.* (NA64), Phys. Rev. Lett. **126**, 211802 (2021), arXiv:2102.01885 [hep-ex] .

[149] J. P. Leveille, Nucl. Phys. B **137**, 63 (1978).

[150] J. L. Feng, K. T. Matchev, and Y. Shadmi, Nucl. Phys. B **613**, 366 (2001), arXiv:hep-ph/0107182 .

[151] M. Abe *et al.*, PTEP **2019**, 053C02 (2019), arXiv:1901.03047 [physics.ins-det] .

[152] A. Adelmann *et al.*, (2021), arXiv:2102.08838 [hep-ex] .

[153] A. Crivellin and M. Hoferichter, JHEP **07**, 135, [Erratum: JHEP 10, 030 (2022)], arXiv:2104.03202 [hep-ph] .

[154] A. Crivellin, M. Hoferichter, and P. Schmidt-Wellenburg, Phys. Rev. D **98**, 113002 (2018), arXiv:1807.11484 [hep-ph] .

[155] P. J. Fitzpatrick, H. Liu, T. R. Slatyer, and Y.-D. Tsai, Phys. Rev. D **106**, 083517 (2022), arXiv:2011.01240 [hep-ph] .

[156] T. Hara, S. Kanemura, and T. Katayose, Phys. Rev. D **105**, 035035 (2022), arXiv:2109.03553 [hep-ph] .

[157] R. T. D'Agnolo and J. T. Ruderman, Phys. Rev. Lett. **115**, 061301 (2015), arXiv:1505.07107 [hep-ph] .

[158] J. Kawamura, S. Okawa, and Y. Omura, Phys. Rev. D **106**, 015005 (2022), arXiv:2204.07022 [hep-ph] .

[159] M. Aaboud *et al.* (ATLAS), Eur. Phys. J. C **78**, 995 (2018), arXiv:1803.02762 [hep-ex] .

[160] A. Osman Acar, O. E. Delialioglu, and S. Sultansoy, (2021), arXiv:2103.08222 [hep-ph] .

[161] K. M. Black *et al.*, (2022), arXiv:2209.01318 [hep-ex] .

[162] W. Altmannshofer, S. Gori, M. Pospelov, and I. Yavin, Phys. Rev. Lett. **113**, 091801 (2014), arXiv:1406.2332 [hep-ph] .

[163] G. Bellini *et al.*, Phys. Rev. Lett. **107**, 141302 (2011), arXiv:1104.1816 [hep-ex] .

[164] S. T. Eu, L. L. Everett, G. Wojcik, and R. Ximenes, .

[165] G. Arcadi, M. Dutra, P. Ghosh, M. Lindner, Y. Mambrini, M. Pierre, S. Profumo, and F. S. Queiroz, Eur. Phys. J. C **78**, 203 (2018), arXiv:1703.07364 [hep-ph] .

[166] M. Kawasaki and K. Nakayama, Ann. Rev. Nucl. Part. Sci. **63**, 69 (2013), arXiv:1301.1123 [hep-ph] .

[167] P. W. Graham, I. G. Irastorza, S. K. Lamoreaux, A. Lindner, and K. A. van Bibber, Ann. Rev. Nucl. Part. Sci. **65**, 485 (2015), arXiv:1602.00039 [hep-ex] .

[168] M. Battaglieri *et al.*, in *U.S. Cosmic Visions: New Ideas in Dark Matter* (2017) arXiv:1707.04591 [hep-ph] .

[169] J. Alexander *et al.* (2016) arXiv:1608.08632 [hep-ph] .

[170] N. Bernal, M. Heikinheimo, T. Tenkanen, K. Tuominen, and V. Vaskonen, Int. J. Mod. Phys. A **32**, 1730023 (2017), arXiv:1706.07442 [hep-ph] .

[171] E. G. M. Ferreira, Astron. Astrophys. Rev. **29**, 7 (2021), arXiv:2005.03254 [astro-ph.CO] .

[172] R. K. Leane, T. R. Slatyer, J. F. Beacom, and K. C. Y. Ng, Phys. Rev. D **98**, 023016 (2018), arXiv:1805.10305 [hep-ph] .

[173] Q. Wang *et al.* (PandaX-II), Chin. Phys. C **44**, 125001 (2020), arXiv:2007.15469 [astro-ph.CO] .

[174] E. Aprile *et al.* (XENON), Phys. Rev. Lett. **121**, 111302 (2018), arXiv:1805.12562 [astro-ph.CO] .

[175] D. S. Akerib *et al.* (LUX), Phys. Rev. Lett. **118**, 021303 (2017), arXiv:1608.07648 [astro-ph.CO] .

[176] R. Agnese *et al.* (SuperCDMS), Phys. Rev. Lett. **120**, 061802 (2018), arXiv:1708.08869 [hep-ex] .

[177] P. Agnes *et al.* (DarkSide), Phys. Rev. D **98**, 102006 (2018), arXiv:1802.07198 [astro-ph.CO] .

[178] N. Aghanim *et al.* (Planck), Astron. Astrophys. **641**, A6 (2020), [Erratum: Astron.Astrophys. 652, C4 (2021)], arXiv:1807.06209 [astro-ph.CO] .

[179] G. N. Wojcik, Phys. Rev. D **108**, 035006 (2023), arXiv:2205.11545 [hep-ph] .

[180] T. G. Rizzo, Phys. Rev. D **106**, 035024 (2022), arXiv:2206.09814 [hep-ph] .

[181] A. Carvunis, N. McGinnis, and D. E. Morrissey, JHEP **01**, 014, arXiv:2209.14305 [hep-ph] .

[182] T. G. Rizzo, Phys. Rev. D **107**, 095014 (2023), arXiv:2302.12698 [hep-ph] .

[183] S. Verma, S. Biswas, A. Chatterjee, and J. Ganguly, Phys. Rev. D **107**, 115024 (2023).

[184] T. Aaltonen *et al.* (CDF), Science **376**, 170 (2022).

[185] L. Allwicher, P. Arnan, D. Barducci, and M. Nardecchia, JHEP **10**, 129, arXiv:2108.00013 [hep-ph] .

[186] A. Tumasyan *et al.* (CMS), Phys. Rev. D **108**, 012011 (2023), arXiv:2207.02254 [hep-ex] .

[187] G. Aad *et al.* (ATLAS), Eur. Phys. J. C **80**, 123 (2020), arXiv:1908.08215 [hep-ex] .

[188] A. M. Sirunyan *et al.* (CMS), Phys. Rev. D **100**, 052003 (2019), arXiv:1905.10853 [hep-ex] .

[189] T. Han, Z. Liu, L.-T. Wang, and X. Wang, Phys. Rev. D **103**, 075004 (2021), arXiv:2009.11287 [hep-ph] .

[190] K. Black, T. Bose, Y. Chen, S. Dasu, H. Jia, D. Pinna, V. Sharma, N. Venkatasubramanian, and C. Vuosalo, in *2022 Snowmass Summer Study* (2022) arXiv:2205.10404 [hep-ex] .

[191] J. Alwall, R. Frederix, S. Frixione, V. Hirschi, F. Maltoni, O. Mattelaer, H. S. Shao, T. Stelzer, P. Torrielli, and M. Zaro, JHEP **07**, 079, arXiv:1405.0301 [hep-ph] .

[192] A. Alloul, N. D. Christensen, C. Degrande, C. Duhr, and B. Fuks, Comput. Phys. Commun. **185**, 2250 (2014), arXiv:1310.1921 [hep-ph] .

[193] K.-Y. Zhang and W.-Z. Feng, Chin. Phys. C **47**, 023107 (2023), arXiv:2204.08067 [hep-ph] .

[194] M. Bauer and P. Foldenauer, Phys. Rev. Lett. **129**, 171801 (2022), arXiv:2207.00023 [hep-ph] .

[195] A. J. Buras, A. Crivellin, F. Kirk, C. A. Manzari, and M. Montull, JHEP **06**, 068, arXiv:2104.07680 [hep-ph] .

[196] D. Geiregat *et al.* (CHARM-II), Phys. Lett. B **245**, 271 (1990).

[197] S. R. Mishra *et al.* (CCFR), Phys. Rev. Lett. **66**, 3117 (1991).

[198] N. Collaboration and T. Adams, Neutrino trident production from nutev (1998), arXiv:hep-ex/9811012 [hep-ex] .

[199] R. L. Workman *et al.* (Particle Data Group), PTEP **2022**, 083C01 (2022).

[200] S. Li, Y. Xiao, and J. M. Yang, Eur. Phys. J. C **82**, 276 (2022), arXiv:2107.04962 [hep-ph] .

[201] J. Halverson, B. Nelson, and F. Ruehle, JHEP **06**, 003, arXiv:1903.11616 [hep-th] .

[202] T. R. Harvey and A. Lukas, JHEP **08**, 161, arXiv:2103.04759 [hep-th] .

[203] S. Nishimura, C. Miyao, and H. Otsuka, JHEP **23**, 021, arXiv:2304.14176 [hep-ph] .

[204] D. P. Aguillard *et al.* (Muon g-2), Phys. Rev. Lett. **131**, 161802 (2023), arXiv:2308.06230 [hep-ex] .

[205] R. Aaij *et al.* (LHCb), JHEP **01**, 036, arXiv:2109.01113 [hep-ex] .

[206] M. Aaboud *et al.* (ATLAS), Eur. Phys. J. C **78**, 110 (2018), [Erratum: Eur.Phys.J.C 78, 898 (2018)], arXiv:1701.07240 [hep-ex] .

[207] T. Aaltonen *et al.* (CDF), Phys. Rev. Lett. **108**, 151803 (2012), arXiv:1203.0275 [hep-ex] .

[208] V. M. Abazov *et al.* (D0), Phys. Rev. Lett. **108**, 151804 (2012), arXiv:1203.0293 [hep-ex] .

[209] J. Abdallah *et al.* (DELPHI), Eur. Phys. J. C **55**, 1 (2008), arXiv:0803.2534 [hep-ex] .

[210] G. Abbiendi *et al.* (OPAL), Eur. Phys. J. C **45**, 307 (2006), arXiv:hep-ex/0508060 .

[211] P. Achard *et al.* (L3), Eur. Phys. J. C **45**, 569 (2006), arXiv:hep-ex/0511049 .

[212] S. Schael *et al.* (ALEPH), Eur. Phys. J. C **47**, 309 (2006), arXiv:hep-ex/0605011 .

[213] V. M. Abazov *et al.* (D0), Phys. Rev. D **66**, 012001 (2002), arXiv:hep-ex/0204014 .

[214] T. Affolder *et al.* (CDF), Phys. Rev. D **64**, 052001 (2001), arXiv:hep-ex/0007044 .

[215] A. Tumasyan *et al.* (CMS), Phys. Rev. D **105**, 072008 (2022), arXiv:2201.07861 [hep-ex] .

[216] G. Abbiendi *et al.* (OPAL), Eur. Phys. J. C **52**, 767 (2007), arXiv:0708.1311 [hep-ex] .

[217] J. Abdallah *et al.* (DELPHI), Eur. Phys. J. C **34**, 127 (2004), arXiv:hep-ex/0403042 .

[218] P. Achard *et al.* (L3), Phys. Lett. B **600**, 22 (2004), arXiv:hep-ex/0409016 .

[219] A. Heister *et al.* (ALEPH), Eur. Phys. J. C **38**, 147 (2004).

[220] G. Abbiendi *et al.* (OPAL), Eur. Phys. J. C **19**, 587 (2001), arXiv:hep-ex/0012018 .

[221] P. Abreu *et al.* (DELPHI), Eur. Phys. J. C **16**, 371 (2000).

[222] M. Acciarri *et al.* (L3), Eur. Phys. J. C **16**, 1 (2000), arXiv:hep-ex/0002046 .

[223] R. Barate *et al.* (ALEPH), Eur. Phys. J. C **14**, 1 (2000).

[224] G. Abbiendi *et al.* (OPAL), Eur. Phys. J. C **21**, 1 (2001), arXiv:hep-ex/0103045 .

[225] K. Abe *et al.* (SLD), Phys. Rev. Lett. **86**, 1162 (2001), arXiv:hep-ex/0010015 .

[226] A. Heister *et al.* (ALEPH), Eur. Phys. J. C **20**, 401 (2001), arXiv:hep-ex/0104038 .

[227] P. Abreu *et al.* (DELPHI), Eur. Phys. J. C **14**, 585 (2000).

[228] M. Acciarri *et al.* (L3), Phys. Lett. B **429**, 387 (1998).

[229] K. Abe *et al.* (SLD), Phys. Rev. Lett. **78**, 17 (1997), arXiv:hep-ex/9609019 .

[230] K. Abe *et al.* (SLD), Phys. Rev. Lett. **74**, 2880 (1995), arXiv:hep-ex/9410009 .

[231] R. H. Parker, C. Yu, W. Zhong, B. Estey, and H. Müller, Science **360**, 191 (2018), arXiv:1812.04130 [physics.atom-ph] .

[232] G. Aad *et al.* (ATLAS), Nature **607**, 52 (2022), [Erratum: Nature 612, E24 (2022)], arXiv:2207.00092 [hep-ex] .

[233] A. Tumasyan *et al.* (CMS), Nature **607**, 60 (2022), [Erratum: Nature 623, (2023)], arXiv:2207.00043 [hep-ex] .

[234] A. M. Baldini *et al.* (MEG), Eur. Phys. J. C **76**, 434 (2016), arXiv:1605.05081 [hep-ex] .

[235] B. Aubert *et al.* (BaBar), Phys. Rev. Lett. **104**, 021802 (2010), arXiv:0908.2381 [hep-ex] .

[236] A. Abdesselam *et al.* (Belle), JHEP **10**, 19, arXiv:2103.12994 [hep-ex] .

[237] W. H. Bertl *et al.* (SINDRUM II), Eur. Phys. J. C **47**, 337 (2006).

[238] Z. Fan, R. Su, W. Zhang, and Y. Yu, arXiv e-prints , arXiv:1903.01344 (2019), arXiv:1903.01344 [cs.LG] .

[239] M. Towers, J. K. Terry, A. Kwiatkowski, J. U. Balis, G. d. Cola, T. Deleu, M. Goulão, A. Kallinteris, A. KG, M. Krimmel, R. Perez-Vicente, A. Pierré, S. Schulhoff, J. J. Tai, A. T. J. Shen, and O. G. Younis, Gymnasium (2023).

[240] M. Fey and J. E. Lenssen, arXiv e-prints , arXiv:1903.02428 (2019), arXiv:1903.02428 [cs.LG] .

[241] G. Aad *et al.* (ATLAS), JHEP **09**, 108, arXiv:1506.01291 [hep-ex] .

[242] G. Aad *et al.* (ATLAS), JHEP **07**, 118, arXiv:2303.05441 [hep-ex] .

[243] J. Kawamura and S. Shin, JHEP **11**, 025, arXiv:2308.07814 [hep-ph] .

[244] P. N. Bhattiprolu and S. P. Martin, Phys. Rev. D **100**, 015033 (2019), arXiv:1905.00498 [hep-ph] .

[245] H. van Hasselt, A. Guez, M. Hessel, V. Mnih, and D. Silver, arXiv e-prints , arXiv:1602.07714 (2016), arXiv:1602.07714 [cs.LG] .

[246] A. Dersy, M. D. Schwartz, and X. Zhang, Int. J. Data Sci. Math. Sci. **1**, 135 (2024), arXiv:2206.04115 [cs.LG] .

[247] Y. Zhai, C. Baek, Z. Zhou, J. Jiao, and Y. Ma, arXiv e-prints , arXiv:2107.03961 (2021), arXiv:2107.03961 [cs.AI] .

[248] D. M. Straub, (2018), arXiv:1810.08132 [hep-ph] .

[249] G. Uhlrich, F. Mahmoudi, and A. Arbey, Comput. Phys. Commun. **264**, 107928 (2021), arXiv:2011.02478 [hep-ph] .

[250] G. Belanger, F. Boudjema, A. Pukhov, and A. Semenov, Nuovo Cim. C **033N2**, 111 (2010), arXiv:1005.4133 [hep-ph] .

[251] T. Stelzer and W. F. Long, Comput. Phys. Commun. **81**, 357 (1994), arXiv:hep-ph/9401258 .

[252] J. Schulman, P. Moritz, S. Levine, M. Jordan, and P. Abbeel, arXiv e-prints , arXiv:1506.02438 (2015), arXiv:1506.02438 [cs.LG] .